Molecular Imaging for Personalized Cancer Immunotherapy

By

Emily B. Ehlerding

A dissertation submitted in partial fulfillment of

the requirements for the degree of

Doctor of Philosophy

(Medical Physics)

at the

UNIVERSITY OF WISCONSIN – MADISON

2019

Date of final oral examination: 12/18/2018

The dissertation is approved by the following members of the Final Oral Committee:

Weibo Cai, Professor, Radiology and Medical Physics

Bradley Christian, Professor, Medical Physics and Psychiatry

Jonathan Engle, Assistant Professor, Medical Physics and Radiology

Douglas McNeel, Professor, Medicine

M. Elizabeth Meyerand, Professor, Medical Physics and Biomedical Engineering

Abstract

The development of checkpoint immunotherapy treatments has greatly improved outcomes for many cancer patients relative to the previous standard-of-care. However, only a subpopulation of patients responds to these groundbreaking therapies, and the mechanisms of response are still largely unknown. Molecular imaging techniques, especially direct imaging of the checkpoint molecules themselves, hold potential for stratifying patients, predicting outcomes, and monitoring response. Therefore, positron emission tomography (PET) imaging of three major checkpoint molecules (PD-1, PD-L1, and CTLA-4) in murine models using clinically-available antibodies will be presented in this dissertation, representing many of the first studies in this area.

We developed radiolabeled tracers for the three aforementioned targets: ^{64}Cu-NOTA(DOTA)-ipilimumab and ^{64}Cu-NOTA-ipilimumab-F(ab')$_2$ targeting CTLA-4; ^{89}Zr-Df-pembrolizumab and ^{89}Zr-Df-nivolumab for imaging of PD-1; and ^{89}Zr-Df-atezolizumab and ^{64}Cu-NOTA-αPD-L1 Fab, binding to PD-L1.

The CTLA-4 tracers were first validated through imaging of CTLA-4+ tumor tissues, wherein significantly higher tracer accumulation was noted in positive tumor xenografts. The tracers were then applied in humanized mouse models (immunodeficient mice engrafted with human PBMCs) to track human T-cells, providing noninvasive insight into their accumulation sites following graft-versus-host disease onset. Similarly, PD-1 imaging was first conducted in naïve humanized mice in the graft-versus-host disease setting to prove the tracers' specificity.

Humanized mice bearing tumor xenografts were then imaged with the PD-1 tracer, in order to visualize tumor-infiltrating T-cells. Finally, the αPD-L1 Fab tracer was used to map the normal tissue biodistribution of PD-L1, and ^{89}Zr-Df-atezolizumab proved useful for imaging radiotherapy-induced changes in tumor PD-L1 expression.

Continued work in the immune-imaging space will inevitably lead to great strides in the understanding of these novel treatments, and may have immense impact on patient care in the future. Particularly for immunotherapy treatments, the dynamic information that can be obtained from molecular imaging of immune targets will be of utmost importance as we strive to better elucidate these revolutionary therapies.

Acknowledgements

I would not have made it to this point without the help of innumerable people. To name a few…

Without my professors at Manchester University, I would never have made the decision to come to graduate school in the first place. Thank you, Dr. Klein, Dr. Watson, Dr. Davis, and Dr. Clark, for pushing me to take this step. Also thank you to my friends who supported me through that tough decision and ever since – thank you Miranda and Stephanie!

I'd like to thank my advisor, Dr. Weibo Cai, for his guidance during my time at UW. Thank you for giving me opportunities beyond what I could have expected as a graduate student and for pushing me to become my best, scientifically and professionally.

Thank you to my thesis committee, Dr. Christian, Dr. Engle, Dr. McNeel, and Dr. Meyerand, for your insight, guidance, and time. Also thank you to our collaborators: The McNeel group for their help with PBMC-related experiments, the Humanized Mouse Core for their assistance with the PBL models, the Cyclotron group for all the radionuclides a girl could want, and the Wang Lab at Temple for the αPD-L1 F(ab) agent.

To my labmates – thank you all, past and present, for inspiring me with your work ethic. Even when I thought I was working hard, you all showed me there was always more to be done... Not to mention that you all worked so hard, I always had papers to proofread.

I'd like to thank my classmates, for not only helping me survive the classes (here's looking at you, Alex!), but also for being great friends throughout my time here. From Badger games with

Sarah to Pub Golfing, Ultimate Frisbee, and everything in between, you all have made grad school enjoyable.

I also owe large thanks to the Chemistry-Biology Interface Training Grant program for not only providing me funding, but also for giving me a community and support system outside of medical physics. I'm so glad I had the opportunity to be a part of this wonderful program. Also thank you to the Radiological Sciences Training grant for support for my last two years of graduate school.

To the people outside of school that kept me sane – thank you. To my Barriques family: thank you for keeping me highly caffeinated, helping (forcing?) me to become a morning person, and always giving me perspective. To the Wonders of Physics crew: thank you for helping me remember why science is amazing and why I love it in the first place. Both these groups of people helped me through these last four years more than you'll know.

I have to thank Andrew Shepard: From that freezing cold tour of campus on literally day one, until now, planning our wedding, I never could have made it through this all without you. Thank you for always calming me down (or trying to), being just as competitive as I am, and teaching me all there is to know about living in Wisconsin: like, is it even a pizza if there's not a whole baaaag of cheese on it?

Finally, without my family, I would never have even made it close to this point. Thank you, mom and dad, for always believing in me. Thank you for teaching me that working hard is always worth it and that I can do anything I set my mind to. And thank you, Stephanie and Robby, for keeping me grounded – but you can refer to me as "Doctor Emily" now.

Table of Contents

Contents

List of Figures

List of abbreviations (alphabetical order)

%ID/g: Percent of injected dose per gram of tissue

ATCC: American Type Culture Collection

BAT: Brown adipose tissue

CAR: Chimeric antigen receptor

CT: Computed tomography

CTLA-4: Cytotoxic T-lymphocyte-associated antigen 4

Df: Desferrioxamine

DOTA: 1,4,7,10-tetraazacyclododecane-1,4,7,10-tetraacetic acid

ELISA: Enzyme-linked immunosorbent assay

FBS: Fetal bovine serum

FDA: Food and Drug Administration

FDG: Fluorodeoxyglucose

FITC: Fluorescein

FWHM: Full width at half maximum

Fx: Fraction

HEPES: 4-(2-hydroxyethyl)-1-piperazineethanesulfonic acid

Her-2: Human epidermal growth factor receptor 2

INF-γ: Interferon-gamma

MIP: Maximum intensity projection

MRI: Magnetic resonance imaging

NBSGW: NOD,B6.*Prkdc*^{scid}*Il2rg*^{tm1Wjl}*/SzJKit*$^{W41/W41}$ *mice*

NIR: Near-infrared

NOTA: 2-S-(4-Isothiocyanatobenzyl)-1,4,7-triazacyclononane-1,4,7-triacetic acid

NSCLC: Non-small cell lung cancer

NSG: NOD.Cg-*Prkdc*^{scid}*Il2rg*^{tm1Wjl}/SzJ mice; nod-scid-gamma mice

PAGE: Polyacrylamide gel electrophoresis

PBL: Peripheral blood lymphocyte (mice)

PBMC: Peripheral blood mononuclear cell

PBS: Phosphate buffered saline

PD-1: Programmed death protein 1

PD-L1: Programmed death protein ligand 1

PET: Positron emission tomography

p.i.: post-injection

ROI: Region-of-interest

rpm: Rotations per minute

SD: Standard deviation

SPECT: Single-photon emission computed tomography

$t_{1/2}$: Half-life

TIL: Tumor-infiltrating lymphocyte

TMR: Tumor-to-muscle ratio

Chapter 1

1. Introduction

Immunotherapy treatments have demonstrated incredible benefits for cancer patients and have justifiably become an exciting new staple in the oncology treatment arsenal. For immune checkpoint blockade therapies, two biological pathways are of notable importance, and form the foundation for the work herein: the programmed death protein-1 (PD-1) and cytotoxic T-lymphocyte associated antigen-4 (CTLA-4) pathways. In both cases, these checkpoints serve as mechanisms for cancer cells to escape immune surveillance; however, through interfering with these key interactions, the immune response can be activated and incredible therapeutic results become possible.

While great success has been achieved therapeutically, many questions still remain in regard to the mechanisms of the therapy, as well as the ability to predict and monitor responses. To this end, molecular imaging, particularly positron emission tomography (PET), of these related immune targets may provide noninvasive insight into these immunotherapies and have a significant impact on the future of these treatments.

To address this challenge in the immunotherapy treatment space, we have conducted some of the seminal research into molecular imaging of immunotherapy targets using clinically-available agents. In particular, this thesis addresses the following aims:

1. *The development and validation of PET tracers for imaging of PD-1 and CTLA-4.*
2. *Imaging the trafficking of T-cells during lung cancer tumor development and progression using PET.*
3. *Evaluation of PD-L1 expression using molecular imaging in a variety of models.*

Following the aforementioned Aims, this thesis will include the following:

- **Chapter 2** presents a storybook view of the work completed for this Thesis. This chapter was developed in coordination with the Wisconsin Initiative for Science Literacy (WISL) as part of the WISL Award for Communicating Ph.D. Research to the Public program.
- **Chapter 3** places the current work into the framework of the field, first describing general molecular imaging strategies in cancer, then honing in on immunotherapy treatments and how molecular imaging has been employed to better understand them. Other groups' related studies in this space are presented as well for greater context.
- **Chapter 4** presents the work on the development of PET imaging tracers for PD-1 and CTLA-4 and their initial validations. CTLA-4 tracers (an intact antibody and its $F(ab')_2$ fragment) were explored in tumor-bearing and humanized mouse models, while the antibody-based PD-1 tracer was used to image T-cells in humanized mouse models.
- **Chapter 5** outlines the application of a PD-1 PET tracer in tumor-bearing, humanized mouse models, in order to explore the potential of tumor-infiltrating lymphocyte imaging.
- **Chapter 6** demonstrates the ability of PD-L1-targeted PET to noninvasively visualize changes in PD-L1 expression following radiotherapy treatments. Additionally, a F(ab)-

based imaging agent was tested, which is able to overcome some of the challenges of antibody-based imaging.

- **Chapter 7** describes the conclusions drawn from this work and presents several potential avenues for further advancement and understanding of the results observed.

Chapter 2

2. Molecular Imaging for Personalized Cancer Immunotherapy – the animated version

This chapter was completed in conjunction with the Wisconsin Initiative for Science Literacy (WISL), as part of the WISL Award for Communicating Ph.D. Research to the Public program (http://scifun.org/Thesis_Awards/thesis_awards.html). This program promotes the goal of WISL, that is, to promote literacy in science, mathematics, and technology among the general public, through sharing of these thesis chapters with the public. This chapter therefore presents a cartoon explanation of immunotherapy and our group's contributions to the field. Many thanks to the science communications program of WISL for their guidance and editorial support.

Normally, cells do what they are supposed to do and grow how they're supposed to grow.

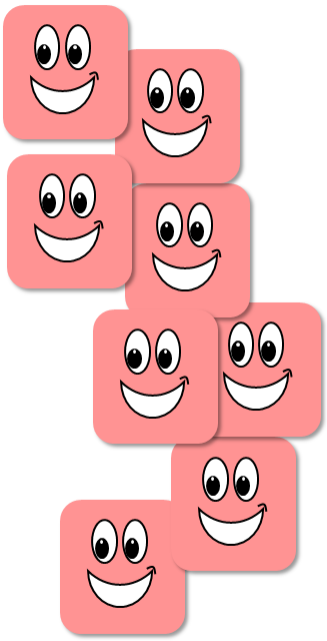

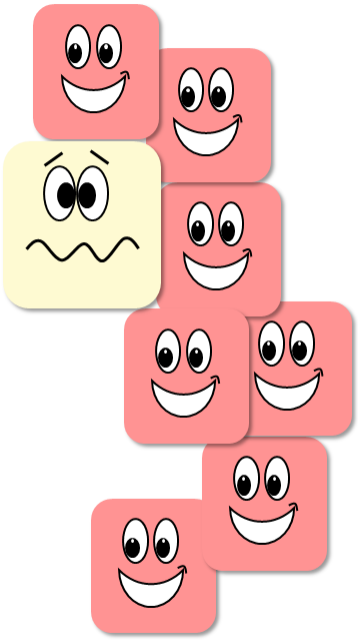

Every now and then, though, one cell mutates and goes rogue.

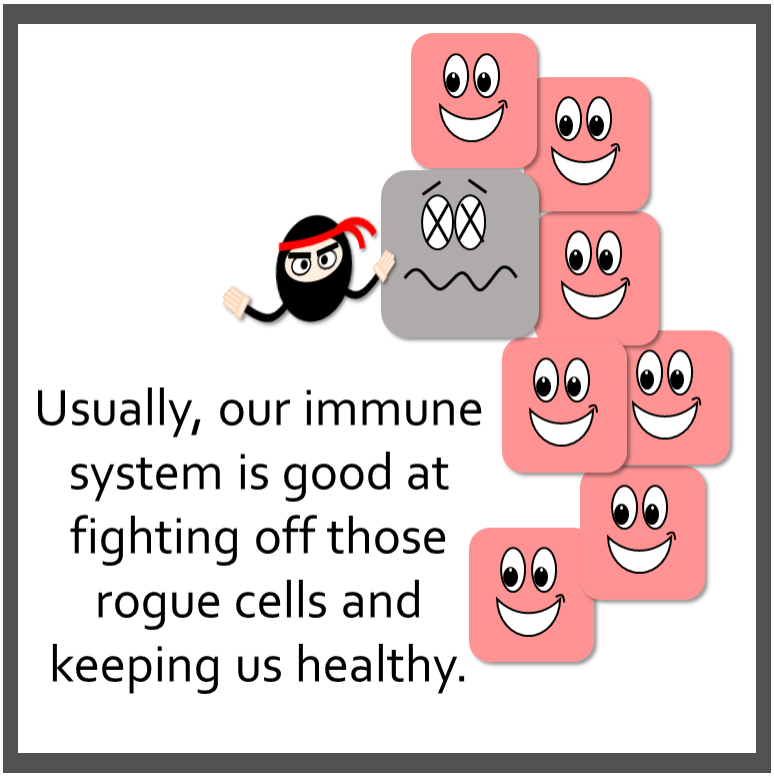
Usually, our immune system is good at fighting off those rogue cells and keeping us healthy.

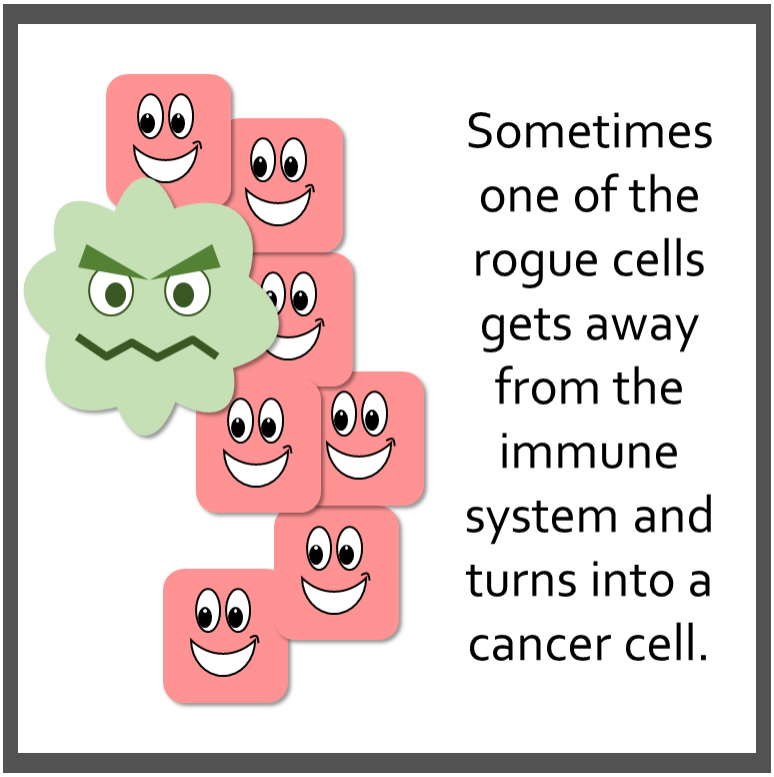
Sometimes one of the rogue cells gets away from the immune system and turns into a cancer cell.

Cancer cells grow really fast and begin to take over.

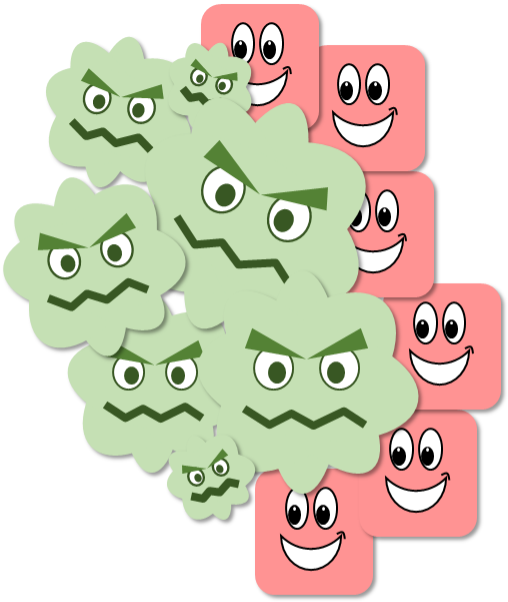

That's what makes them cancer cells.

The cancer cells can hide from the immune system, and the immune cells can't fight them off, because they can't "see" them.

Cancer cells hide from immune cells by covering themselves in molecules that make them look like normal cells. The immune cells think they're seeing a healthy cell, when it's actually cancerous.

The important immune cells for fighting off cancer cells are known as T-helper cells and T-killer cells.

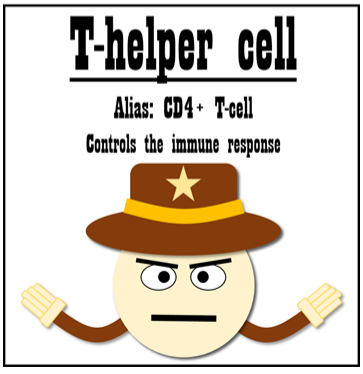

When cancer cells hide from the immune system, the T-killer and T-helper cells can't do anything.
They're not able to fight.

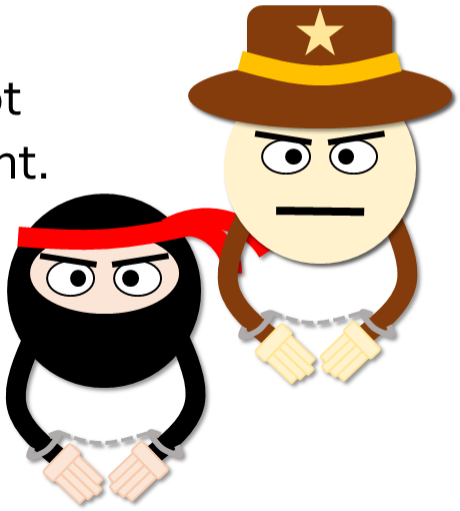

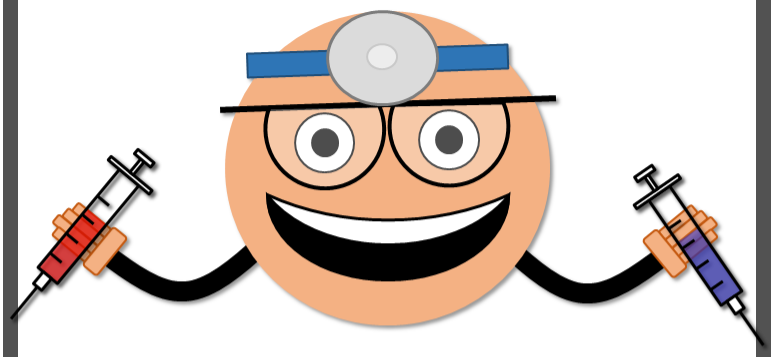

In the last few years, though, some scientists and doctors have made drugs that can help immune cells fight off cancer, called "immunotherapies".

When these immunotherapy drugs are given to cancer patients, the handcuffs can be taken off their immune cells.

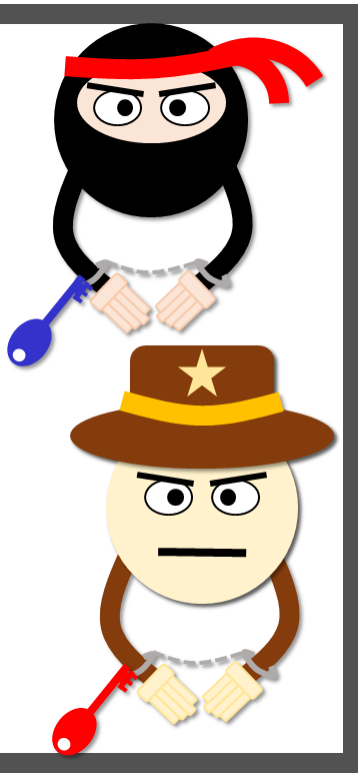

This lets the T-cells do their job and fight off the cancer cells.

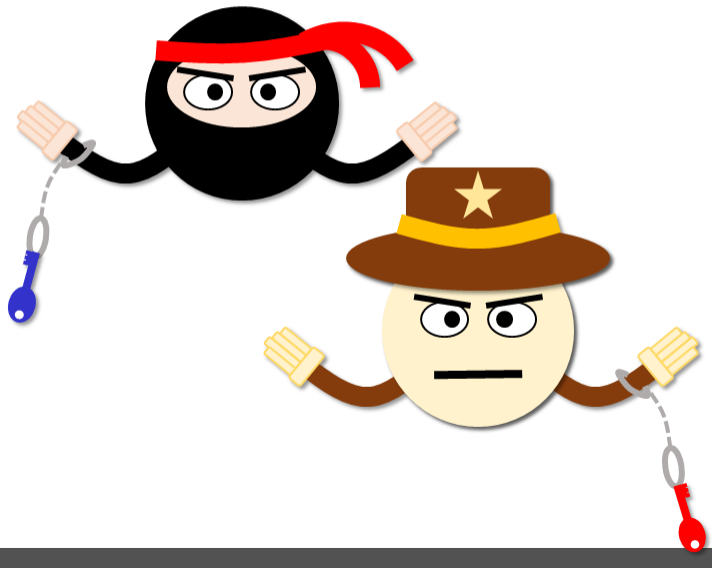

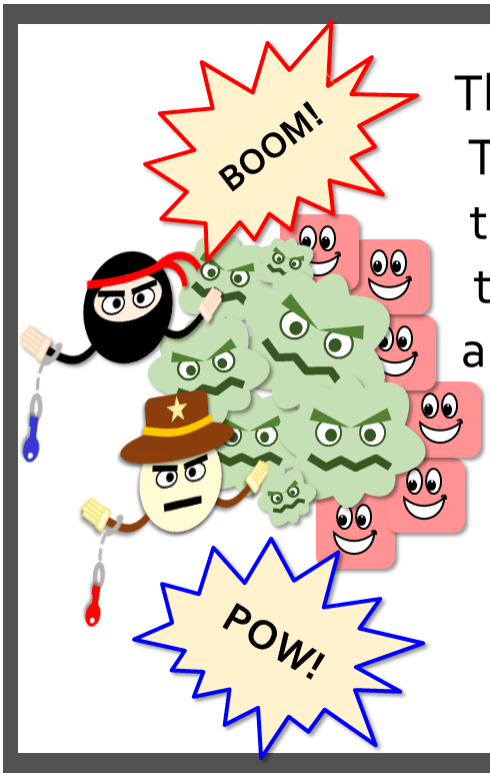

These freed T-cells can then go to the tumor and attack!

For some types of cancer, and certain patients, these treatments can completely destroy their cancer.

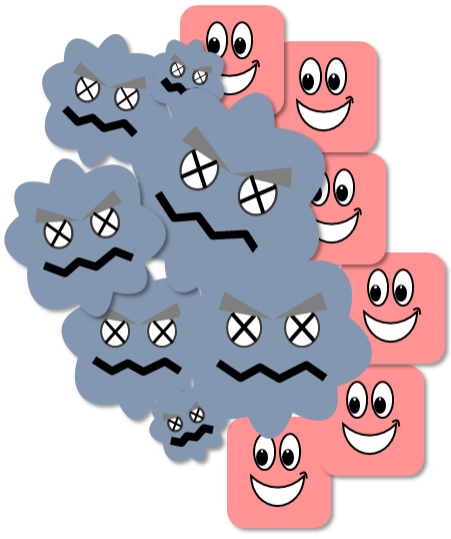

Once in a while, these immune cells get over-excited and can start attacking normal cells.

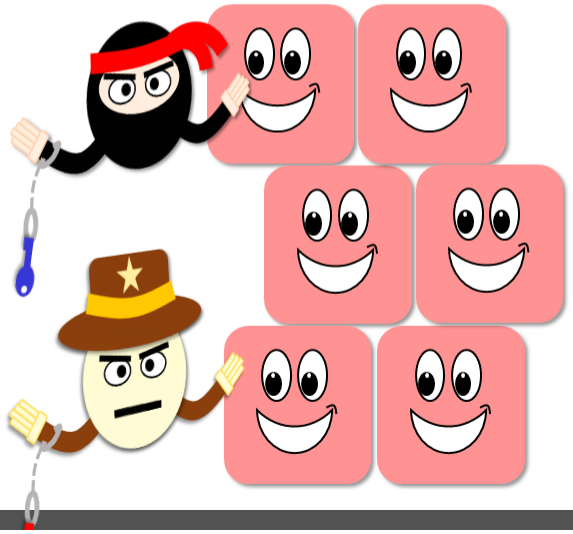

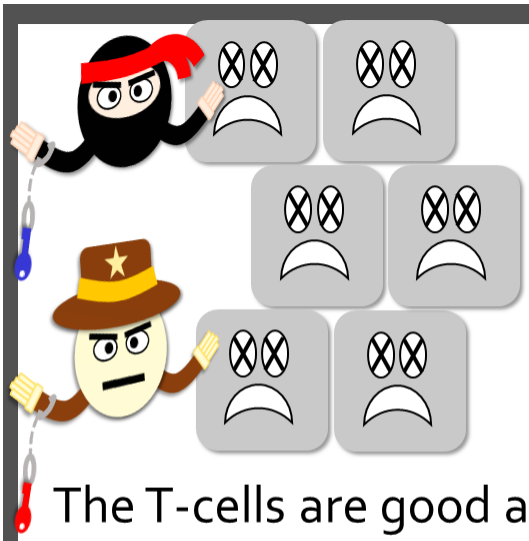

This is bad news for these normal cells…

The T-cells are good at their job and can kill them too.
This leads to many of the side effects of these drugs.

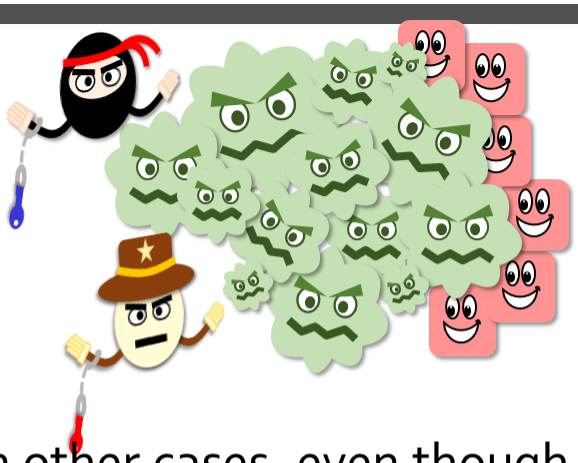

In other cases, even though the immune cells can fight, they aren't strong enough to fight off a tumor, and it keeps growing.

This is where the smart people at the University of Wisconsin come into the picture.

We developed a way to track where these drugs are going, to see where the freed T-cells are going in the body.

We do this by *radiolabeling* the drugs. This means attaching a radioactive atom to the drug, so that when a patient is given the drug, we can see where it goes by tracking that radioactive atom.

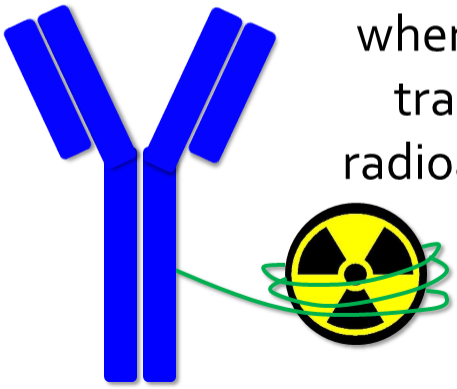

Side note:

When an atom is radioactive, this means it's not stable. To become more stable, the atom releases a particle (in our case, known as a *positron*). After emitting the particle, the atom is more stable. This process is called *radioactive decay.*

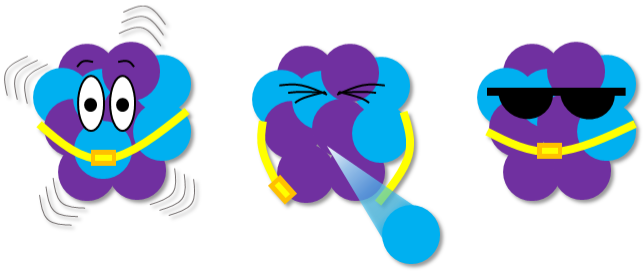

Positrons are the *anti-particle* to the common electron. When two anti-particles meet, they annihilate and turn into pure energy.

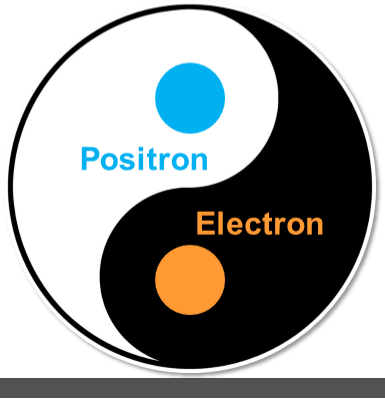

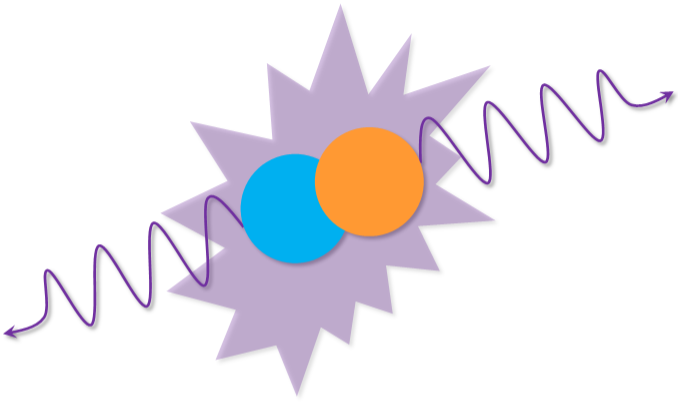

That pure energy is given off, in our case, as two back-to-back gamma rays.

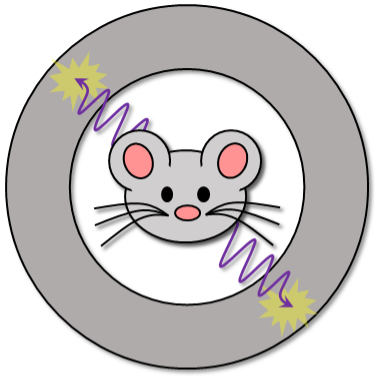

We can see where the positrons are in the body by imaging the patient with a PET scanner, which can detect these two gamma rays.

The "PET" in PET scanner stands for *Positron Emission Tomography*, because these scans use radioactive atoms that release positrons.

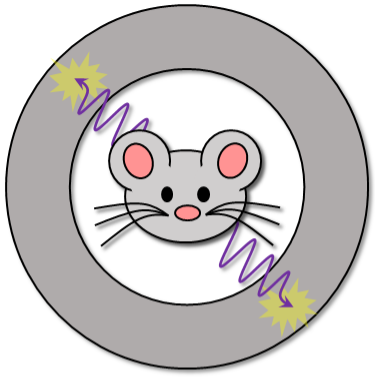

For a PET scan, the patient lays on a bed that moves inside a circular scanner. They stay there for a while so the scanner can detect the radioactive drug.

After detecting all the radioactive decays, we can calculate where in the body those decays happened and figure out where the drug was.

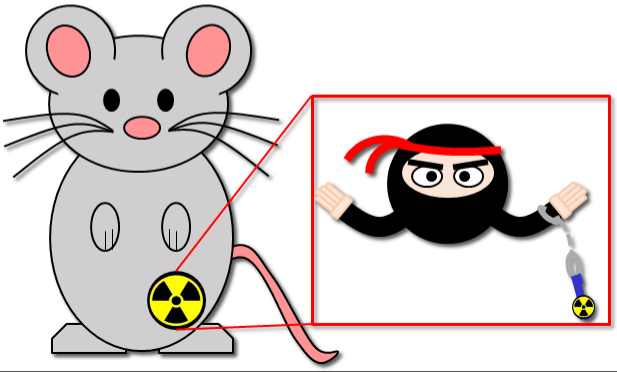

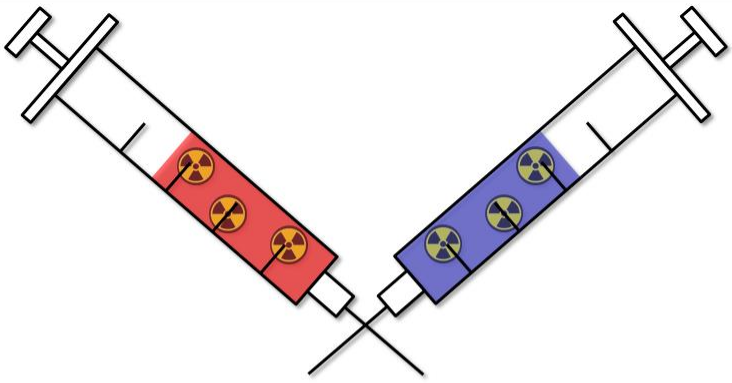

Radiolabeled drugs can be given to patients in very small doses to see how they behave before the right treatment is chosen for someone.

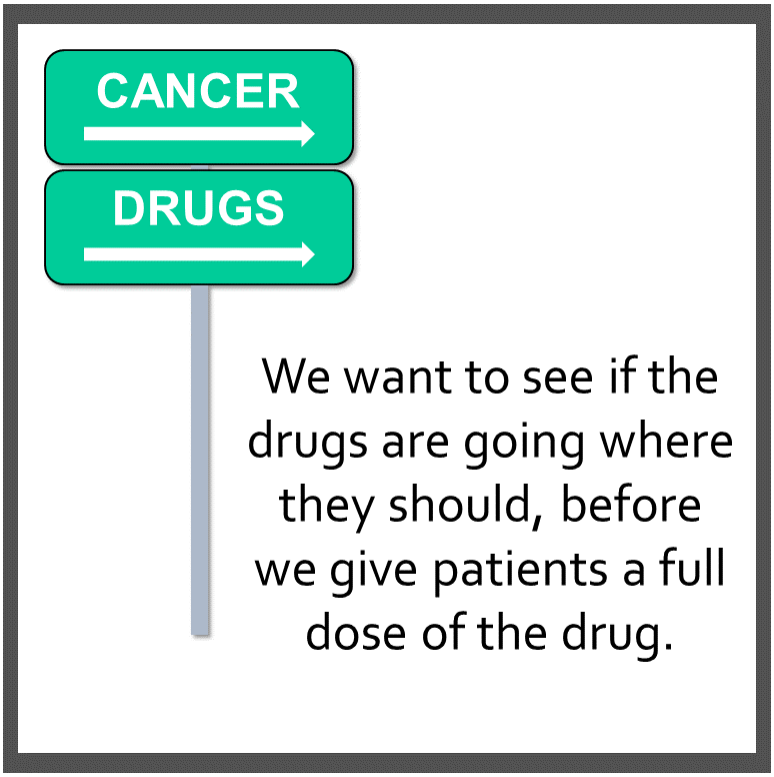
CANCER
DRUGS
We want to see if the drugs are going where they should, before we give patients a full dose of the drug.


Our patients in these studies are actually mice.

These mice have tumors on their back.

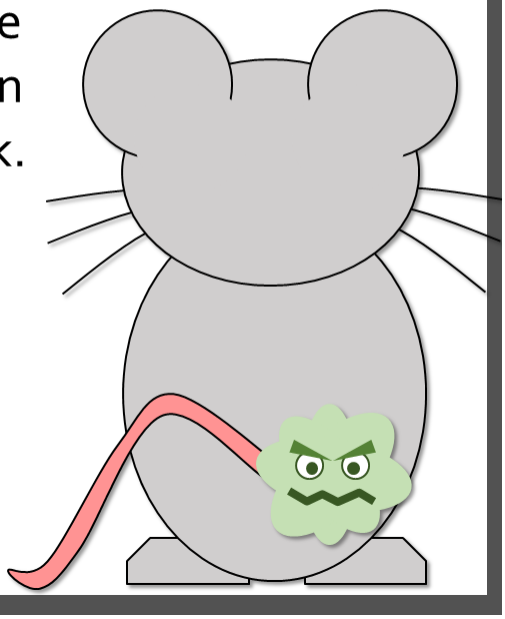

We used three different drugs in these studies. These drugs are already given to cancer patients today, but we want to better understand how they work.

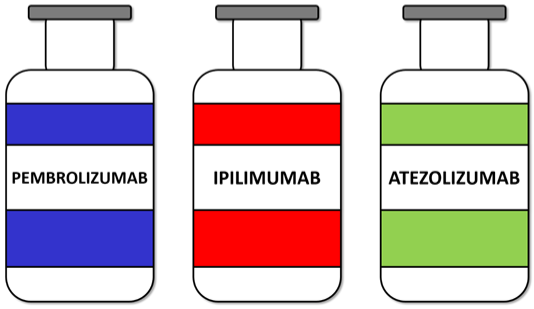

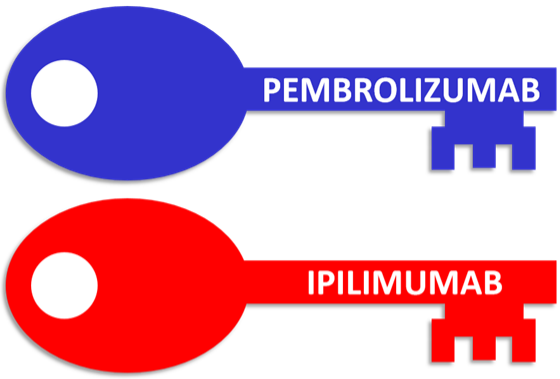

Two of the drugs we use – pembrolizumab and ipilimumab – can unlock the immune cells so they can fight.

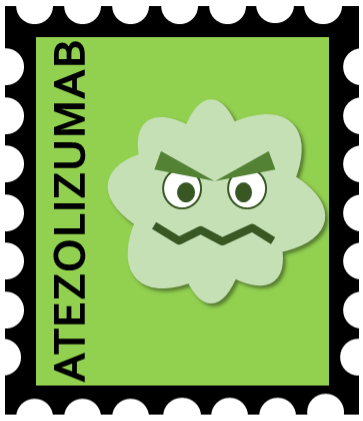

The other - atezolizumab – attaches to cancer cells, and also some other types of cells. It binds to the molecules cancer cells express to hide from the immune system.

If the drugs that unlock the immune cells are radiolabeled, we can see where the drugs (and therefore the T-cells) go.

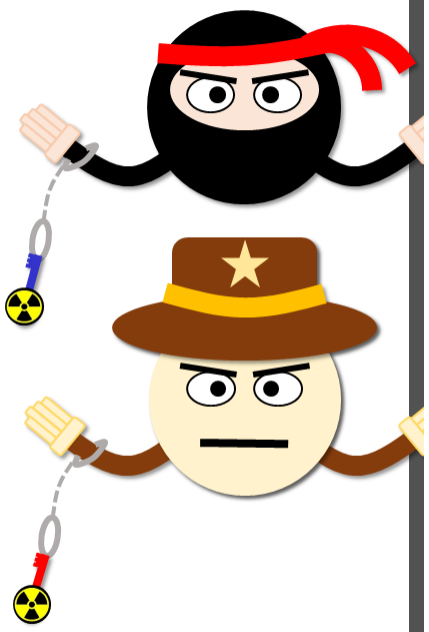

This means we can watch the T-cells fight off the cancer, or even go somewhere they shouldn't be.

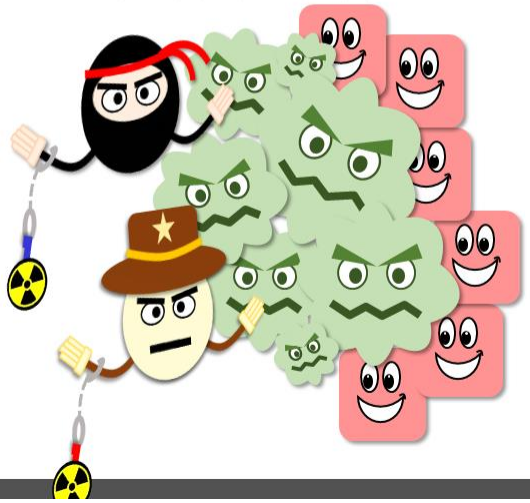

When we inject a radiolabeled drug that attaches to T-cells, we can see where they are in the body.

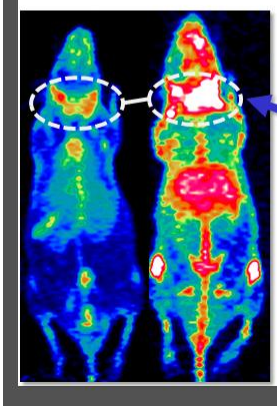

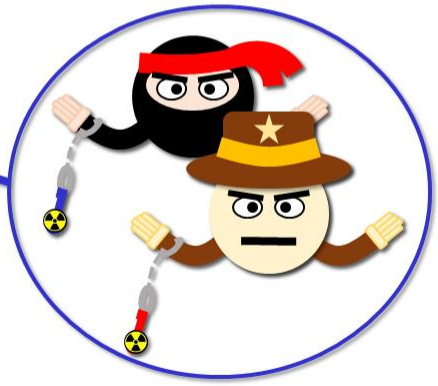

We can also give a drug that attaches to cancer cells and see where they are.

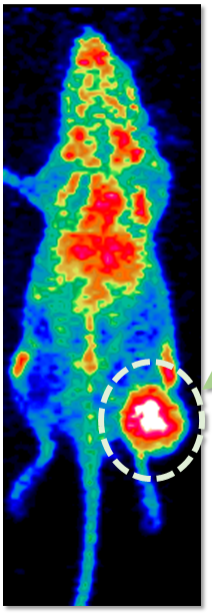

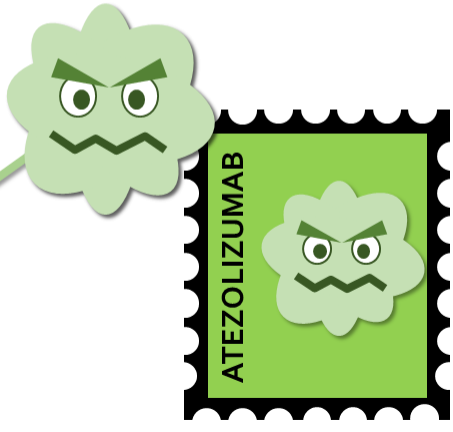

By watching immune cells work, or seeing where cancer cells are, the doctor could then decide what kind of treatment is best for a patient.

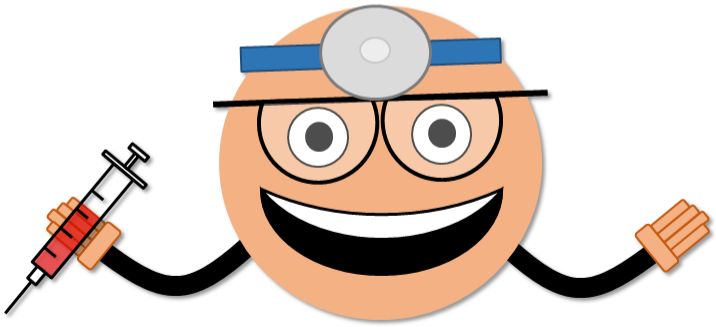

For instance, someone might have a tumor that lights up when we image with atezolizumab.

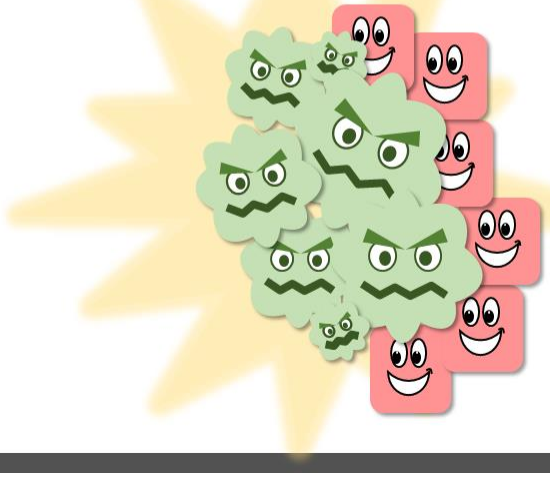

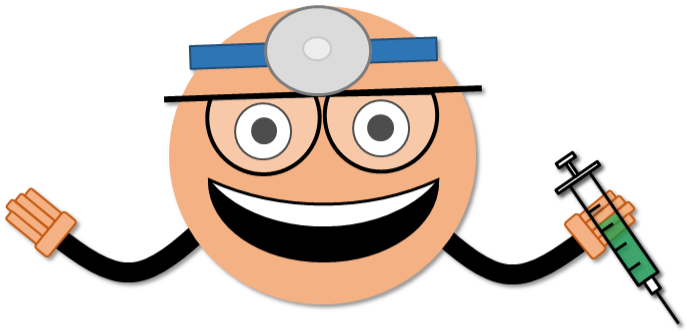

This means that drug might be a good choice because we already know the drug goes to the tumor like it should.

Or let's say we saw a lot of immune cells going to someone's heart instead of their tumor.

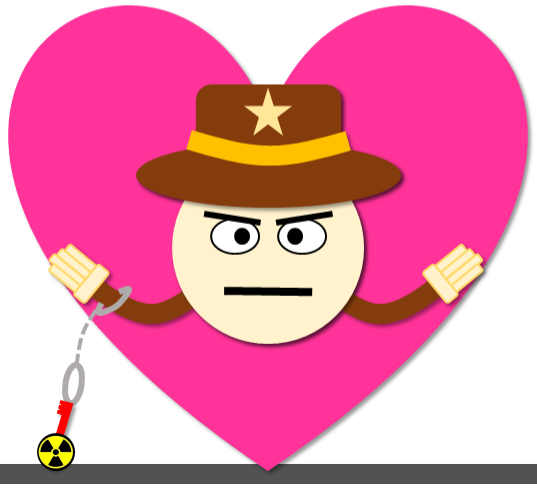

That probably means this person might be susceptible to side effects, and we should either keep a close eye on them or choose a different drug.

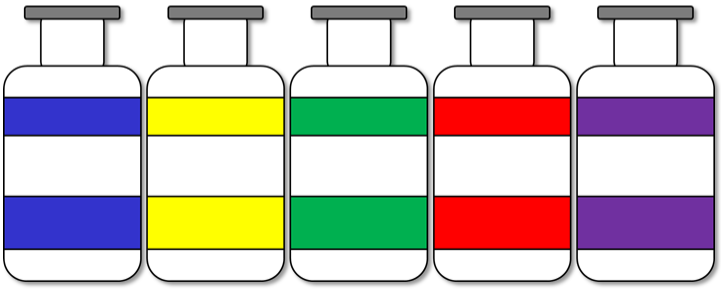

Our group at Wisconsin was the first one to radiolabel these drugs and see where they go in living organisms.

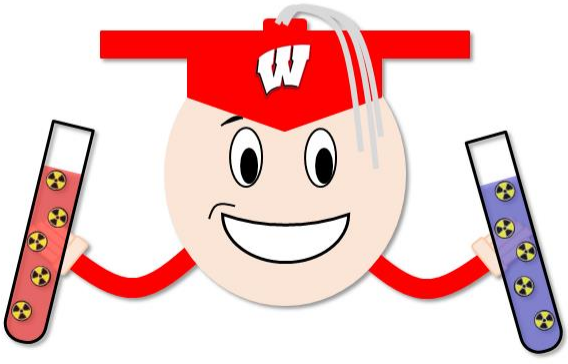

In the future, we hope to use these imaging techniques in people, instead of mice, so we can help doctors better understand their patients.

Picking the right treatment can help cancer patients get back to normal as fast as possible!

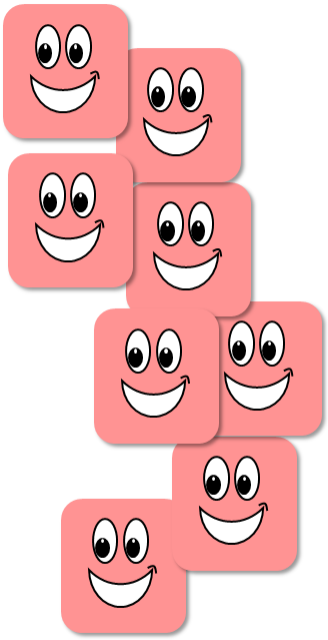

Chapter 3

3. Immunotherapy and molecular imaging*

3.1. Imaging strategies in cancer

Imaging techniques play a critical role in the assessment of cancer patients at all stages of disease including diagnosis, on-treatment monitoring, and therapeutic evaluation. A wide variety of imaging modalities are available to the oncology clinician, each providing complementary information. These modalities can be broadly categorized as providing either anatomical or functional information, or in limited instances, both anatomical and functional insight. **Figure 1** compares the various imaging modalities used clinically for cancer patients.

3.1.1. Anatomical Imaging

Traditional anatomical imaging modalities used in the cancer clinic include computed tomography (CT), X-ray imaging, magnetic resonance imaging (MRI), and ultrasound. These techniques provide a picture of the physical extent of disease, relying on differences in the

* Much of this chapter has been previously published in **9.** Ehlerding EB, England CG, McNeel DG, Cai W. Molecular Imaging of Immunotherapy Targets in Cancer. *J Nucl Med.* 2016. and **10.** Ehlerding EB, Cai W. ImmunoPET: The future of response evaluation for cancer immunotherapy. In: Lopci E, Fanti S, eds. *Atlas of Response to Immunotherapy.* Vol In preparation.: Springer; 2018.

appearance of normal or diseased tissue. These images are invaluable for not only diagnosing and localizing disease, but also for planning of treatments such as external beam radiotherapy. Anatomical imaging modalities are thus indispensable in the cancer clinic; however, they are not without their limitations. Relying on anatomical differences between healthy and diseased tissue does not always provide an accurate representation of the disease state of a patient as adequate contrast is not always present, and competing processes (such as inflammation) can modify the appearance of lesions.

3.1.2. Functional Imaging

To combat these issues, functional imaging techniques can be employed. Molecular imaging strategies such as positron emission tomography (PET), single photon emission computed tomography (SPECT), and optical imaging can enable insight into the molecular processes at play within a cancer patient. Depending on the tracer of choice, different information can be obtained, depending on what biomarker is targeted. PET relies on the use of compounds that are radiolabeled with a positron-emitting radionuclide. This imaging strategy will be outlined in further detail in **Section 3.1.3**, as it forms the basis for much of this work.

SPECT and gamma imaging, like PET, use a radiolabeled tracer which is administered to the patient[11]. For these scans, the radionuclide of choice is a gamma-emitter. The most widely-used gamma-emitting isotope for medical applications is ^{99m}Tc, with a half-life ($t_{1/2}$) of six hours, high gamma emission fraction, and a gamma energy of 140 keV. Other nuclides commonly used in SPECT scans include ^{111}In ($t_{1/2}$: 2.8 days) and ^{123}I ($t_{1/2}$: 13.2 hours). Planar imaging using "gamma cameras" allows for 2D visualization of radiolabeled tracers within a patient, also known as scintigraphy. Such techniques are commonly applied for functional evaluation of the heart and

lungs, for example. Unlike scintigraphy, however, SPECT (as the name implies) provides a 3D tomographic reconstruction of the radionuclide distribution within a patient. While SPECT allows for higher resolution imaging than planar imaging, its resolution is currently limited to about 1 cm, due to the intrinsic properties of the emitted gammas.

Optical imaging employs a tracer with an attached dye, which can emit in the optical or near-infrared (NIR) windows. While still mainly preclinical, this technique allows for high-resolution imaging. The most common application of optical imaging in the cancer clinic is for image-guided surgery, in order to ensure proper margins are removed[12]. In this setting, a tracer that will specifically accumulate in cancerous lesions is administered to a patient, allowing for determination of the extent of disease with an optical imaging probe. The surgeon can then ensure that infiltrating disease is removed by excising all tissue that is marked with the probe. Optical imaging has been limited thus far to these intraoperative applications due to the tissue penetration limit of these probes (much less than 1 cm).

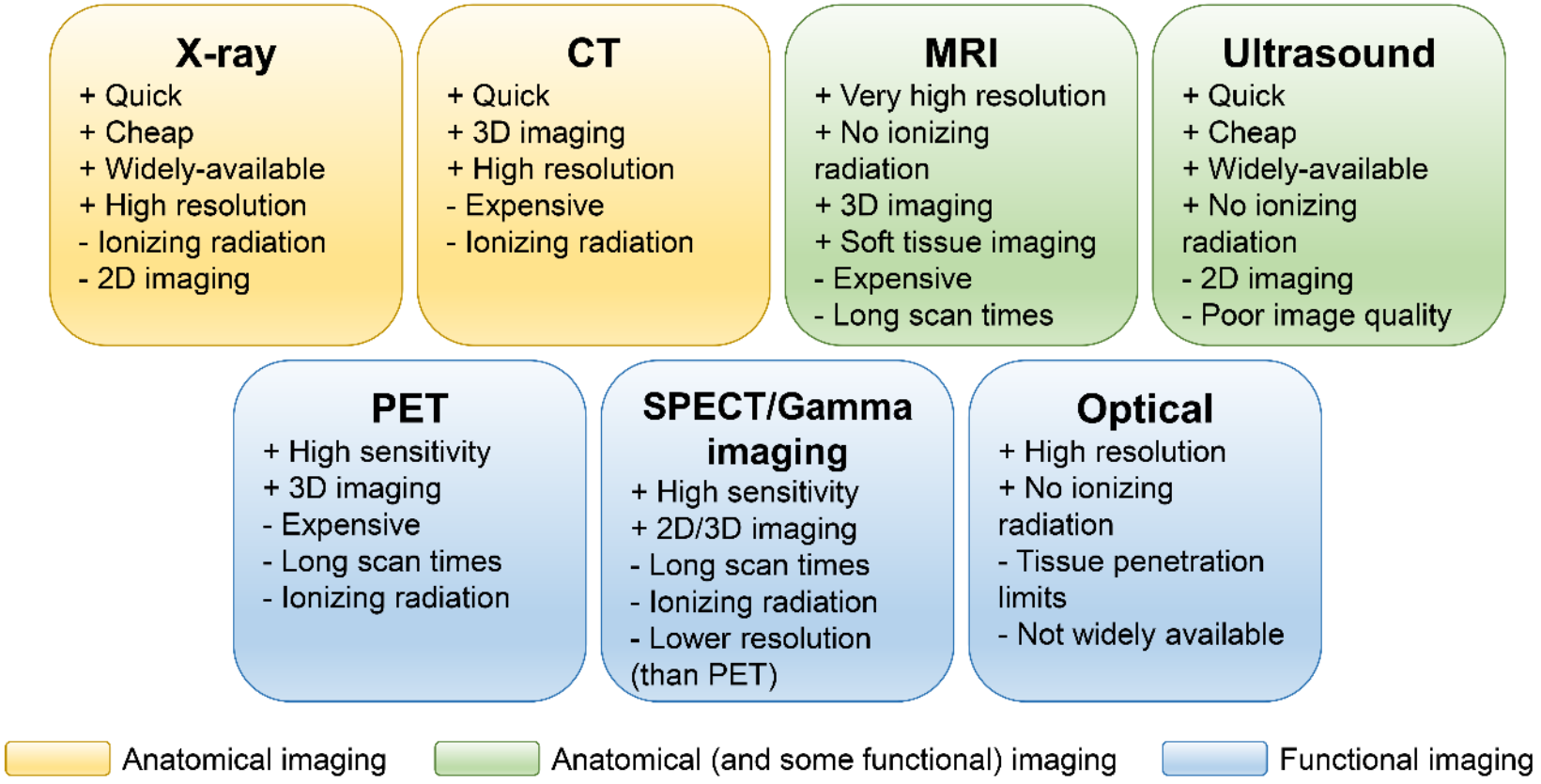

Figure 1. Medical Imaging Tools. *The common imaging modalities used for cancer patients, along with some of their strengths and weaknesses. Modalities on the top row traditionally provide anatomical imaging, although some advanced techniques for functional imaging are being developed. Imaging modalities on the bottom row are functional techniques.*

3.1.3. Positron Emission Tomography

Positron emission tomography (PET) utilizes a positron-emitting radionuclide-labeled tracer to visualize lesions with high sensitivity and contrast[11]. Positron decay can be described by:

$$p^+ \rightarrow n + e^+ + \upsilon + energy$$

and

$${}^{A}_{Z}X \overset{\beta^+}{\rightarrow} {}^{A}_{Z-1}Y$$

where p^+ is a proton, n is a neutron, e^+ is a positron (also β^+), and υ is a neutrino. Thus, a proton is converted to a neutron and positron during radioactive decay, leading to the emission of the positron and a neutrino. This leads to an isobaric decay and a transmutation of elements. When a positron is emitted during radioactive decay, it is able to travel some distance, depending on its energy and the material in which it is traveling, before annihilation with an electron. During annihilation, the masses of both the positron and electron are converted to energy in the form of 511 keV gamma rays.

A PET scanner is comprised of a ring (or other geometrical arrangement) of detectors that are able to capture the back-to-back 511 keV photons that result from the annihilation of the emitted positron and an electron. Because PET scanners rely on the detection of coincident events, they typically do not require absorptive collimators, allowing for higher levels of sensitivity relative to collimated SPECT or gamma cameras. Using so-called “electronic collimation”, scanners are able to determine relatively well which gamma detections originated from the same annihilation event, and thus localize the site of positron emission.

In practice, this localization is limited by several factors, both intrinsic to the system and due to the physics of positron decay as well. Intrinsic contributors to the spatial resolution degradation can include the resolution of the detectors themselves, any applied filters, and the sampling methods in use. Positrons also are able to travel some distance before annihilation, depending on the energy at which they were emitted, meaning that the site of annihilation and the location of the radioactive nucleus are not necessarily the same. Other sources of noise and image degradation include false-positive coincidence registrations, often due to either scattering events (in which one or both of the annihilation photons scatters and veers off the 180° path) or random coincidences (in which photons from two separate annihilations are detected at once). If the radionuclide also emits gammas with energies near 511 keV, these may also be detected and degrade image quality. However, even given all of these factors, most preclinical imaging systems, like the one used in this dissertation work, can achieve spatial resolution on the order of 1.5 mm.

In these studies, a Siemens Inveon small animal PET/CT was used. The PET scanner includes LSO scintillators, which provide an absolute sensitivity of ≥10%. The scanner also allows for 1.4 mm FWHM spatial resolution at the center of the field of view, with an axial field of view of 12.7 cm. The radionuclides of choice in these studies are ^{89}Zr and ^{64}Cu, and their important properties are listed in **Table I**[13]. As radiometal compounds, these nuclides are easily attached to antibody-based tracers using chelation techniques[14].

Table I. Common PET Radiometals. *The radionuclides used in this work. DOTA: 1,4,7,10-tetraazacyclododecane-1,4,7,10-tetraacetic acid; NOTA: 1,4,7-triazacyclononane-1,4,7-triacetic acid.*

Radionuclide	Half-life	Positron fraction	Maximum positron energy	Mean positron range in water	Common chelator(s)
^{89}Zr	78.4 h	0.23	902 keV	1.27 mm	Desferrioxamine (Df)
^{64}Cu	12.7 h	0.19	580 keV	0.56 mm	DOTA or NOTA

3.2. Immunotherapy treatments

The idea of using a person's own immune system to combat disease can be traced back over a century[1, 15]. In the late 19th century, Dr. William Coley (now known as the "Father of Immunotherapy") pioneered the first cancer treatments to harness the power of the immune system[16]. Upon observing that some cancer patients underwent remission after developing skin infections, he began administering both live and inactivated Streptococcus pyogenes to his patients. Presumably, the immune system activation that resulted from these infections lead to the remissions he observed in patients with many types of cancer, including sarcoma and testicular carcinoma. This form of immunotherapy was, however, largely left by the wayside due to the controversy and risks associated with infecting patients.

In the 1950s, a more modern approach to immunotherapy was proposed by Burnet and Thomas with the introduction of the immunosurveillance hypothesis, stating that the immune system plays important roles in identifying and destroying malignant cells[17]. In the following half-century, a large number of studies slowly garnered support for their hypothesis, both preclinically and clinically. Notably, strong correlations were observed between the immunodeficiency of the patient (murine or human) and a higher cancer incidence, indicating that the immune system may indeed play a major role in controlling malignancy. These early studies are well-summarized in the review by Dunn *et al*[17].

Recent years have seen an immense increase in the work in this area. Notably, with a greater understanding of the role of the immune system in cancer prevention and development came the discovery of the so-called "immune checkpoints"[18]. The innate immune system contains a number of checkpoints that ensure immune cells capable of recognizing self-antigens do not destroy healthy tissues (**Figure 2**). Thus, as tumors are self-derived tissues, they often display

these same antigens and avoid immune surveillance[15]. By interrupting these immune checkpoints that have been hijacked by tumors, checkpoint blockade therapy allows the immune system to recognize tumor-associated antigens and consequently destroy these malignant cells[1]. Clinically, two pathways have been extensively studied, and form the foundation of the work herein: the cytotoxic T-lymphocyte-associated antigen 4 (CTLA-4) and programmed death protein 1 (PD-1) pathways[15, 18].

CTLA-4 is predominately expressed on T_{reg} cells and in healthy individuals is critical for preventing autoimmunity[19]. CTLA-4 competitively binds CD80 and CD86 and upon their binding to CTLA-4, immune inhibitory signals are produced. However, CD80 and CD86 also bind to CD28, leading to upregulation of the immune response. In normal situations, then, there is a delicate balance between the stimulatory and inhibitory signals in these pathways. As cancer is able to escape immune surveillance, it was thus hypothesized that blocking this CTLA-4-associated inhibitory pathway could lead to enhanced T-cell activation[20]. The development of CTLA-4-targeted antibodies, including ipilimumab (Yervoy®, Bristol-Myers Squibb), has allowed validation of this hypothesis both preclinically and clinically. By binding to CTLA-4 expressed on T-cells and preventing its binding with CD80 or CD86, a reduction in inhibitory signals has been observed with ipilimumab treatments. Ipilimumab has been extensively utilized in advanced melanoma patients, a population for which 1-year survival rates were historically near 25%[21]. The introduction of ipilimumab, both as a monotherapy and in combination with other treatments, has increased this 1-year survival to above 40% on average[20].

PD-1 expression is found on a variety of immune cells, including T, B, and myeloid cells[22]. Interaction with its ligands, PD-L1 or PD-L2, can induce T-cell suppression in a similar manner to that of the CTLA-4 pathway. The observation that PD-L1 is highly expressed on tumor samples

led to investigation of this pathway for therapeutic interventions. It was determined that the presence of interferon-gamma (IFN-γ) in tumor tissues caused the upregulation of PD-L1 expression by cancer cells, and, upon their interaction with PD-1-expressing immune cells, downregulation of the immune response[23]. Two FDA-approved antibodies have been developed to block this interaction of PD-1 and PD-L1 by binding PD-1: nivolumab (Opdivo®, Bristol-Myers Squibb) and pembrolizumab (Keytruda®, Merck). In melanoma trials, both antibody therapies have demonstrated objective response rates well over 20%[22]. Antibodies targeting the other end of this pathway, namely through binding to PD-L1, have also been developed, including atezolizumab (Tecentriq®, Genentech) and avelumab (Bavencio®, EMD Serono), and have demonstrated similar promising therapeutic outcomes.

There are distinct differences in the mechanisms of the CTLA-4 and PD-1 pathways, although both are considered "immune checkpoints". CTLA-4 mainly functions to regulate system-wide autoimmunity, and as such, the efficacy of CTLA-4 targeted treatments is thought to result from a non-specific upregulation of the immune response. In contrast, the PD-1 pathway is critical for control of inflammatory responses (as PD-L1 is upregulated by IFN-γ), and is thus more focused on the tumor environment. Comparisons of CTLA-4 and PD-1 blockades as monotherapies have indicated that PD-1-targeted treatments may perform better than CTLA-4 therapies, a finding that certainly merits further investigation[24]. Interested readers are referred to the review by Buchbinder *et al*. for further information on the mechanisms of these pathways[25].

As these immune checkpoint treatments are predicated on the upregulation of an immune response, severe immune-related toxicities have manifested in patients treated with these antibodies[26]. Common sites of toxicity include the skin, gastrointestinal tract, liver, and endocrine system. In some cases, these side effects become severe enough that patients have to suspend or

stop treatment altogether, since the problems can even lead to death. As these treatments have become more common, the clinical data regarding the management of immune-related adverse effects has grown and made management of them simpler. However, there is still no reliable measure to identify or predict patients who will be susceptible to side effects prior to their clinical manifestation.

Likewise, the existing data for prediction of response to immune checkpoint blockade is an often-confusing story[27]. In some instances, a correlation has been found between receptor expression and the efficacy of immune interventions[28]; however, this expression seems to be dynamic and heterogeneous and as a result, single-point (both in time and space) immunohistochemical analyses may not provide accurate information at the time of treatment[29]. PD-L1 expression in tumor tissues has been implicated as an important predictive marker for response to blockade of the PD-1 pathway[27]; however, a PD-L1(+) immunohistochemical test is not a universal marker for response to the therapies as PD-L1(-) patients can also demonstrate responses. These biopsy-based companion diagnostic tests provide a detailed look at the cellular distribution of a given marker (in this case, PD-L1). The limitation of these tests is, however, that the tissue sample only represents a single point, or sometimes a limited number of points, within the tumor at a single time. The expression of cancer biomarkers can vary widely across a single lesion, and particularly from primary to metastatic sites. This is especially highlighted in the immunotherapy space through findings that the presence of CTLA-4 in tumor tissues can change widely from primary tumors to lymph node metastases[30]. There is thus an unmet need to not only identify predictive and prognostic biomarkers for cancer immunotherapy patients, but also to obtain a whole-body longitudinal picture of the immune marker status of patients as well.

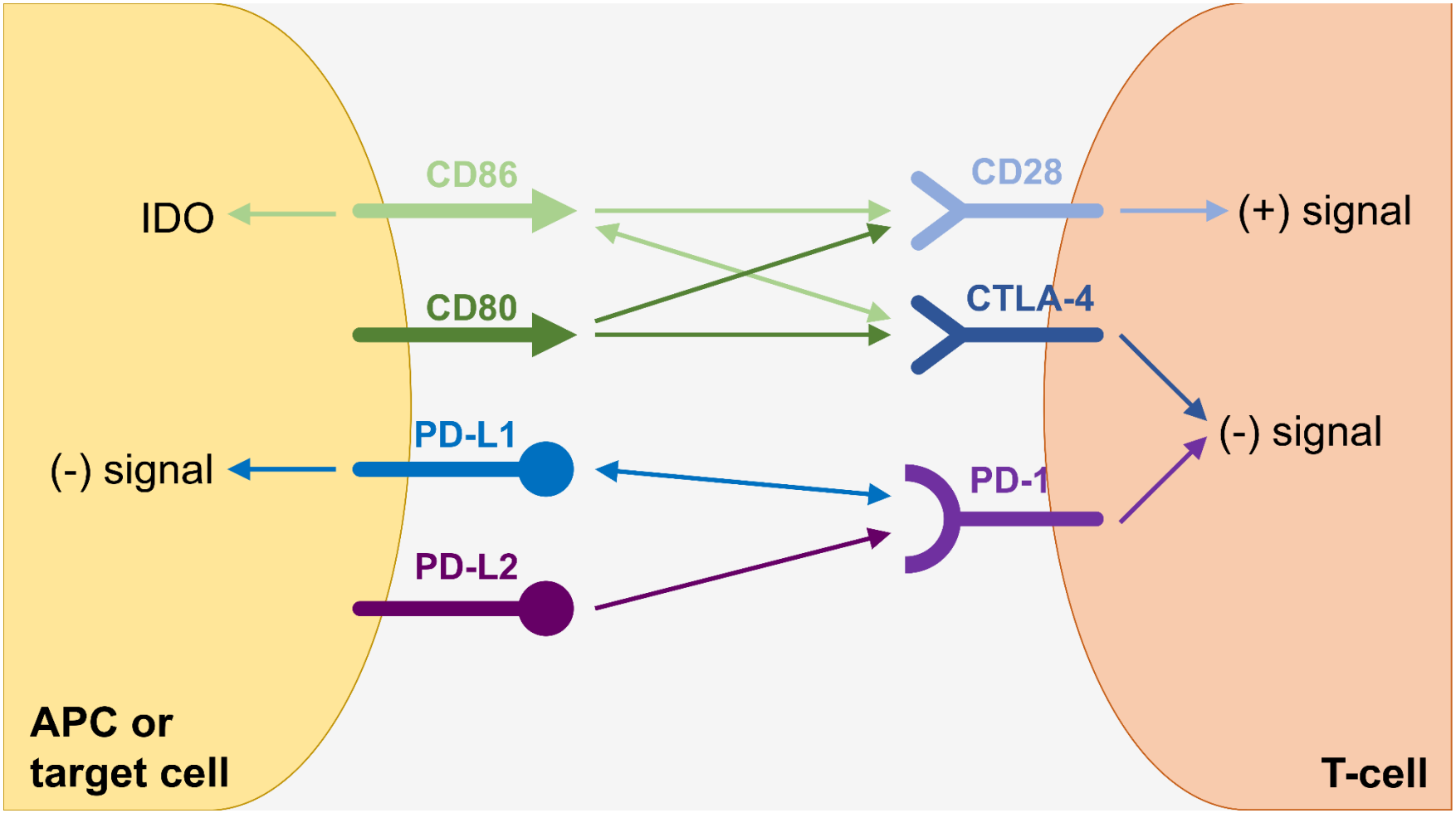

Figure 2. Immune Checkpoint Pathways. *Adapted from [1]. Arrows indicate binding pathways that may either inhibit or up-regulate the action of T-cells and antigen presenting cells. Abbreviations: IDO: Indoleamine 2,3-dioxygenase; CD: cluster of differentiation; PD-L1/2: programmed death protein ligand 1/2; APC: antigen-presenting cell; CTLA-4: cytotoxic T-lymphocyte associated antigen 4; PD-1: programmed death protein 1.*

3.3. Molecular imaging and immunotherapy

Molecular imaging can provide nearly real-time information about receptor expression levels, allowing physicians to predict which patients may benefit from immunotherapy and account for response differences between individual patients. In return, these prescreening measures may not only spare patients ineffective therapy and potential adverse effects, but will also have implications economically as cancer therapy remains costly and time-intensive[31]. In addition to patient stratification, molecular imaging of immunotherapy targets may provide insight into the status of the immune system and overall disease progression. From a scientific perspective, imaging these targets can enable a greater understanding of disease mechanisms and therapeutic outcomes.

Since ^{18}F-fluorodeoxyglucose (FDG) PET monitors cellular metabolism and immunotherapy elicits a natural inflammatory response, traditional PET imaging using ^{18}F-FDG has proven inadequate in examining responses to immunotherapy[32]. Nonetheless, immunotherapy patients are still routinely examined with ^{18}F-FDG, causing disease monitoring to be inherently subjective. Clearly, a decrease in tumor metabolism would indicate an effective intervention for more traditional treatments like chemotherapy, but this is not always the trend observed with immunomodulatory interventions. So-called “pseudo-progression”, in which increased FDG accumulation is observed after patients who eventually respond have received therapy, has warranted many studies to be performed for evaluation of FDG patterns in immunotherapy patients[33]. As immunotherapy treatments become more common, the typical findings on FDG scans of these patients have become better-studied, and a few trends have emerged. For instance, there is some evidence that increased uptake of FDG in normal lymphoid organs after checkpoint

treatment may be a marker for immune activation and subsequent response[34]. In addition, a decrease in tumor metabolic volume has been noted in responsive patients[35]. In some instances, the manifestations of response even seem to be contrary to one another. For example, in metastatic melanoma patients four patterns of response have been described: (1) shrinkage in baseline lesions without new lesion appearances; (2) durable stable disease; (3) response after an initial increase in total tumor burden; (4) response in the presence of new lesions[33, 36]. However, it appears that for every trend, there is a patient who displays the opposite findings. There is therefore a great need for development of better molecular imaging monitoring techniques in the immunotherapy space.

3.3.1. Previous immunoPET studies for immunotherapy checkpoint targets

Several preclinical trials have shown that noninvasive imaging techniques using PET, SPECT, and optical imaging are viable platforms for determination of receptor density and hold promise for stratification of patients for future immune therapies. In addition, by tracking the fate of immune cells *in vivo*, researchers may be able to monitor adverse effects related to the on-target but off-tissue accumulation of antibodies and elucidate the mechanisms that underlie these restrictive toxicities. Molecular imaging techniques thus have nearly limitless potential to revolutionize the emerging field of immunotherapy.

3.3.1.1. Programmed Cell Death Protein 1 (PD-1)

PD-1 is expressed on the surface of T-cells, B-cells, and natural killer cells and acts as a negative regulator of T-cell activity[37]. PD-1 expression was also recently reported in certain subpopulations of melanoma cells[38]. PD-1 may interact with one of its two endogenous ligands, known as PD-L1 or PD-L2, which are found on the surface of antigen-presenting cells or tumor

cells. Upon PD-1 interaction, a kinase signaling pathway that normally results in T-cell activation is inhibited; thus, immunotherapy strategies that interfere with the PD-1 checkpoint have shown enhanced anticancer activity in the clinic. There are currently two FDA-approved antibodies targeting PD-1: pembrolizumab (Keytruda®, Merck & Company, Inc.) and nivolumab (Opdivo®, Bristol-Myers Squibb)[39]. While these two antibodies have the same biological target, their binding affinities and production source are different. The binding affinity of pembrolizumab (<100 pM) for PD-1 is nearly 10-fold higher than that of nivolumab (3 nM). The source of production also differs, as pembrolizumab is a humanized murine antibody while nivolumab is a fully human antibody. Despite these differences, the objective response rates in advanced melanoma were similar between pembrolizumab (26-38%) and nivolumab (31-40%)[39], suggesting that the therapeutic dosages may be saturating the receptor in therapy. Since it is more tumor-focused, PD-1 targeted treatments have shown fewer adverse effects than those employing the CTLA-4 pathway; however, significant immune-mediated adverse events were still reported during clinical trials[40, 41].

Imaging techniques targeting PD-1 are unique because they do not allow visualization of the primary tumor; rather, PD-1-targeted probes allow for imaging of PD-1 expressed on immune cells. For example, Natarajan *et al.* developed a PET tracer to image PD-1-expressing tumor-infiltrating lymphocytes (TILs)[3]. The murine anti-PD-1 monoclonal antibody was prepared with 1,4,7,10-tetraazacyclododecane-1,4,7,10-tetraacetic acid (DOTA) for radiolabeling with ^{64}Cu ($t_{1/2}$: 12.7 h). The biodistribution of the tracer was mapped in a transgenic mouse model of melanoma. The tracer effectively accumulated in the tumor with 7.4 ± 0.71 percent injected dose per gram of tissue (%ID/g) at 48 h post-injection (p.i.), resulting in a tumor-to-muscle ratio of approximately 11 (**Figure 3A**). Blocking studies using excess antibody decreased

tumor uptake to 4.51 ± 0.26 %ID/g at 48 h p.i., which further validated the tracer's specificity for PD-1. Additionally, bioluminescent imaging of luciferase-transfected TILs confirmed that the tumor uptake was due to lymphocyte infiltration of the tumor (**Figure 3B**), showing that PET may be used for the noninvasive imaging and determination of PD-1 expression *in vivo*.

In another study, Hettich *et al*. developed novel radiotracers for PET imaging of both PD-1 and PD-L1[8]. Melanoma tumor-bearing mice were locally irradiated to induce TIL infiltration into the tumor, most of which were CD8+ effector cytotoxic lymphocytes uniformly expressing PD-1. The researchers employed a ^{64}Cu-labeled anti-PD-1 tracer for PET imaging, and found that the tracer had increased uptake in the irradiated tumor, consistent with higher CD8+ TIL levels. Uptake could also be reduced by blocking the antigen (**Figure 3C**). Furthermore, the authors employed a PD-L1 imaging tracer that will be discussed in the PD-L1 section.

As will be further presented in this work, there are a number of advantages to using clinically-available antibodies for molecular imaging strategies. A major benefit is that these agents are much more readily translatable to human patients than murine platforms. To this end, a number of studies have been performed using clinically-approved antibodies, as well as novel human antibody platforms. Notably, the work presented in **Chapters 4 and 5** of this work laid much of the foundation for the following studies.

We developed and first reported ^{89}Zr-labeled nivolumab and validated its potential for identifying tumor-infiltrating T-cells, as will be outlined in **Chapter 5**[42]. Cole *et al*. further tested ^{89}Zr-labeled nivolumab in healthy non-human primates to determine its natural biodistribution[43]. Consistent with the clearance patterns of intact antibodies, the authors noted significant accumulation of the tracer in the liver. Through co-administration of cold (non-radiolabeled) nivolumab at both 1 mg/kg and 3 mg/kg, the uptake of ^{89}Zr-nivolumab was significantly reduced

in the spleen, indicating that this organ was a site of specific PD-1 binding. This study pointed to the importance of determining sites of specific binding for tracers, even in non-therapeutic settings.

As will be presented in **Chapter 4**, our group developed ^{89}Zr-labeled pembrolizumab and validated it in humanized mouse models[44]. Gambhir's group expanded upon this work and further developed both ^{64}Cu- and ^{89}Zr-labeled pembrolizumab and explored their ability to detect tumor-infiltrating lymphocytes[45]. Using NSG mice engrafted with both human peripheral blood cells and human skin cancer xenografts, significantly higher uptake of the tracer was observed in tumor regions when compared to mice without human immune cells, indicating specific binding of the tracer to these cells. These reports also included dosimetric studies in preparation for possible clinical translation of ^{64}Cu-labeled pembrolizumab[46].

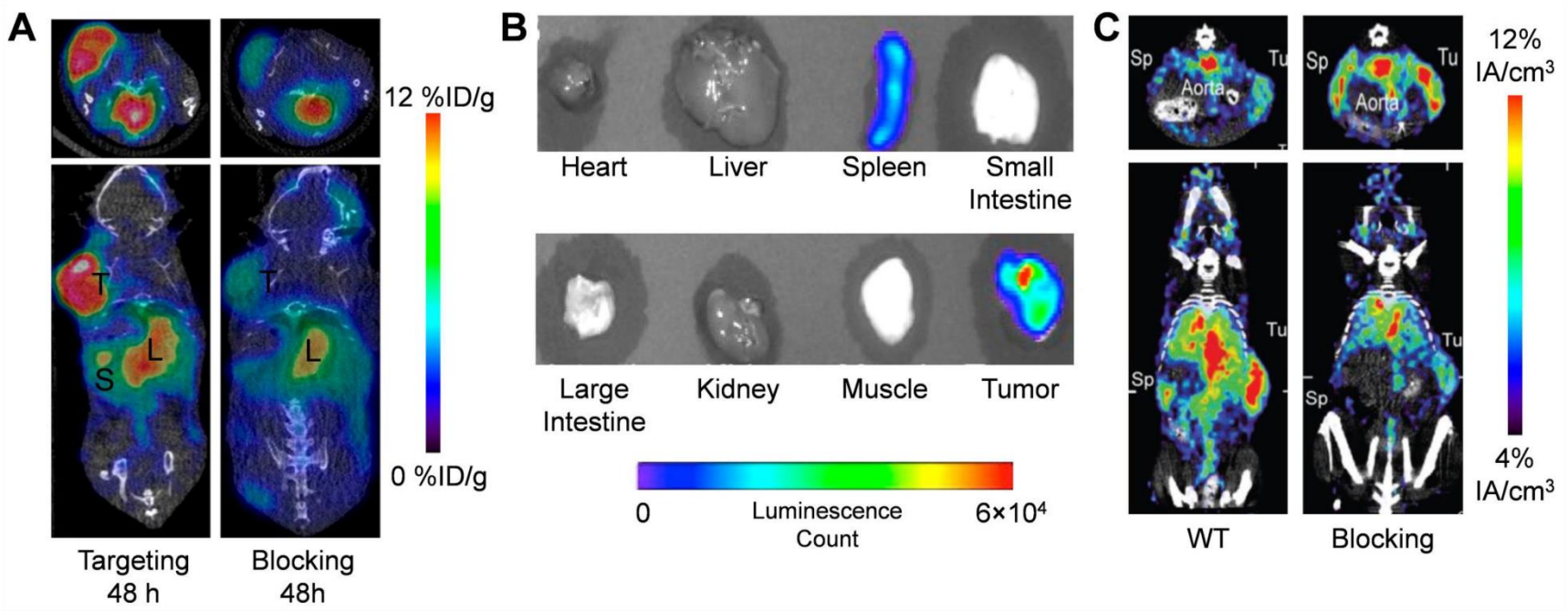

Figure 3. Previous PD-1-targeted Imaging Studies. *(A) Subcutaneous melanoma xenografts could be visualized upon injection of a ^{64}Cu-labeled anti-PD-1 antibody. The specificity of the tracer was confirmed through a blocking study. Adapted from [3]. (B) Bioluminescence imaging of luciferase-transfected PD-1-expressing T_{reg}-cells validated the binding and tumor infiltration of T lymphocytes. Adapted from [3]. (C) PET imaging of melanoma tumor-bearing mice 24 h after injection with a ^{64}Cu-NOTA-PD-1 antibody, following tumor irradiation to increase lymphocyte infiltration. For the blocking study, mice were injected with cold antibody 24 h before tracer injection. Sp: spleen; Tu: tumor. Adapted from [8].*

3.3.1.2. Programmed Death Ligand 1 (PD-L1)

In contrast to PD-1, PD-L1 is naturally expressed on a number of tissues, including some tumor cells, vascular endothelium, hepatocytes, mesenchymal stem cells, T- and B-cells, macrophages, and mast cells[47]. Immune-privileged tissues such as the eye and placenta also display high levels of PD-L1. The blockade of PD-L1 leads to enhanced T-cell activity and inhibition of immune-mediated tumor evasion[47, 48]. As PD-L1 is often expressed on the actual tumor cells, models for imaging this target have proven to be more attainable than those for targets that are only expressed on immune cells. PD-L1 expression is often heterogeneous even within a given cancer subtype, and immunohistochemistry techniques are susceptible to errors as a result[29]. Of note, treatment with pembrolizumab requires >1% of NSCLC cells to be PD-L1 positive, so a PD-L1 tracer may also find application in the planning of these treatments. Consequently, several anti-PD-L1 imaging agents have been developed to quantify PD-L1 expression in preclinical settings.

Maute *et al.* engineered a high-affinity PD-1 non-antibody variant for both immunoPET imaging and immunotherapy in a colon cancer model[4]. Rather than an agent that behaves like PD-L1 and binds to PD-1, directed evolution by yeast-surface display was utilized to create a high affinity (110 pM) competitive antagonist of human PD-L1. Genetically engineered CT26 colon cancer models that were either PD-L1 negative or positive were employed for tumor treatment studies, where the PD-L1 antagonist was shown to decrease tumor growth out to two weeks. Additionally, conjugation of the antagonist with ^{64}Cu-DOTA allowed for PET visualization of its distribution in both xenografts, with a nearly two-fold increase in signal for the positive tumors over negative as seen in **Figure 4A**. Thus, this agent shows significant promise in theranostics for PD-L1-expressing cancers.

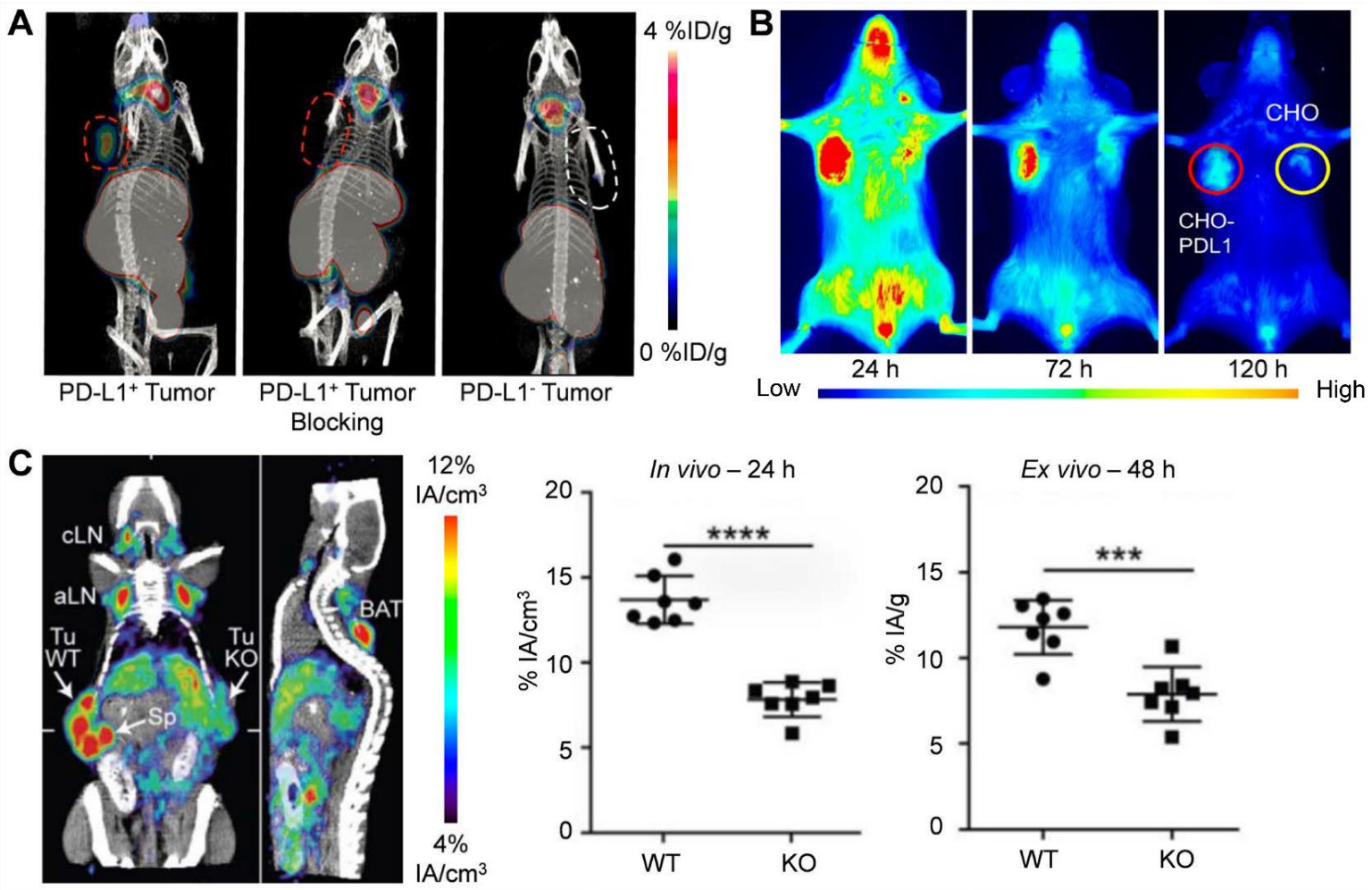

Figure 4. Previous PD-L1-targeted Imaging Studies. *(A) A ^{64}Cu-labeled PD-L1 antagonist allows for distinction between tumors with high and low expression levels of PD-L1 at 1 h post-injection. Adapted from [4]. (B) Near-infrared images acquired in the 800 nm channel show significant differences in uptake of PD-L1-antibody between PD-L1 positive and negative tumors. Adapted from [7]. (C) PET imaging of mice subcutaneously implanted with PD-L1 positive (WT) or PD-L1 knockout (KO) tumor cells was performed 24 h after mice were injected with ^{64}Cu-NOTA-PD-L1 antibody. Sp: spleen; Tu WT: wild-type tumor; Tu KO: PD-L1 KO tumor; cLN: cervical lymph node; aLN: axillary lymph node; BAT: brown adipose tissue. Adapted from [8].*

Using the mouse and human cross-reactive antibody MPDL3280A (atezolizumab), Chatterjee *et al.* developed a multimodality SPECT and near-infrared imaging agent for visualizing PD-L1-expressing tumors[7]. Previously, MPDL3280A was proven effective in clinical trials for non-small cell lung cancer, bladder cancer, melanoma, renal cell carcinoma, and others[49], prompting researchers to utilize this antibody for imaging of PD-L1 expression. Specifically, Chinese hamster ovary tumor xenografts with and without constitutive stable PD-L1 expression were studied using the ^{111}In-labeled antibody ($t_{1/2}$: 2.8 days), as well as a dye-labeled version. Both studies indicated that relative PD-L1 expression could be determined (**Figure 4B**). Also, predosing with cold antibody was found to improve tumor uptake through saturation of receptors on splenocytes and increased blood circulation time. Triple-negative breast cancer xenografts, where PD-L1 expression was not genetically engineered, were also evaluated in this study, with higher reported values of PD-L1 expression corresponding to higher %ID/g values. These studies indicate that clinically-employed antibodies may be modified with imaging agents to determine their biodistribution prior to the administration of therapeutic levels, and patients could ultimately be selected for particular therapies based upon these results.

Similarly, Heskamp *et al.* radiolabeled an anti-PD-L1 antibody with Indium-111 for SPECT imaging. The biodistribution of the tracer was mapped in mice bearing subcutaneously-implanted breast cancer cells with varying PD-L1 expression levels[50]. MDA-MB-231 was found to express PD-L1 in over 90% of cells, while MCF-7 exhibited only minimal expression (0.1%). Tracer uptake values were found to correlate with PD-L1 expression levels; thus, this tracer was able to distinguish PD-L1 expression levels within cell lines of the same cancer type.

As previously discussed, Hettich *et al.* designed two PET tracers for targeting PD-1 and PD-L1[8]. Mice were subcutaneously implanted with PD-L1 positive and PD-L1 knockout cells on opposing flanks. Both *in vivo* imaging and *ex vivo* analysis confirmed that uptake of the anti-PD-L1 tracer was specific for PD-L1-expressing melanoma tissue, while the PD-L1 knockout tumors showed minimal uptake of the tracer (**Figure 4C**). Interestingly, the authors noted increased uptake of the PD-L1 tracer in brown adipose tissue, suggesting that this tissue may be immunologically relevant.

In another study, Josefsson *et al.* developed an ^{111}In-labeled murine anti-PD-L1 antibody for SPECT biodistribution studies and potential radioimmunotherapy application[51]. Imaging in mice bearing NT2.5 murine mammary xenografts revealed high uptake in the tumor, as well as the spleen, liver, and thymus. However, spleen uptake was greatly reduced upon predosing with cold antibody, from nearly 60 %ID/g with pure tracer to 11 %ID/g with the administration of 100-fold excess antibody. While this predosing strategy allowed for researchers to clearly visualize the tumors, this also resulted in the administration of high doses of antibody prior to imaging - a non-ideal situation clinically. However, the authors note that radioimmunotherapy may be performed in conjunction with the traditional antibody-based therapy, and it is in this situation that predosing becomes valuable. Theoretical dosimetry calculations using uptake data from pure tracer injections indicate therapeutic absorbed doses to the tumor using both ^{90}Y ($t_{1/2}$: 64.1 h) and ^{177}Lu ($t_{1/2}$: 6.65 days), but also high spleen doses that may be toxic. Further evaluation of the proposed radioimmunotherapy with this anti-PD-L1 agent is therefore warranted.

Using a murine-specific anti-PD-L1 antibody, Kikuchi *et al.* visualized changes in PD-L1 expression following various treatment regimens[52]. Significantly increased tracer accumulation was noted in both head and neck squamous cell carcinoma and melanoma models after

radiotherapy, although the two tumor types required different irradiation schedules in order for the PD-L1 expression to change. The authors also subjected the mice to anti-PD-1 therapy, but did not note any significant differences in the PET tracer accumulation after this intervention. In a similar manner, Truillet and co-workers visualized changes in PD-L1 expression after standard-of-care chemotherapy in murine models[53]. Other PET imaging agents, including peptides[54], proteins[55], and antibody variants[56] have also been employed for imaging PD-L1. Our imaging work with PD-L1 will be presented in **Chapter 6**.

3.3.1.3. Cytotoxic T-lymphocyte associated antigen 4 (CTLA-4)

CTLA-4 is a transmembrane inhibitory receptor expressed on activated T lymphocytes, including activated T-cells, memory T-cells, and T_{reg}-cells[57]. In addition, it was recently discovered that CTLA-4 may be expressed by many tumor types[58]. The interaction between CD80/CD86 and CTLA-4 offsets CD28-mediated costimulatory signals, which effectively downregulates T-cell activation through several mechanisms including raising of the T-cell activation threshold and attenuation of clonal expansion[57]. CTLA-4 blockade with antibodies effectively limits this interaction, resulting in enhanced T-cell proliferation and the generation of effector T-cells; thus, CTLA-4-targeted antibodies have shown efficacy in the treatment of many cancers. While targeting of CTLA-4 provides therapeutic benefits, anti-CTLA-4 therapies can lead to severe autoimmune adverse effects. Clinical trials have been performed with two anti-CTLA-4 agents, ipilimumab (Yervoy®, Bristol-Myers Squibb)[59] and tremelimumab (AstraZeneca)[60], in which tumor response rates for the drugs as monotherapy were approximately 10%. These therapies have been shown to be extremely effective in a subpopulation of patients; thus, molecular imaging may assist in prescreening patients to identify individuals more likely to respond to anti-CTLA-4 immunotherapy.

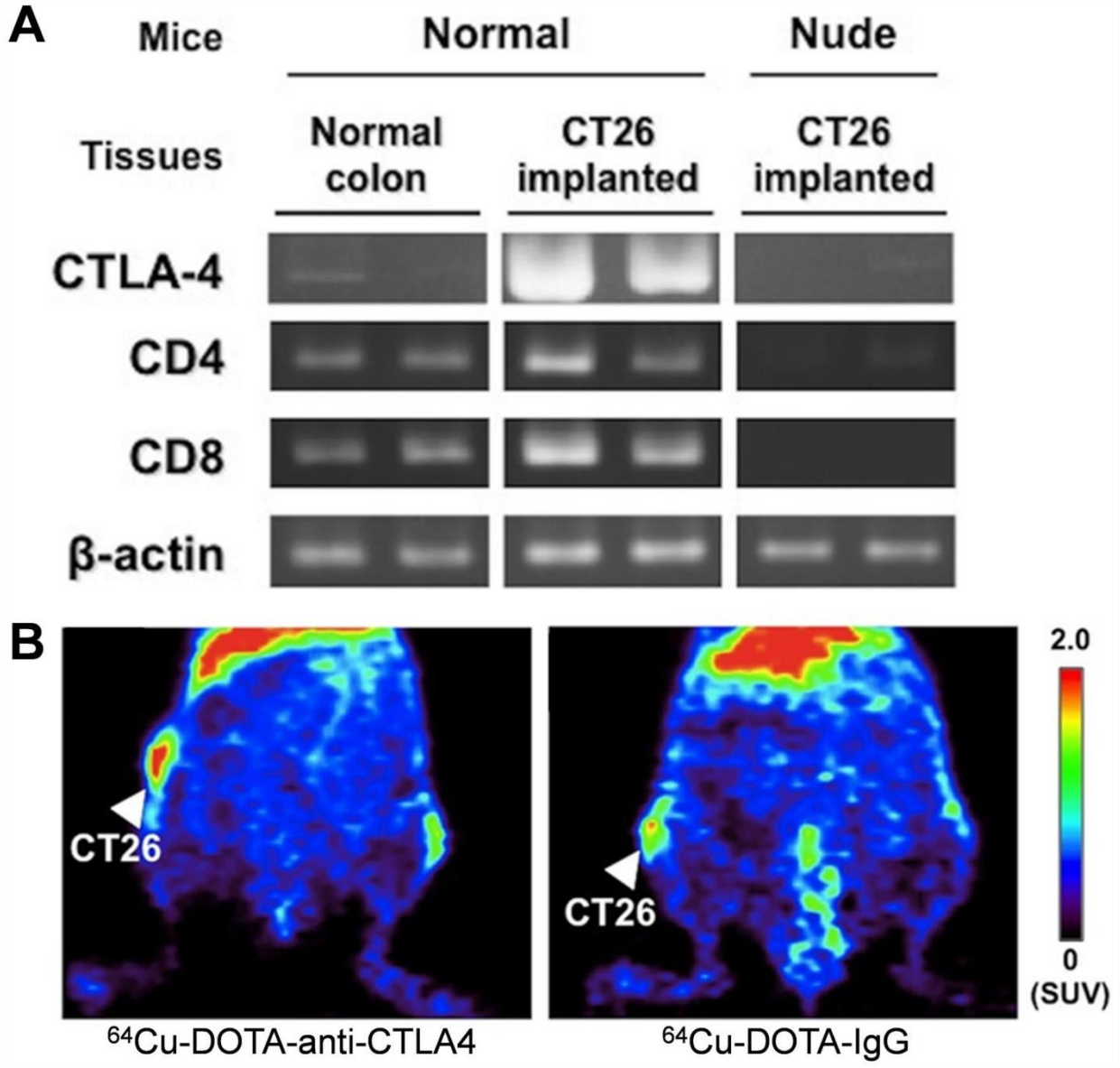

Figure 5. Previous CTLA-4-targeted Imaging Study. *(A) CTLA-4 expression was low in normal colon tissue and completely absent in CT26 tumors implanted in immunodeficient mice. However, CTLA-4 expression was high in tumors implanted into immunocompetent mice. (B) At 48 h p.i., the ^{64}Cu-labeled antibody showed higher uptake in CT26 tumors in comparison to the nonspecific antibody control (^{64}Cu-DOTA-IgG). Adapted from* [5].

Recently, PET imaging was employed to determine levels of CTLA-4-positive TILs in CT26 colon cancer-bearing mice[5]. Here, Higashikawa *et al.* developed a ^{64}Cu-labeled anti-mouse CTLA-4 antibody to study subcutaneously-implanted xenografts in mice. The antibody was constructed to recognize the extracellular domain of CTLA-4, similar to the behavior of the FDA-approved antibody ipilimumab. Through this study, the authors verified that CTLA-4 expression on TILs, not the tumor cells themselves, was the cause of tracer uptake as minimal levels of CTLA-4 were detected in cell culture or tumors implanted into immunodeficient mice (**Figure 5**). Only when mice were immunocompetent were high CTLA-4 expression levels observed in Western blot analysis of *ex vivo* tumors. PET imaging evaluation of the antibody indicated slightly higher uptake of the anti-CTLA-4 antibody with respect to a control IgG in immunocompetent models (7.5 %ID/g vs. 5.8 %ID/g at 48 h p.i.), as seen in **Figure 5**. While the anti-CTLA-4 antibody provided enhanced uptake in comparison to the nonspecific antibody, the agent has yet to be evaluated in models where varying levels of CTLA-4 expression are present. However, this first study successfully demonstrated the use of a ^{64}Cu-labeled anti-CTLA-4 antibody to noninvasively image CTLA-4 levels on TILs in cancer models. Our work in this area, representing the first studies using human-specific tracers, will be outlined in **Chapter 4**.

3.3.1.4. Related immune marker imaging

A number of other strategies are being explored for monitoring of immunotherapy treatments, including cell tracking techniques and using tracers specific for other non-checkpoint targets[61].

The term “immunotherapy” not only refers to checkpoint inhibition treatments, but also encompasses a wide variety of other options, including cell-based therapies[62]. Chimeric antigen receptor (CAR) T-cell therapies have recently been approved by the FDA, including

tisagenlecleucel (Kymriah®, Novartis) and axicabtagene ciloleucel (Yescarta®, Gilead Sciences) for the treatment of B-cell malignancies[63]. In these treatments, T-cells are removed from a cancer patient and modified with a CAR for CD19, a common biomarker for B-cell leukemia. Given the incredible efficacy observed in clinical trials (overall response rates above 70%), these treatments were readily approved for this patient population. However, in a similar manner to blockade therapies, there are complications associated with these treatments and not all patients respond. Since CAR T-cells are already modified *ex vivo*, the introduction of an imaging component has been widely studied as well[64]. This can take the form of a reporter gene system[65] for nuclear or optical imaging, direct labeling of the cells outside of the body with compounds such as ^{18}F-FDG, ^{111}In-Oxime, and ^{64}Cu-PTSM[64], or compounds targeting these engineered cells that can be administered separately.

Other imaging tracers more related to immune checkpoint treatments, specifically for PET, have been reported that do not target the checkpoints themselves but still display importance for understanding these therapies.

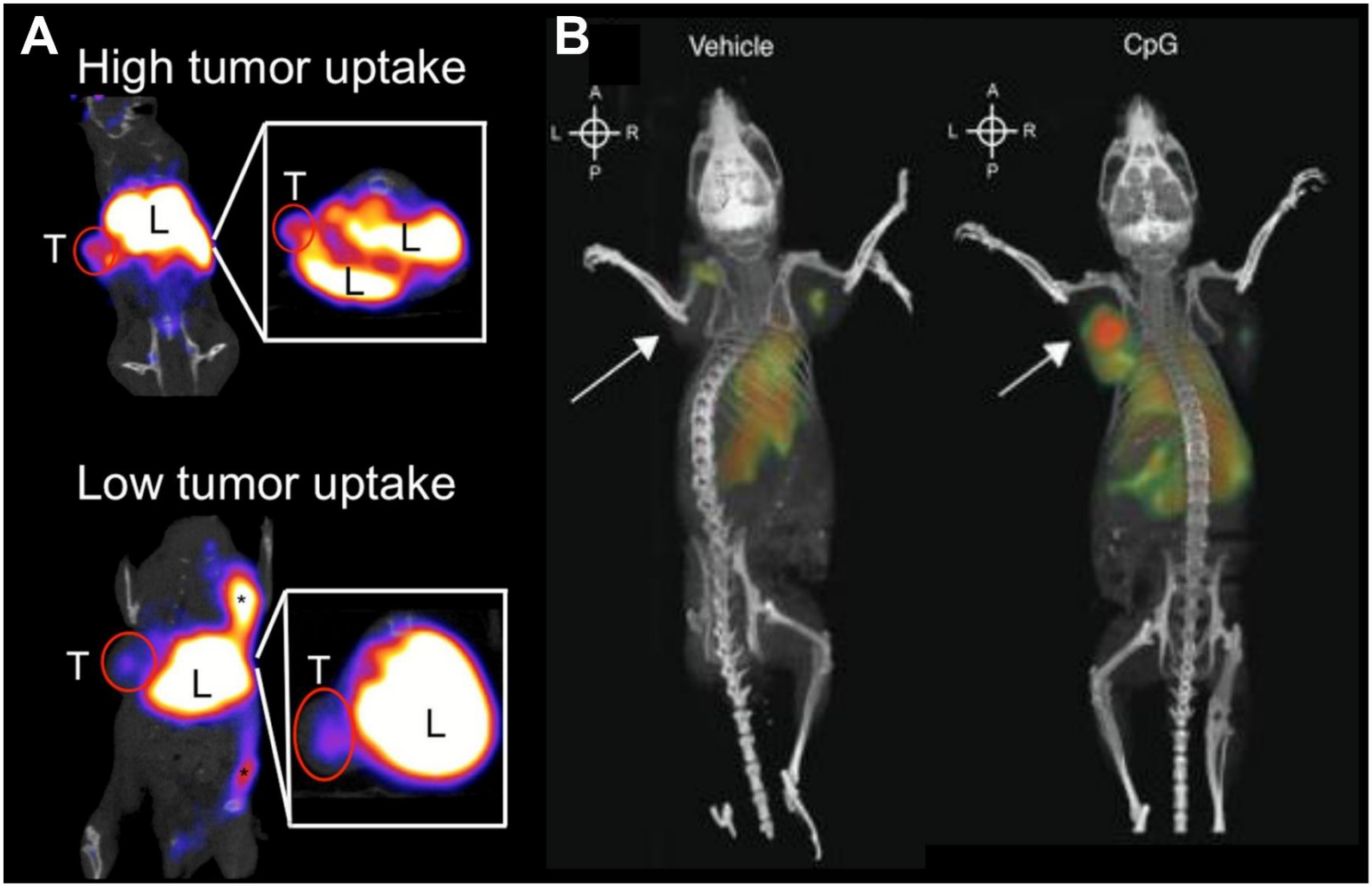

Figure 6. Previous Immune Cell Marker-targeted Imaging Studies. *(A) CD3-targeted PET of mice bearing CT26 tumors. High tumor uptake of the tracer indicated eventual response to CTLA-4 blockade treatment. Adapted from [2]. (B) OX40-targeted PET of mice treated either with vehicle control or a CpG vaccination. Vaccination increased active lymphocyte infiltration and thus tracer uptake, as indicated by the white arrow. Adapted from [6].*

More universal T-cell markers such as CD3, CD4, and CD8 have been the targets of several developed imaging agents. Parrott's group reported an ^{89}Zr-labeled anti-murine CD3 antibody and validated its use to detect tumor-infiltrating lymphocytes[66]. Larimer *et al* explored the use of CD3 PET to predict responses to CTLA-4 blockade therapy as well[2]. Using a murine anti-CD3 antibody, it was shown that two tracer uptake patterns were evident in mice bearing CT26 tumors: the high-uptake group had tumor-to-liver SUV_{mean} ratios of 0.48 ± 0.09 and a low uptake group with ratios of 0.19 ± 0.04, shown in **Figure 6A**. When mice were given three doses of anti-CTLA-4 therapy, divergent trends in the tumor growth were also noted, with the high-PET-uptake group showing significantly smaller tumor volumes than the low-uptake group at the end of the study. This study certainly indicates that PET has potential as a companion diagnostic tool for immune checkpoint treatments.

In a similar manner, CD8 PET imaging has been correlated with responses to CTLA-4 blockade by Rashidian *et al*[67]. Using a ^{89}Zr-labeled PEGylated single-domain antibody fragment specific for mouse CD8, it was found that the spatial distribution of the tracer within B16 tumor tissue was prognostic for response to CTLA-4-targeted treatment. Mice with a more homogeneous distribution of the tracer (corresponding to a single cluster of CD8 T-cells) exhibited significantly slower tumor growth than those mice with a heterogeneous distribution. Ferrara *et al.* was also able to image differences in CD8 T-cell infiltration into tumors following immunotherapy interventions using a ^{64}Cu-labeled cys-diabody[68]. Likewise, Tavaré and co-workers noninvasively monitored CD8 T-cell dynamics with a ^{89}Zr-labeled cys-diabody[69].

Upon T-cell activation, unique molecular signatures are often present in tumor tissues due to these activated immune cells – unique biomarkers that are ripe for imaging. CD25+ T-cells

express interleukin-2 receptors when activated, and this inducible expression has been targeted for PET imaging with ^{18}F-FB-IL-2 by Hartimath *et al*[70]. The authors noted 10- and 27-fold higher accumulation of their tracer in tumor tissues after irradiation alone or irradiation and immunization, respectively. OX40 is also upregulated on the surface of T-cells upon activation. Alam and co-workers have developed a ^{64}Cu-labeled anti-OX40 antibody for imaging this activation and validated it in vaccination treatment models (**Figure 6B**)[6]. Based on the uptake of the tracer two days after therapeutic intervention, the tumor burden of the mice on day 9 could be predicted, and the whole-body change in activated T-cell dynamics after intervention could be monitored. Granzyme B is released by CD8+ T-cells during an immune response and thus serves as the target for a ^{68}Ga-labeled peptide by Larimer *et al*[71]. This imaging technique was also able to stratify mice as responders or non-responders to combination PD-1 and CTLA-4 checkpoint blockade, with higher accumulation of the tracer indicating a greater response to the treatment.

3.3.2. Clinical trials of immunotherapy targets

The immense success of preclinical immunotherapy imaging studies has led to the initiation of many clinical trials with similar agents. **Table II** provides examples of such studies. Results have yet to be disclosed in these trials.

Table II. Clinical ImmunoPET Imaging Studies. *Abbreviations: CTLA-4: cytotoxic T-lymphocyte associated antigen 4; PD-1: programmed death protein 1; PD-L1: programmed death protein ligand 1; IL-2: interleukin-2; dCK: deoxycytidine kinase; dGK: deoxyguanosine kinase.*

ClinicalTrials.gov number	Imaging agent	Target	Indication
NCT03313323	^{89}Zr-ipilimumab	CTLA-4	Metastatic melanoma
NCT03065764	^{89}Zr-pembrolizumab	PD-1	Non-small cell lung cancer
NCT03514719	^{89}Zr-avelumab	PD-L1	Non-small cell lung cancer
NCT02453984	^{89}Zr-atezolizumab	PD-L1	Breast, urinary tract, non-small cell lung cancer
NCT03107663	^{89}Zr-IAB22M2C	CD8	Non-Hodgkins lymphoma, select solid tumors
NCT02922283	^{18}F-FB-IL2	IL-2	Metastatic melanoma
NCT02888301	^{18}F-Clofarabine	dCK	Any cancers
NCT03409419	^{18}F-Clofarabine	dCK	Advanced melanoma
NCT03311672	^{18}F-AraG	dCK/dGK	Non-small cell lung cancer
NCT03142204	^{18}F-AraG	dCK/dGK	Any cancers
NCT03129061	^{18}F-AraG	dCK/dGK	Squamous cell carcinoma of the head and neck
NCT02323893	^{18}F-AraG	dCK/dGK	Healthy volunteers

3.4. Looking forward

Cancer immunotherapy blockade interventions have the potential to revolutionize cancer management strategies, and are already doing so today. The causes of considerable immune-related adverse effects and limited success rates may be elucidated through the use of noninvasive imaging. Molecular imaging of immunotherapy targets such as PD-1, PD-L1, and CTLA-4 has shown promise in preclinical studies, and successful application to the clinic will provide great strides in the fight against cancer. However, to make this leap to the clinic, human-specific imaging tracers need to be developed and validated. We therefore outline our work in this emerging research area, and strongly believe that in the future molecular imaging of immunotherapy targets may enhance patient stratification and provide insight for development of novel immunotherapy targets.

Chapter 4

4. Developing PD-1 and CTLA-4 – targeting PET tracers†

To achieve our goal of noninvasively monitoring immunotherapy treatments, we first developed and validated PET imaging tracers for both the cytotoxic T-lymphocyte associated antigen 4 (CTLA-4) and programmed death protein 1 (PD-1)[44, 72, 73]. These tools were able to noninvasively and specifically image positive tissues in a variety of models, laying the groundwork for future studies in this area.

4.1. Methods and Materials

In this chapter, we present our work on the initial development and validation of immune checkpoint-targeting PET tracers. As many of the procedures for development of the different tracers were similar, we will first outline the general methods utilized, pointing out differences in

† Much of this chapter has been previously published in: **44.** England CG, Ehlerding EB, Hernandez R, et al. Preclinical Pharmacokinetics and Biodistribution Studies of 89Zr-Labeled Pembrolizumab. *J Nucl Med.* 2017;58:162-168, **72.** Ehlerding EB, England CG, Majewski RL, et al. ImmunoPET imaging of CTLA-4 expression in mouse models of non-small cell lung cancer. *Molecular pharmaceutics.* 2017;14:1782-1789, **73.** Ehlerding EB, Lee HJ, Jiang D, et al. Antibody and fragment-based PET imaging of CTLA-4+ T-cells in humanized mouse models. *Am J Cancer Res.* 2019;9:53-63.

the studies as necessary. The results of the various studies will then be presented individually, and the impact of these studies will be discussed.

4.1.1. Tracer preparation

4.1.1.1. Antibody platforms

For development of a PD-1-targeting PET tracer, the clinically-available antibody pembrolizumab (Keytruda®, Merck) was employed, while for CTLA-4-targeting, ipilimumab (Yervoy®, Bristol-Myers Squibb) was used. All antibodies were obtained in their clinically-available forms from the UW Pharmacy, and purified into phosphate buffered saline (PBS) for further use.

Pembrolizumab was used in its intact form, while both intact ipilimumab and its $F(ab')_2$ fragment were employed. Ipilimumab $F(ab')_2$ fragmentation was completed using the IdeS protease (Promega) following the manufacturer's protocol to remove the Fc portion from ipilimumab. In short, the antibody was purified into 1X PBS and then incubated with the IdeS protease for 1 h at 37°C. To purify the digested sample, Magne™ Protein A beads (Promega) were incubated with the solution for 1 h in an end-over-end mixer at room temperature. The magnetic beads and bound Fc portions were removed and discarded. The supernatant (containing the $F(ab')_2$ fragments) was saved for analysis and further studies.

To verify the digestion product identity and purity, polyacrylamide gel electrophoresis (PAGE) was run using a standard protocol. Into each well, 30 µg of protein (either digestion products or pure antibody) was loaded along with loading dye. The gel was then run at 120V for 1 h at 4°C. After rinsing, the gel was incubated with Coomassie blue dye for 1.5 h, rinsed, and imaged using a gel imaging system.

4.1.1.2. Chelator conjugation

To prepare the antibody platforms for radiolabeling and use as PET agents, they were conjugated with various bifunctional chelators. Pembrolizumab was conjugated with p-SCN-Deferoxamine (Df; Macrocyclics), while ipilimumab and ipilimumab-F(ab')$_2$ were conjugated with either p-SCN-Bn-DOTA (1,4,7,10-tetraazacyclododecane-1,4,7,10-tetraacetic acid, Macrocyclics) or p-SCN-Bn-NOTA (2-S-(4-Isothiocyanatobenzyl)-1,4,7-triazacyclononane-1,4,7-triacetic acid). All reactions were conducted using standard procedures: Antibody solutions were adjusted to pH = 8-9, and reacted with the appropriate chelator at a molar ratio of 1:10 antibody:chelator for 1 h at room temperature. PD-10 columns (GE Healthcare) were then used to remove excess unreacted chelator from solution. Protein concentrations were measured using a NanoDrop system (ThermoFisher). Similar techniques were employed to generate a nonspecific human isotype control antibody tracer for certain studies.

4.1.1.3. Radiolabeling procedures

Radionuclides used in these studies were obtained from the University of Wisconsin – Madison cyclotron group and used without further purification. ^{89}Zr was obtained as ^{89}Zr-oxalate, while ^{64}Cu was in the form of $^{64}CuCl_2$.

To prepare ^{89}Zr-Df-pembrolizumab, Df-pembrolizumab was incubated with ^{89}Zr-oxalate in HEPES buffer at 37°C under constant shaking for one hour at a ratio of >50 µg protein per 1 mCi radionuclide. For ^{64}Cu labeling, DOTA-ipilimumab or NOTA-ipilimumab were incubated with $^{64}CuCl_2$ at a ratio of >30 µg per 1 mCi radionuclide at 37°C for one hour. After the incubation period, all solutions were purified using PD-10 columns with PBS as the mobile phase, and prepared for injection.

4.1.2. In vitro studies

4.1.2.1. Cancer cell expression of CTLA-4

To determine the expression of CTLA-4 by lung cancer cells, several experiments were performed. A549, NCI-H358 (H358), NCI-H460 (H460), CALU-1, NCI-H23 (H23), and NCI-H522 cell lines were obtained from the American Type Culture Collection (ATCC). A549 cells were grown in F-12K medium, while CALU-1 cells were grown in ATCC-formulated McCoy's 5a medium. The other cell lines (H358, H460, H23, and H522) were cultured in Roswell Park Memorial Institute (RPMI)-1640 medium. All media was supplemented with 10% fetal bovine serum (FBS; Gibco, ThermoFisher Scientific) and 1% penicillin-streptomycin solution (Gibco, ThermoFisher Scientific). Cells were grown in a humidified incubator at 37ºC with 5% CO_2 and utilized for studies at 60-70% confluency.

CTLA-4 expression by cancer cells was quantitatively assessed via an enzyme-linked immunosorbent assay (ELISA, R&S Systems). The procedures were outlined in the manufacturer's protocol. Briefly, 10 µL of cell lysate was added to wells in triplicate with sample diluent. Next, the biotin-conjugate was added to wells and incubated at room temperature for 2 h with shaking at 400 rpm. Wells were washed three times before the diluted Streptavidin-HRP was added to the wells. The plate was sealed and incubated at room temperature for 1 h with shaking at 400 rpm. Again, wells were then washed three times. The TMB substrate solution was added to the wells and incubated at room temperature for 10 min with no light exposure. The enzyme reaction was halted by adding the stop solution to the wells. The optical density was measured at 450 nm using a microtiter plate reader (BioTek).

Western blot analysis was also performed. Cells were lysed using Radio Immuno Precipitation Assay (RIPA) buffer (Boston BioProducts) supplemented with 1:100 Halt Inhibitor

Cocktail (Thermo Fisher Scientific) and EDTA for 10 min at 4 ºC. Next, the cells were centrifuged and protein concentration was measured using the Pierce Coomassie (Bradford) Protein Assay kit (Thermo Fisher Scientific). Twenty micrograms of total protein were loaded into the wells of a 4-12% Bolt Bis-Tris Plus gel (Thermo Fisher Scientific). Following electrophoresis at 120 mV for 45 min at 4 ºC, proteins were transferred to a nitrocellulose membrane using the iBlot 2 system (ThermoFisher Scientific). The membrane was blocked in the Odyssey PBS Blocking Buffer (LI-COR Biosciences) for 12 h at 4 ºC. The iBind Western Device (Thermo Fisher Scientific) was prepared by adding the primary and secondary antibody solutions and washes to the corresponding chambers. In accordance with the manufacturers' protocol, dilutions of 1:200 and 1:400 were made of the goat-derived CTLA-4 antibody (Novus Biotechnologies) and mouse β-actin (LI-COR Biosciences) with the iBind Fluorescent Detection Solution Kit (Thermo Fisher Scientific). Similarly, the secondary antibodies (donkey anti-goat 800CW and donkey anti-mouse IRDye 680RD) were obtained from LI-COR and diluted at 1:10,000 before being placed into their corresponding chambers. The membrane was removed from the iBind system after 12 h and scanned using the LI-COR Odyssey Infrared Imaging System (LI-COR Biosciences).

Finally, binding assays were also performed to determine the internalization properties of the antibody. Ipilimumab was incubated with 800CW dye (LI-COR Biosciences) at a 1:3 molar ratio at room temperature for 2 h, then passed through a PD-10 size-exclusion column for purification. Next, 100,000 cells were plated onto 24-well plates supplemented with the proper media for each cell line (A549, H460, and H358). For the internalization assay, a solution of dye-conjugated ipilimumab in media was generated, and 1 mL was added to each well. After 0.5, 1, 8, or 24 h of incubation, media was removed (media fraction) and 0.2 M sodium acetate was added to each well to remove the cell surface-bound antibody. After one minute of incubation, the acetate

was also removed (surface-bound fraction) and cells were rinsed with PBS. Cells were then trypsinized and removed from the well plate (internalized fraction). Fluorescence intensity was quantified in each of these fractions using the IVIS optical imaging system (PerkinElmer), and data were presented as the total fluorescence in the internalized and bound fractions, normalized to fluorescence in the removed media.

4.1.2.2. Binding assays with human PBMCs

For the T-cell targeting studies, flow cytometry was used to determine the binding of the antibodies to human peripheral blood mononuclear cells (PBMCs) and any potential impact of chelation on this binding. For PD-1 studies, human PBMCs were isolated from blood samples collected under an institutional review board-approved protocol from patients giving informed consent via density gradient centrifugation using Ficoll-Histopaque (GE Healthcare). PBMCs were thawed, washed, and resuspended at a concentration of $2x10^6$ cells/mL in AB Media (RPMI-1640 + 10% AB sera/2% Penicillin-Streptomycin/1% NaPyr/0.1% βME) and stimulated with phorbol myristate acetate (40 ng/mL, Sigma) and ionomycin (1.3 ug/mL, MP Biomedicals) for 18 h. Cells were washed and stained with the indicated concentration of pembrolizumab or Df-pembrolizumab for 1 h at 4°C. Cells were then washed and stained with 2 μg/mL AlexaFluor488-anti-human IgG secondary antibody (Life Technologies), as well as CD3-v500, CD4-PE, and CD8-APC antibodies (BD Biosciences) at a concentration of 2 tests / mL and a 1:1000 dilution of GhostDye Red-780 (Tonbo Biosciences). Cells were washed, resuspended in FACS Wash (phosphate buffered saline/3% FCS) and analyzed on a BD LSRFortessa cytometer. The gating strategy was: Alive/FSCxSSC/Singlets/CD3+ and CD4 or CD8+. The PD-1 positive gate was determined using both no primary and no secondary antibody control-stained samples.

To analyze the binding of ipilimumab and ipilimumab-F(ab')$_2$, cryopreserved PBMCs were thawed, rinsed in HBSS, and incubated in RPMI 1640 containing 10% human AB serum, 200U/mL Pen/Strep, 1% NaPyr, 50μM β-MeOH, and 2.5 μg/mL Phytohaemagglutinin (PHA) to activate T-cells and induce expression of CTLA-4. After 72 h, cells were collected, rinsed in FACS wash buffer (PBS +3%FCS +1mM EDTA), stained with Ipilimumab-FITC, Ipilimumab-F(ab')$_2$-FITC, or IgG isotype control for 30 min at 4ºC, and analyzed by flow cytometry using a BD LSR Fortessa. Histogram overlay was made using FlowJo 10.5.3.

4.1.3. Animal studies

4.1.3.1. Animal models

All animal studies were conducted under a protocol approved by the University of Wisconsin Institutional Animal Care and Use Committee, with n = 3-6 mice per study group in all experiments. For the studies of CTLA-4 tumor expression, three cell lines were employed: A549, H460, and H358. Once the cells reached 60-70% confluency, they were detached using Accutase (Innovative Cell Technologies) and 100 μL (1×10^6 cells) of a 1:1 mixture of lung cancer cells and Matrigel Matrix Basement Membrane (Corning) were subcutaneously implanted into the lower flank of 4 to 7-wk-old female athymic nude mice (Crl: NU(NCr)-Foxn1nu; Envigo). Tumor sizes were monitored until they reached 5-8 mm diameter, at which time the mice were used for imaging studies.

In order to image human T-cells, humanized mouse models were utilized. The Humanized Mouse Core at the University of Wisconsin – Madison provided the humanized mice for this study. Briefly, non-irradiated NOD,B6.SCID *Il2rγ*$^{-/-}$*Kit*$^{W41/W41}$ (NBSGW) mice or NOD scid gamma (NSG) mice were engrafted with human peripheral blood mononuclear cells and monitored via

blood draws and flow cytometry for successful engraftment[74]. These humanized mice are designated as PBL (peripheral blood lymphocytes) mice. NBSGW or NSG mice not engrafted with human cells were used as controls.

4.1.3.2. PET imaging studies

PET scans were acquired in an Inveon microPET/microCT rodent model scanner (Siemens Medical Solutions). For all imaging studies, mice were injected with 5-10 MBq of the appropriate imaging agent intravenously via the tail vein. They were then anesthetized using 3%/1.5% isoflurane induction/maintenance for scans. Static scans were obtained of at least 20 million coincidence events per mouse, and images were reconstructed using the 3D ordered subset expectation maximization algorithm. The imaging protocols for these studies are listed in **Table III**.

The PET results in tissues of interest were quantified through region-of-interest analysis using the Inveon Research Workspace software and data is presented as percentage of injected dose per gram of tissue (%ID/g).

Table III. **Study Outline.** Relevant information about the PET imaging studies performed in this aim.

Imaging agent	Target	Mouse model(s)	Imaging timepoints	Control group(s)
^{89}Zr-Df-pembrolizumab	PD-1 on human PBMCs	PBL mice	0.5, 6, 12, 24, 48, 72, 120, 168 h	NSG mice
^{64}Cu-DOTA-ipilimumab	CTLA-4 on tumor cells	Nude mice with lung cancer xenografts	3, 24, 48 h	Blocking study in positive tumor xenografts
^{64}Cu-NOTA-ipilimumab and ^{64}Cu-NOTA-ipilimumab-F(ab')$_2$	CTLA-4 on human PBMCs	PBL mice	0.5, 3, 12, 24, 48 h	NBSGW mice, control IgG in PBL mice

4.1.3.3. Biodistribution studies

After the final imaging time point, mice were euthanized via CO_2 asphyxiation. Major organs were excised, wet-weighed, and their radioactive contents were measured using an automated gamma counter (PerkinElmer). Biodistribution data is also presented as %ID/g.

4.1.3.4. Immunofluorescent analyses

For the studies of CTLA-4 expression of tumor cells, fluorescence immunohistochemistry was performed to confirm CTLA-4 expression levels in *ex vivo* lung cancer xenograft tissues. Tumor tissues were collected, frozen in Optimal Cutting Temperature compound (Sakura Finetek), and sectioned in 5 µm slices. For staining, slides were dried for 15 min at room temperature and fixed in 4% paraformaldehyde (Santa Cruz Biotechnologies), then washed twice with 1X PBS. Slides were then permeabilized in 0.2% Triton X (Sigma-Aldrich) in PBS for 15 min, washed with PBS, and blocked for 2 h in blocking solution at room temperature (5% donkey serum, 0.3% Triton X in PBS). Primary incubation with ipilimumab (25 µg/mL) in the blocking solution was performed overnight at 4°C. To reduce background, slides were then washed twice with 0.2% Triton X for 30 min and washed with PBS prior to incubation with goat anti-human 800CW secondary dye (LI-COR) for 1 h. Slides were subsequently washed twice with 0.2% Triton X for 20 min and twice with PBS for 5 min, mounted with VectaShield hard mount containing DAPI (Vector Laboratories) and coverslipped. Imaging was performed with a Nikon A1R confocal microscope.

For T-cell imaging studies, the salivary gland tissues were removed from both PBL and NBSGW/NSG mice and embedded in Optimal Cutting Temperature Compound (Sakura Finetek) and frozen. Tissue sections of 5 or 10 µm thickness were then stained using procedures similar to

those aforementioned. The presence of human T-cells in this tissue was verified through staining of both human CTLA-4 (goat anti-human antibody, R&D Systems) or PD-1 (goat anti-human antibody, R&D Systems) and CD3 (rabbit anti-human, Biolegend) and the appropriate secondary antibodies. These slides were also imaged with a Nikon A1R confocal microscope.

4.1.4. Dosimetric extrapolation

For the T-cell imaging studies, dosimetry analysis was performed using OLINDA/EXM software[75]. Estimated human dosimetry was calculated based on the %ID/g values from the serial PET scans on the PBL and NSG/NBSGW mice, which were converted to %ID for each analyzed organ in humans. It was assumed that the biodistribution in adult humans was the same as in the animal models, and a mono-exponential model was utilized for the time-activity curves. OLINDA provides effective dose outputs; thus, weighting factors from International Commission on Radiological Protection Publication 103 were employed to convert to absorbed dose in each organ[76].

4.2. Results

4.2.1. Tumor CTLA-4 imaging[72]

4.2.1.1. CTLA-4 expression by lung cancer cells

Both ELISA and Western blot studies were performed to determine the abundance of CTLA-4 in the lung cancer cell lines. Before choosing three cell lines for animal studies, six lung cancer cell lines were screened by ELISA for CTLA-4 expression (**Figure 7A**). The cell lines showed different levels of CTLA-4 expression, with A549 displaying the highest concentration of CTLA-4 at 39.92 ± 1.46 ng per 20 µg total protein. The second highest was H460, which expressed CTLA-4 at 30.76 ± 4.61 ng per 20 µg total protein. Next, H358 and H522 showed similar CTLA-4 expression levels at 15.76 ± 2.48 and 16.22 ± 2.09 ng per 20 µg total protein, respectively (n=3

for each cell line). The lowest levels of CTLA-4 expression were detected in CALU-1 and H23 cell lines. A549, H460, and H358 cell lines were chosen for the remainder of the study. Before implanting mice, the ELISA results were verified using Western blot analysis (**Figure 7B**). For the Western blot, β-actin was used as a control with a band near 43 kDa, while CTLA-4 was expected to produce a band slightly lower at 38 kDa. The most intense band for CTLA-4 was seen from A549 cells, followed by H460 with a moderate band, further validating the results obtained from ELISA. Lastly, H358 only showed a negligible band for CTLA-4. These *in vitro* tests provided the foundation for further *in vivo* analysis of the three cell lines.

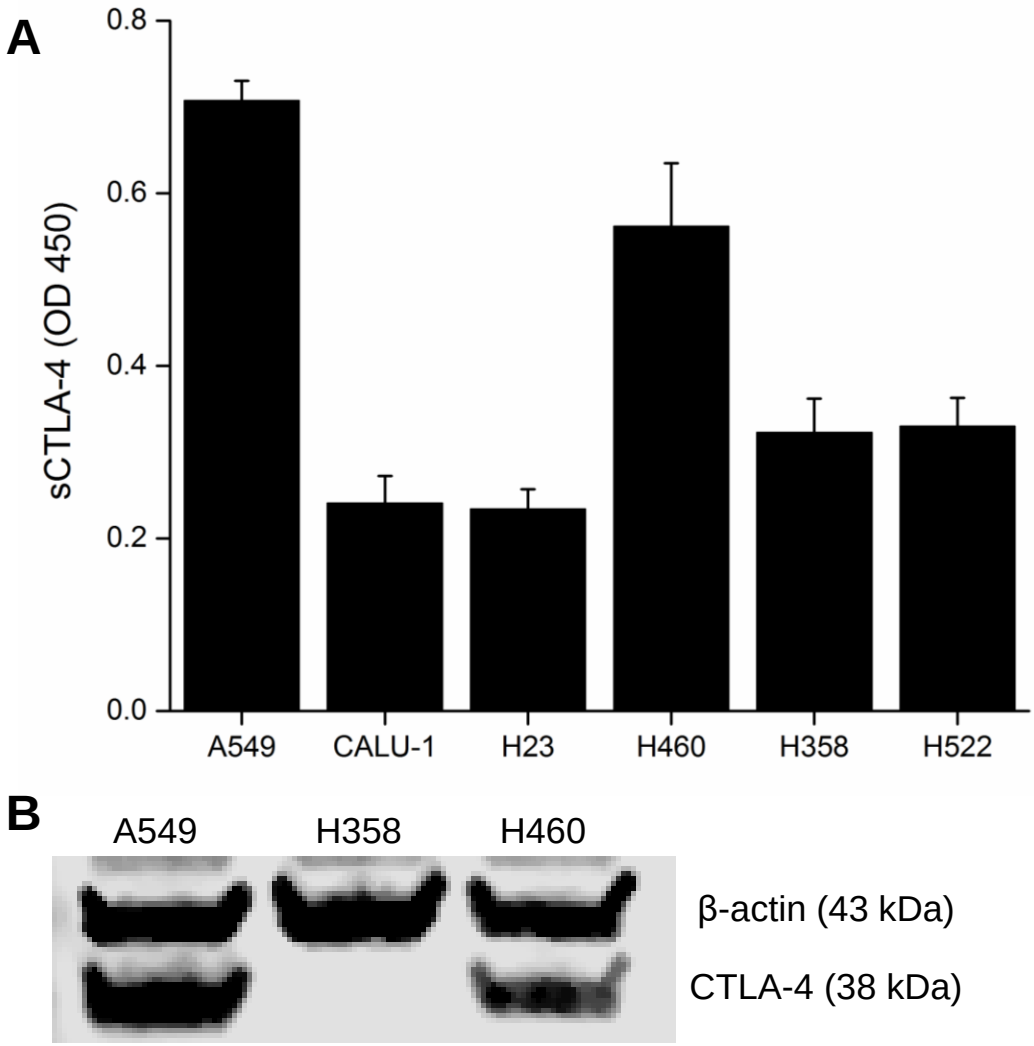

Figure 7. Lung Cancer CTLA-4 Expression. *Results of screening lung cancer cell lines for expression of CTLA-4 by (A) ELISA and (B) Western blot. A549 cells were found to have the highest expression.*

4.2.1.2. Ipilimumab binding assay

Fluorescent internalization assays were performed on the three lung cancer cell lines to further verify that ipilimumab would bind and internalize in the three lung cancer cell lines. The binding and internalization of fluorescently-labeled ipilimumab was monitored for 24 h (**Figure 8**). A549 cells displayed higher binding and internalization of ipilimumab over both H460 and H358 cells at the 24 h timepoint (n=4, $p < 0.05$). As expected, the amount of ipilimumab that was bound or internalized increased over time in highly CTLA-4-expressing A549 cells.

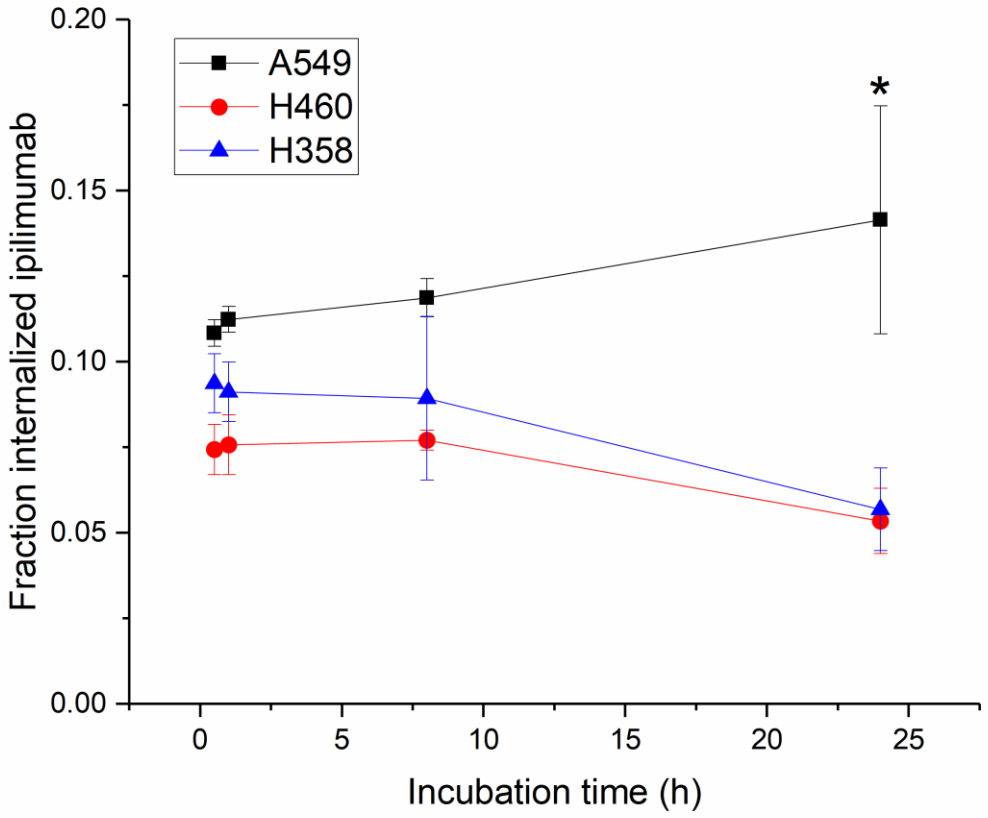

Figure 8. Lung Cancer Ipilimumab Binding Assay. *A binding assay was performed in the three selected lung cancer cell lines using fluorescently-labeled ipilimumab. CTLA-4-expressing A549 cells demonstrated the highest cell-associated fluorescence, indicating the highest level of binding.*

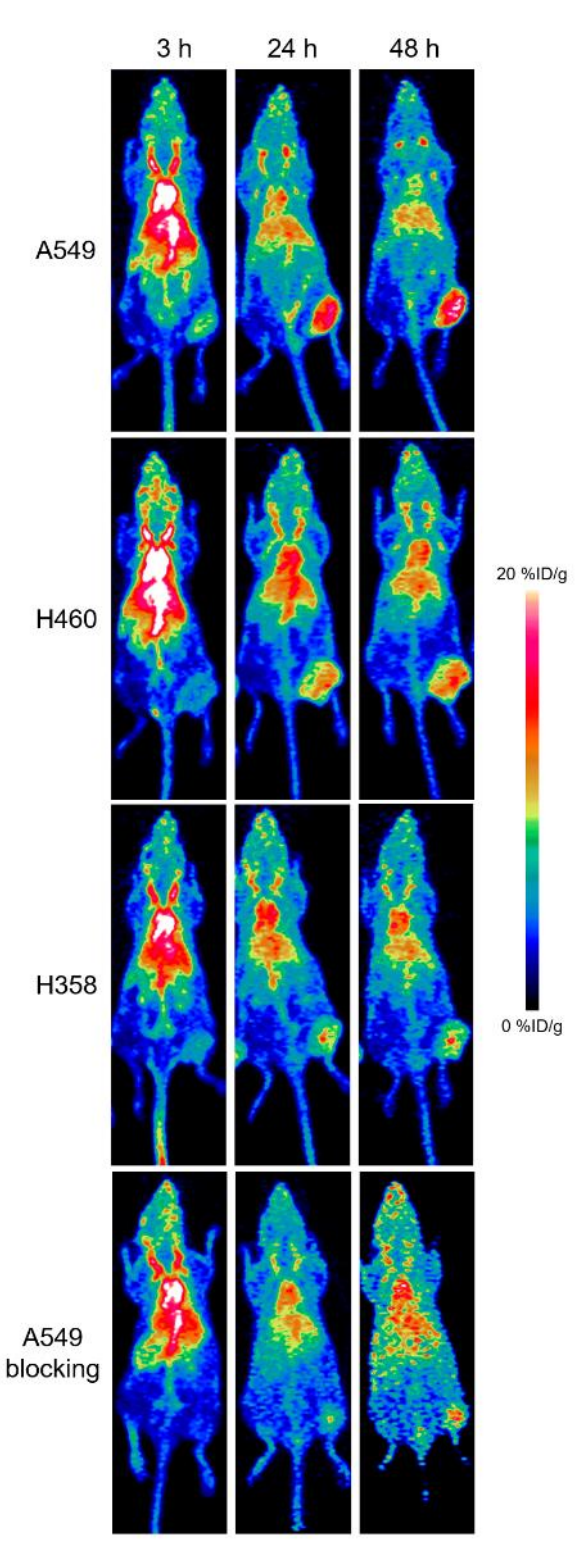

Figure 9. ***^{64}Cu-DOTA-ipilimumab PET.*** *Results of PET imaging studies using ^{64}Cu-DOTA-ipilimumab in lung cancer xenografted mice. Images are maximum intensity projections with tumors located on the right hip of the mice.*

4.2.1.3. PET visualization of CTLA-4+ tumors

PET imaging was utilized to examine the biodistribution and pharmacokinetic properties of the CTLA-4 tracer, ^{64}Cu-DOTA-ipilimumab, in mice bearing lung cancer xenografts. Maximum intensity projections of the PET images allowed for clear visual delineation of tumor margins in CTLA-4-expressing tissues, with A549 and H460 tumor xenografts showing higher uptake than H358 (**Figure 9**). PET region-of-interest analysis verified the *in vitro* results (**Figure 10, Table I in Appendix 1**), with A549 tumor uptake peaking after 48 h at 9.80 ± 0.22 %ID/g, H460 at 9.37 ± 0.26 %ID/g, and H358 at 7.43 ± 0.05 %ID/g (n=3-4). To ensure that tracer accumulation in the tumor was specific, the CTLA-4 receptor was blocked by injecting excess cold (un-radiolabeled) ipilimumab 24 h prior to the injection of radiolabeled ipilimumab in A549 tumor-bearing mice. Blocking of the receptor demonstrated decreased tracer uptake of 6.90 ± 0.51 %ID/g at 48 h post-injection (n=4). Both A549 and H460 tumors displayed statistically significant increased uptake of the tracer over H358 tumors at all imaging time points. Statistically significant decreased uptake was also evident in the blocking group tumors compared to A549 (n=4; $p<0.05$). Since the tracer remained in circulation for the length of the study, tumor uptake increased over time in all groups. Notable accumulation was also observed in the liver, as it serves as the primary antibody clearance organ, with other off-target organs displaying minimal uptake. Tumors were easily delineated at all time points due to high tumor-to-muscle ratios in all groups. A549, H358, and the blocking group demonstrated peak tumor-to-muscle ratios at 48 h (9.51, 5.87, and 6.29, respectively) while H460 peaked at 24 h p.i. at 5.90. Similarly, A549 tumors demonstrated the highest tumor-to-blood ratio of 1.16 at 48 h post-injection, followed by H460 at 0.79, H358 at 0.71, and the blocking group at 0.66.

After the terminal imaging time point at 48 h after injection, mice were sacrificed and various organs were harvested, wet-weighed, and their radioactive content was determined through gamma counting (**Figure 11, Table I in Appendix 2**). The uptake values calculated from this study verified the trends found in the PET region-of-interest quantification, as A549 had the highest uptake (9.5 ± 2.4 %ID/g), followed by H460 (7.6 ± 1.2 %ID/g), the blocking group (6.8 ± 0.5 %ID/g), and the H358 mice (4.6 ± 1.3 %ID/g). The liver remained the organ with the highest off-target accumulation, ranging from 5-10 %ID/g. Other organs showed minimal tracer accumulation considered as background signal.

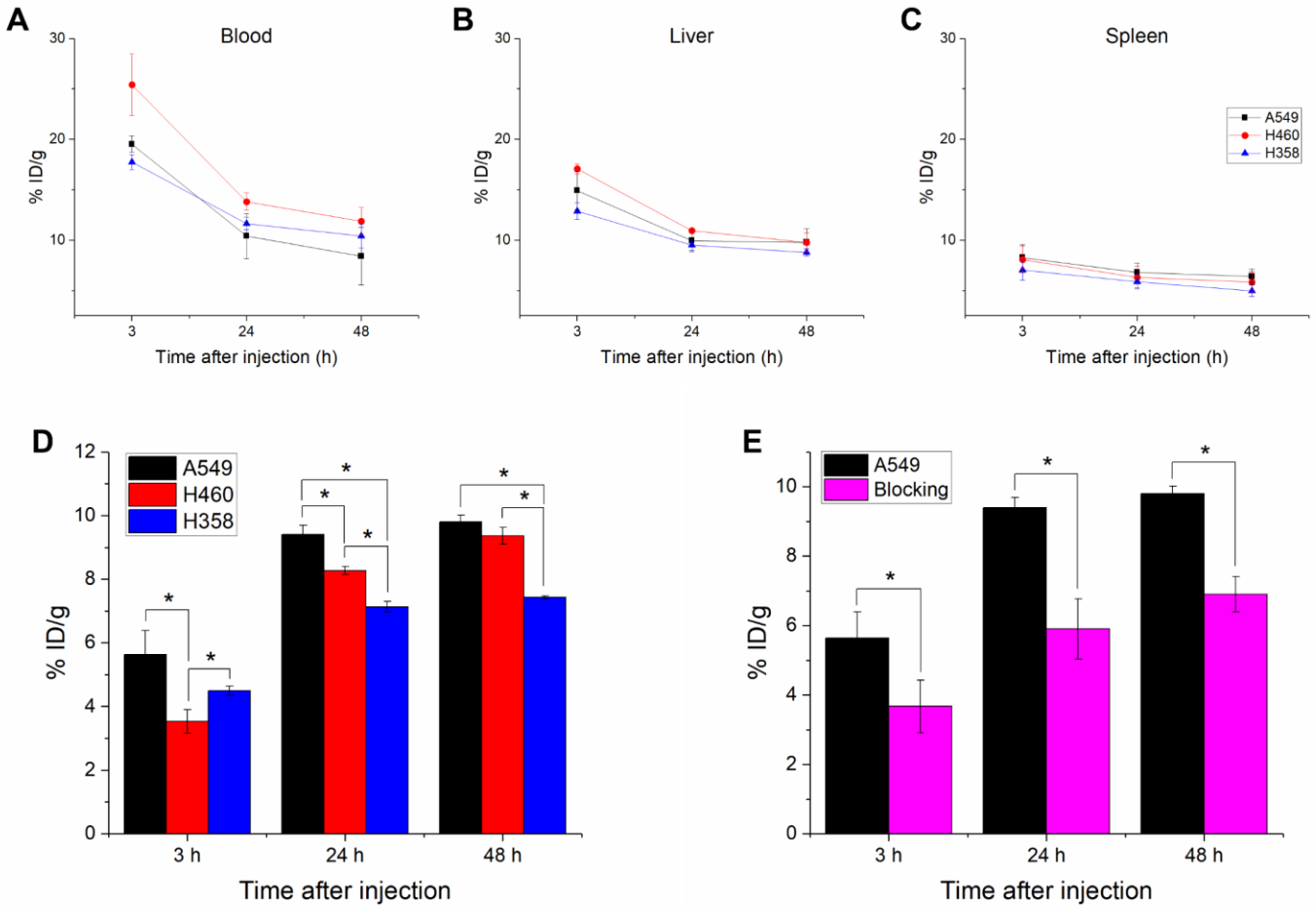

Figure 10. ^{64}Cu-DOTA-ipilimumab Quantification. *Quantification of PET tracer accumulation in (A) the blood pool; (B) the liver; and (C) the spleen. (D) Comparison of tumor uptakes of ^{64}Cu-DOTA-ipilimumab in the three cell lines. (E) The uptake in A549 tumors was partially blocked by an excess of unlabeled ipilimumab. *p<0.05; n=3-4.*

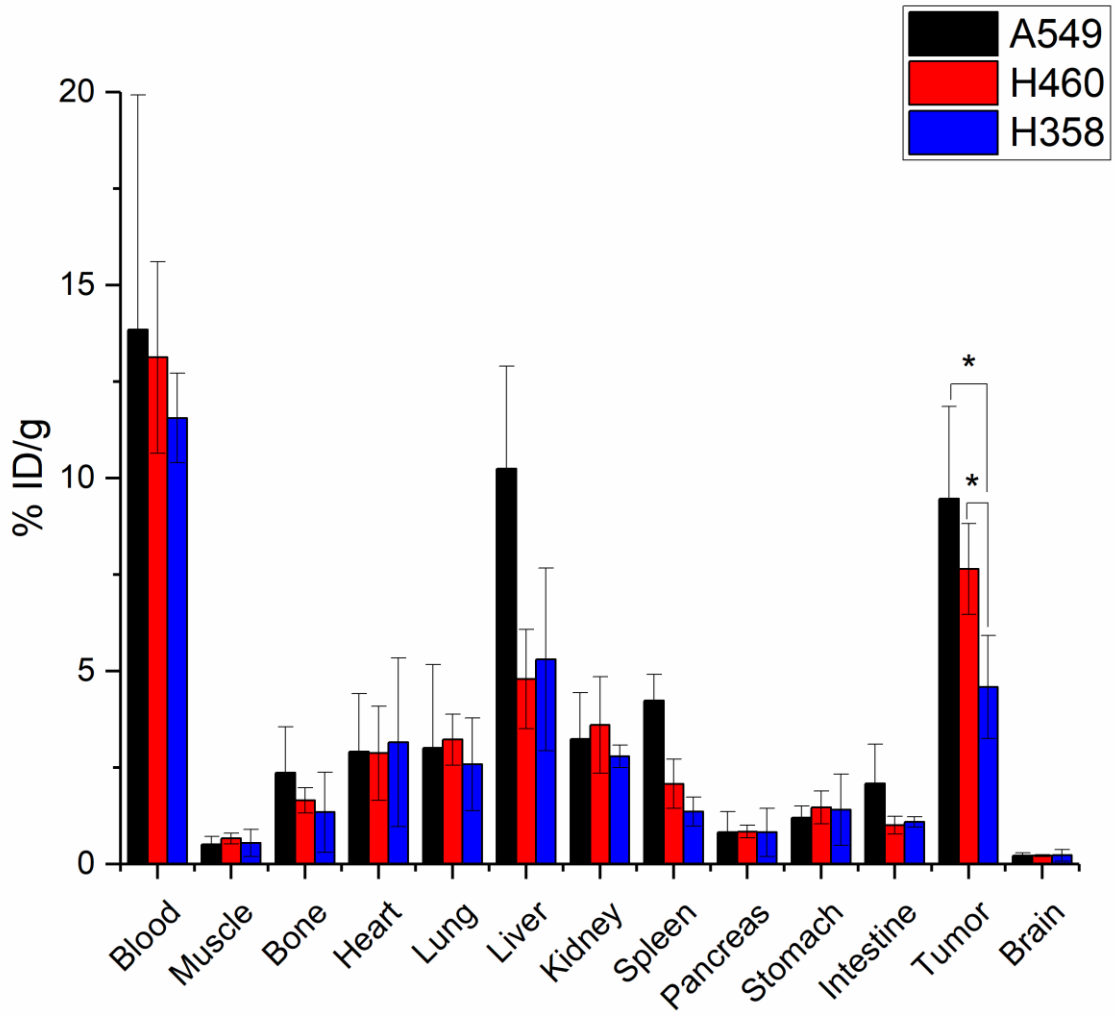

Figure 11. ***^{64}Cu-DOTA-ipilimumab Biodistribution Results****. Results of the ex vivo biodistribution study. Significant differences in the accumulation of ^{64}Cu-DOTA-ipilimumab in tumor tissues was observed. *p<0.05; n=3-4.*

4.2.1.4. Ex vivo verification of CTLA-4 expression

Immunofluorescence staining of *ex vivo* xenograft tissues further validated the varying expression levels of CTLA-4 in lung cancer. Both CTLA-4 and nuclei were stained to determine the relative location of CTLA-4 on the cells (**Figure 12**). A549 tissues displayed the highest staining levels, which was primarily localized to the surface of the cells as shown through the merged images. H460 tumor sections showed slightly lower staining of CTLA-4, which was more heterogeneously expressed. Lastly, H358 showed the lowest staining intensity, suggesting the lowest expression of CTLA-4, further validating previous *in vitro* assays and PET imaging. This tissue analysis corroborated the finding that the cancer cells themselves, rather than just tumor-infiltrating lymphocytes, express varying levels of CTLA-4.

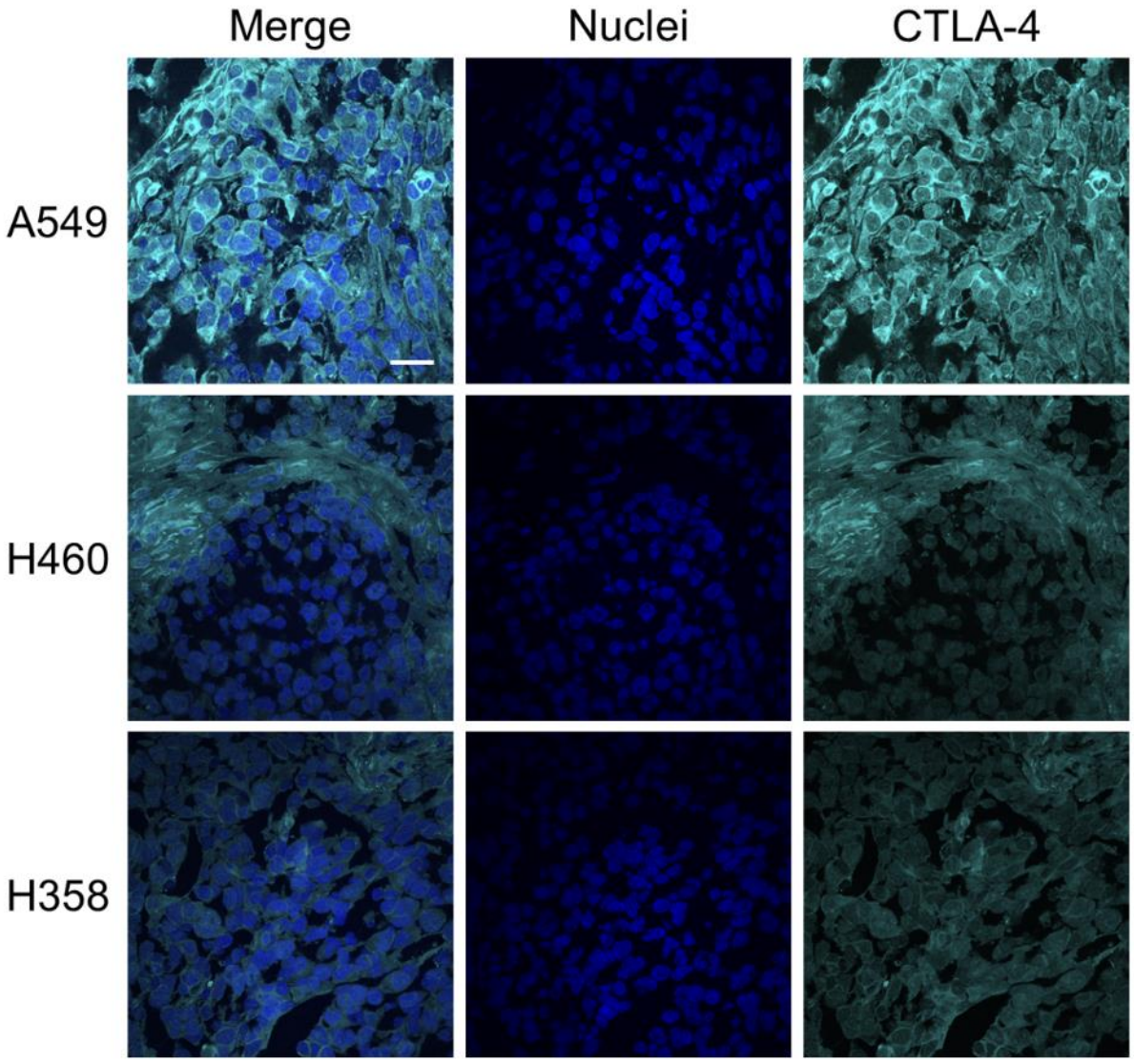

Figure 12. CTLA-4 Staining in Tumor Tissues. *Immunofluorescent staining of tumor tissues for CTLA-4 verified high expression in A549 cells.*

4.2.2. Imaging CTLA-4 expression of T-cells[73]

4.2.2.1. CTLA-4+ T-cell localization in salivary glands

From previous experience with PBL mice[42, 44], significant infiltration of engrafted human immune cells in the salivary glands of the PBL mice as a result of graft-versus-host disease onset was expected[77]. By staining PBL salivary gland tissue slides for both human CD3 and CTLA-4, it was verified that human T-cells were indeed localized in this tissue, evidenced by co-staining of the two markers. As seen in **Figure 13A**, infiltration was also heterogeneous, and not all infiltrating T-cells (CD3+ staining) were also CTLA-4+. No staining of CD3 or CTLA-4 was noted in control NBSGW tissues.

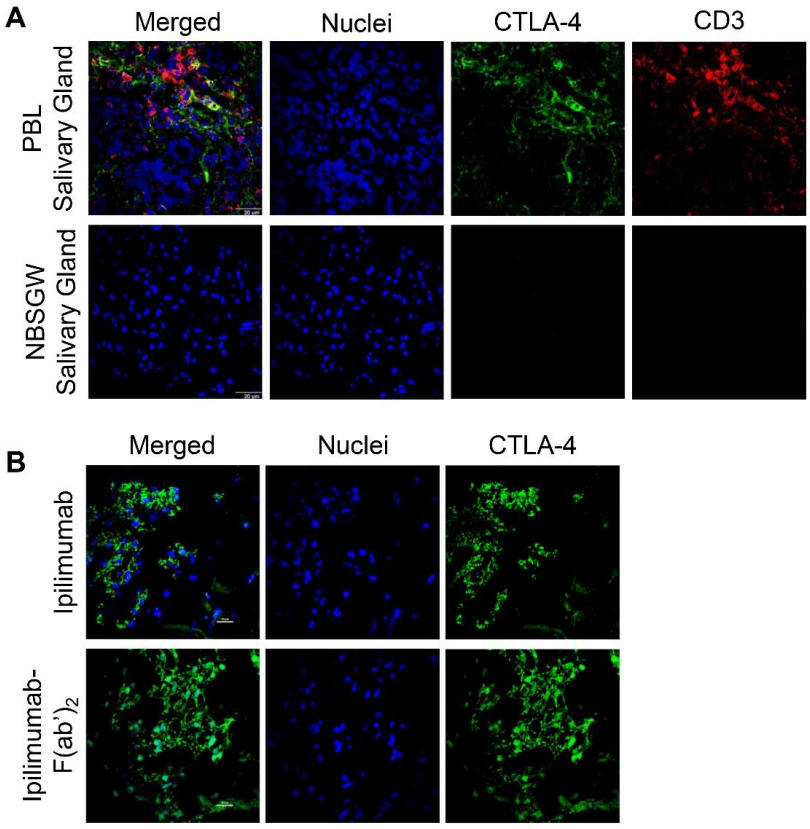

Figure 13. CTLA-4 Salivary Gland Staining. *(A) Immunofluorescent staining of salivary gland tissues verified high levels of human CD3 and CTLA-4 in PBL mice that was absent in NBSGW controls. (B) Both ipilimumab and ipilimumab-F(ab')$_2$ maintained binding to salivary gland tissues after conjugation with FITC.*

4.2.2.2. Ipilimumab-F(ab')$_2$ generation and binding assays

Ipilimumab was digested using the Promega IdeS protease. To verify the digestion and purification, PAGE was performed (**Figure 14A**). The full antibody localized near 150 kDa, while the F(ab')$_2$ fragment was near 110 kDa. No band at 150 kDa was seen in the F(ab')$_2$ lane, meaning the digestion was complete; additionally, there was minimal evidence of the Fc fragment in the F(ab')$_2$ sample as well.

To verify the binding of both ipilimumab and ipilimumab-F(ab')$_2$, each agent was conjugated with fluorescein (FITC, both to allow visualization and to serve as a surrogate for the presence of NOTA) and staining was performed on salivary gland tissues (**Figure 13B**). Both tracers displayed binding that was similar to that of the commercial CTLA-4 antibody used in the CD3 and CTLA-4 co-staining, proving that both tracers retain their specificity even in the presence of conjugated dye (or NOTA).

For a more quantitative measure of binding, flow cytometry was employed. The fluorescein-conjugated agents were once again employed, as seen **Figure 14B-C**. Shown are the mean fluorescent intensities of fluorescein on living lymphocytes (as selected by size) from each of the three conditions. These results demonstrate that, when used on the same cells, both ipilimumab and ipilimumab-F(ab')$_2$ display higher intensities than the control tracer, indicating greater binding affinity, evidenced by the longer tail regions of the histogram plot and resulting higher mean fluorescent intensities.

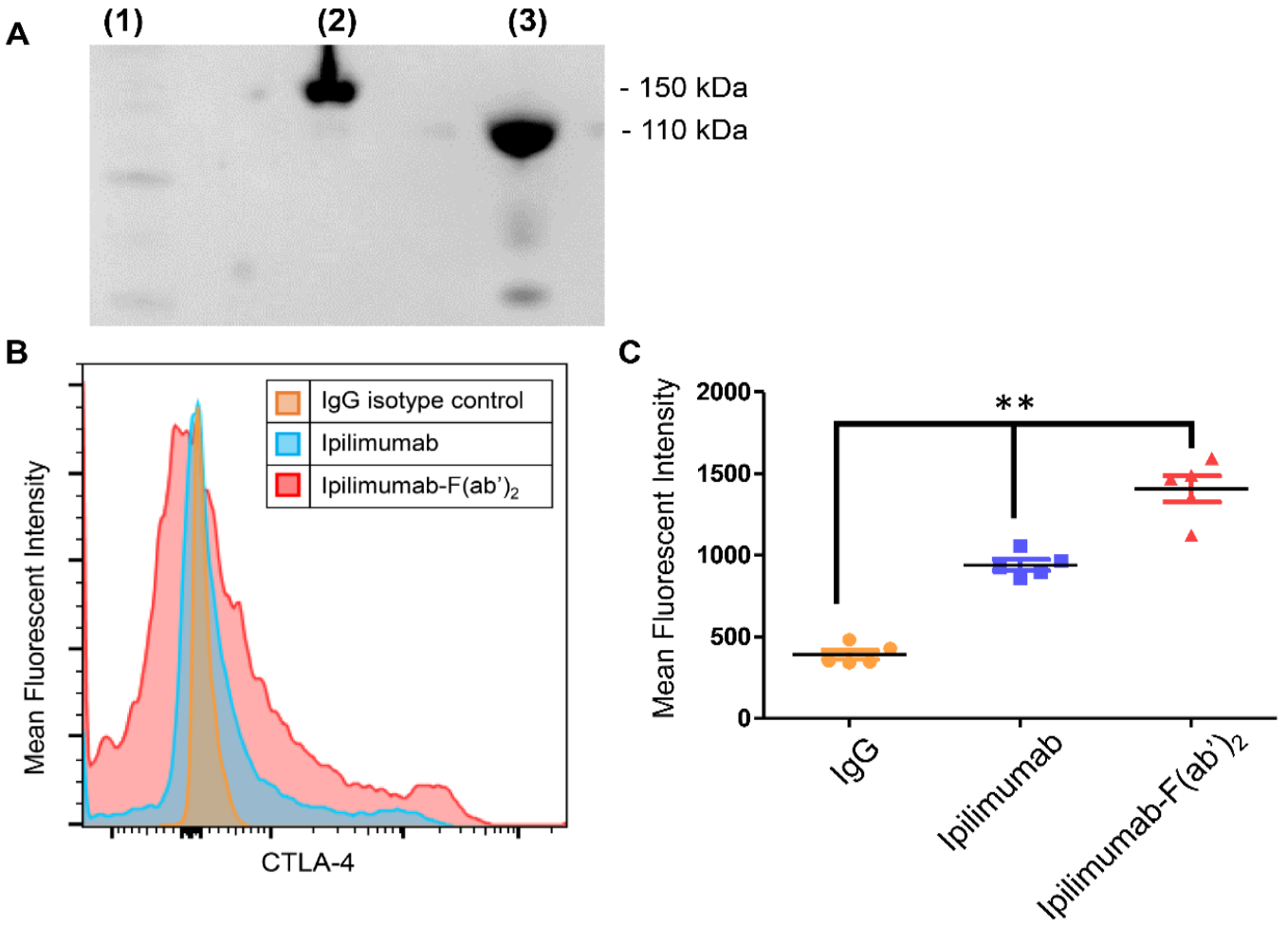

Figure 14. Characterization of CTLA-4 Tracers. *(A) Gel electrophoresis verified the digestion of ipilimumab to create the F(ab')$_2$ fragment. (1) Ladder; (2) Intact ipilimumab; (3) F(ab')$_2$. (B) Results of flow cytometry binding assay with human PBMCs indicate higher binding of the targeted over nontargeted agents. (C) Significantly higher binding of ipilimumab and ipilimumab-F(ab')$_2$ to PBMCs is verified through quantitative mean fluorescence intensity analysis of flow results. **p<0.05; n=5 replicates.*

4.2.2.3. PET localization of CTLA-4+ T-cells

Three tracers were investigated in the PBL mice: ^{64}Cu-NOTA-ipilimumab, ^{64}Cu-NOTA-ipilimumab-F(ab')$_2$, and ^{64}Cu-NOTA-IgG, while two tracers were also studied in control NBSGW mice: ^{64}Cu-NOTA-ipilimumab and ^{64}Cu-NOTA-ipilimumab-F(ab')$_2$.

The clearance patterns of the tracers were well-visualized in the PET imaging (**Figure 15, Figure 16, Figure 17**). For the full antibody-based tracers (^{64}Cu-NOTA-ipilimumab and ^{64}Cu-NOTA-IgG), this clearance mainly proceeded through the hepatobiliary pathway, evidenced through high liver uptake which slowly decreased over time (between 10 and 20 %ID/g in PBL mice). The F(ab')$_2$ tracer was excreted through renal clearance, visualized by notable kidney and urinary bladder accumulation (kidneys: 10-30 %ID/g throughout the study).

The salivary glands served as a site for localization of human T-cells as a result of the graft-versus-host disease that was present in these humanized mice. In PBL mice (n = 3-5), the highest salivary gland uptake was found following injection of ^{64}Cu-NOTA-ipilimumab at 24 h post-injection at 7.00 ± 2.19 %ID/g. The salivary gland uptake of ^{64}Cu-NOTA-ipilimumab-F(ab')$_2$ was highest immediately after injection, but was also 2.40 ± 0.86 %ID/g at the 24 h scan. The control tracer, ^{64}Cu-NOTA-IgG, displayed uptake of 4.2 ± 0.6 %ID/g at the same time point as well. In the control NBSGW mice, ^{64}Cu-NOTA-ipilimumab uptake at 24 h in the salivary glands was at 4.60 ± 0.10 %ID/g, while ^{64}Cu-NOTA-ipilimumab-F(ab')$_2$ was 1.05 ± 0.11 %ID/g. At the 24 h scan, the salivary gland uptake of ^{64}Cu-NOTA-ipilimumab was significantly ($p<0.05$, n=3-6) higher than all groups, except for ^{64}Cu-NOTA-IgG in PBL mice (**Figure 18A, Table II in Appendix 1**).

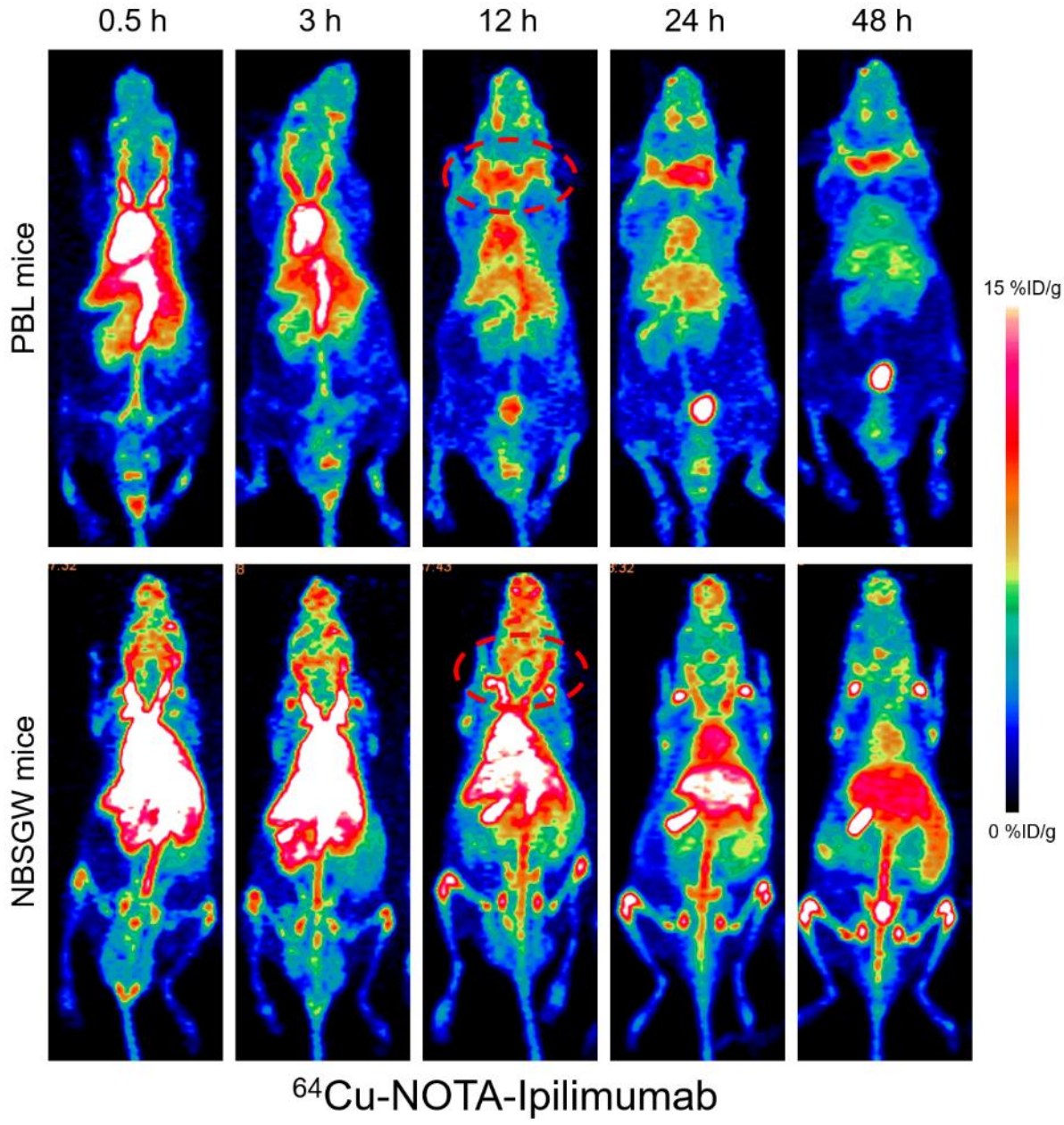

Figure 15. ***^{64}Cu-NOTA-ipilimumab PET Imaging.*** *PET imaging with ^{64}Cu-NOTA-ipilimumab in PBL (top) and control NBSGW (bottom) mice. Salivary gland tissues are outlined in red in the MIPs.*

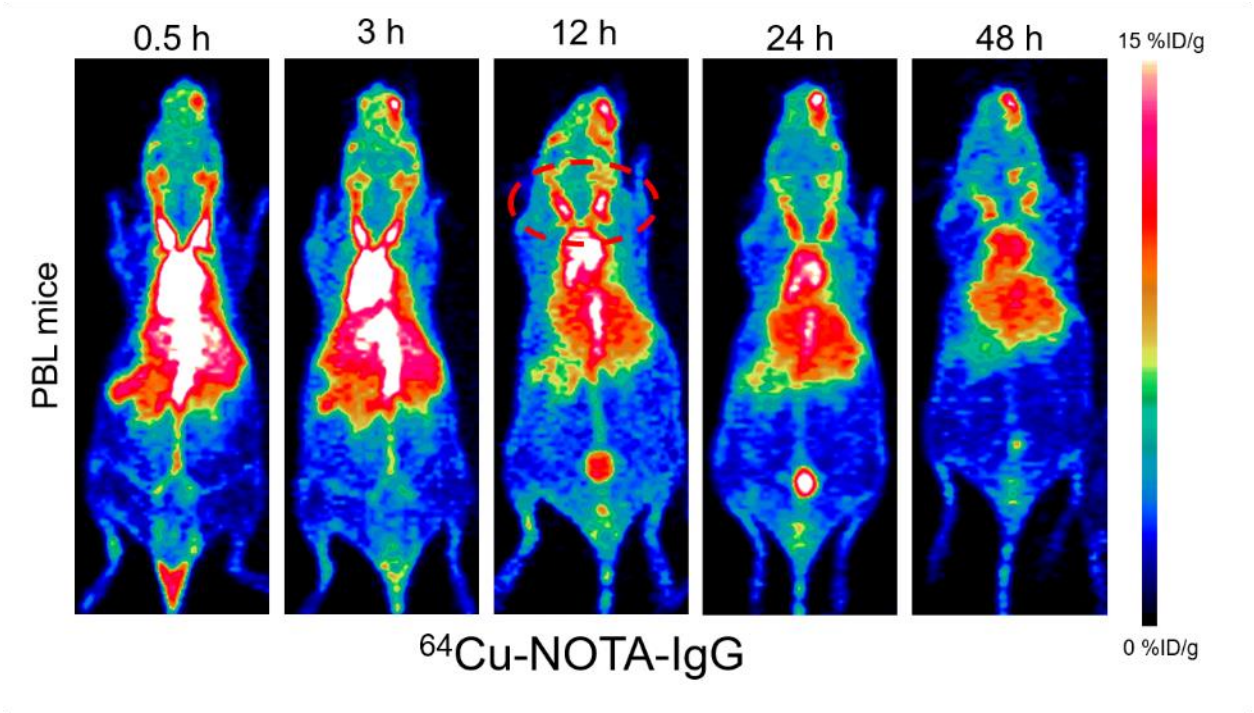

Figure 16. ***^{64}Cu-NOTA-IgG PET Imaging.*** *PET with a control nonspecific IgG in PBL mice showed minimal uptake in salivary gland tissues in the MIP images.*

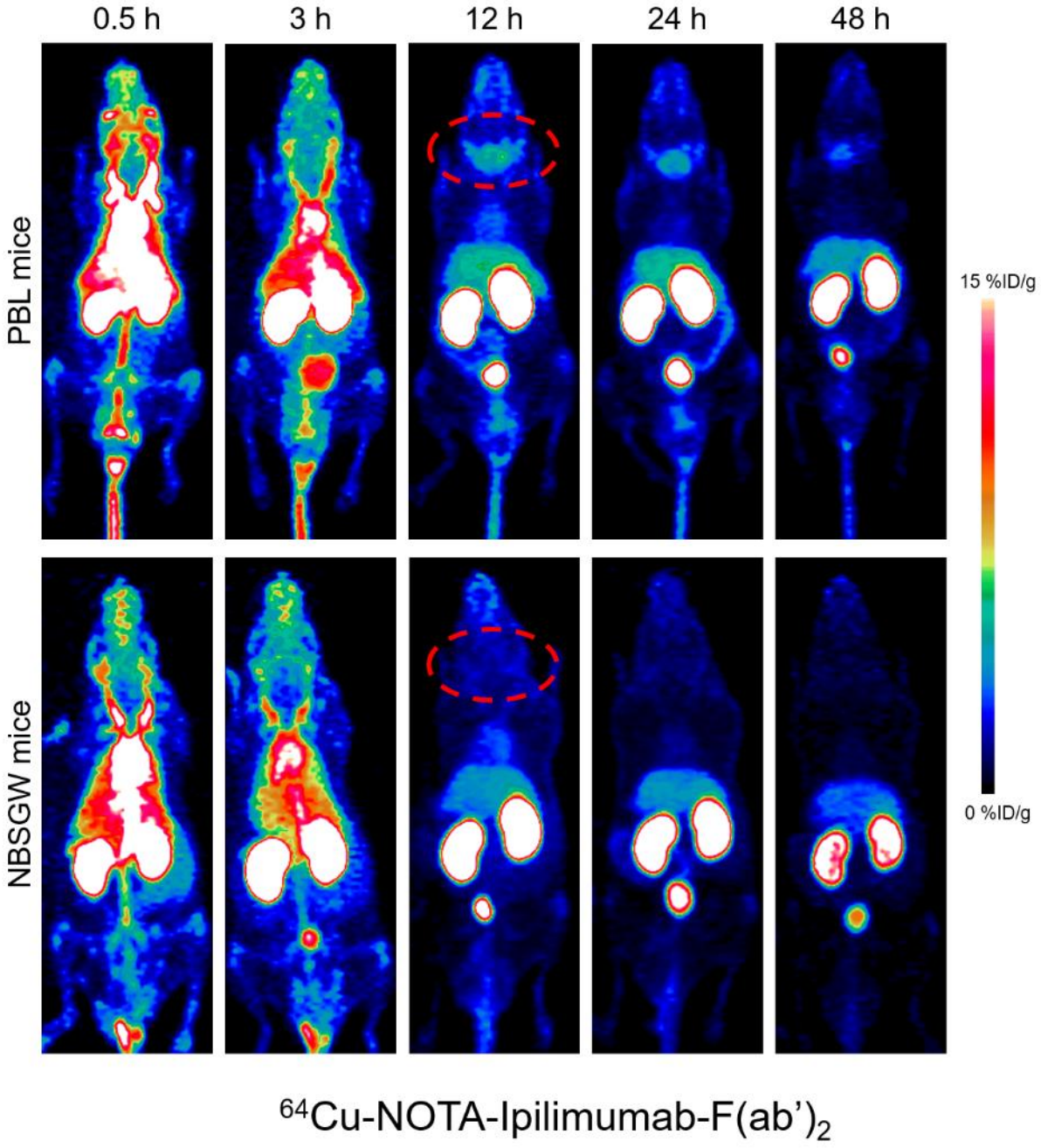

Figure 17. ^{64}Cu-NOTA-ipilimumab-F(ab')$_2$ PET Imaging. *PET with ^{64}Cu-NOTA-ipilimumab-F(ab')$_2$ in humanized PBL (top) and control NBSGW (bottom) mice. Salivary gland tissues are outlined in red in the MIPs.*

While the absolute uptake of the F(ab')$_2$ tracers was much lower in the salivary glands when compared to their full antibody counterparts, the quick clearance of this tracer enabled higher contrast to be achieved, and at earlier time points. This is evidenced by the salivary gland – to – blood ratios (**Figure 18B**). In the PBL mice, ^{64}Cu-NOTA-ipilimumab-F(ab')$_2$ had the highest ratio of 1.78 ± 0.72 at 48 h post-injection, followed by ^{64}Cu-NOTA-ipilimumab at 1.19 ± 0.49, and ^{64}Cu-NOTA-IgG at 0.34 ± 0.08 (n = 3-6). The ratios were lower in the control NBSGW mice: 0.82 ± 0.11 for ^{64}Cu-NOTA-ipilimumab-F(ab')$_2$ and 0.77 ± 0.19 for ^{64}Cu-NOTA-ipilimumab.

As a corroboration for the salivary glands as a site of human immune cell infiltration, as well as to support the PBL model for validating T-cell targeting tracers, a linear correlation was found between the humanization status of the PBL mice and the salivary gland uptake of ^{64}Cu-NOTA-ipilimumab, shown in **Figure 19**. Additionally, extrapolating this trend to 0% humanization well-predicted the accumulation of the non-targeted tracer in PBL mice, and of ^{64}Cu-NOTA-ipilimumab in NBSGW mice.

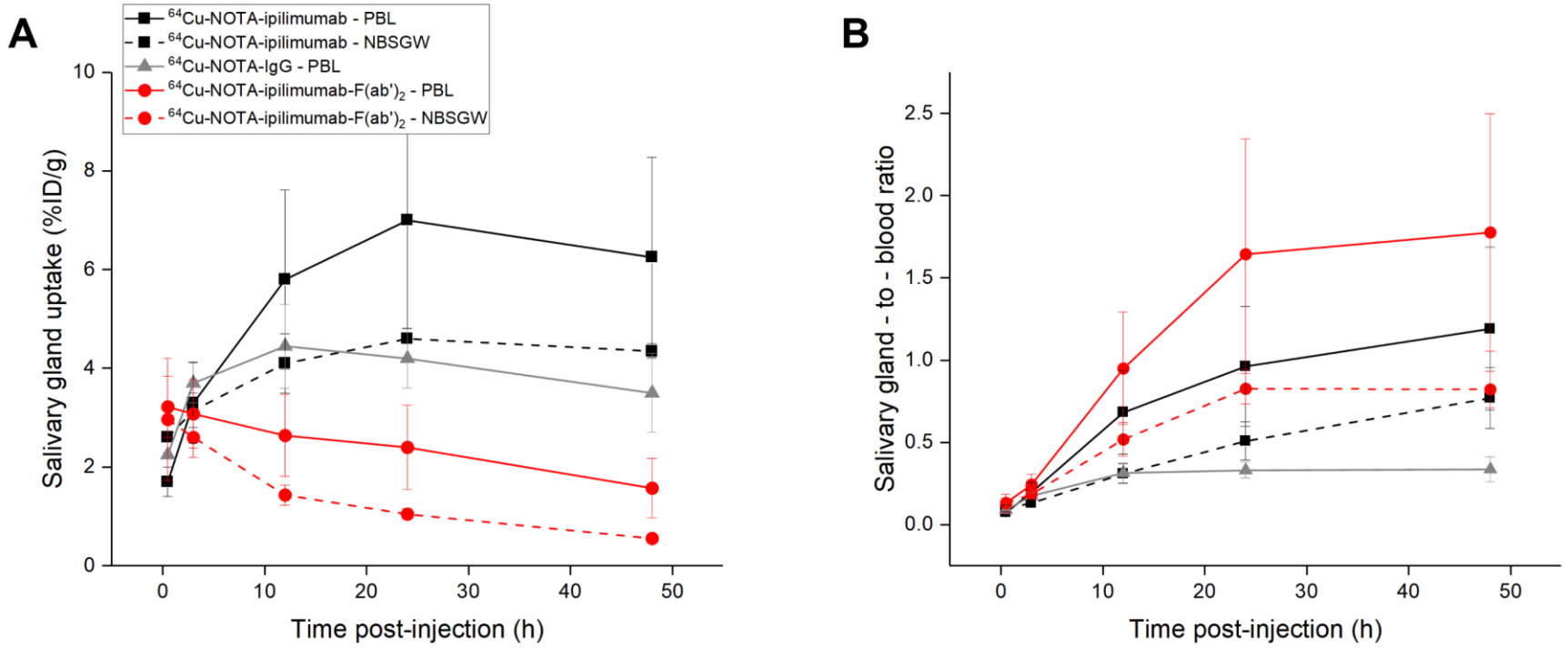

Figure 18. Quantification of CTLA-4 T-cell PET Results. *(A) Absolute uptake of the given tracers in the salivary gland tissues of PBL and NBSGW mice, as determined through ROI analysis of PET images. (B) Salivary gland – to – blood ratios show the high contrast achieved with the targeted tracers. n=3-6.*

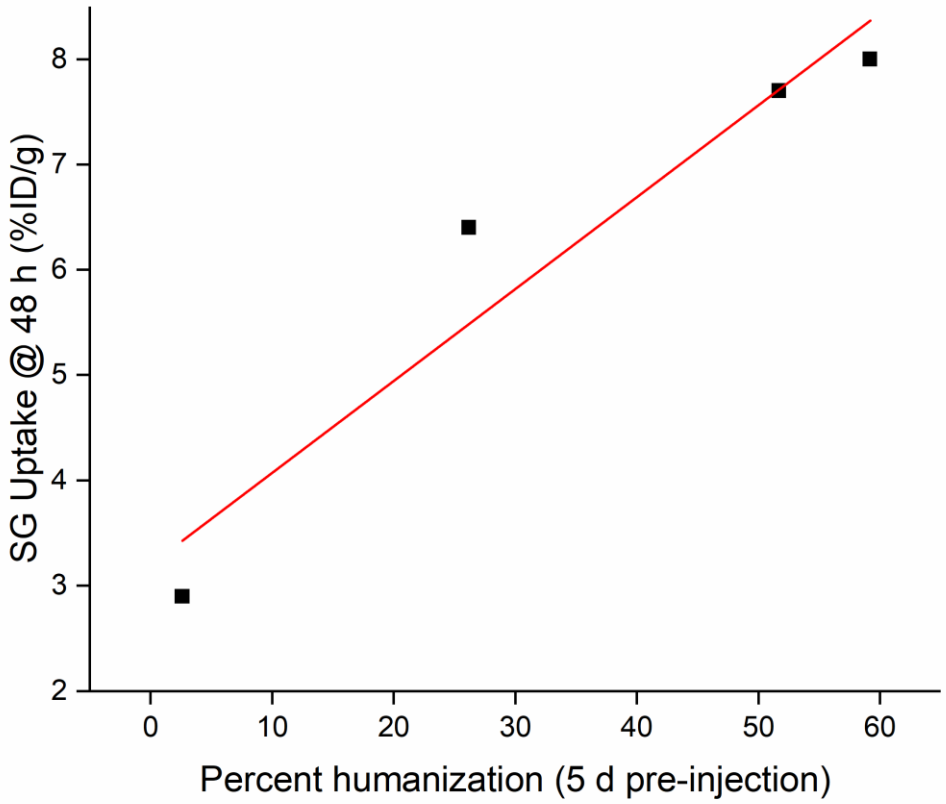

Figure 19. Correlation of Humanization and CTLA-4 Salivary Gland Uptake. *The correlation of salivary gland uptake of ^{64}Cu-NOTA-ipilimumab and the humanization status of the PBL mice shows a positive relationship.*

4.2.2.4. Biodistribution studies

The trends found through quantification of PET regions-of-interest were corroborated through *ex vivo* biodistribution studies (**Figure 20, Table II in Appendix 2**). Notably, the salivary gland uptakes as calculated through gamma counting were very well-matched to the image-derived values at the final time point. The highest accumulation in the salivary glands was noted in PBL mice injected with ^{64}Cu-NOTA-ipilimumab, at 6.27 ± 2.14 %ID/g. This was followed by ^{64}Cu-NOTA-ipilimumab in NBSGW mice at 5.53 ± 0.18 %ID/g, ^{64}Cu-NOTA-IgG in PBL mice at 3.43 ± 0.28 %ID/g, ^{64}Cu-NOTA-ipilimumab-F(ab')$_2$ in PBL mice at 1.53 ± 0.65 %ID/g, and ^{64}Cu-NOTA-ipilimumab-F(ab')$_2$ in NBSGW mice at 0.87 ± 0.19 %ID/g.

With the F(ab')$_2$ tracer, the uptake of the tracer in most normal organs was comparable, with the highest accumulation found in the kidneys. However, the distribution of ^{64}Cu-NOTA-ipilimumab was quite different in NBSGW mice when compared to PBL, likely a result of Fc-dependent effects which have been documented in immunodeficient mice[78]. This led to extremely high accumulation of the tracer in the spleen (84.57 ± 13.30 %ID/g, n = 3), and significant bone uptake as well (9.93 ± 0.45 %ID/g), which is not an expected site of uptake for copper-labeled tracers. For comparison, the spleen accumulation of ^{64}Cu-NOTA-ipilimumab in PBL mice was 8.89 ± 3.51 %ID/g, while the bone uptake was only 0.91 ± 0.36 %ID/g (n = 5).

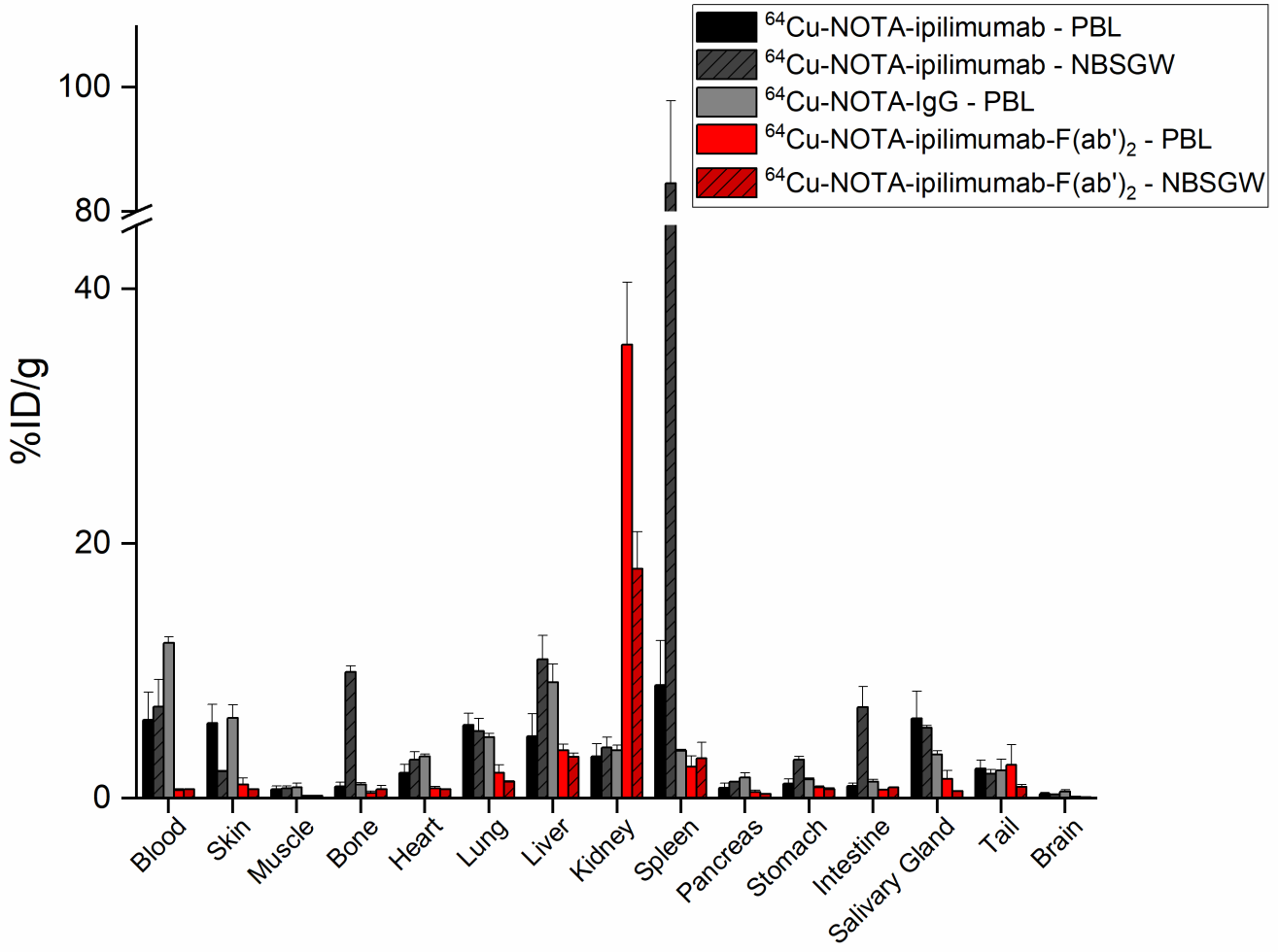

Figure 20. CTLA-4 Biodistribution Study Results. *Results of ex vivo gamma counting biodistribution studies of ^{64}Cu-NOTA-ipilimumab and F(ab')$_2$ in PBL and NBSGW mice. n=3-6.*

4.2.2.5. Dosimetric evaluation of tracers

The results of the dosimetric study well-mirrored the biodistribution of the respective tracers (**Figure 21, Table I in Appendix 3**). Across all groups injected with full-length antibodies, the salivary glands received the highest dose (between 0.015 – 0.018 mSv/MBq). As aforementioned, this uptake was due to graft-versus-host disease onset and would not be expected in a human patient so the dose to the salivary glands would be much lower. Consistent with the clearance patterns of antibodies, the liver and gastrointestinal tract also received doses over 0.004 mSv/MBq in these groups. For the $F(ab')_2$ groups, the highest doses were calculated for the bladder wall (0.009 – 0.013 mSv/MBq), since this tracer is primarily cleared from the kidneys. Kidney doses in these groups were also notably larger than that from the full-antibody groups, but still below 0.004 mSv/MBq.

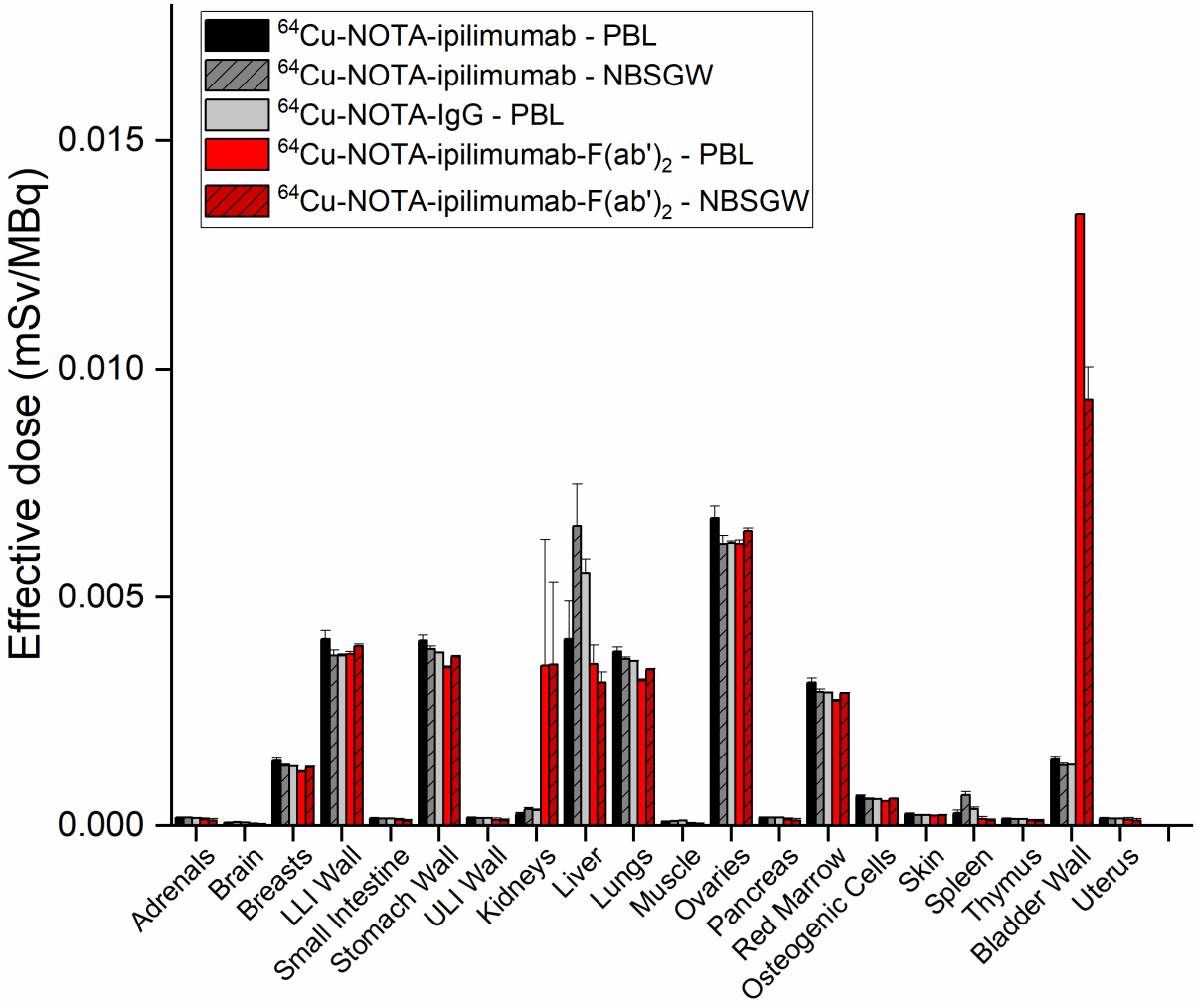

***Figure 21. CTLA-4 Dosimetry**. Results of dosimetric extrapolation of CTLA-4 targeting tracers to an adult human female using OLINDA. n=3-6.*

4.2.3. PD-1 imaging[44]

4.2.3.1. Pembrolizumab binding assays

A binding assay of pembrolizumab to CD4+ and CD8+ T-cells was carried out to ensure that that Df conjugation to pembrolizumab did not hinder or alter its binding affinity or specificity. T-cells were stimulated for 18 h before the addition of pembrolizumab or Df-pembrolizumab. Chelated pembrolizumab was shown to bind specifically to activated CD4+ and CD8+ T-cells and chelation was not found to substantially alter its binding affinity for these activated cells (**Figure 22**).

4.2.3.2. Radiolabeled pembrolizumab characterization

Post-radiolabeling, the purified ^{89}Zr-Df-pembrolizumab was shown to be labeled with a specific activity of 740 mBq/mg antibody. Labeling efficiency was determined by instant thin-layer chromatography and shown to be greater than 60%.

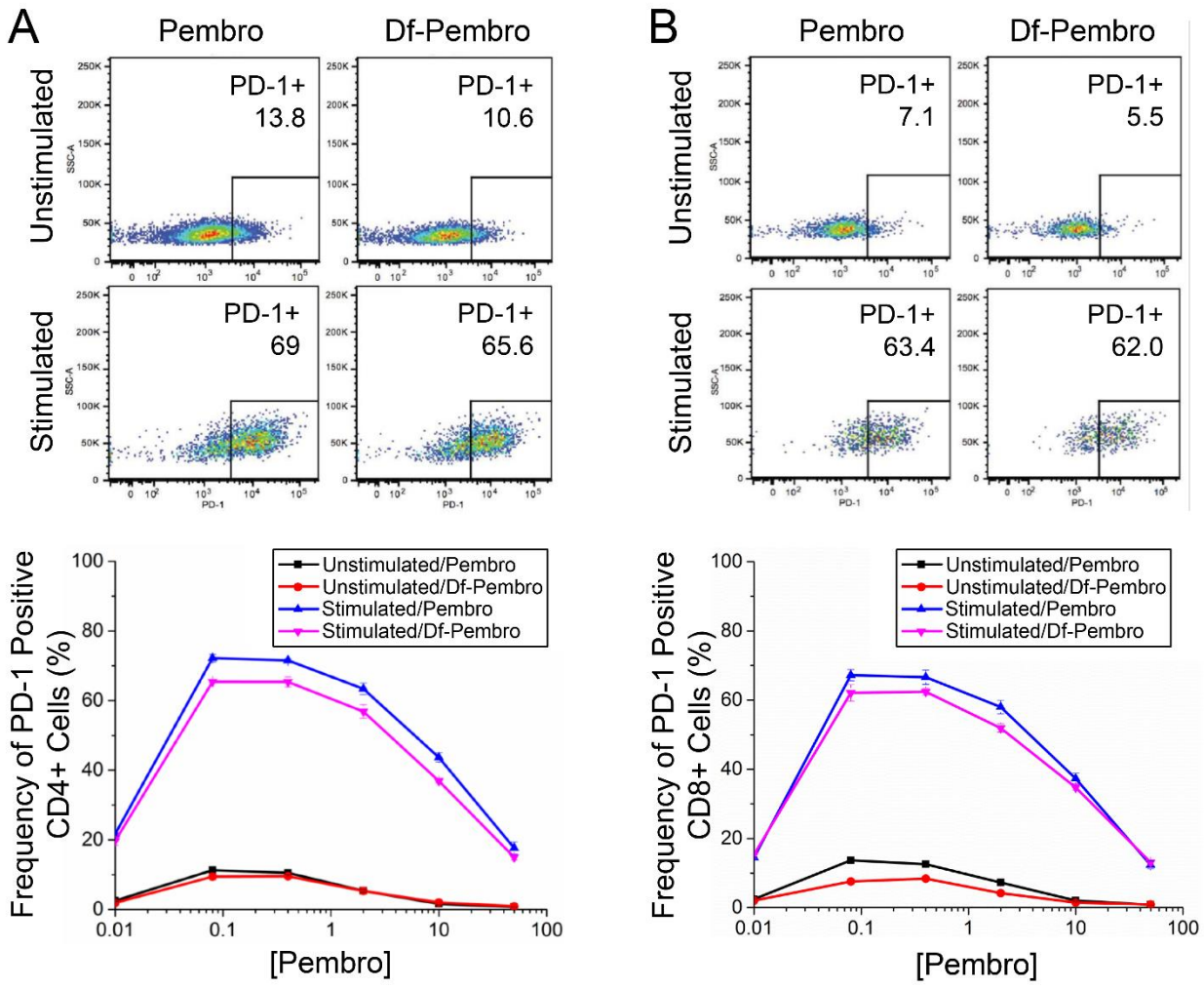

Figure 22. PD-1 Tracer Characterization. *Flow cytometry was utilized to verify the binding of pembrolizumab and Df-conjugated pembrolizumab to PD-1+ PBMCs. (A) CD4+ cells and (B) CD8+ cells.*

4.2.3.3. PET imaging of PD-1+ cells

The biodistribution of ^{89}Zr-Df-pembrolizumab was mapped in NSG and PBL mice. PBL mice were generated by engrafting 10^6 human PBMCs into 4-6 week old NSG mice. Thus the PBL model was utilized to demonstrate that ^{89}Zr-Df-pembrolizumab may function as a potential radiotracer for imaging of human PD-1 expression *in vivo*. PET imaging of NSG and PBL mice showed similar findings in most organs, including the spleen, kidney, and muscle tissues (**Figure 23, Table III in Appendix 1**). However, there were two main differences between the tracer biodistribution in PBL and NSG mice (**Figure 24**). First, PBL mice showed a shorter blood circulation in comparison to NSG mice. A statistically significant difference was found between the blood pool activity of NSG (9.78 ± 0.80 %ID/g) and PBL (6.13 ± 0.41 %ID/g) mice at 48 h and continued through 168 h post-injection (n=4). Second, the PBL mice displayed high uptake in the salivary glands. This difference in tracer accumulation was statistically significant at 6 h and each time point afterward.

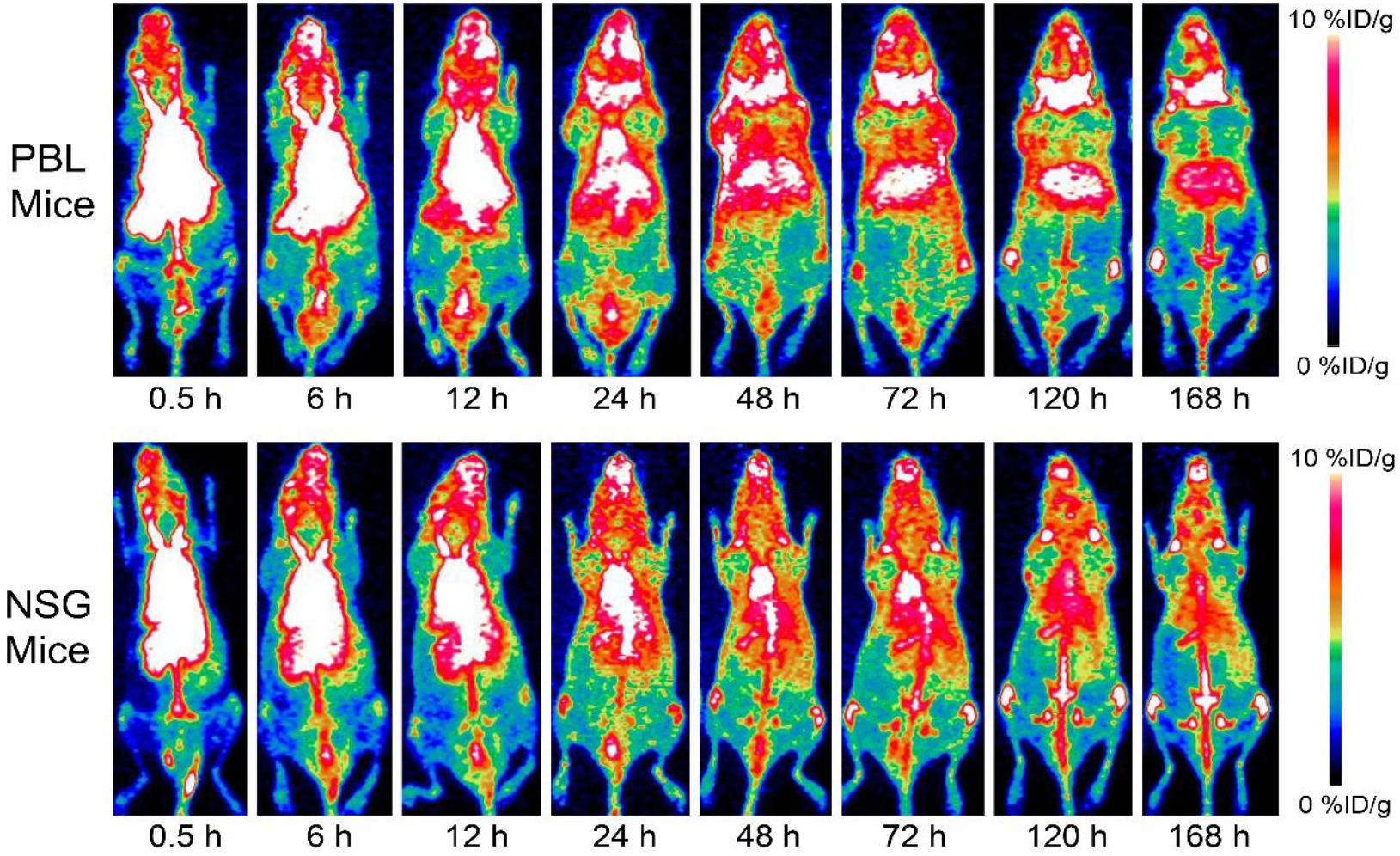

Figure 23. PD-1 PET Imaging. *PET imaging with ^{89}Zr-Df-pembrolizumab in both humanized PBL (top) and control NSG (bottom) mice.*

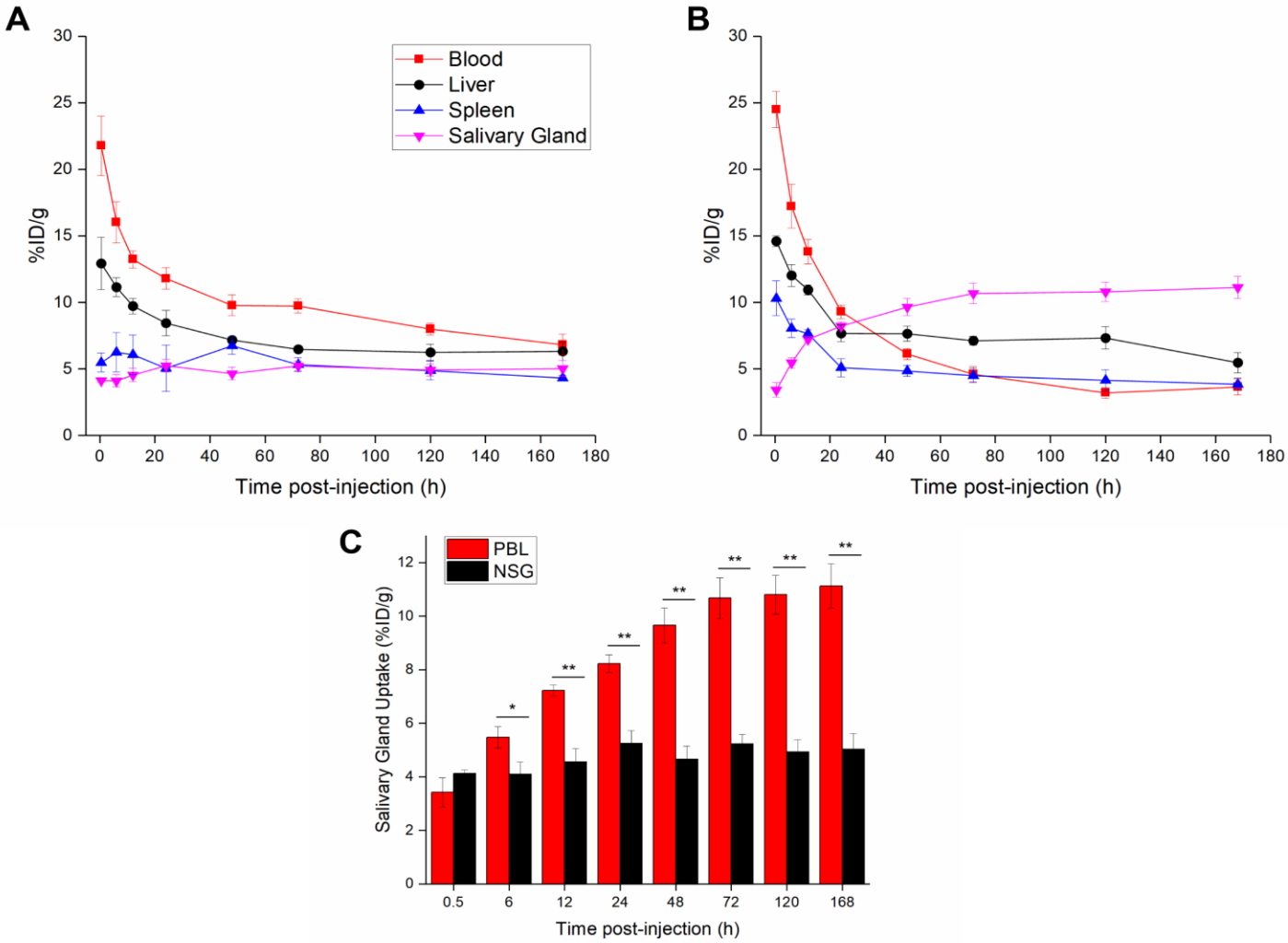

Figure 24. PD-1 PET Imaging Quantification. *Measurement of ^{89}Zr-Df-pembrolizumab uptakes. (A) Major organs in NSG mice; (B) major organs in PBL mice; (C) salivary gland uptakes throughout the course of the study. *p<0.05; **p<0.01.*

4.2.3.4. Staining of salivary gland tissues

Histological studies further validated that the salivary glands of PBL mice contained human T-cells expressing PD-1 through staining of the T cell markers CD3 and PD-1, while NSG mice showed minimal staining as expected (**Figure 25**).

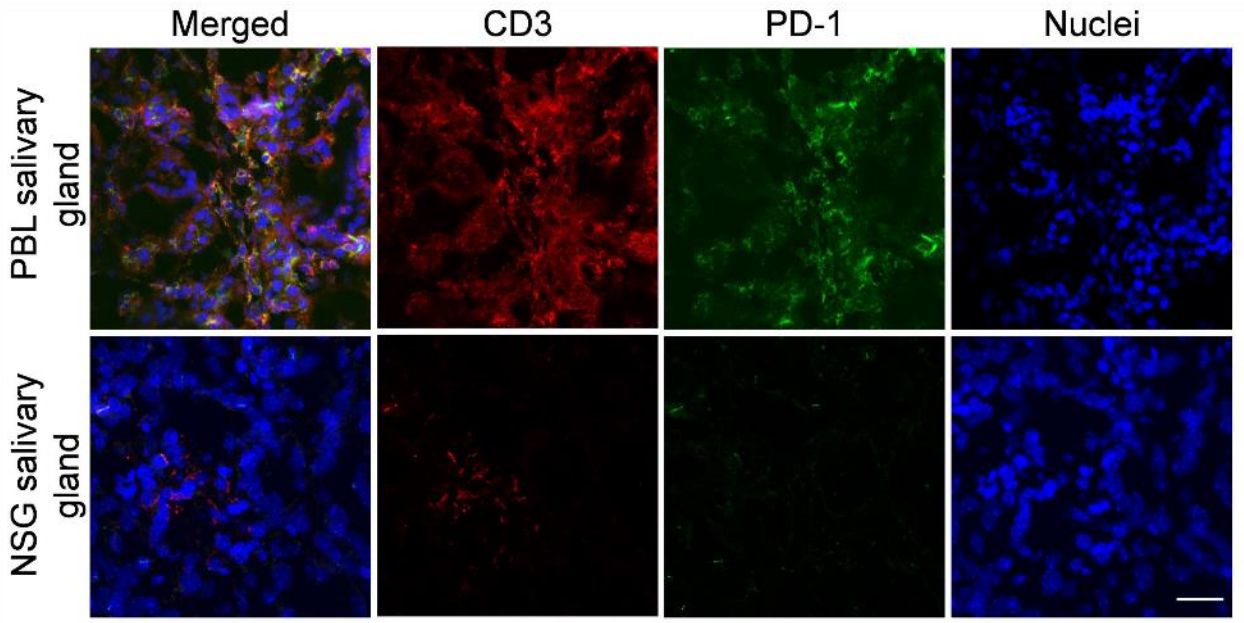

Figure 25. PD-1 Salivary Gland Staining. *Staining of salivary gland tissues revealed extensive human CD3 and PD-1 presence in PBL mice that was absent in control NSG.*

4.2.3.5. Radiation Dosimetry

Estimations of human absorbed doses to normal tissues, based on the biodistribution of ^{89}Zr-Df-pembrolizumab in mice, are summarized in **Figure 26**. PBL dosimetry showed high doses to the liver (1.207 mGy/MBq) and ovaries (1.591 mGy/MBq in PBL), as shown in **Table II in Appendix 3.** A key difference in tracer biodistribution was the elevated uptake observed in the salivary glands of PBL mice, which resulted in higher total body doses to PBL mice (1.246 mGy/MBq vs. 0.838 mGy/MBq for PBL and NSG mice, respectively).

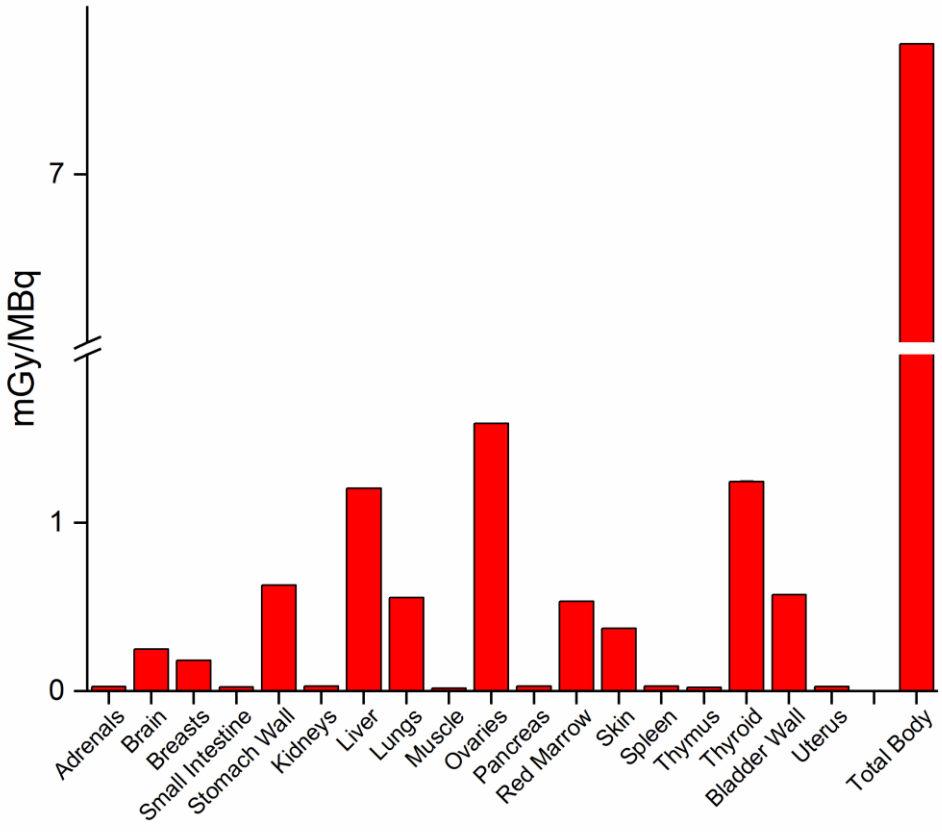

Figure 26. PD-1 Radiation Dosimetry. *Results of dosimetric extrapolation of ^{89}Zr-Df-pembrolizumab in PBL mice to that expected in an adult human female.*

4.2.4. Comparison of PD-1 and CTLA-4 tracers

A comparison of the salivary gland accumulations of both ^{89}Zr-Df-pembrolizumab and ^{64}Cu-NOTA-ipilimumab showed a number of trends, as visualized in **Figure 27**. Overall, the PD-1 tracer accumulated to a higher absolute level than that of the CTLA-4 tracer, as seen in **Figure 27B**. This may be due to a number of phenomena. Most likely, the difference is due to the different mouse models employed in these studies – PD-1 was founded on NSG mice, while CTLA-4 was based upon NBSGW mice, which resist graft-versus-host disease to a greater extent. There may also be varied levels of PD-1+ and CTLA-4+ cells in the mice and in the salivary gland tissues. The expression of these markers may also display differing dynamic patterns – PD-1 may be more stably expressed than CTLA-4. However, a comparison of the salivary gland – to – blood ratios (**Figure 27A**) for these tracers shows no statistically significant difference between targeting of PD-1 or CTLA-4 in the PBL mice, indicating that both tracers are reasonable options for imaging T-cells *in vivo*. Notably, the difference between the salivary gland uptake in the PBL and control mice with the PD-1 tracer was larger than that observed with the CTLA-4 tracer, which may indicate increased specificity of pembrolizumab.

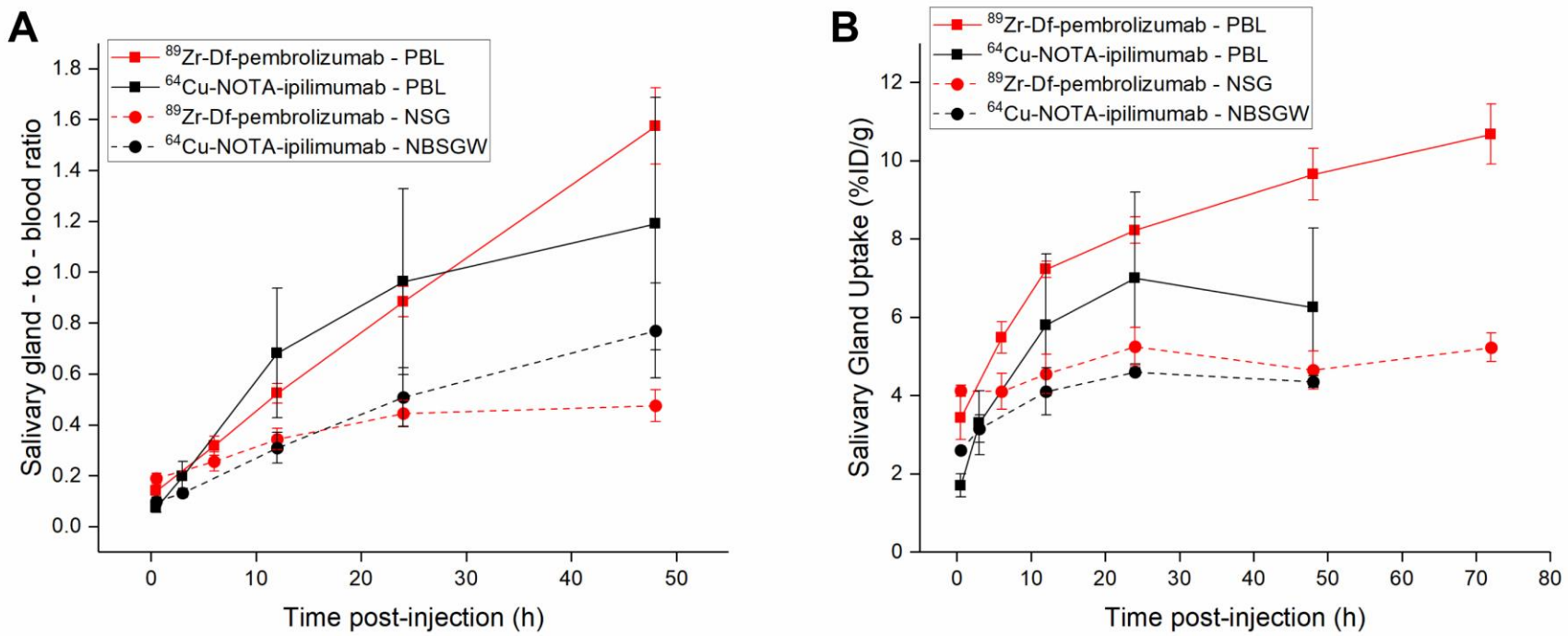

Figure 27. PD-1 vs. CTLA-4 PET. *A comparison of the PD-1 and CTLA-4 PET tracers' salivary gland-to-blood ratios (A) and salivary gland accumulations (B). n=3-6.*

4.3. Discussion

In recent years, immunotherapy has increasingly become a major player in the management of many cancers. The immune system is programmed to recognize foreign and invasive cells, while at the same time protecting host tissues which express self-antigens. However, many cancers hijack these protection mechanisms in order to escape detection by the immune system, effectively impeding both innate and adaptive immune responses[15]. Interventional interference with these protection pathways has been found to reactivate the immune system toward malignant cells and can lead to cancer remission in some patients[1]. CTLA-4 and PD-1, expressed by activated T-cells, have recently been recognized as important targets in cancer immunotherapy treatments. Blockade of these receptors has been shown to improve patient survival in several cancers, using the FDA-approved antibodies ipilimumab[59, 79] for CTLA-4, or pembrolizumab and nivolumab for PD-1[80, 81].

The efficacy of CTLA-4-targeted therapy is closely correlated to activated lymphocyte expression of CTLA-4, yet other factors may play a role in the overall success of immunotherapies. For example, it was recently determined that many tumor cell lines express CTLA-4, but few studies have investigated the role of CTLA-4 expression by tumor cells, making this expression still of debatable import[82, 83]. In this aim, we first evaluated the biodistribution of ^{64}Cu-labeled ipilimumab in mice bearing CTLA-4-expressing lung tumor xenografts[72]. The presence of CTLA-4 on tumor cells provides a simple, albeit artificial, model for tracking of CTLA-4 expression in this study, as CTLA-4 expression was solely localized on these tumor cells in the mice while in human patients its expression would be more widespread.

To validate that CTLA-4 was expressed in our lung cancer cell lines, we employed both ELISA and Western blot assays (**Figure 7**). Both assays confirmed that CTLA-4 was expressed in the cancer cells at relatively low levels, but did not provide insight into the subcellular localization of the protein. It has been extensively documented that CTLA-4 may be found on both intracellular membranes and the cell surface, yet our tracer would only have access to CTLA-4 expressed on the cell surface[84]. For this reason, we did not expect to find a linear correlation between *in vivo* tracer uptake and total CTLA-4 expression and this expectation was confirmed through PET imaging. While A549 was shown to have higher CTLA-4 expression through *in vitro* studies, PET imaging revealed that both A549 and H460 showed similar tumor uptakes of ^{64}Cu-DOTA-ipilimumab (**Figure 9, Figure 10, Figure 11).** Also, accumulation of ipilimumab in H358 xenografts, and the blocking experiment, seems to be mostly nonspecific, as H358 cells were found to have low CTLA-4 expression levels. The use of these human lung cancer cell line xenografts provided a simple *in vivo* model to monitor CTLA-4 levels as a proof-of-concept for CTLA-4 PET imaging. Only the tumor exhibited specific binding of ^{64}Cu-DOTA-ipilimumab, as this is the only tissue with human CTLA-4 expression.

For a more clinically-representative situation, we employed similar CTLA-4 PET tracers in humanized mice in order to visualize the distribution of CTLA-4+ PBMCs. These studies utilized the same ipilimumab backbone, but NOTA served as the chelator since this compound has demonstrated enhanced radiolabeling stability[85]. Radiolabeled full-length antibodies are beginning to see clinical translation for cancer imaging[86, 87], given their high specificity. However, the high background that occurs in antibody-based imaging may preclude their use in certain situations. Therefore, other biological platforms, such as antibody fragments, are also being explored. In this study, both full-length ipilimumab and its F(ab')$_2$ fragment were labeled with ^{64}Cu to allow for

PET imaging. Ipilimumab provided higher absolute uptake in target organs, while ipilimumab-F(ab')$_2$ allowed higher contrast imaging at earlier timepoints, albeit at lower absolute uptake values.

It has recently been reported that anti-CTLA-4 therapy requires an Fc domain to be effective[88, 89]; therefore, the F(ab')$_2$ tracer may have an additional benefit for imaging: this agent should not induce a therapeutic effect, especially at the small tracer dose levels. This could allow for repeated imaging without fear of pharmacologic response. A recent study also reported interesting findings with radiolabeled antibodies in immunodeficient mice[78] – a finding that was mirrored in the present study. In the control NBSGW mice, very high spleen and bone uptakes were observed, which was hypothesized to be as a result of the Fc interactions in this group of mice that would not have been present in any other groups. For instance, the F(ab')$_2$ tracers do not contain Fc portions, and the PBL mice would have already been exposed to human Fc through the humanization process; therefore, this anomalous distribution of the tracer was not seen in these groups.

Finally, we developed ^{89}Zr-Df-pembrolizumab for imaging PD-1+ PBMCs in humanized mice. This tracer demonstrated similar uptake patterns as were observed in the CTLA-4 T-cell studies, with notable accumulation in salivary gland tissues. Similar to our findings, several research groups have reported that engrafted immune cells infiltrate the salivary glands and lacrimal glands in PBL mice[77, 90, 91]. In this study, the salivary glands of PBL mice displayed the highest uptake of ^{89}Zr-Df-pembrolizumab of 11.13 ± 0.82 %ID/g at 168 h post-injection, while NSG mice showed only 5.03 ± 0.59 %ID/g at the same time point (**Figure 23, Figure 24**; n=4). Thus, this study successfully demonstrated the ability to use a noninvasive immunotherapeutic-based imaging agent to monitor PD-1 localization and expression *in vivo*.

PBL mice provide a simplistic system to image human immune cells *in vivo*. However, this model is not without fault. The onset of graft-versus-host disease in these mice[92] causes certain organs to dysfunction and limits the mouse's lifespan. However, this also provides targeted sites of localization for the engrafted human immune cells, such as the salivary glands. Additionally, with this model, it is difficult to control the level of engraftment of the human cells; that is, the percent of circulating blood cells that are human versus murine can vary anywhere from 1-80+%, leading to unpredictable levels of graft-versus-host disease and therefore salivary gland dysfunction[74]. This level can increase quite rapidly once engraftment is successful, and, since engraftment is monitored through blood draws and time-intensive flow cytometry analysis, precise monitoring can be difficult. This wide range of humanization levels leads to the relatively large range of salivary gland uptake values of the tracers in the PBL mice. However, comparison with the nonspecific antibody in these mice provides confidence that the salivary gland uptake is on-target. In particular, a comparison of the salivary gland-to-blood ratios for radiolabeled ipilimumab and IgG shows the specificity of that particular targeted tracer. Additionally, simple correlative studies between the salivary gland uptake of tracers and the percent humanization of the PBL mice indicate a positive correlation.

The salivary glands are not an expected site of uptake of these T-cell-targeting tracers in humans. In a clinical immunotherapy setting, the tracers could be employed to identify tumor-infiltrating T-cells; however, they could also find application in visualizing potential side effects of the treatment. In this sense, the graft-versus-host disease model herein is quite applicable, as autoimmune reactions are quite common in checkpoint blockade treatments[93]. These tracers may thus be able to stratify patients for potential responses based on their tumor-infiltrating lymphocyte population, and additionally identify those who may be particularly susceptible to adverse effects.

One important limitation of this work is that several studies have shown that preclinical investigation of antibody biodistribution in rodent models greatly varies from the observed kinetics in human patients[94]. High uptake in the liver and spleen of the mice was likely a result of expected nonspecific binding and hepatobiliary clearance[95]. These intramodel differences are a limitation to the successful translation of some therapeutic antibodies, yet data obtained from rodent models may be conservatively extrapolated to humans through dosimetry analysis. This provides essential information regarding the expected human internal radiation doses to normal organs associated with the administration of radiolabeled antibodies. While all animals maintain similar biological machinery for the metabolism and elimination of drugs, these metabolic capabilities differ between different animal species[94]. For example, it has been shown that mice and rats display enhanced biliary excretion rates, while humans and other primates exhibit poor biliary excretion of most drugs[94, 96]. Dosimetry data may help predict potential toxicities before they occur in humans, while also assisting scientists in determining optimal initial dosing strategies when needed. The pattern of absorbed dose values obtained in these studies indicate that these agents localize in several tissues, further confirming the optimal circulation and low toxicity profile found in clinical trials.

The imaging tools developed in this aim are expected to serve important roles in the future for immunotherapy patients. By noninvasively visualizing the highly dynamic immune checkpoints CTLA-4 and PD-1, researchers and clinicians alike will be able to gain an unprecedented understanding of the mechanisms of these treatments, and better design these therapies for optimal patient outcomes.

Chapter 5

5. Imaging PD-1+ Tumor-Infiltrating Lymphocytes‡

Despite being the most preventable malignancy, lung cancer remains the leading cause of cancer-related death worldwide, accounting for nearly 1.6 million estimated deaths in 2017[97]. Detection of early disease remains critical to successful treatment, yet the lack of physical symptoms results in more than 70% of patients presenting with advanced stage disease (stage III/IV) at the time of diagnosis. While surgical intervention yields the highest cure rates, most patients with advanced stage disease are not candidates for surgery. Hence, these patients rely on radiation therapy, chemotherapy, and newer targeted therapies like immune checkpoint inhibitors. With this in mind, the newly approved immunotherapy agents pembrolizumab and nivolumab have significantly improved the survival rates in a subset of lung cancer patients[80].

In spite of an increase in the popularity of immunotherapies, limited studies have characterized the biodistribution and pharmacokinetic properties of immune checkpoint inhibitor antibodies *in vivo* outside of clinical trials. Therefore, we developed and validated ^{89}Zr-Df-nivolumab to image PD-1+ T-cells as they infiltrated tumor tissues, a clinically-relevant situation. In the future, such imaging may be able to identify patients with "hot" tumors who are

‡ Much of this chapter has been previously published in: **42.** England CG, Jiang D, Ehlerding EB, et al. 89Zr-labeled nivolumab for imaging of T-cell infiltration in a humanized murine model of lung cancer. *European Journal of Nuclear Medicine and Molecular Imaging.* 2018;45:110-120.

more likely to respond to immunotherapies since they have higher levels of infiltrating lymphocytes.

5.1. Materials and Methods

5.1.1. Flow cytometry

This protocol was approved by an institutional review board at the University of Wisconsin – Madison, and all patients consented to the study. Blood samples were collected from patients for isolation of PBMCs using the Ficoll-Histopaque (GE Healthcare) technique by density gradient centrifugation. The cells were washed and stimulated for 18 h with 40 ng/mL phorbol myristate acetate (Sigma-Aldrich) and 1.3 µg/mL ionomycin (MP Biomedicals). After stimulation of the PBMCs, cells were stained with nivolumab or the chelator-antibody conjugate (Df-Nivolumab) for 1 h at 4°C. Next, the cells were washed and stained with AlexaFluor488-labeled anti-human IgG (Life Technologies) for 2 h at room temperature. Also, cells were stained with the primary antibodies CD3-v500, CD4-PE, and CD8-APC antibodies (BD Biosciences) and GhostDye Red-780 (Tonbo Biosciences). Cells were washed and resuspended in phosphate buffered saline (PBS) with 3% fetal calf serum, and analyzed on a BD LSRFortessa cytometer.

5.1.2. Chelation and radiolabeling procedures

Nivolumab was obtained commercially from Bristol-Myers Squibb Company. The antibody was reconstituted in PBS before conjugation with p-SCN-desferrioxamine (Df; Macrocyclics) through the exposed lysine residues using methods previously described in the literature[44]. After mixing the antibody and chelator at a molar ratio of 1:5, the pH was adjusted to ~8.5 using Na_2CO_3 and the mixture was incubated at room temperature for 2 h. After reacting, the

solution was purified via PD-10 column (size exclusion chromatography) with PBS as the mobile phase. The radionuclide (^{89}Zr) was produced in a GE PETtrace cyclotron by irradiation of natural yttrium foils (250 μm, 99.9%) with 13.8 MeV protons using methods previously described[98]. For radiolabeling, 74-148 MBq of neutralized ^{89}Zr-oxalate was added to the antibody-chelator solution at a ratio of 0.25 mg of Df-nivolumab per 37 MBq of ^{89}Zr. Before incubating at 37°C for 1 h, the volume was adjusted to 1 mL with HEPES buffer. The radiolabeled antibody was purified by PD-10 columns into PBS and injected into mice.

5.1.3. Animal models

All animal studies were conducted under a protocol approved by the University of Wisconsin Institutional Animal Care and Use Committee. NOD *scid* gamma (NSG), also known as NOD-*scid* IL2Rgamma^{null} mice, were obtained from the UW-Madison Humanized Mouse Core Service. For generation of the humanized tumor-bearing model (PBL mice with tumors), NSG mice at 3-5 weeks of age were subcutaneously injected with 100 μL (1×10^6 cells) of a 1:1 mixture of A549 lung adenocarcinoma cells and Matrigel Matrix Basement Membrane (Corning) into the lower flank of the mice. Tumors were allowed to reach 1-2 mm in diameter before the mice were reconstituted with 0.5×10^6 human PBMCs via tail-vein injection. The animals were allowed to engraft for 14-16 days before use, ensuring that both PBL and NSG mice of the same age and similar engraftment were used for imaging studies. Engraftment efficiency values were provided by the UW-Madison Humanized Mouse Core Service, determined through flow cytometry analysis of blood samples.

5.1.4. PET imaging and analysis

Mice were injected intravenously with 5 – 10 MBq of the tracer (^{89}Zr-Df-nivolumab) for PET imaging. For imaging, mice were placed in the prone position in the Inveon microPET/microCT rodent model scanner (Siemens Medical Solutions). Scans were performed with 40 million coincidence events being recorded. Images were reconstructed using the 3D ordered subset expectation maximization algorithm and quantified via region-of-interest (ROI) analysis in the Inveon Research Workplace software (Siemens Medical Solutions). Signal quantification was expressed as the percent of injected dose per gram of tissue (%ID/g).

5.1.5. Ex vivo biodistribution studies

Mice were euthanized via CO_2 asphyxiation after the final scan for *ex vivo* biodistribution and immunohistochemistry studies. Major tissues, organs, and blood were collected for measurement of radioactivity. Each sample was wet-weighed before the radioactivity was counted using a PerkinElmer Wizard2 automatic gamma-counter (Waltham). Values were recorded as %ID/g.

5.1.6. Immunohistochemistry

Tumor, salivary gland, spleen, and lung tissue were embedded in Tissue-Tek optimal cutting temperature compound (Sakura Finetek). Frozen tissues were sectioned at 5 μm thickness and fixed with ice-cold acetone for 10 min before being rehydrated in PBS for 5 min. Slides were blocked with 10% normal donkey serum in 0.25% Triton-X in PBS for 1 h at room temperature. For primary antibodies, 1:200 dilutions of rabbit anti-human CD3 (Novus Biologicals) and goat

anti-human PD-1 (Novus Biologicals) were prepared in the blocking solution and incubated with the tissue for 12 h at 4 ºC. Slides were washed three times with PBS for 15 min at room temperature. For secondary antibodies, dilutions of 1:1000 donkey-anti rabbit IgG DyLight 550 (Novus Biologicals) and 1:2000 donkey anti-goat IgG DyLight 488 (Novus Biologicals) were made using the blocking solution. The slides were incubated with secondary antibodies for 1 h at room temperature. Next, slides were washed three times with PBS for 10 min before mounting using a mixture of Fluoromount (Novus Biologicals) and Vectashield with DAPI (Vector Labs). The Nikon A1RS confocal microscopy system was used to image slides.

5.1.7. Radiation dosimetry extrapolation to humans

The OLINDA/EXM software was used for dosimetry analysis[75]. The %ID/g values obtained from PET imaging of the tracer in mice were used to estimate human dosimetry. The biodistribution of the tracer was assumed to be the same between humans and mice, and a monoexponential model was employed. OLINDA provides effective dose outputs and weighting factors from International Commission on Radiological Protection Publication 103 were employed to convert to absorbed dose in each organ[76].

5.1.8. Statistical analysis

Quantitative data were expressed as the mean ± standard deviation with all error bars denoting the standard deviation. Means were compared using the student *t*-test and p-values ≤ 0.05 were considered statistically significant.

5.2. Results

5.2.1. Nivolumab binding assay

Binding of nivolumab to PD-1 expressed on the surface of stimulated and unstimulated $CD4^+$ and $CD8^+$ T-cells was assessed via flow cytometry (**Figure 28**). PMA-Ionomycin is a potent stimulator of lymphocytes known to quickly upregulate PD-1 expression *in vitro*[99]. Increased binding of nivolumab to both $CD4^+$ and $CD8^+$ T-cells was detected when the cells were stimulated; however, this interaction was 3 to 4-fold lower for unstimulated cells. To further demonstrate the specificity, a nonspecific human IgG was used in place of nivolumab. In return, minimal binding was detected between stimulated/unstimulated T-cells and the non-specific human IgG. Also, flow cytometry was used to evaluate if conjugation of the chelator (Df) would inhibit or alter the binding affinity of nivolumab. Both nivolumab and Df-nivolumab showed similar mean fluorescence intensities when incubated with stimulated $CD4^+$ and $CD8^+$ T-cells, indicating that the chelation and radiolabeling of nivolumab would not affect its binding affinity *in vivo*.

5.2.2. Chelation and radiolabeling of nivolumab

Nivolumab was conjugated with the chelator desferrioxamine (Df) for radiolabeling with ^{89}Zr. The purified radiolabeled antibody displayed a specific activity of ~700 mBq per mg antibody. The radiolabeling efficiency was high with more than 85% of the isotope being chelated after 1 h of incubation, as determined by instant thin-layer chromatography.

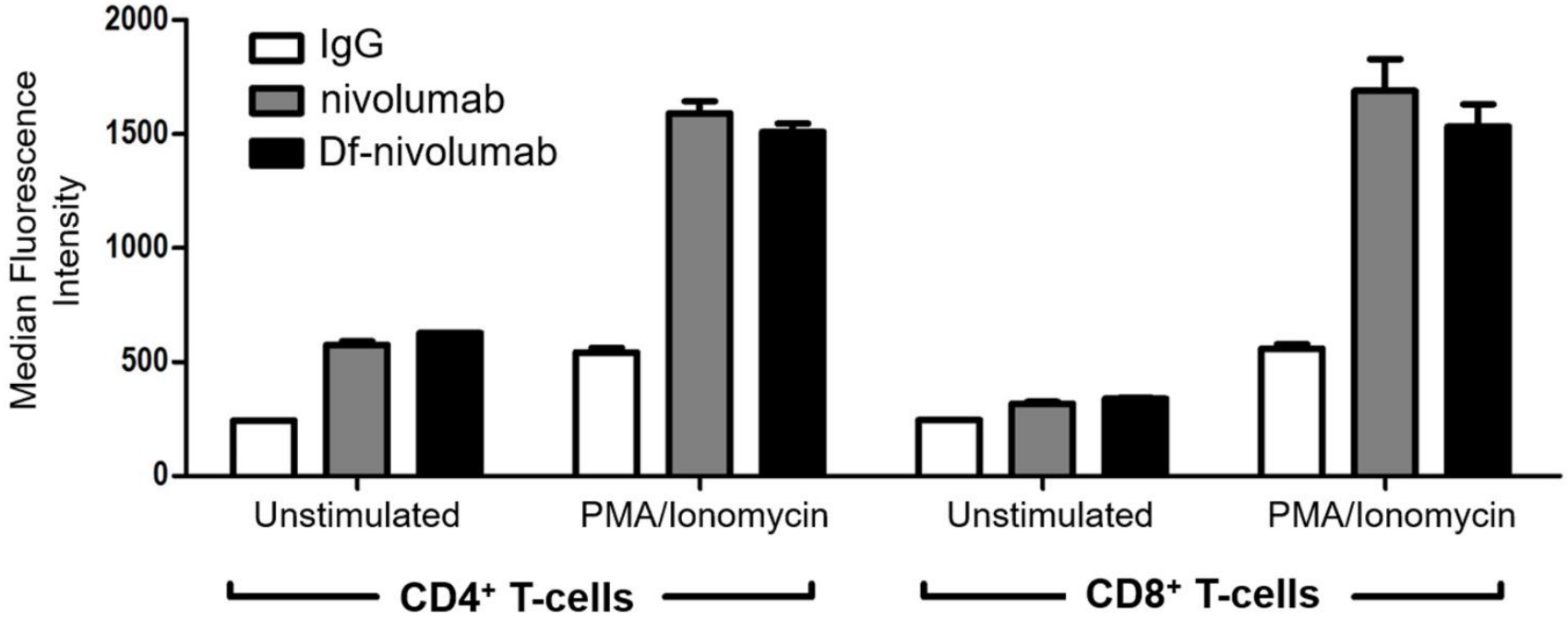

Figure 28. Nivolumab Binding Assay. *Flow cytometry-based analysis of nivolumab binding to human PBMCs indicated high binding to activated T-cells that was not impacted by the addition of a chelator.*

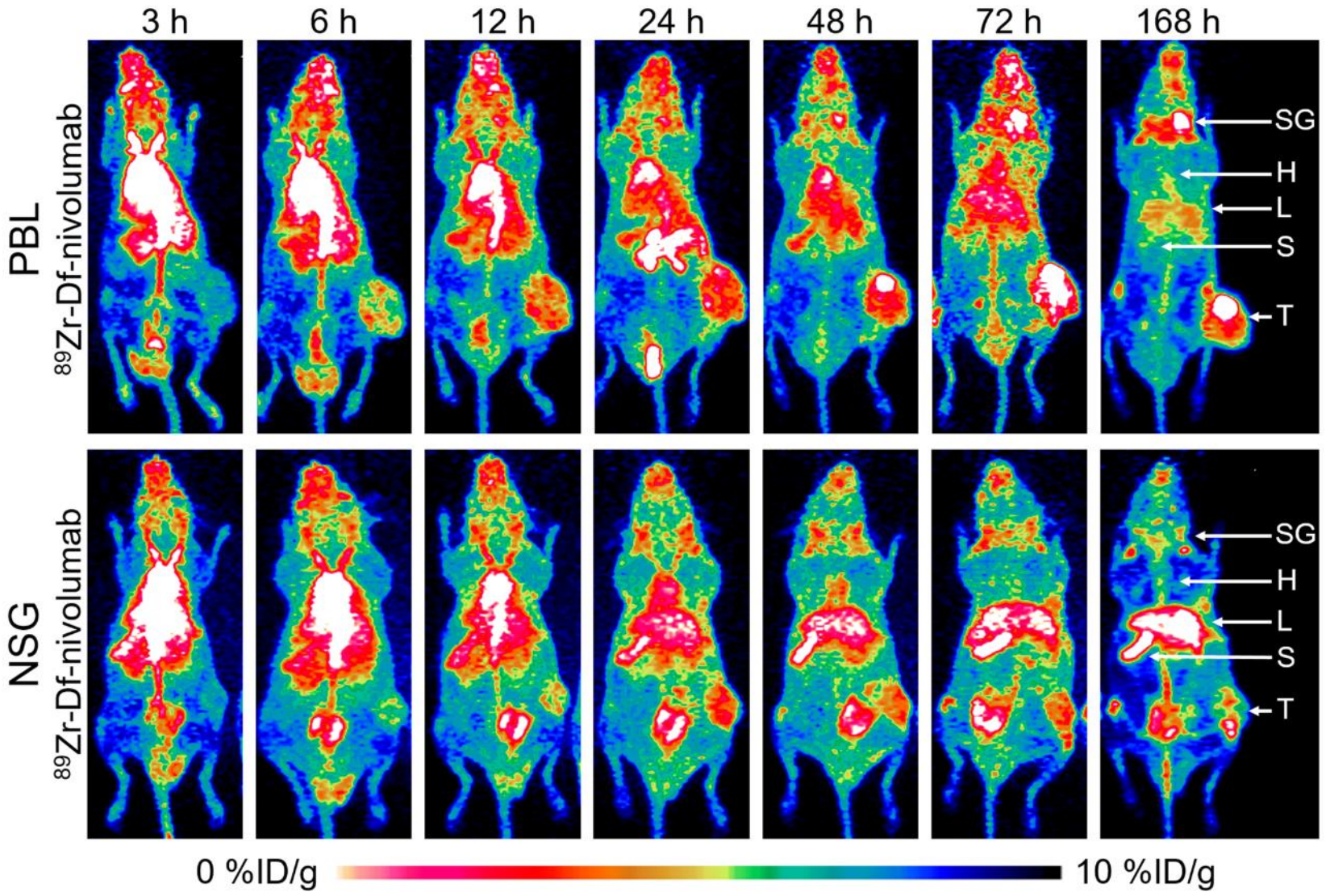

Figure 29. ^{89}Zr-Df-nivolumab PET Imaging. *PET imaging of human PD-1+ tumor-infiltrating T-cells in humanized PBL mice (top) and control NSG (bottom). Abbreviations: SG: salivary gland; H: heart; L: liver; S: spleen; T: A549 tumor.*

5.2.3. PET imaging and biodistribution of ^{89}Zr-Df-nivolumab

After purification, ^{89}Zr-Df-nivolumab was injected intravenously and longitudinal PET imaging studies were performed at 3, 6, 12, 24, 48, 72, and 168 h post-injection. Initial imaging time points revealed similar pharmacokinetic properties of the tracer in NSG and PBL mice (**Figure 29**). Differences in the whole-body biodistribution profile of the tracer became visible by 24 h post-injection. Quantification of PET data via ROI analysis allowed for comparison between tracer uptake in various organs and tissues, including the tumor, salivary glands, blood, liver, spleen, kidney, and muscle tissues. In both PBL and NSG mice, tumors were delineated on the left flank by 6 h post-injection. While tumor uptake in PBL mice continued to increase gradually throughout the study, uptake in NSG mice was significantly lower, reached maximum values by 24 h post-injection, and slowly declined by later time points.

As suggested by the maximum intensity projection images (**Figure 29**), tumor accumulation was similar between NSG and PBL mice initially; however, PBL mice displayed higher uptake starting at 72 h after injection and onward (**Figure 30A**, **Table IV in Appendix 1,** n=4, $p<0.05$). More specifically, mean tumor uptake values of 9.85 ± 2.73 and 3.88 ± 0.38 were obtained 168 h post-injection of ^{89}Zr-Df-nivolumab in PBL and NSG mice, respectively. In a previous study (**Aim 1**), our group verified that development of graft-versus-host disease results in infiltration and permanent residence of lymphocytes into the lacrimal and salivary glands[44]. As expected, similar results were found in this study with PBL mice displaying significantly higher salivary gland uptake of ^{89}Zr-Df-nivolumab in comparison to NSG mice (**Figure 30B**, n=4, $p<0.05$). By 168 h post-injection, there was a 2-fold difference in salivary gland signal between PBL (8.38 ± 0.98 %ID/g) and NSG mice (3.30 ± 0.22 %ID/g), further validating the binding

specificity of our tracer to its native receptor found on the surface of activated T-cells localized in the tumor and salivary glands.

The tracer showed fairly similar characteristics in reference to blood circulation in both PBL and NSG mice. For PBL mice, tracer uptake in the blood pool was 15.5 ± 1.29 %ID/g and 2.70 ± 0.42 %ID/g at the initial and final time points, respectively. Similarly, blood pool uptake in NSG mice was 13.1 ± 0.79 %ID/g and 1.88 ± 0.10 %ID/g (n=4) at the same time points, suggesting that the tracer remained relatively stable in circulation. Tracer uptake in the kidney and muscle tissues was similar between both groups of mice. After the final imaging session, select organs and tissues were extracted for further biodistribution evaluation by *ex vivo* gamma counting studies. Similar to PET findings, *ex vivo* biodistribution studies revealed key differences between tumor and salivary gland uptake, which were 2 to 3-fold higher in PBL mice (**Figure 31, Table III in Appendix 2**). Additionally, bone and spleen uptakes were higher in NSG mice, once again due to Fc-mediated effects[78]; however, these differences were difficult to quantitatively determine through ROI analysis because of partial volume effects[100].

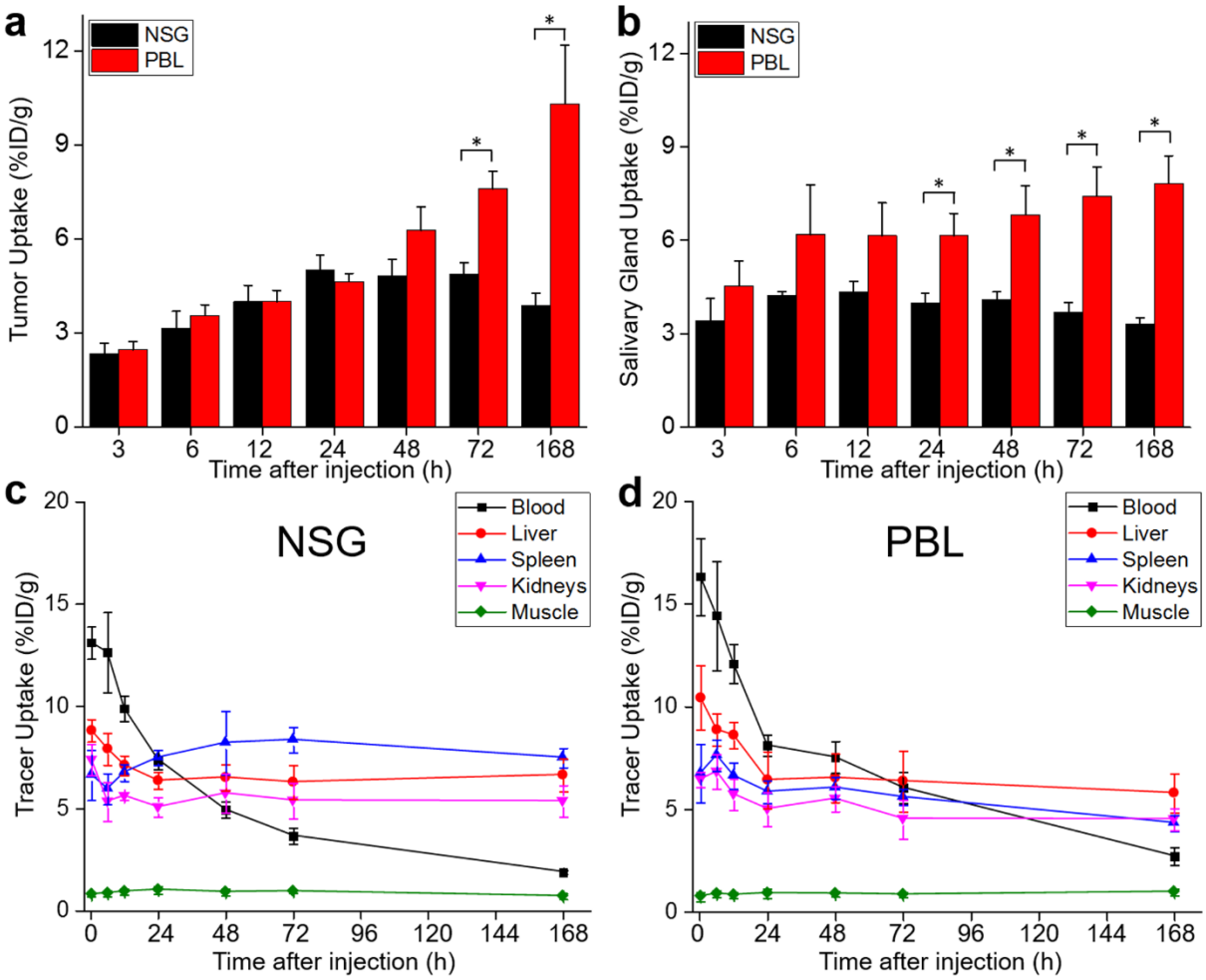

Figure 30. ***^{89}Zr-Df-nivolumab PET Quantification.*** *(a) Significantly higher uptake of the tracer was observed in tumors from PBL mice; (b) Significant uptake was once again noted in the salivary glands of PBL mice; (c) and (d) longitudinal ROI measurements of several critical organs.*

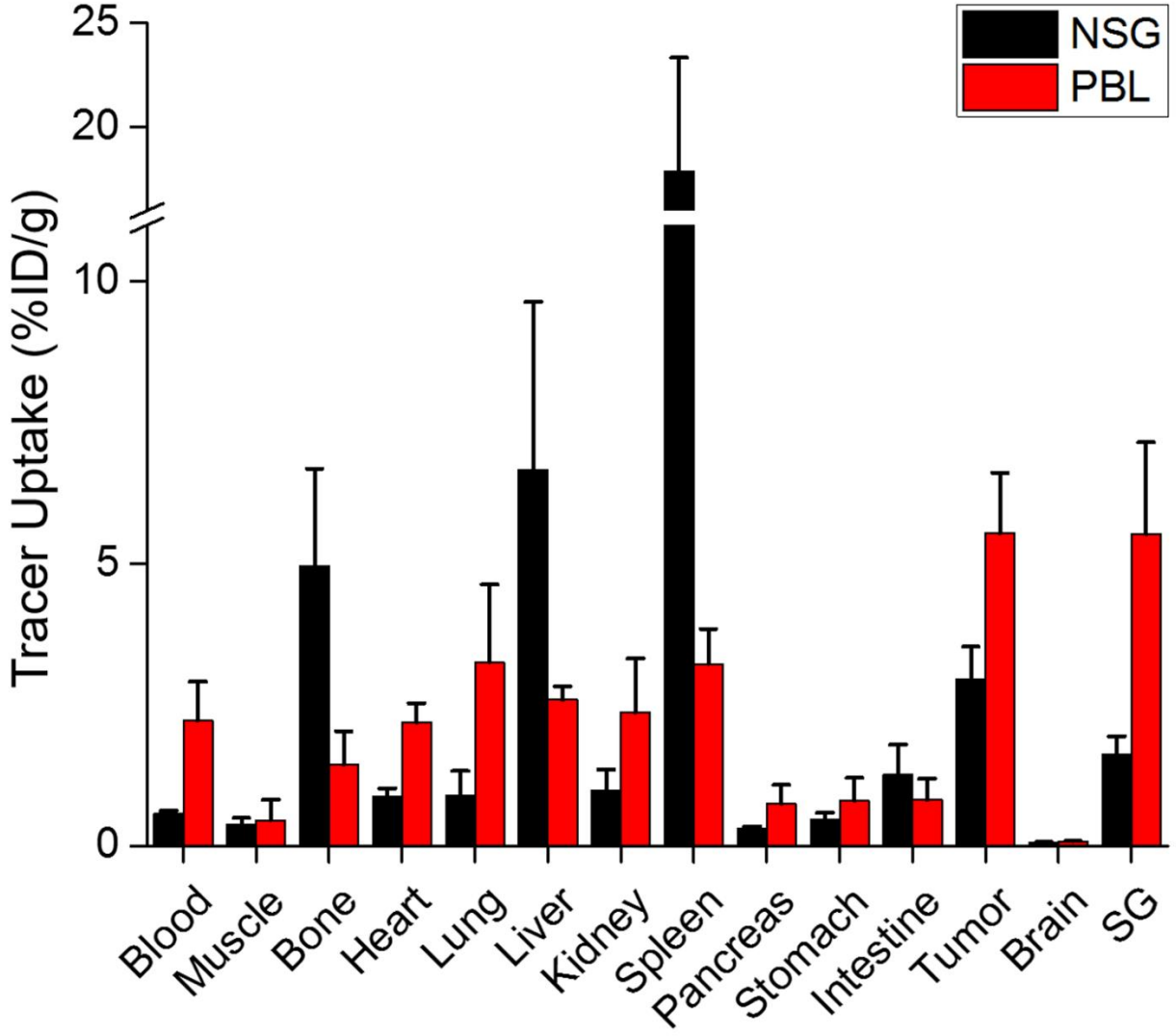

Figure 31. ^{89}Zr-Df-nivolumab Biodistribution Study. *Ex vivo biodistribution verifies the organs of significant uptake of ^{89}Zr-Df-nivolumab. The abnormal Fc-mediated uptake was once again noted in NSG mice, resulting in an anomalous distribution in the spleen, liver, and bones. n=4.*

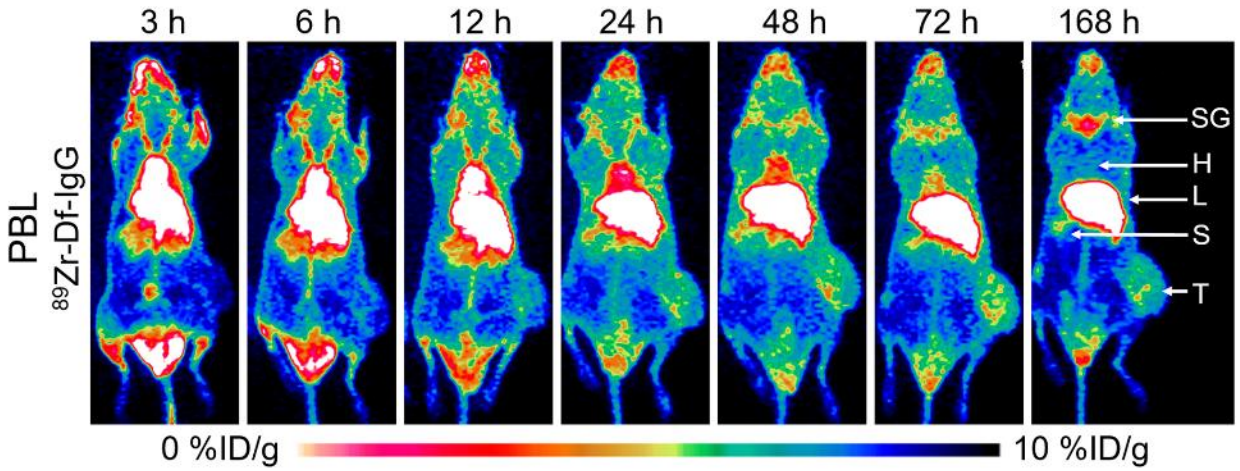

Figure 32. ^{89}Zr-Df-IgG PET Imaging. *A control antibody, ^{89}Zr-Df-IgG, was tested in humanized PBL mice to prove the specificity of nivolumab. SG: salivary glands; H: heart; L: liver; S: spleen; T: A549 tumor.*

To verify the specificity of the tracer, PBL mice were injected with a nonspecific tracer (^{89}Zr-Df-IgG) for imaging (**Figure 32**). Imaging studies revealed lower tumor and salivary gland uptake in PBL mice injected with the nonspecific tracer in comparison to ^{89}Zr-Df-nivolumab. For example, tumor signal was significantly lower in PBL mice injected with the nonspecific tracer as compared to ^{89}Zr-Df-nivolumab at 3 h post-injection (0.74 ± 0.32 versus 2.46 ± 0.26 %ID/g) and all time points thereafter (**Figure 33A**, **Table V in Appendix 1,** n=4, $p<0.05$). At the final time point (168 h), ^{89}Zr-Df-nivolumab uptake in the tumors was 3-fold higher than ^{89}Zr-Df-IgG, with values of 9.85 ± 2.73 %ID/g and 2.85 ± 0.39 %ID/g, respectively. With respect to the salivary gland uptake, there was a 2-fold difference between the two tracers, with ^{89}Zr-Df-nivolumab (8.38 ± 0.98 %ID/g) being significantly higher than ^{89}Zr-Df-IgG (4.65 ± 0.39 %ID/g) at 168 h after injection (**Figure 33B**, n=4, $p<0.05$). Time activity curves show that blood pool uptake steadily decreased after injection, while spleen and muscle accumulation remained steady throughout the study. As demonstrated by PET imaging, the high liver uptake observed in mice injected with the nonspecific tracer was verified by *ex vivo* biodistribution studies (**Figure 33D**).

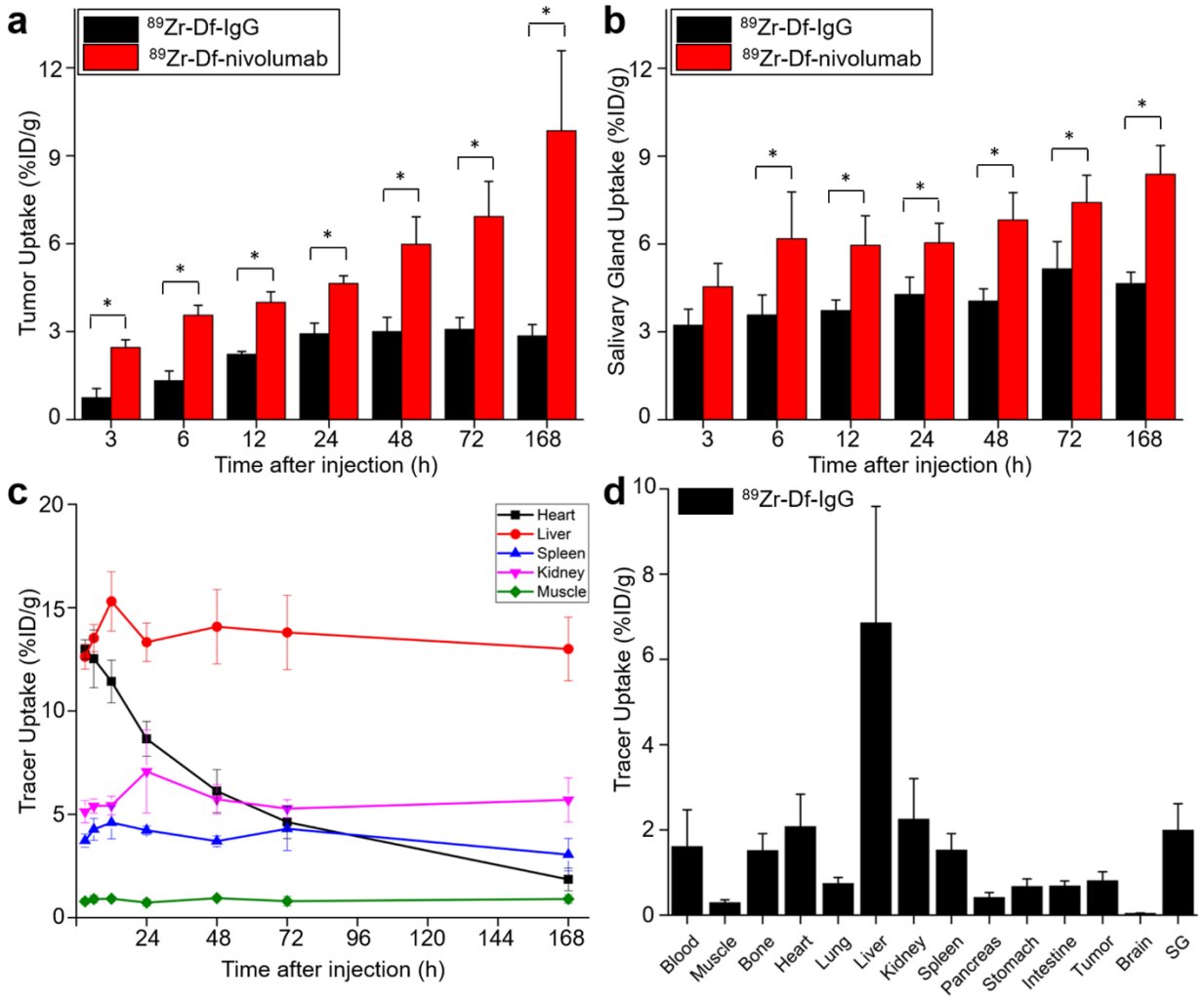

Figure 33. ^{89}Zr-Df-IgG PET Quantification. *Measurement of ^{89}Zr-Df-IgG uptakes relative to that of ^{89}Zr-Df-nivolumab, (a) in tumors and (b) in salivary glands. (C) Longitudinal ROI analysis; (D) ex vivo biodistribution results. n=4.*

5.2.4. PD-1+ T-cells localized in tumors and salivary glands

Immunofluorescent staining was used to further validate the imaging findings (**Figure 34**). An anti-cluster of differentiation (CD3) antibody was used as a T-cell marker as shown in green, while PD-1 expression was signified by the red color. PD-1 expression was detected in the tumor, salivary gland, spleen, and lung sections of PBL mice, with the strongest signal being in the tumor and spleen. CD3 signal was also detectable in the four tissue sections with the tumor showing the highest degree of CD3. The nuclei were stained blue to verify the presence of cells. In the NSG tissue sections, only nonspecific background CD3 and PD-1 staining were seen.

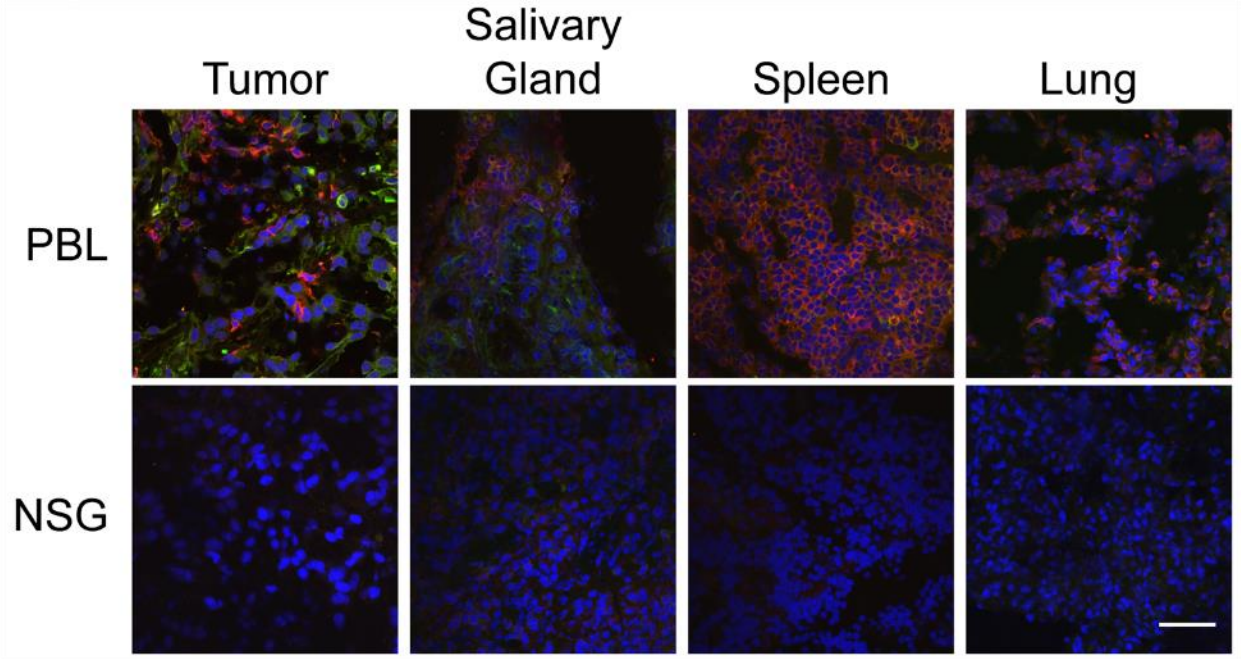

Figure 34. PD-1 Tissue Staining. *Evidence of human PBMCs was found in tumor, spleen, and salivary gland tissues in PBL mice, but not in NSG. Green: CD3, Red: PD-1; Blue: nuclei.*

5.2.5. Radiation dosimetry

Dosimetry studies were performed to extrapolate the doses to mice following injection of ^{89}Zr-Df-nivolumab or ^{89}Zr-Df-IgG to adult human females (**Figure 35, Table III in Appendix 3**). Notable differences in dose were observed for the liver and salivary glands across groups, with other organs providing uniform results. In PBL mice, higher doses to the liver were found with the nonspecific antibody with values of 1.71 ± 0.11 mGy/MBq and 0.98 ± 0.12 mGy/MBq for ^{89}Zr-Df-IgG and ^{89}Zr-Df-nivolumab, respectively (n=4). In addition, notable doses to the salivary glands in all PBL mice (1.61 ± 0.15 mGy/MBq in Nivolumab PBL and 1.0 ± 0.15 mGy/MBq in IgG PBL) were the result of the graft-versus-host disease process. Additionally, low doses to tumors were observed across all groups. For example, doses of 0.025 ± 0.003 mGy/MBq for radiolabeled nivolumab in PBL mice, 0.020 ± 0.002 mGy/MBq for radiolabeled nivolumab in NSG mice, and 0.013 ± 0.001 mGy/MBq for radiolabeled nonspecific IgG in PBL mice, reported for a tumor mass of 2 g. Even considering these differences, similar total body effective doses were calculated across all groups to be about 0.3 mSv/MBq.

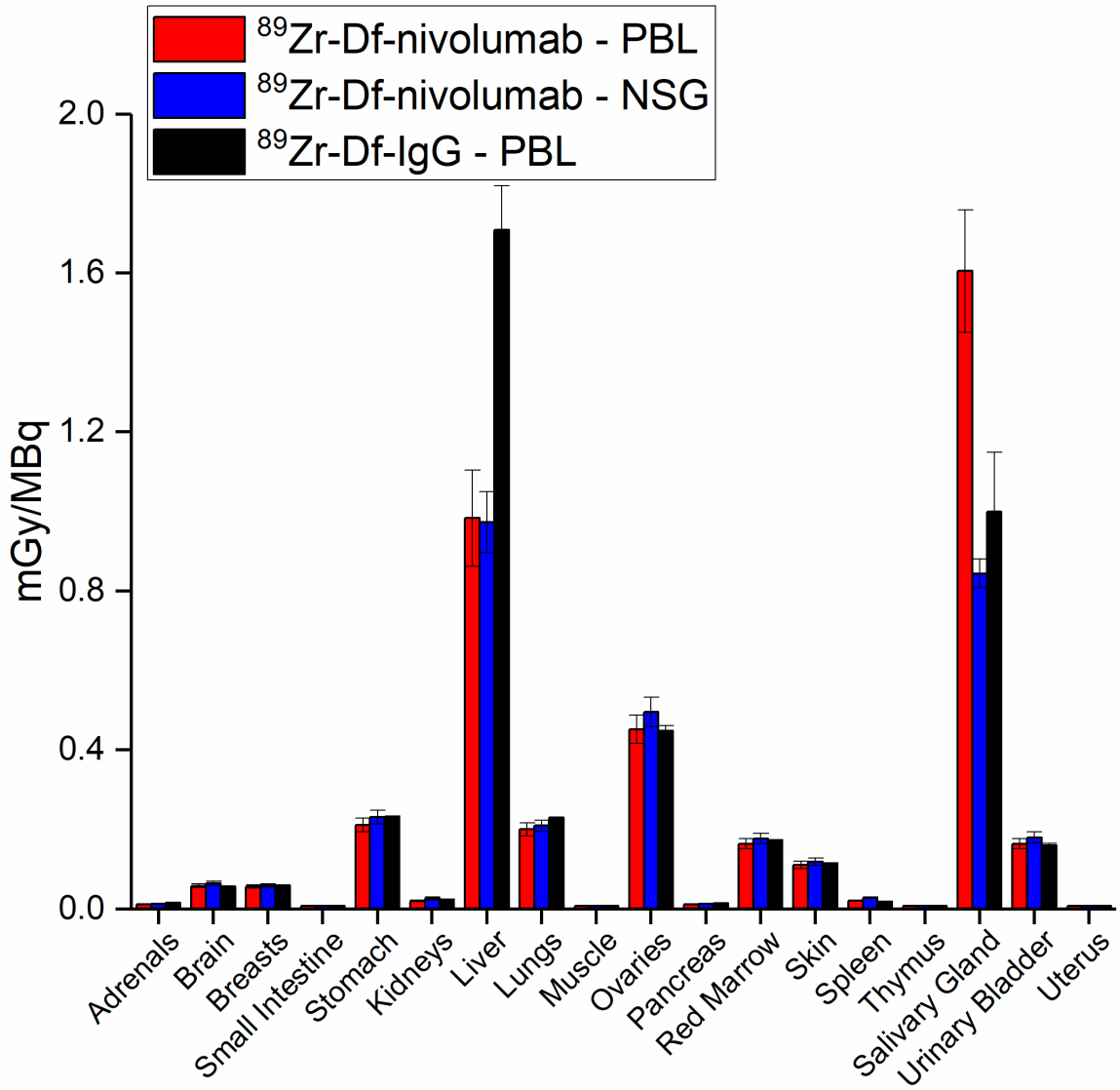

Figure 35. PD-1 TIL Dosimetric Extrapolation. *Human dosimetry extrapolation resulting from quantification of tracer uptake in mice. n=4.*

5.3. Discussion

In this study, we demonstrated that T-cells expressing PD-1 could be effectively visualized using our novel PD-1 tracer, ^{89}Zr-Df-nivolumab. Previously, Natarajan *et al*. demonstrated the specificity of a murine PD-1 tracer for imaging PD-1-expressing tumor infiltrating lymphocytes using ^{64}Cu in a transgenic mouse model of melanoma[101]. Tumor uptake was 7.4 ± 0.71 %ID/g at the final imaging time point in that study (48 h post-injection), which was lower than the final tumor accumulation found in this study (9.85 ± 2.73 %ID/g). However, our value was obtained at 168 h post-injection, providing the antibody a longer time to accumulate in the tumors. Therefore, the murine tracer may have continued to accumulate if the study was not halted at 48 h post-injection; however, the short half-life of ^{64}Cu (12.7 h) was a limiting factor. By employing the long-lived ^{89}Zr (3.3 days), the present study allowed for the tracking of PD-1-expressing T-cells' infiltration into the tumor over the course of 168 h. In addition, it is important to note that tumor uptake in this experiment is less than that usually noted with anti-tumor antibodies; however, this is because this imaging agent targets T-cells localized in the tumor and not the actual tumor cells.

In our previous study (**Chapter 4**), we demonstrated for the first time that radiolabeled pembrolizumab showed a unique biodistribution profile in humanized mice injected with human PBMCs when compared to non-humanized mice. Radiolabeled pembrolizumab was shown to accumulate in the salivary glands of PBL mice. Similarly, this study revealed increased salivary gland uptake of the tracer, which has been attributed to T-cells trafficking to the salivary glands as a result of graft-versus-host and other autoimmune diseases[102]. Also, just as in the studies in Aim 1, we observed highly increased uptake of the tracer in the spleen, liver, and bones of NSG mice, again due to the Fc interactions in these immunodeficient hosts[78].

This study demonstrated that humanized murine models of cancer may play important roles in the study and development of future immunotherapy agents. Herein, tracer accumulation is attributed to T-cell infiltration into the tumor, since the tumor cells do not display PD-1 expression. Additionally, the tumor cells employed in these models (A549) express extremely low levels of PD-L1, meaning that the PD-1+ T-cells that trafficked there would not be inactivated through binding to the ligand. The process of tumor infiltration by lymphocytes has been extensively documented and this type of study may provide additional data regarding the process[103]. Using PBL mice injected with ^{89}Zr-Df-IgG, we verified that the accumulation of our novel tracer was highly specific and not due to off-target accumulation. In the future, the use of more complex humanized models of cancer may provide added benefits. For example, a limitation of this study was the innate variability caused by the lack of a stable model, as the xenograft efficiency of both tumors and PBMCs varied between mice. Despite ensuring that all mice met the minimum xenograft efficiency required for study inclusion, the slight variations in xenograft efficiency and graft-versus-host severity could have resulted in the small differences we found in mice of the same group.

There are many potential applications likely to benefit from the PD-1 imaging agents. As described earlier, PD-1-based imaging agents may allow physicians to determine which patients are more apt to benefit from anti-PD-1 or anti-PD-L1 therapies in the future. In return, this could save thousands of patients from the unnecessary adverse effects associated with immune checkpoint therapies. Also, PD-1 imaging may be utilized to track T-cells that have become activated by various therapies to gain insight into the interactions between T-cell activation, homing, and tumor residence. These new imaging agents may play an essential role in helping researchers and physicians determine other potential toxicities that may be associated with newer

anti-PD-1 therapies in the future by identifying on-target, off-tumor activated T-cells. A limitation for use of immune checkpoint antibodies as imaging agents is that immune checkpoint pathway receptors are heterogeneously expressed in multiple areas of the body, which complicates potential imaging strategies. Hence, innovative approaches are required to target many immunotherapy biomarkers.

This study demonstrates that radiolabeled nivolumab may be used to noninvasively image PD-1 expression in humanized tumor-bearing mice. More specifically, the infiltration of PD-1-expressing T-cells was effectively imaged in a humanized mouse model implanted with A549 tumors. As the field of cancer immunotherapy is expected to undergo rapid growth, improved strategies like noninvasive PET are valuable tools for investigating the biodistribution of newly developed antibody therapies. In the future, imaging of immunotherapy biomarkers may be used for therapeutic monitoring and patient stratification.

Chapter 6

6. Monitoring PD-L1 dynamics with PET

There is some evidence that the expression of PD-L1 may correlate with the success of PD-1 or PD-L1-targeted immunotherapies[27, 29, 49, 104, 105]. In current clinical practice, this expression is monitored through biopsy; however, this approach is greatly limited by the amount of tissue that can be sampled and the highly dynamic nature of PD-L1 expression. Molecular imaging may help complement the existing strategies, as it is able to noninvasively visualize these dynamics. In this aim, we explored the potential of PET imaging to visualize PD-L1 expression, even in the presence of high background normal-tissue expression of the same marker.

6.1. Materials and Methods

6.1.1. Cell culture

H460 and A549 cells were purchased from the American Type Culture Collection, and maintained in Roswell Park Memorial Institute-1640 or Dulbecco's Modified Eagle's medium supplemented with 10% fetal bovine serum and 1% penicillin-streptomycin in a 37°C humidified incubator with 5% CO_2. For all studies, cells were utilized at 60-70% confluence.

6.1.2. In vitro PD-L1 expression studies

To monitor changes in PD-L1 protein levels and expression, several *in vitro* studies were performed. To measure protein concentrations, Western blot analysis was employed. When cells were at about 60% confluence, they were plated into T25 flasks and supplemented with 10 mL of media each (corresponding to approximately 2-3 mm of media above the cell layer). For the first study, protein was simply extracted from H460 and A549 cells at 60% confluence to explore baseline PD-L1 levels.

The cells were then subjected to one of three radiotherapy regimens: five fractions of 2 Gy each; one fraction of 5 Gy; or no radiation (but still the sham procedure of being removed from the incubator, etc). These treatments were administered using an XRAD320 biological irradiator (Precision X-Ray), and fractionated treatments were administered 24 ± 1 hours apart. Protein was then extracted from the cells at the completion of their respective schedules at 24 h after completion. Cells were lysed using Radio Immuno Precipitation Assay buffer (Boston BioProducts) supplemented with 1:100 Halt Inhibitor and EDTA (ThermoFisher Scientific). Supernatant protein concentration was measured using the NanoDrop One (ThermoFisher Scientific). Western blotting was performed using standard procedures[106], with the following reagents: Chameleon Duo ladder protein marker (LI-COR Biosciences), anti-hB7-H1 antibody (R&D Systems), anti-β-actin antibody (Novus Biologicals), donkey anti-goat IRDye 800CW, and donkey anti-mouse IRDye 680RD (LI-COR Biosciences). The final prepared membrane was scanned using a LI-COR Odyssey infrared imaging system (LI-COR Biosciences).

Verification of tracer binding was performed using flow cytometry. The binding properties of both atezolizumab and Df-atezolizumab to irradiated H460 cells were analyzed at 48 h after the fractionated irradiation. Preparation of cells for flow cytometry and analysis were conducted using

standard procedures[106]. Samples were run on a MacsQuant cytometer (Miltenyi Biotec) and analyzed with FlowJo V10 (FlowJo LLC).

6.1.3. Animal models

All animal studies were conducted under an approved protocol by the Institutional Animal Care and Use Committee. Lung cancer xenograft models were generated by inoculating 4-6 week-old female athymic nude mice (Envigo) with a 1:1 mixture of H460 or A549 cells in Matrigel Matrix Basement Membrane (Corning) subcutaneously in the lower flank. When tumors reached 5-8 mm in diameter, mice were used for subsequent studies.

6.1.4. Radiation treatments

Similar to cell studies, three radiotherapy regimens were administered to H460- or A549-bearing mice (n=4-5 per group) using the XRAD320 irradiator: five daily fractions of 2 Gy (2 Gy x 5 Fx), one fraction of 5 Gy (5 Gy x 1 Fx), or no radiation. Prior to irradiation, mice were placed and taped in the prone position in lead body shields (**Figure 36**) to minimize radiation exposure to organs other than the tumor. Mice were irradiated one at a time, and the x-ray field was collimated to leave ~0.5 cm margins on each side of the unshielded area of the mouse.

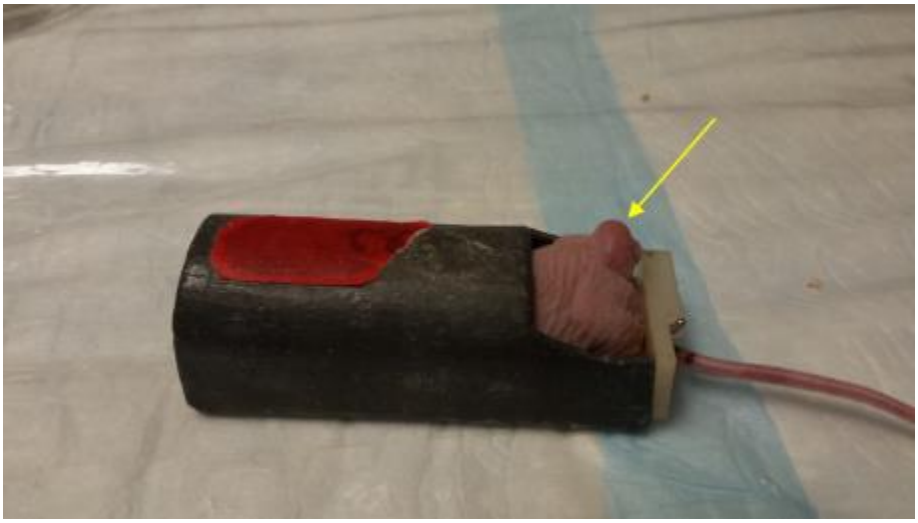

Figure 36. Irradiation setup. *Mice were placed in lead shields to minimize normal tissue dose. Tumor is indicated by the yellow arrow.*

6.1.5. PET tracer preparation

Atezolizumab (Genentech Oncology) was obtained in its clinically-available IV-injectable form and run through a PD-10 column (GE Healthcare) with phosphate buffered saline mobile phase to remove any stabilizers. The antibody was then conjugated with desferrioxamine (Df, Macrocyclics) using previously-reported methods in preparation for radiolabeling with ^{89}Zr[107, 108]. ^{89}Zr ($t_{1/2}$: 78.4 h) was produced through proton irradiation of yttrium foils[109]. For development of the radiolabeled tracer, Df-atezolizumab was mixed with ^{89}Zr-oxalate at a ratio of 50 µg protein to 1 mCi radionuclide and incubated for 1 h at 37°C. PD-10 columns were then used to purify the reactants and products and formulate the final tracer into phosphate buffered saline for injection.

6.1.6. PET imaging and biodistribution studies

One day after completion of the respective radiotherapy regimens, mice were intravenously injected with 4-9 megabecquerels (5-12 µg) of ^{89}Zr-Df-atezolizumab. PET scans were acquired using an Inveon microPET/CT scanner (Siemens) at 1, 6, 12, 24, 48, 72, and 96 h post-injection, with 20 million counts per mouse obtained at each timepoint. OSEM/3DMAP reconstructions were employed. After the 96 h scan, mice were euthanized through CO_2 asphyxiation and major organs were removed, wet-weighed, and counted using an automated gamma counter (PerkinElmer). Quantitative data from these studies are presented as percent of injected dose per gram of tissue (%ID/g), mean ± standard deviation.

6.1.7. Anti-PD-L1 Fab imaging studies

Additionally, a site-specifically-modified anti-PD-L1 Fab tracer was used for imaging as well. This compound was obtained from collaborators at Temple University with NOTA chelator

specifically attached, enabling radiolabeling with ^{64}Cu as described in **Aim 1**. A human Her2-targeted agent was also employed as an isotype control, which would not bind specifically in the mice models.

Both C57/BL6 mice and athymic nude mice were employed in the studies with these tracers, to investigate the tracer in models with varying immune competency. For imaging, mice were injected with 4-10 MBq of the respective tracer, and PET scans of 20 million counts per mouse were obtained at 5, 15, 45, and 90 min post-injection. The PD-L1 and Her2 tracers were tested in C57/BL6 mice, while the same two tracers and a blocking study were used in nude mice. For the blocking study, mice were injected with 200 μg of unlabeled anti-PD-L1 Fab 30 min prior to injection of the ^{64}Cu-NOTA-αPD-L1 agent to saturate PD-L1 receptors and prove specificity of the tracer. Standard techniques were employed for quantification of PET ROI data and biodistribution studies.

6.1.8. Ex vivo verification

Organs of significant tracer uptake, including the spleen, lymph nodes, and H460 tumor, were excised from mice, embedded in TissueTek Optimal Cutting Temperature Compound (Sakura), sliced, and mounted for immunofluorescent analysis. Using the human anti-PD-L1 antibody atezolizumab (since mouse and human PD-L1 share structural similarities), rat anti-mouse F4/80 (for macrophages), and mouse anti-mouse CD45 (myeloid cells) primary antibodies, the tissues were stained to determine which cells express PD-L1. Secondary antibodies were used to complete the staining using standard procedures[44]: donkey anti-rat Cy3, donkey anti-human DyLight650, and goat anti-mouse AlexaFluor488. Slides were then mounted with DAPI-containing hard mount (Vector Laboratories), and coverslipped. Confocal imaging was performed using a Nikon A1RS

microscope (Nikon Corporation). For the PD-L1 Fab studies, the brown fat was also excised from mice and stained for PD-L1 to verify this tissue as an expected site of uptake.

6.1.9. Statistical analysis

For the statistical analysis in this study (PET imaging and biodistribution), with five mice per group, a Student's t-test which can detect a difference of 1.68 standard deviations with 80% power at 5% significance level was utilized ($p<0.05$, two-sided).

6.2. Results

6.2.1. *In vitro* PD-L1 expression analysis

Screening of H460 and A549 lung cancer cells revealed notable expression of PD-L1 at baseline by H460 cells that was absent in the other line (**Figure 37**). Therefore, H460 cells formed the basis for the majority of these studies. A549 served as a negative control. Following irradiation of H460 cells *in vitro*, Western blot analysis revealed upregulated PD-L1 expression in the 2 Gy x 5 Fx group (**Figure 38**). An over four-fold increase in the PD-L1/β-actin ratio was observed at 24 h after completion of this fractionated regimen. Similar levels of PD-L1 were measured in the 5 Gy x 1 Fx group and the control, indicating that fractionated radiotherapy was more effective at inducing PD-L1. These findings were mimicked in flow cytometry analyses as well.

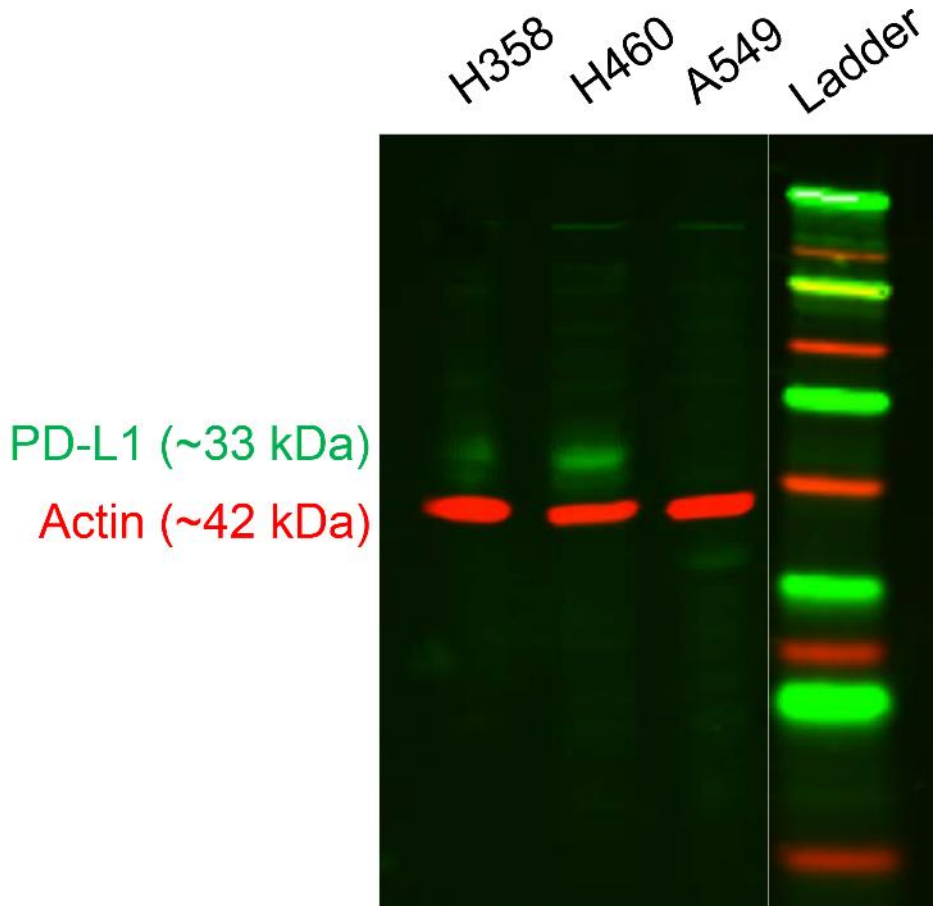

Figure 37. PD-L1 Screen. *A representative Western blot analysis of PD-L1 expression by naïve lung cancer cells.*

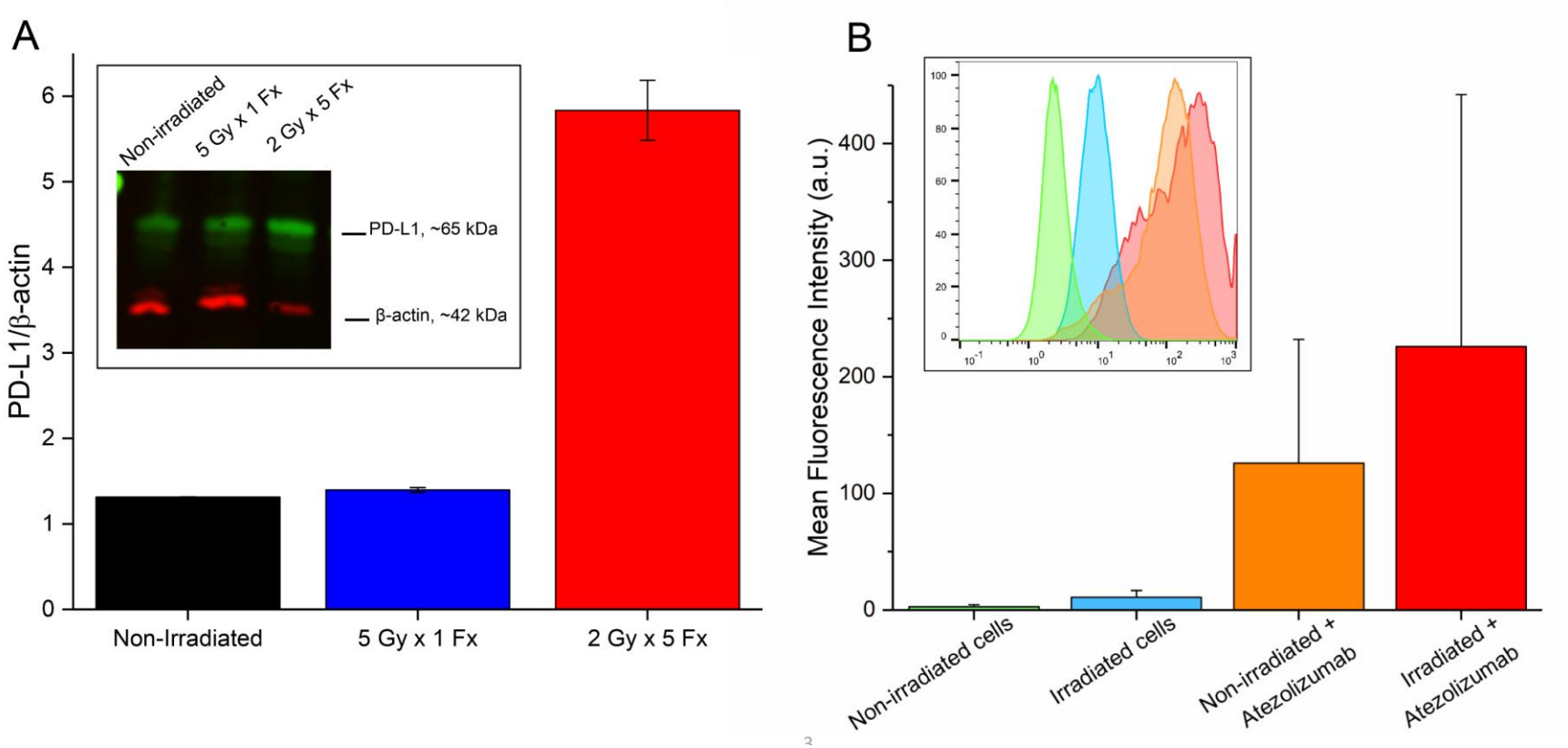

Figure 38. In vitro PD-L1 Studies. *(A) Analysis of Western blot data shows a trend toward higher expression of PD-L1 in H460 cells receiving five fractions of 2 Gy; n=3 replicates. (B) Flow cytometry of H460 cells similarly shows a slight shift toward higher PD-L1 expression following fractionated irradiation.*

6.2.2. PET imaging visualizes PD-L1 expression changes

Following completion of the respective radiotherapy regimens, 24 h later mice were administered ^{89}Zr-Df-atezolizumab through tail vein injection. Serial PET scans were then conducted to visualize the distribution of PD-L1 expressing tissues.

Several trends were evident following analysis of H460-bearing mouse images. Most notably, the PD-L1 tracer accumulated to a very high level in the spleen (18-19 %ID/g at 96 h) and lymph nodes (8-12 %ID/g at 96 h) of all tumor-bearing mice (**Figure 39, Figure 40, Figure 41, Table VI in Appendix 1,** n=4-5). This enabled clear visualization of the entire lymph node network with high contrast, especially at later timepoints. The uptake of the tracer in all other normal organs was similar across all groups, and below 10 %ID/g at 96 h.

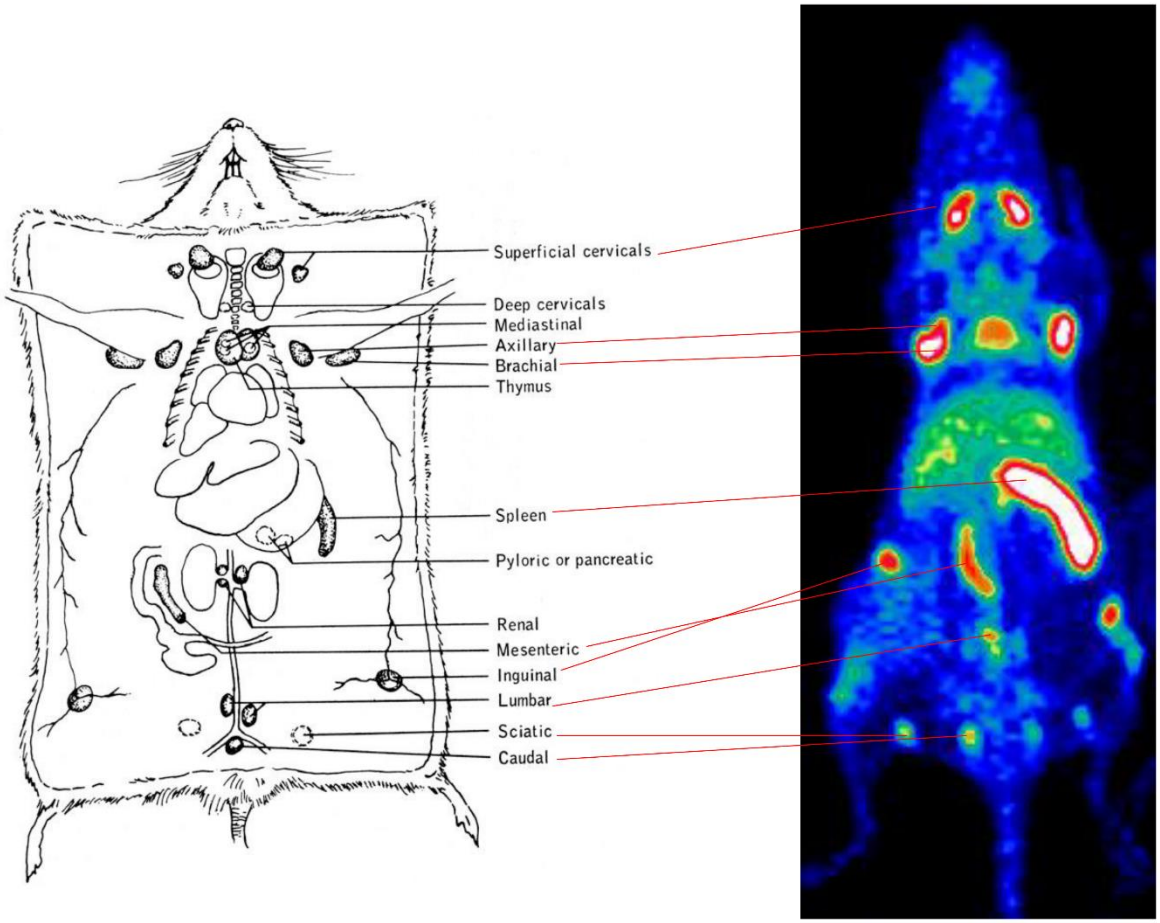

Figure 39. PD-L1 PET Lymphoid Mapping. *In a naïve nude mouse model, many lymph nodes and lymphoid organs can be visualized following injection of* ^{89}*Zr-Df-atezolizumab.*

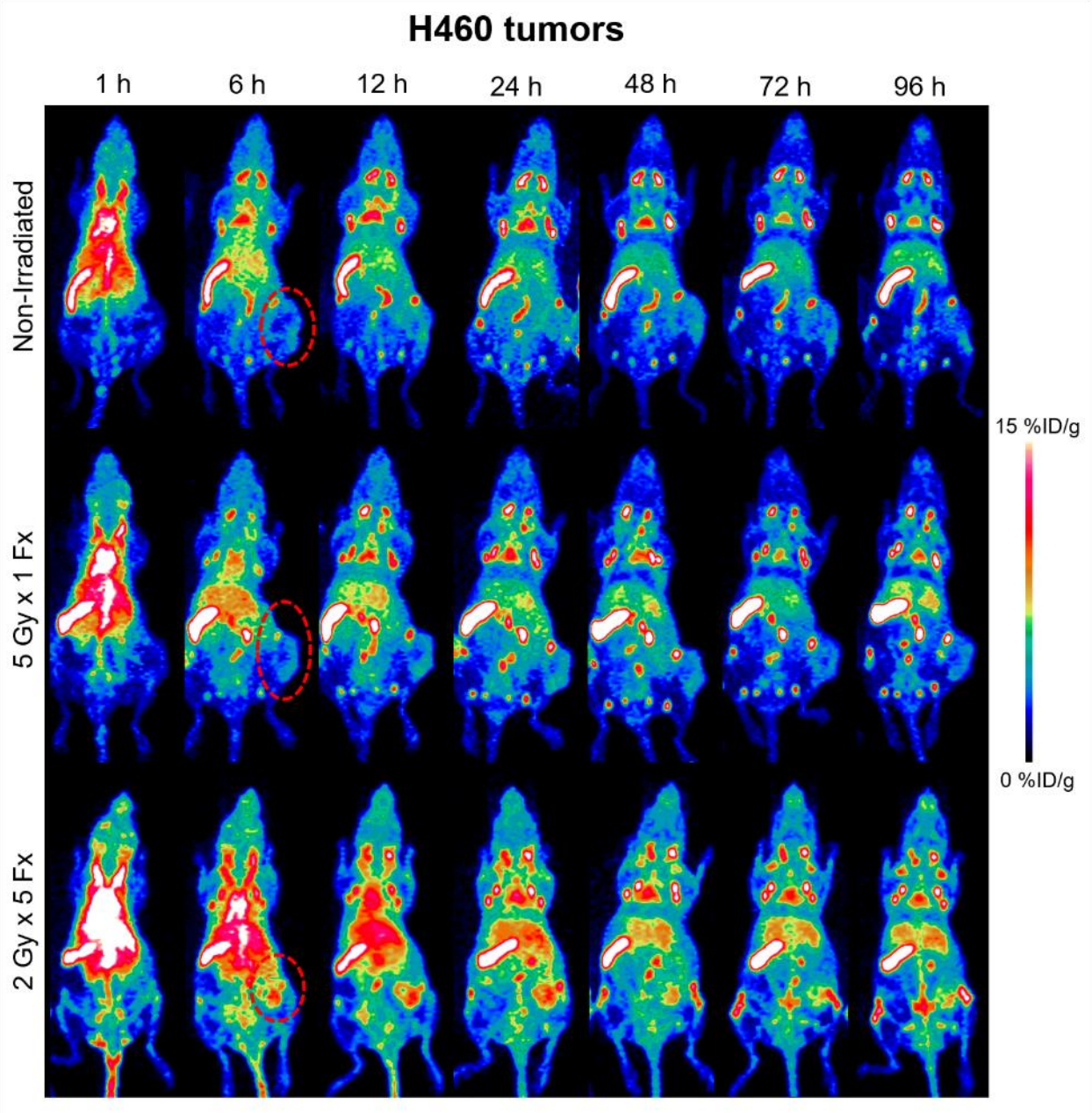

Figure 40. H460 PD-L1 PET. *Longitudinal PET imaging of mice with H460 tumors following injection of ^{89}Zr-Df-atezolizumab shows the highest tumor uptake in the 2 Gy x 5 fractions group. Tumors are indicated by red dashed circles in the MIPs.*

Given the high, specific uptake of the tracer in the lymphatic organs, the absolute amount of tracer binding in H460 tumor tissues was low. However, significant differences in the tumor accumulation were seen following the different treatment schedules. In non-irradiated mice, tumor uptake peaked at 24 h post-injection, at 2.10 ± 0.52 %ID/g. In contrast, in the 5 Gy x 1 Fx group, the accumulation was 2.44 ± 1.18 %ID/g at the same timepoint, and tumor uptake of 4.44 ± 1.52 %ID/g was measured for the 2 Gy x 5 Fx mice also (**Figure 41A, Table VI in Appendix 1**). At the 24 h scan, this corresponded to a statistically significant higher tracer accumulation in 2 Gy x 5 Fx mice as compared to the non-irradiated group ($p<0.05$, n=4-5). While the highest absolute uptake in the tumors was observed at the 24 h scan, peak tumor-to-muscle ratios (TMRs) were calculated at the final imaging timepoint, 96 h (**Figure 41B**). Mice receiving the 2 Gy x 5 Fx regimen had the highest TMRs at 3.59 ± 1.53, compared to the 5 Gy x 1 Fx group at 2.59 ± 1.48 and non-irradiated mice at 2.33 ± 0.81.

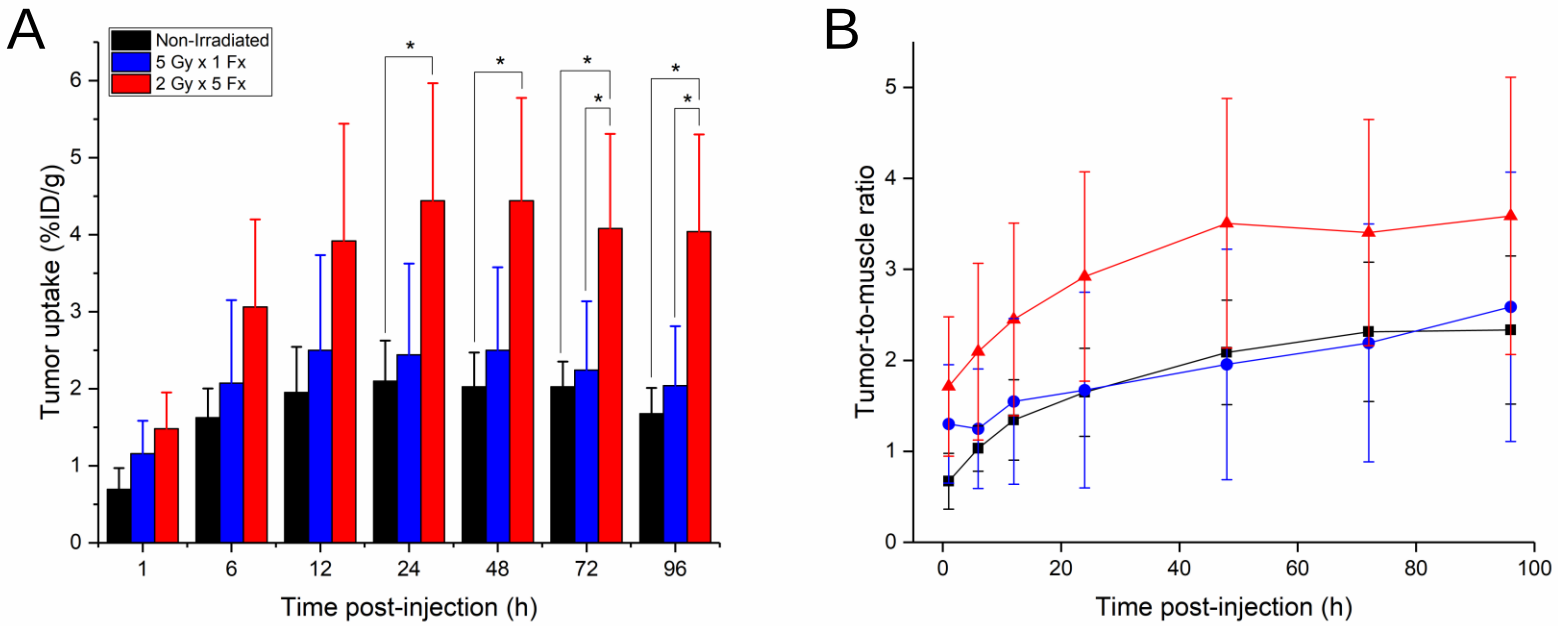

Figure 41. H460 PD-L1 PET Quantification. *(A) Uptake of ^{89}Zr-Df-atezolizumab in tumors as determined through region-of-interest analysis of H460 PET images. (B) Tumor-to-muscle ratios for all studied H460 groups over time. Both analyses indicate the highest accumulation of ^{89}Zr-Df-atezolizumab in the fractionated radiotherapy group. *p<0.05, n=4-5.*

As a negative control, mice bearing A549 tumors were also employed to determine non-specific accumulation of atezolizumab in tumor tissues (**Figure 42**). This control was determined to be most appropriate, since many traditional control experiments (blocking, nonspecific IgG) were not applicable to this model (see discussion section). From PET ROI analysis, non-irradiated A549 xenografts displayed the highest uptake of ^{89}Zr-Df-atezolizumab at 12 h post-injection, at 2.38 ± 0.67 %ID/g. When irradiated with 5 Gy in a single fraction, the peak A549 tumor accumulation was noted at 24 h, peaking at 2.10 ± 0.97 %ID/g. In mice receiving fractionated radiotherapy, a peak tumor uptake of 1.64 ± 0.65 %ID/g was calculated at 24 h post-injection as well. This provides support to a PD-L1-mediated mechanism for the increase in uptake of ^{89}Zr-Df-atezolizumab in H460 tumors, since the accumulation at the same timepoint (24 h) in these tumors after fractionated radiotherapy was 4.44 ± 1.53 %ID/g, a statistically significant difference ($p<0.02$, n=4-5; **Figure 43A**). In fact, the A549 tumor uptake in both irradiated and non-irradiated mice was nearly identical to that of non-irradiated H460 xenografts at all timepoints, indicating that this ~2 %ID/g can be attributed to nonspecific accumulation in tumor regions, likely due to the enhanced permeability and retention effect. No notable difference was noted for other organs and tissues between the two groups of tumor-bearing mice, as seen in the gamma counting biodistribution studies (**Figure 43B**).

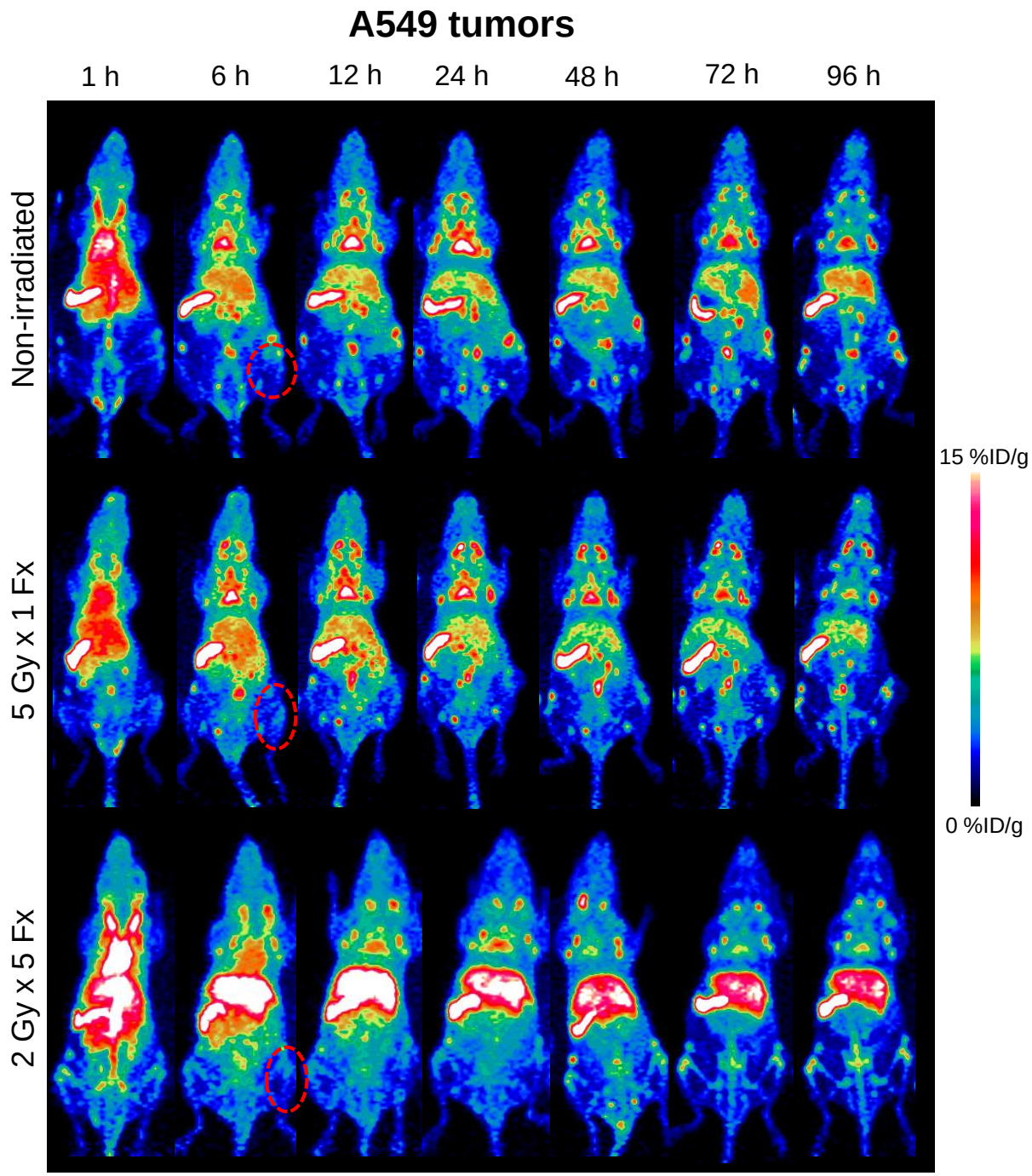

Figure 42. A549 PD-L1 PET. *PET imaging of mice with PD-L1(-) A549 xenografts with ^{89}Zr-Df-atezolizumab. Tumors are indicated by red dashed circles in the representative MIPs.*

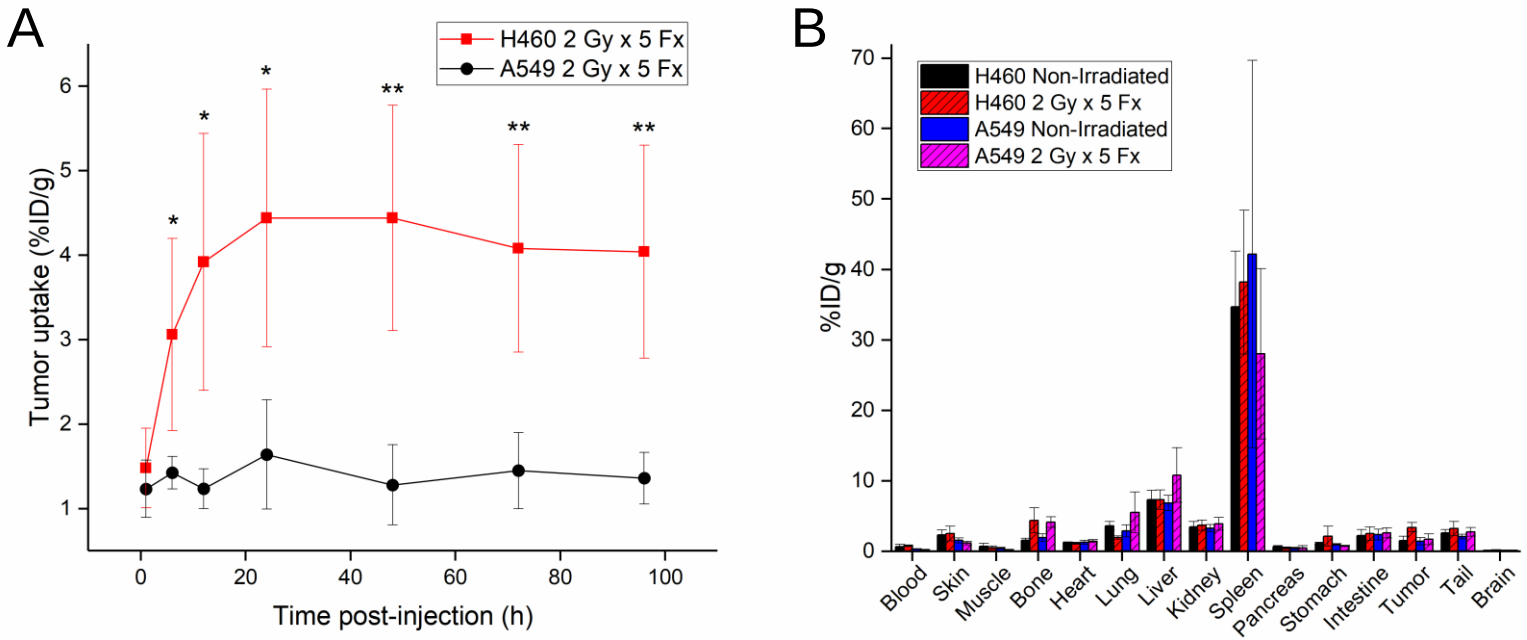

Figure 43. PD-L1 PET Comparison. *(A) Tumor uptake over time in H460 and A549 tumor xenografts receiving 2 Gy x 5 Fx. (B) Ex vivo biodistribution study results in the two tumor models. *p<0.05; **p<0.01; n=3-5.*

6.2.3. Fab tracer visualizes PD-L1+ tissues

Using the anti-PD-L1 Fab agent, the brown adipose tissue (BAT) and spleen were clearly visualized, even with the short time of the agent in circulation. In C57/BL6 mice, the BAT was easily delineated in maximum intensity projection images (MIPs), especially at the end of the 90-minute study (**Figure 44**). At this timepoint, the BAT accumulation of ^{64}Cu-NOTA-αPD-L1 was 4.47 ± 1.46 %ID/g, while only 1.27 ± 0.09 %ID/g remained in the blood pool, as determined through *ex vivo* gamma counting biodistribution (**Figure 47, Table IV in Appendix 2,** n=3-4). On the other hand, ^{64}Cu-NOTA-αHer-2 displayed minimal BAT accumulation at 0.87 ± 0.19 %ID/g, and 0.81 ± 0.10 %ID/g remained in circulation. Similarly, the spleen accumulation of the two tracers in BL6 mice was significantly different: 20.63 ± 10.4 %ID/g for the PD-L1 agent, and 2.73 ± 0.29 %ID/g for Her-2 (**Figure 46C, Table IX in Appendix 1**).

Similar observations were noted in the nude mouse models, as the highest BAT accumulation of ^{64}Cu-NOTA-αPD-L1 was noted at 15 min post-injection (5.70 ± 2.15 %ID/g, n=3-4). At the same timepoint, the BAT uptake of ^{64}Cu-NOTA-αHer-2 was 1.83 ± 0.25 %ID/g, and in the blocking group accumulation of 2.13 ± 0.40 %ID/g was measured (**Figure 45, Figure 46, Table VIII in Appendix 1**). Although quantification of spleen uptake from PET ROI analysis may be complicated by partial-volume effects, notable differences were observed in this organ's uptake between the three groups as well. ^{64}Cu-NOTA-αPD-L1 accumulated to a peak of 9.88 ± 3.39 %ID/g at 45 min post-injection, and could be blocked to 2.24 ± 1.26 %ID/g at the same timepoint by excess cold compound. ^{64}Cu-NOTA-αHer-2 displayed spleen uptake of only 2.30 ± 0.37 %ID/g at 45 min as well.

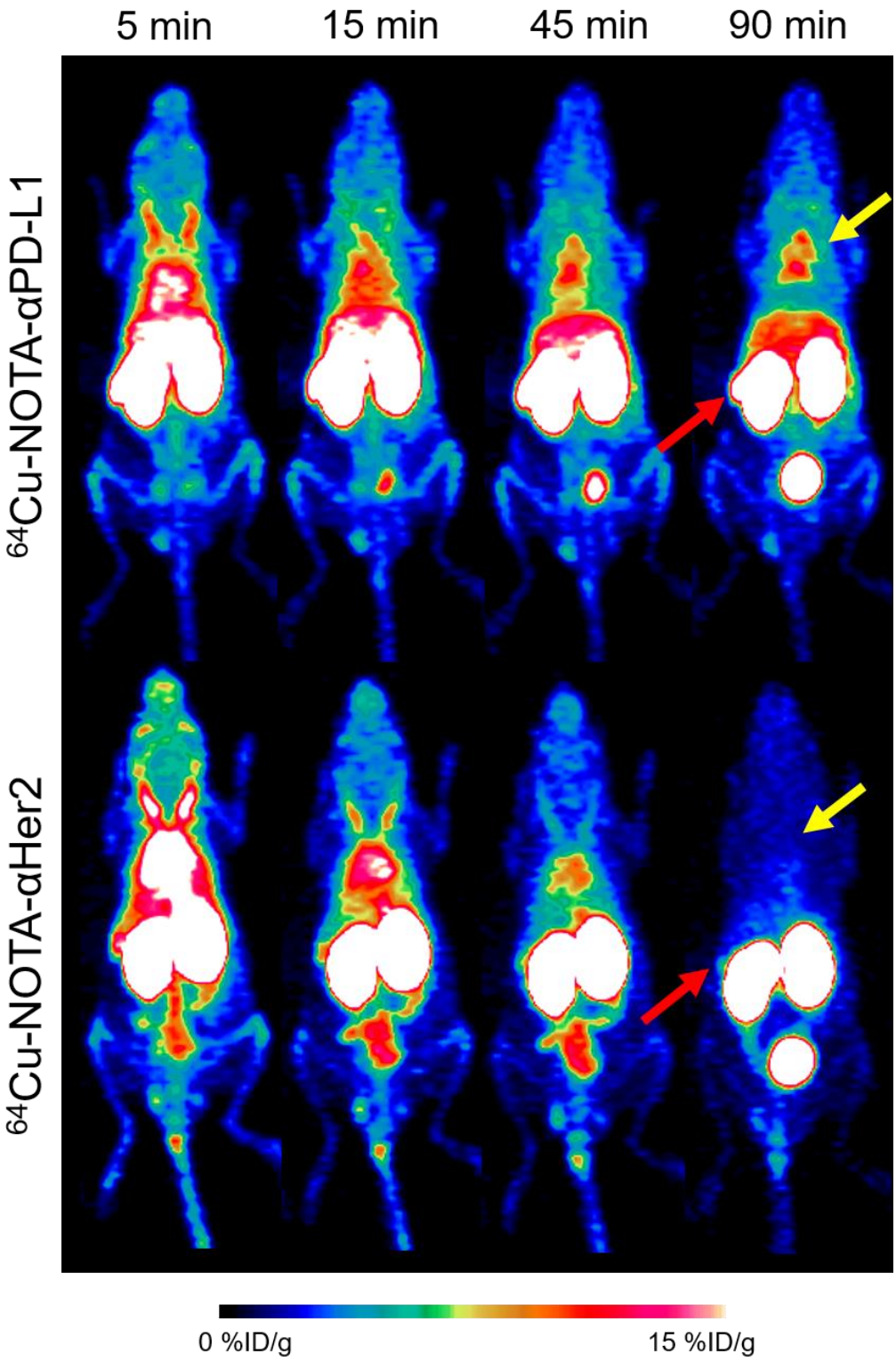

Figure 44. C57/BL6 PD-L1 PET. *PET imaging MIPs of C57/BL6 mice with the respective Fab-based tracers. The spleen (red arrow) and brown adipose tissue (yellow arrow) were expected sites of PD-L1 expression and therefore accumulation of that tracer.*

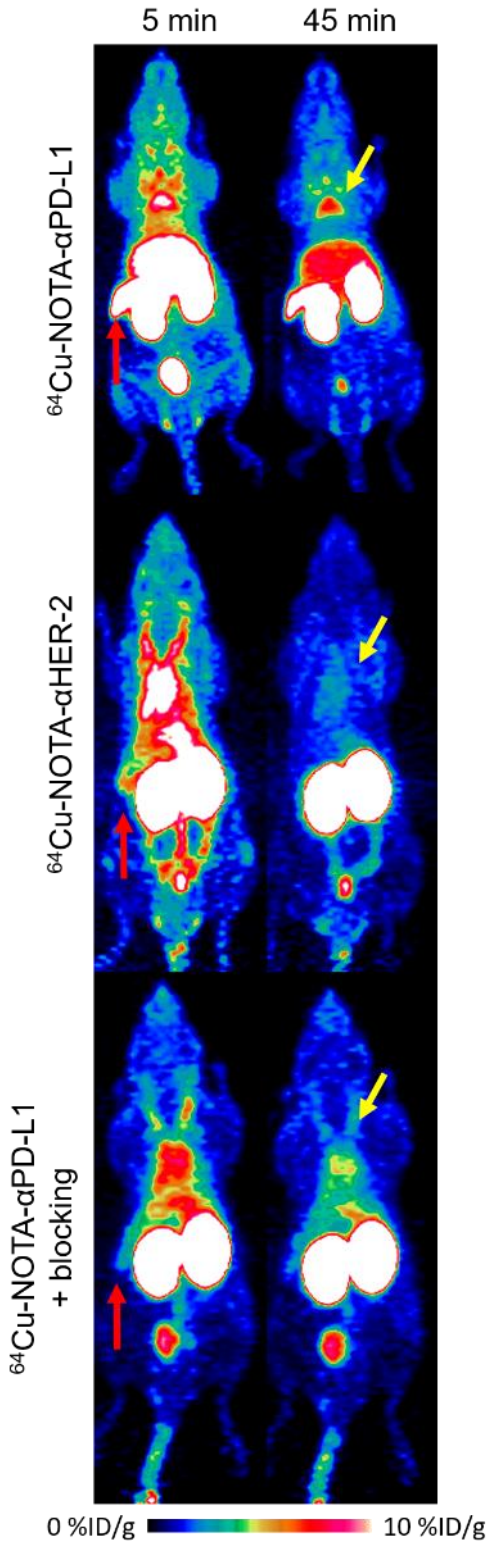

Figure 45. Athymic PD-L1 PET. *PET imaging in athymic nude mice. BAT (yellow) and spleen (red) uptake was observed with the PD-L1 agent, could be blocked, and was absent when a Her-2-targeted tracer was employed.*

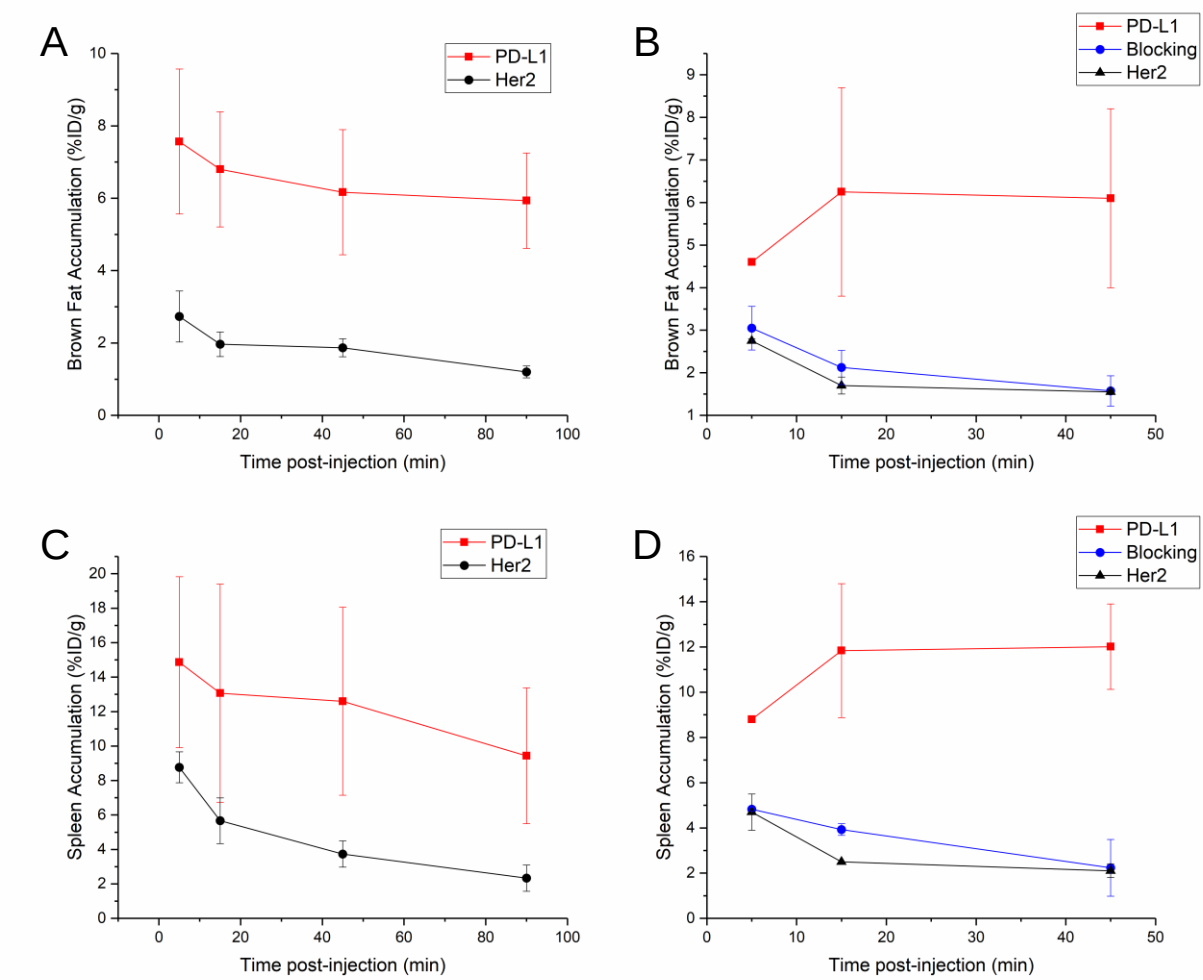

Figure 46. PD-L1 Fab PET Quantification. *Region-of-interest quantification of the Fab agents in C57/BL6 (left column) and athymic nude mice (right column). (A) and (B) present brown fat uptakes over time, while (C) and (D) show spleen accumulation. The uptake of ^{64}Cu-NOTA-αPD-L1 was significantly higher than all other groups at all timepoints in these two organs; n=3-4.*

6.2.4. *Ex vivo* verification of *in vivo* trends

Ex vivo biodistribution studies verified the trends found through analysis of PET images of ^{89}Zr-Df-atezolizumab (**Figure 48, Table V in Appendix 2**). The highest uptake of the tracer was noted in the spleen (33-38 %ID/g) in all groups, followed by the lymph nodes (13-25 %ID/g). Notably, the uptake measured by gamma counting was higher than that through PET ROI analysis, likely due to partial volume effects in the ROI measurements. Low levels of accumulation were also noted in the liver (7-8 %ID/g), as this is the clearance organ for antibody-based tracers. Tumor uptake was significantly higher in the group receiving 2 Gy x 5 Fx, at 3.38 ± 0.66 %ID/g, compared to 2.18 ± 0.80 %ID/g and 1.51 ± 0.61 %ID/g for the 5 Gy x 1 Fx and non-irradiated groups, respectively ($p<0.05$, n=4-5).

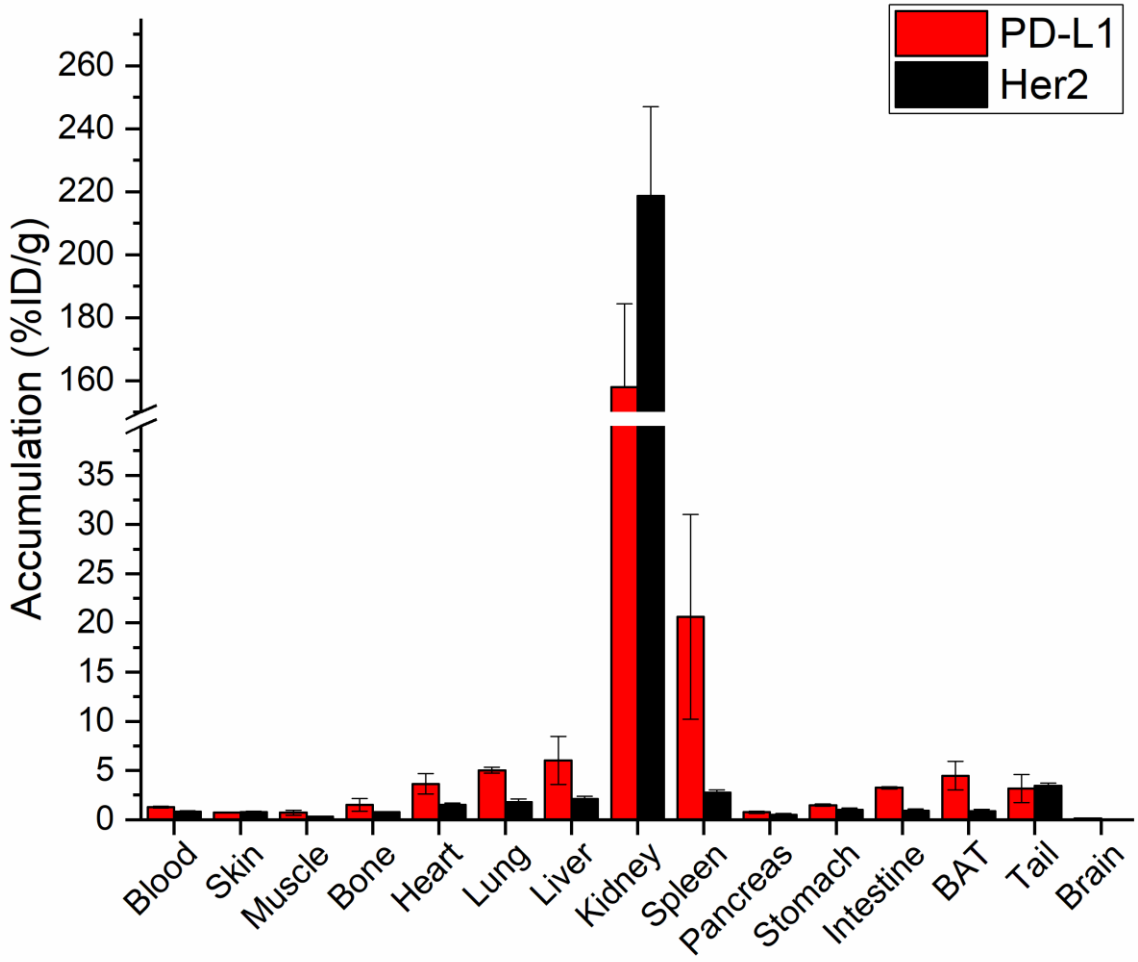

Figure 47. PD-L1 Fab Biodistribution Studies. *Gamma counting biodistribution studies in C57/BL6 mice following injection of either ^{64}Cu-NOTA-αPD-L1 or ^{64}Cu-NOTA-αHer-2; n=3-4.*

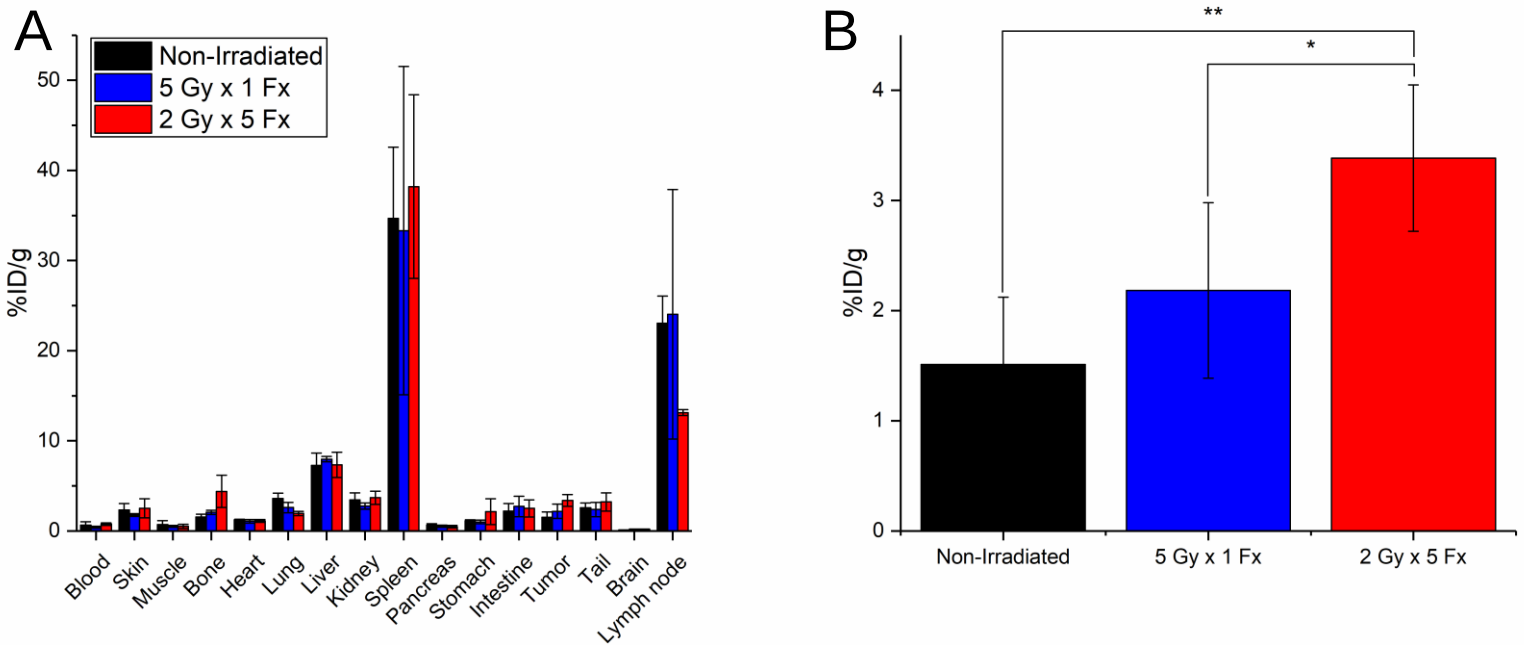

Figure 48. Atezolizumab Biodistribution Study. *(A) Results of the gamma counting biodistribution study following injection of ^{89}Zr-Df-atezolizumab. (B) Tumor uptakes of ^{89}Zr-Df-atezolizumab as determined by gamma counting. *p<0.05, **p<0.01; n=4-5.*

Tissues of significant tracer uptake were also excised at the time of necropsy, including the spleen and tumors (**Figure 50, Figure 49, Figure 51**). Immunofluorescent staining of these tissues verified the expression of PD-L1 and therefore specific binding of ^{89}Zr-Df-atezolizumab. Notably, the intensity of staining was higher in the lymphoid organs compared to H460 tumors, but also more heterogeneous. PD-L1 appeared to be expressed by a subpopulation of the cells in the spleen, with much co-localization with CD45 expression correlating with myeloid cell expression of PD-L1. In non-irradiated tumor tissues, some infiltrating myeloid cells were visualized and correlated with some PD-L1 expression. Following irradiation, an increase in CD45+ cells was observed, especially around the periphery of the tumor tissues. However, PD-L1 staining was observed in tumor tissues that also did not overlay with CD45 or F4/80, indicating tumor cell expression. Additionally, the morphology of CD45+ cells was clearly different than that of tumor cells themselves, with myeloid cells presenting as circular (top panels of **Figure 49** and **Figure 51**) while tumor cells were more elongated and abnormal shapes (bottom panels of **Figure 51** and **Figure 49**). The PD-L1 staining in irradiated tumors was more uniform than that observed in non-irradiated tissues. Staining of brown fat tissues for PD-L1 additionally revealed high expression in this tissue, verifying that the uptake seen there is on-target for PD-L1 (**Figure 52**).

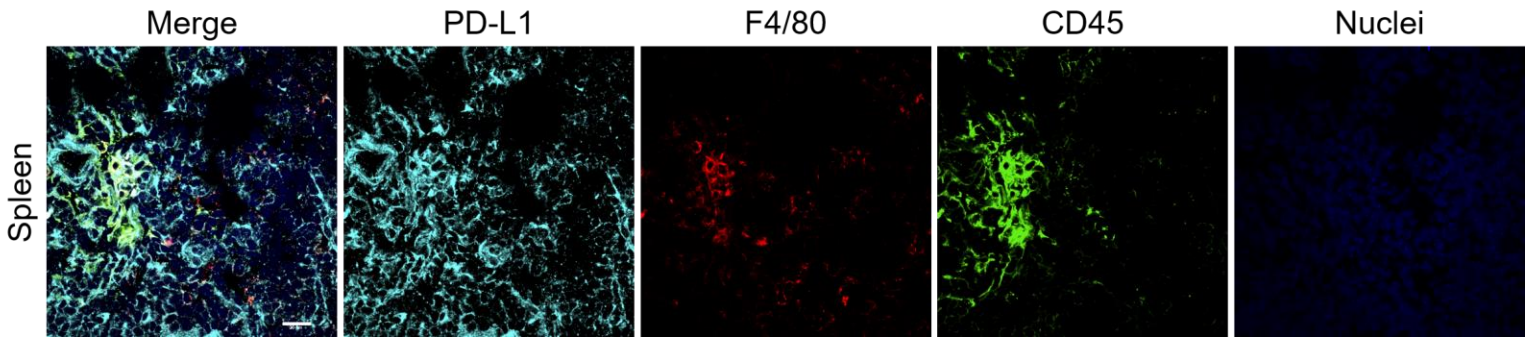

Figure 50. Spleen PD-L1 Staining. *Immunofluorescent staining of spleen tissue reveals high PD-L1 expression.*

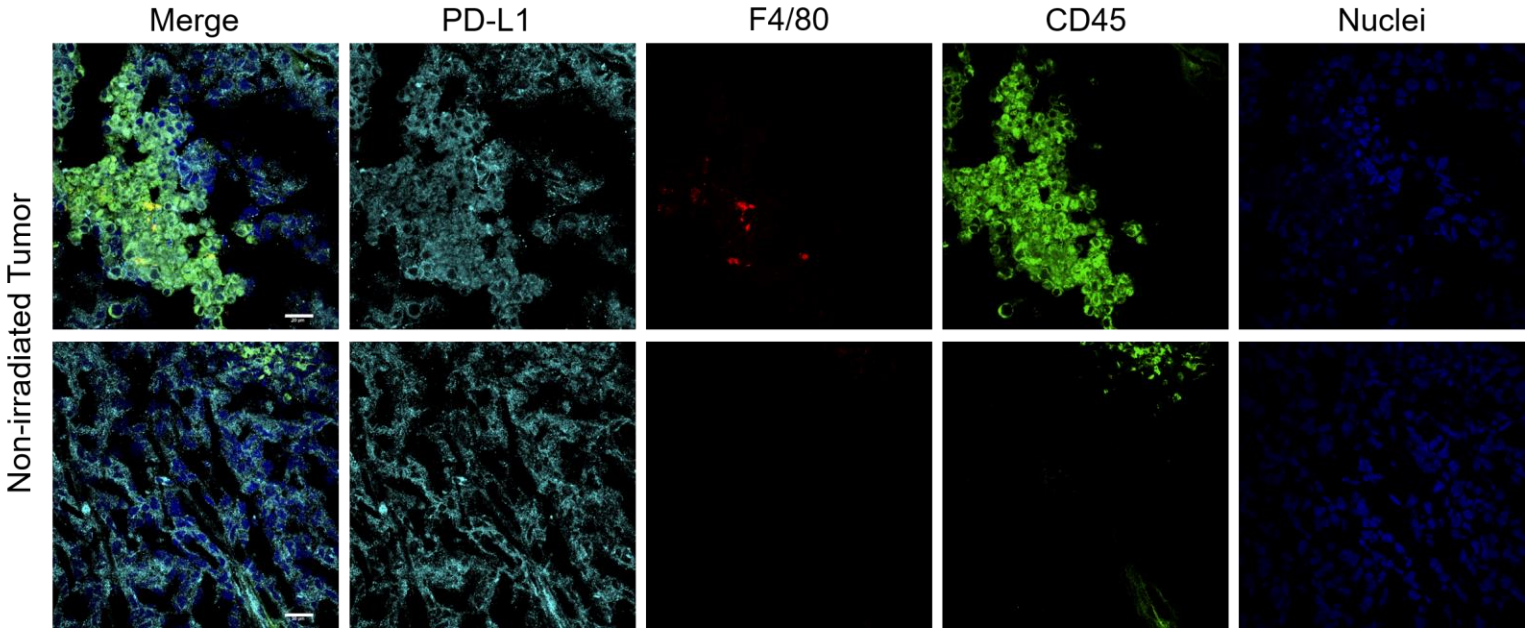

Figure 49. Non-irradiated H460 Tumor PD-L1 Staining. *Immunofluorescent staining of non-irradiated tumors shows baseline PD-L1 expression, and heterogeneous myeloid cell infiltration.*

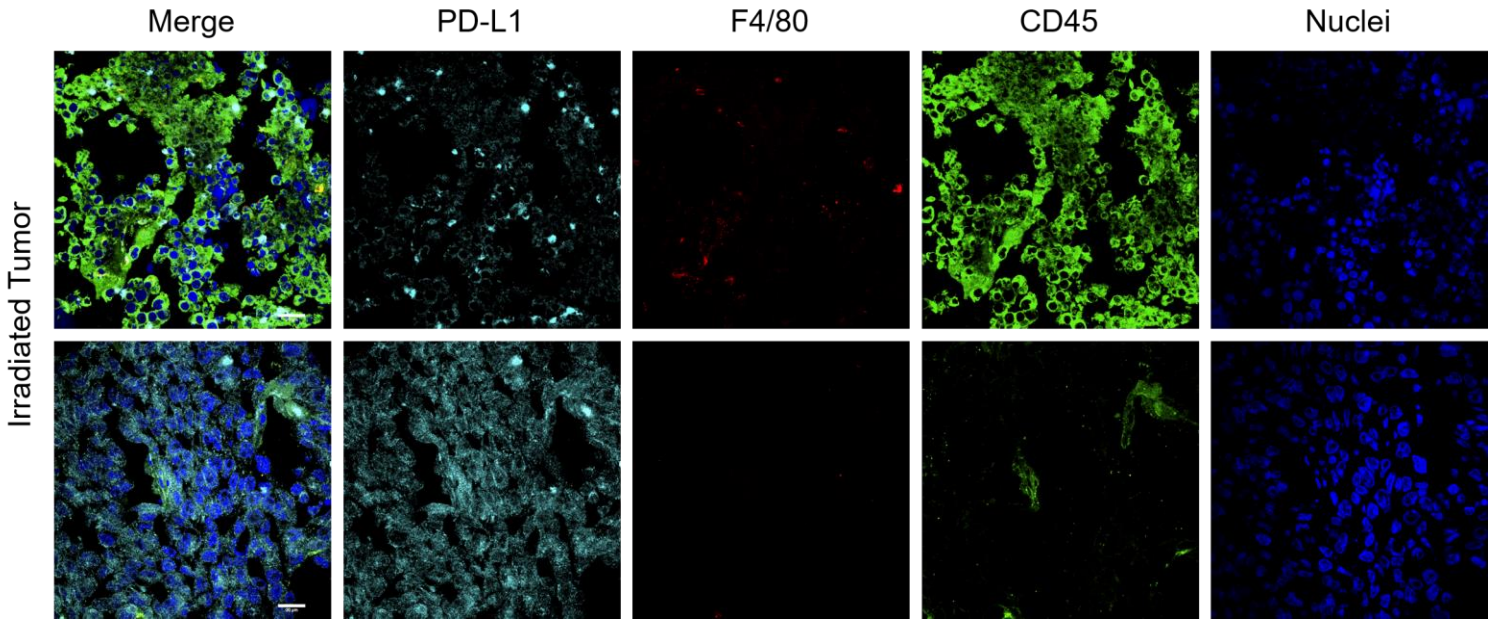

Figure 51. Irradiated H460 Tumor PD-L1 Staining. *After five fractions of 2 Gy radiotherapy, an increase in myeloid cell infiltration was noted around the periphery of the tumors. PD-L1 expression on tumor cells was also slightly increased in intensity.*

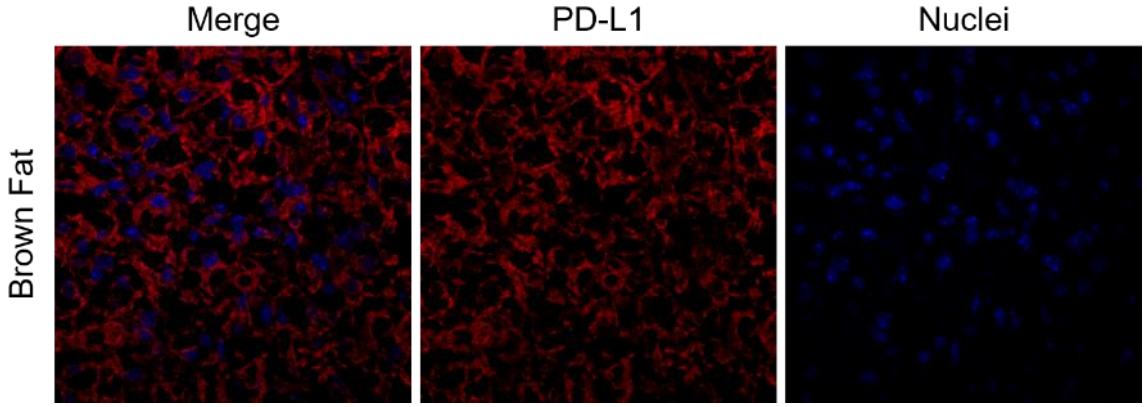

Figure 52. Brown Fat PD-L1 Staining. *Brown adipose tissues display high expression of PD-L1.*

6.3. Discussion

While the value of PD-L1 as a prognostic or predictive marker is still under debate[110, 111], the importance of monitoring changing biomarker expressions throughout treatment is well-recognized[112, 113]. We have therefore demonstrated that noninvasive PET imaging can monitor the dynamic expression of PD-L1 in naïve subjects as well as following radiation. Monitoring changes in PD-L1 expression in real-time has important implications clinically, especially for the optimization of synergistic therapy regimens[114-116]. PD-L1 PET therefore not only has value as a diagnostic agent for simple tumor detection, but also as a means of monitoring tumor response and allocating patients to proper therapies.

A number of studies have investigated tumor detection through molecular imaging based upon PD-L1 expression, often using murine models[8, 52-54, 117-120]. The present study varies from these previous ones on a few key points. First, we utilized an anti-human PD-L1 antibody that also cross-reacts with murine PD-L1. This means that these results should be more easily clinically-translated than those studies which use entirely murine systems, and we also have representative off-target binding of the tracer to lymphatic organs. This off-target binding will certainly be seen in patients, and thus needs to be considered in preclinical studies, which often use human-specific antibodies (which therefore do not bind to the analogous murine molecules). Second, our positive cell line herein (H460) only expresses native levels of PD-L1, rather than being engineered to express high, unnatural levels of the protein – a strategy that has been employed in past studies. While this expression level is low compared to lymphatic organs' PD-L1 levels (spleen and lymph nodes), we are still able to visualize the tumor burden by PET after therapeutic intervention. Finally, many other studies employ a pre-dosing strategy to minimize this off-target lymphatic uptake by

administering excess cold anti-PD-L1 antibody either before the tracer injection, or as a co-injection. While this technique does provide higher tumor uptake and contrast, such pre-dosing may induce a pharmacologic response, which is not desired for an imaging tracer. We only administered the radiolabeled protein, at a low per-mouse level, in order to avoid this.

As aforementioned, PD-L1 imaging is more complicated than imaging other traditional tumor markers. Since it is so widely expressed, not only is the imaging signal in the tumor reduced, but the traditionally-used control experiments cannot be applied. For instance, since administration of a blocking dose would first saturate the spleen and lymph nodes, this technique would be expected to actually result in a higher tracer accumulation in the tumor, and would not prove specificity for the cancer cells as in traditional studies. Additionally, another control technique is the use of a nonspecific, isotype-matched antibody. However, a nonspecific antibody would not bind to the PD-L1 that is ubiquitous throughout the body, and may actually accumulate once again to a higher level in the tumor tissue. We have tested a control IgG in A549 tumors in other studies, for example, and achieved 5.05 ± 1.70 %ID/g at 120 h post-injection. This is higher than any tumor uptake observed in these studies; therefore, these controls would not be helpful. For this reason, we employed the A549 xenografts as a control, since PD-L1 expression cannot be induced on them with the radiotherapy regimens employed here. This would provide a measure of the nonspecific accumulation of atezolizumab in tumor tissues that do not express PD-L1, while maintaining the same background uptake in lymphoid organs. Additionally, this provides a verification that, for instance, disruption of blood vessel architecture by radiotherapy is not to blame for increased tumor accumulation of ^{89}Zr-Df-atezolizumab.

The absolute uptake of ^{89}Zr-Df-atezolizumab in the H460 tumor tissues was low (1-5 %ID/g), even in the 2 Gy x 5 Fx group, when compared to that of tumor PET tracers targeted to markers

other than PD-L1. As partially mentioned before, this is likely due to a few factors. Most importantly, the expression of PD-L1 is not limited to the tumor tissue and several other tissues (including the spleen, lymph nodes, and brown fat) represent sinks for the tracer. Additionally, the number of cells expressing PD-L1, or even the number of copies of PD-L1 per cell, is lower than that of other commonly-used imaging targets. Notably, the cutoff for PD-L1 positivity in a tumor is often that 1-5% of the total cells express the target[121], compared to, for example, the definitions of Her-2 positivity (>10% of cells)[122]. Even though the absolute uptake is low and there is notable off-target binding, high tumor-to-muscle ratios allowed clear visualization of irradiated tumors, especially at later timepoints. This is a well-recognized benefit of ^{89}Zr-labeled antibodies – the long radioactive half-life allows for high-contrast imaging after the antibody has cleared from nonspecific binding. The results obtained herein may not be generally-applicable to all cancer types, models, and treatments. The expression of PD-L1 is expected to change in different cell lines and with different treatment regimens; therefore, future studies should fully explore these options.

Using the αPD-L1 Fab agent in these studies once again showed the ubiquitous expression of PD-L1 in normal tissues. The Fab agent has an extremely short *in vivo* half-life, providing high-contrast imaging at early timepoints. While this short circulation time may even further limit the tumor accumulation capabilities of the agent relative to an intact antibody, this small tracer may still serve important roles in monitoring immunotherapy treatments. As mentioned in **Chapter 3**, immune activation can be found in tissues other than the tumor, and this modulation may perhaps be visualized by ^{64}Cu-NOTA-αPD-L1 PET.

The dynamic nature of immune checkpoint molecules is beginning to be realized. There is therefore a great need to longitudinally monitor this expression in cancer patients receiving any

number of treatments. We have herein demonstrated that PET of tumor PD-L1 expression using ^{89}Zr-Df-atezolizumab is able to monitor changes in PD-L1 expression following various radiotherapy regimens. Additionally, normal tissue expression of PD-L1 was verified using ^{64}Cu-NOTA-αPD-L1. Such techniques may find application clinically for monitoring patient responses and determining proper therapies, giving clinicians another tool in their personalized medicine arsenal.

Chapter 7

7. Conclusion and Future Directions

Visualizing the complex interactions between the immune system and tumor cells can provide vital insight into biomarkers that may be excellent candidates for future immunotherapies. Immunotherapy blockade strategies are becoming more common in the management of several types of cancer; thus, the field is expected to grow exponentially during the coming years. As immune checkpoint inhibitors rely upon adequate receptor expression levels, noninvasive imaging to detect PD-1/PD-L1 or CTLA-4 may allow for enhanced patient identification, stratification, and the early assessment of therapeutic response. As many novel immune checkpoints for therapeutic targeting are investigated[15], imaging strategies for prescreening patients will be crucial to the success of these treatments.

Since most studies to date in this area have been preclinical, a few steps will be critical for future clinical translation, as outlined in this chapter.

7.1. Humanized tracers and appropriate models

Most of the agents outlined herein from others' works are murine antibodies and may not display specificity for human receptors; thus, human or humanized antibodies will need to be created for clinical translation, as was performed in the studies in this work. However, humanized or transgenic models used in preclinical research often fall short of mimicking the conditions found

in human patients. Imaging of these immune checkpoint pathways may also be limited by external conditions, including therapeutic intervention and certain bacterial or viral infections that may modify the immune system that are often issues in preclinical studies[123]. Caution should therefore be exercised when extrapolating preclinical results to those expected in humans.

Immunotherapy-related imaging is a unique and challenging imaging setting, and ideal preclinical models have not yet been developed. While using fully-murine systems enables imaging and therapy in an intact immune system, this will not translate to humans – neither in terms of the specificity of the agents, or the biological phenomena that are observed, as preclinical models are often quite different from the human situation. The choice of an appropriate model is thus often a choice between scientific foundation or translational potential.

7.2. Validation in therapeutic settings

More specific to the studies performed in this work, the imaging tracers developed should be explored in more advanced murine models, as they represent the best option for validation at this time. Transgenic mouse models that express the human immune checkpoint targets have been engineered and shown to respond to checkpoint blockade interventions. To truly evaluate the prognostic capabilities of immune checkpoint imaging, our tracers should be tested in these models. We would ideally observe a reliable difference in the biodistribution of the tracers between responding and non-responding mice and could subsequently utilize this difference as a stratification biomarker. Similar studies have been performed with other tracers in murine models (as outlined in **Chapter 3**) with interesting results. Showing strong correlations in these studies should enable the tracers to move forward into the clinic, which is certainly the end-goal of this work.

7.3. Comparative imaging pre- and post-therapy

Many preclinical studies utilize a pre-dosing strategy with non-labeled antibody to increase the tracer uptake in targeted tissues of interest[124]. While this certainly provides greater visual contrast between background and malignant tissues, this need for saturating receptor binding is one of the critical pitfalls of immunotherapy. While most biomarkers targeted for imaging are found solely on tumor cells, these immune checkpoint pathway receptors are heterogeneously expressed throughout the entire body, complicating potential imaging strategies, as was seen in **Chapter 6**. Thus, molecular imaging of immunotherapy targets requires creative approaches that may extend beyond traditional oncological tracer development, as does the generation of adequate preclinical animal models.

It is expected that agents for imaging of immunotherapy targets will play a role that is quite distinct from other traditional cancer imaging agents. Rather than serving as diagnostic tools to identify tumor sites and expression levels, immune imaging agents may be used to evaluate the dynamic nature of these targets and their expression and distribution within the body following therapeutic interventions. Instead of imaging for the sake of imaging, these agents have the potential of truly impacting clinical decision-making. For example, imaging T-cells prior to and after initiation of therapy may provide insight as to the immune activation levels that can be achieved and provide a measure of therapeutic efficacy. Future studies in this area should evaluate this comparative imaging strategy; that is, the changes in tracer uptakes or distribution following therapy.

7.4. Optimization of tracer properties for clinical translation

While the majority of the work herein was founded upon antibody-based agents, these platforms may not be the most conducive to clinical translation[125]. For instance, depending on

dosage and the antibody source, they may induce pharmacological effects *in vivo*. For the low doses involved in imaging, this is a relatively small concern when compared to some of the considerations more unique to imaging. Importantly, antibodies exhibit long circulation times and high background accumulations. The *in vivo* half-lives of antibodies are often on the order of days, which is desirable for a therapeutic drug (since it maximizes the chances for tissue exposure) but is non-ideal for imaging. While multiple imaging timepoints are not a problem in preclinical studies, requiring a patient to return to the imaging clinic many days after tracer administration is an unnecessary and often prohibitory complication. Additionally, this may result in a delay in care. This long circulation time, combined with the off-target passive accumulation of large antibody macromolecules, necessitates the use of later imaging timepoints to achieve the highest possible signal-to-background. For this reason, antibody fragments or other engineered agents (such as presented in **Chapters 5 and 6**) may be more clinically-suitable. The majority of clinically-available PET agents are small molecules, and for good reason – they are the most suited to the current clinical workflow. The ideal PET tracer candidate is therefore a delicate balance between retention of the high specificity of antibodies with the quick target accumulation and clearance of smaller entities. Future work should explore these engineered tracers to develop an ideal candidate for clinical translation.

7.5. Exploration of alternative immunotherapy biomarkers

Imaging the immune checkpoints themselves certainly provides scientific insight into their still-quite-mysterious behavior. However, alternative immune cell markers may serve important roles for future imaging agents applied to immunotherapy. A number of studies have begun exploring this possibility[61], and immune cell-specific agents have been tested in other therapeutic and disease settings (for instance, autoimmunity[126]). These already-developed tracers may find

perfect application in preclinical immunotherapy settings, where immense scientific insight could be achieved through monitoring the dynamics of a wide variety of cell types during immunotherapy. Imaging different subpopulations of immune cells may provide insight into the important players in immunotherapy response – for instance employing imaging agents for PD-1, CTLA-4, CD8, CD3, and other activation markers to determine which cells play critical roles. The molecular imaging arsenal should be fully deployed to understand these novel treatments.

While a great deal of work has yet to be done for imaging in immunotherapy settings, great strides have been made in recent years, and the fruits of these labors are already beginning to be seen clinically. A greater scientific understanding of these interventions will enable more intelligent design of clinical trials and selection of patients for proper therapies. The work presented herein formed much of the foundation for research in this field, and we expect that future studies will help continue the immunotherapy revolution for cancer treatments.

Appendix 1

PET Region-of-interest data

All results were obtained using region-of-interest analysis in the Inveon Research Workspace Software and are presented as the mean ± standard deviation.

Table I.* ^{64}*Cu-DOTA-ipilimumab Quantification. *Quantification of the accumulation of* ^{64}*Cu-DOTA-ipilimumab in major organs throughout the CTLA-4 tumor imaging study; n=3-4.*

Organ	PET ROI quantification at 3 h after injection (%ID/g ± SD)		
	A549	**H460**	**H358**
Blood	19.53 ± 0.79	25.43 ± 3.06	17.77 ± 0.76
Liver	14.93 ± 1.88	17.10 ± 0.50	12.90 ± 0.82
Spleen	8.30 ± 1.26	8.10 ± 1.34	7.07 ± 1.02
Brain	1.37 ± 0.12	1.57 ± 0.09	1.33 ± 0.09
Muscle	1.47 ± 0.09	1.33 ± 0.25	1.27 ± 0.09
Tumor	5.63 ± 0.76	3.53 ± 0.37	4.50 ± 0.14
Organ	**PET ROI quantification at 24 h after injection (%ID/g ± SD)**		
	A549	**H460**	**H358**
Blood	10.43 ± 2.25	13.83 ± 0.85	11.67 ± 0.60
Liver	9.97 ± 1.11	10.97 ± 0.12	9.53 ± 0.54
Spleen	6.83 ± 0.91	6.33 ± 1.08	5.90 ± 0.70
Brain	0.68 ± 0.15	1.20 ± 0.14	0.82 ± 0.13
Muscle	1.13 ± 0.09	1.40 ± 0.16	1.40 ± 0.16
Tumor	9.40 ± 0.29	8.27 ± 0.12	7.13 ± 0.17
Organ	**PET ROI quantification at 48 h after injection (%ID/g ± SD)**		
	A549	**H460**	**H358**
Blood	8.43 ± 2.87	11.90 ± 1.37	10.43 ± 1.21
Liver	9.80 ± 1.34	9.80 ± 0.94	8.80 ± 0.36
Spleen	6.43 ± 0.70	5.87 ± 1.03	5.00 ± 0.57
Brain	0.92 ± 0.36	1.03 ± 0.26	0.92 ± 0.06
Muscle	1.03 ± 0.12	1.60 ± 0.22	1.27 ± 0.12
Tumor	9.80 ± 0.22	9.37 ± 0.26	7.43 ± 0.05

Table II. CTLA-4 T-cell PET ROI Quantification. *Quantification of PET signals throughout the CTLA-4 T-cell imaging study; n=3-6.*

	PET ROI quantification at 0.5 h after injection (%ID/g ± SD)				
Organ	**^{64}Cu-NOTA-ipilimumab – PBL**	**^{64}Cu-NOTA-ipilimumab-F(ab')$_2$ – PBL**	**^{64}Cu-NOTA-IgG – PBL**	**^{64}Cu-NOTA-ipilimumab – NBSGW**	**^{64}Cu-NOTA-ipilimumab-F(ab')$_2$ - NBSGW**
Heart	23.03 ± 4.46	24.40 ± 2.22	24.85 ± 0.15	26.35 ± 5.05	22.77 ± 1.51
Liver	12.43 ± 2.99	14.80 ± 1.44	13.25 ± 0.45	20.55 ± 1.95	14.00 ± 0.78
Spleen	4.57 ± 0.39	5.80 ± 1.09	12.75 ± 2.95	13.55 ± 2.55	
Kidney	6.78 ± 1.01	18.88 ± 1.80	7.95 ± 0.65	11.25 ± 1.45	19.17 ± 2.28
Salivary Gland	1.70 ± 0.30	3.22 ± 0.62	2.25 ± 0.05	2.60 ± 0.10	2.97 ± 1.24
Muscle	0.91 ± 0.30	0.85 ± 0.11	1.45 ± 0.15	0.795 ± 0.18	0.74 ± 0.02
Brain	1.53 ± 0.28	1.64 ± 0.24	1.50 ± 0.10	1.70 ± 0.10	1.33 ± 0.19
	PET ROI quantification at 3 h after injection (%ID/g ± SD)				
Organ	**^{64}Cu-NOTA-ipilimumab – PBL**	**^{64}Cu-NOTA-ipilimumab-F(ab')$_2$ – PBL**	**^{64}Cu-NOTA-IgG – PBL**	**^{64}Cu-NOTA-ipilimumab – NBSGW**	**^{64}Cu-NOTA-ipilimumab-F(ab')$_2$ - NBSGW**
Heart	16.73 ± 2.67	12.62 ± 1.62	21.15 ± 0.35	23.90 ± 2.00	13.93 ± 0.68
Liver	9.88 ± 2.10	10.08 ± 1.20	11.90 ± 0.20	17.45 ± 2.25	9.20 ± 0.96
Spleen	6.00 ± 0.78	5.03 ± 1.03	9.85 ± 1.55	12.75 ± 0.25	
Kidney	5.90 ± 1.50	39.44 ± 2.91	8.00 ± 0.30	10.25 ± 1.15	32.60 ± 2.28
Salivary Gland	3.30 ± 0.82	3.08 ± 0.70	3.70 ± 0.40	3.15 ± 0.35	2.60 ± 0.41
Muscle	0.80 ± 0.12	0.75 ± 0.16	1.50 ± 0.20	1.30 ± 0.10	0.78 ± 0.18
Brain	1.18 ± 0.13	0.90 ± 0.18	1.40 ± 0.10	1.55 ± 0.15	0.84 ± 0.09
	PET ROI quantification at 12 h after injection (%ID/g ± SD)				
Organ	**^{64}Cu-NOTA-ipilimumab – PBL**	**^{64}Cu-NOTA-ipilimumab-F(ab')$_2$ – PBL**	**^{64}Cu-NOTA-IgG – PBL**	**^{64}Cu-NOTA-ipilimumab – NBSGW**	**^{64}Cu-NOTA-ipilimumab-F(ab')$_2$ - NBSGW**
Heart	8.50 ± 1.71	2.78 ± 0.48	14.15 ± 0.25	13.25 ± 1.65	2.77 ± 0.39
Liver	6.72 ± 1.59	5.16 ± 1.32	9.70 ± 0.60	11.55 ± 2.35	4.17 ± 0.34
Spleen	5.30 ± 0.57	3.00 ± 0.96	5.35 ± 0.05	13.20 ± 2.10	
Kidney	3.85 ± 0.73	36.58 ± 8.02	6.05 ± 0.05	5.70 ± 0.80	26.13 ± 0.34
Salivary Gland	5.80 ± 1.82	2.64 ± 0.84	4.45 ± 0.85	4.10 ± 0.60	1.43 ± 0.21
Muscle	0.88 ± 0.25	0.38 ± 0.06	1.50 ± 0.10	1.15 ± 0.05	0.33 ± 0.04
Brain	0.78 ± 0.13	0.32 ± 0.07	1.04 ± 0.17	0.97 ± 0.24	0.29 ± 0.02

Organ	PET ROI quantification at 24 h after injection (%ID/g ± SD)				
	^{64}Cu-NOTA-ipilimumab – PBL	**^{64}Cu-NOTA-ipilimumab-F(ab')$_2$ – PBL**	**^{64}Cu-NOTA-IgG – PBL**	**^{64}Cu-NOTA-ipilimumab – NBSGW**	**^{64}Cu-NOTA-ipilimumab-F(ab')$_2$ - NBSGW**
Heart	7.28 ± 1.56	1.46 ± 0.34	12.70 ± 0.30	9.05 ± 2.05	1.27 ± 0.05
Liver	6.85 ± 1.51	4.68 ± 0.51	10.35 ± 0.65	10.75 ± 1.65	3.93 ± 0.29
Spleen	6.63 ± 2.24	1.63 ± 0.47	6.70 ± 1.50	14.25 ± 0.45	
Kidney	3.68 ± 0.60	30.76 ± 1.78	5.90 ± 1.10	4.75 ± 0.65	17.93 ± 1.03
Salivary Gland	7.00 ± 2.19	2.40 ± 0.86	4.20 ± 0.60	4.60 ± 0.10	1.05 ± 0.11
Muscle	0.94 ± 0.27	0.29 ± 0.05	1.45 ± 0.25	1.03 ± 0.18	0.31 ± 0.06
Brain	0.69 ± 0.23	0.27 ± 0.06	0.83 ± 0.10	0.82 ± 0.38	0.21 ± 0.03
Organ	**PET ROI quantification at 48 h after injection (%ID/g ± SD)**				
	^{64}Cu-NOTA-ipilimumab – PBL	**^{64}Cu-NOTA-ipilimumab-F(ab')$_2$ – PBL**	**^{64}Cu-NOTA-IgG – PBL**	**^{64}Cu-NOTA-ipilimumab – NBSGW**	**^{64}Cu-NOTA-ipilimumab-F(ab')$_2$ - NBSGW**
Heart	5.25 ± 1.37	0.89 ± 0.12	10.40 ± 0.10	5.65 ± 1.35	0.67 ± 0.05
Liver	5.65 ± 1.53	3.58 ± 0.43	10.00 ± 1.30	8.60 ± 1.00	2.97 ± 0.24
Spleen	5.93 ± 1.22	1.43 ± 0.33	4.10 ± 0.20	16.20 ± 3.90	
Kidney	3.50 ± 0.46	18.34 ± 2.14	4.65 ± 0.15	4.20 ± 0.50	10.60 ± 1.44
Salivary Gland	6.25 ± 2.03	1.57 ± 0.61	3.50 ± 0.80	4.35 ± 0.15	0.55 ± 0.06
Muscle	0.77 ± 0.26	0.21 ± 0.03	1.30 ± 0.20	1.12 ± 0.18	0.14 ± 0.01
Brain	0.58 ± 0.10	0.19 ± 0.02	0.68 ± 0.08	0.63 ± 0.10	0.16 ± 0.03

Table III. PD-1 T-cell PET ROI Quantification. *Measurement of ^{89}Zr-Df-pembrolizumab uptake in PBL and NSG mice, evaluated through ROI analysis of PET images; n=4.*

Organ	PET ROI quantification at 0.5 h after injection (%ID/g ± SD)		Organ	PET ROI quantification at 48 h after injection (%ID/g ± SD)	
	^{89}Zr-Df-pembrolizumab - PBL	**^{89}Zr-Df-pembrolizumab - NSG**		**^{89}Zr-Df-pembrolizumab - PBL**	**^{89}Zr-Df-pembrolizumab - NSG**
Blood	24.50 ± 1.35	21.78 ± 2.23	Blood	6.13 ± 0.41	9.78 ± 0.78
Liver	14.60 ± 0.39	12.93 ± 1.96	Liver	7.65 ± 0.57	7.18 ± 0.19
Spleen	10.30 ± 1.31	5.48 ± 0.71	Spleen	4.85 ± 0.40	6.75 ± 0.65
Kidney	11.50 ± 0.53	8.80 ± 1.91	Kidney	5.13 ± 0.13	6.15 ± 0.53
Salivary Gland	3.43 ± 0.55	4.13 ± 0.13	Salivary Gland	9.65 ± 0.66	4.65 ± 0.49
Muscle	0.85 ± 0.15	0.75 ± 0.22	Muscle	0.95 ± 0.23	1.23 ± 0.16
Organ	**PET ROI quantification at 6 h after injection (%ID/g ± SD)**		**Organ**	**PET ROI quantification at 72 h after injection (%ID/g ± SD)**	
	^{89}Zr-Df-pembrolizumab - PBL	**^{89}Zr-Df-pembrolizumab - NSG**		**^{89}Zr-Df-pembrolizumab - PBL**	**^{89}Zr-Df-pembrolizumab - NSG**
Blood	17.23 ± 1.63	16.03 ± 1.56	Blood	4.60 ± 0.56	9.73 ± 0.54
Liver	12.03 ± 0.83	11.15 ± 0.71	Liver	7.13 ± 0.33	6.48 ± 0.20
Spleen	8.05 ± 0.69	6.25 ± 1.49	Spleen	4.50 ± 0.53	5.33 ± 0.53
Kidney	8.18 ± 1.27	8.53 ± 0.75	Kidney	4.23 ± 0.44	5.15 ± 0.11
Salivary Gland	5.48 ± 0.40	4.10 ± 0.46	Salivary Gland	10.68 ± 0.77	5.23 ± 0.36
Muscle	0.96 ± 0.11	0.88 ± 0.10	Muscle	0.75 ± 0.15	1.10 ± 0.21
Organ	**PET ROI quantification at 12 h after injection (%ID/g ± SD)**		**Organ**	**PET ROI quantification at 120 h after injection (%ID/g ± SD)**	
	^{89}Zr-Df-pembrolizumab - PBL	**^{89}Zr-Df-pembrolizumab - NSG**		**^{89}Zr-Df-pembrolizumab - PBL**	**^{89}Zr-Df-pembrolizumab - NSG**
Blood	13.80 ± 0.92	13.23 ± 0.66	Blood	3.20 ± 0.41	8.00 ± 0.45
Liver	10.95 ± 0.38	9.73 ± 0.58	Liver	7.33 ± 0.84	6.25 ± 0.62
Spleen	7.65 ± 0.30	6.08 ± 1.49	Spleen	4.15 ± 0.79	4.88 ± 0.72
Kidney	6.68 ± 0.48	7.73 ± 0.62	Kidney	3.73 ± 0.45	5.90 ± 0.70
Salivary Gland	7.23 ± 0.20	4.55 ± 0.50	Salivary Gland	10.80 ± 0.72	4.93 ± 0.46
Muscle	0.88 ± 0.18	0.97 ± 0.25	Muscle	0.88 ± 0.26	1.04 ± 0.22

Organ	PET ROI quantification at 24 h after injection (%ID/g ± SD)		Organ	PET ROI quantification at 168 h after injection (%ID/g ± SD)	
	^{89}Zr-Df-pembrolizumab - PBL	^{89}Zr-Df-pembrolizumab - NSG		^{89}Zr-Df-pembrolizumab - PBL	^{89}Zr-Df-pembrolizumab - NSG
Blood	9.30 ± 0.51	11.80 ± 0.81	Blood	3.65 ± 0.59	6.83 ± 0.78
Liver	7.68 ± 0.64	8.45 ± 0.96	Liver	5.48 ± 0.76	6.32 ± 0.68
Spleen	5.10 ± 0.67	5.05 ± 1.74	Spleen	3.85 ± 0.47	4.33 ± 0.18
Kidney	5.33 ± 0.66	6.75 ± 0.50	Kidney	3.33 ± 0.66	5.08 ± 0.43
Salivary Gland	8.23 ± 0.33	5.25 ± 0.48	Salivary Gland	11.13 ± 0.83	5.03 ± 0.59
Muscle	0.90 ± 0.31	1.05 ± 0.18	Muscle	0.95 ± 0.21	0.94 ± 0.09

Table IV. ^{89}Zr-Df-nivolumab TIL PET Quantification. *Results from ROI analysis of ^{89}Zr-Df-nivolumab in humanized PBL mice and control NSG; n=4.*

Organ	PET ROI quantification at 3 h after injection (%ID/g ± SD)		Organ	PET ROI quantification at 48 h after injection (%ID/g ± SD)	
	^{89}Zr-Df-nivolumab - PBL	^{89}Zr-Df-nivolumab - NSG		^{89}Zr-Df-nivolumab - PBL	^{89}Zr-Df-nivolumab - NSG
Blood	15.52 ± 1.29	13.1 ± 0.79	Blood	7.52 ± 0.78	4.93 ± 0.39
Liver	10.42 ± 1.57	8.8 ± 0.55	Liver	6.52 ± 1.18	6.50 ± 0.64
Spleen	6.74 ± 1.43	6.625 ± 1.23	Spleen	6.04 ± 0.53	8.20 ± 1.54
Kidney	6.44 ± 0.36	7.375 ± 0.77	Kidney	5.50 ± 0.62	5.73 ± 0.95
Salivary Gland	4.54 ± 0.80	3.425 ± 0.70	Salivary Gland	6.82 ± 0.93	4.10 ± 0.24
Tumor	2.46 ± 0.26	2.325 ± 0.35	Tumor	5.98 ± 0.93	5.13 ± 0.72
Muscle	0.74 ± 0.23	0.78 ± 0.09	Muscle	0.87 ± 0.13	0.90 ± 0.18
Organ	**PET ROI quantification at 6 h after injection (%ID/g ± SD)**		**Organ**	**PET ROI quantification at 72 h after injection (%ID/g ± SD)**	
	^{89}Zr-Df-nivolumab – PBL	^{89}Zr-Df-nivolumab – NSG		^{89}Zr-Df-nivolumab – PBL	^{89}Zr-Df-nivolumab – NSG
Blood	14.02 ± 2.03	12.625 ± 1.95	Blood	6.04 ± 0.77	3.65 ± 0.39
Liver	8.86 ± 0.78	7.9 ± 0.78	Liver	6.36 ± 1.48	6.28 ± 0.83
Spleen	7.62 ± 0.76	5.95 ± 0.76	Spleen	5.58 ± 0.39	8.35 ± 0.62
Kidney	6.82 ± 0.83	5.325 ± 0.95	Kidney	4.52 ± 0.95	5.38 ± 0.87
Salivary Gland	6.18 ± 1.60	4.225 ± 0.13	Salivary Gland	7.42 ± 0.93	3.70 ± 0.29
Tumor	3.56 ± 0.34	3.15 ± 0.54	Tumor	6.56 ± 1.32	5.20 ± 0.37
Muscle	0.87 ± 0.16	0.8325 ± 0.14	Muscle	0.82 ± 0.13	0.93 ± 0.09
Organ	**PET ROI quantification at 12 h after injection (%ID/g ± SD)**		**Organ**	**PET ROI quantification at 120 h after injection (%ID/g ± SD)**	
	^{89}Zr-Df-nivolumab – PBL	^{89}Zr-Df-nivolumab – NSG		^{89}Zr-Df-nivolumab – PBL	^{89}Zr-Df-nivolumab – NSG
Blood	12.08 ± 0.94	9.88 ± 0.62	Blood	3.58 ± 0.56	2.88 ± 0.53
Liver	8.60 ± 0.62	7.10 ± 0.48	Liver	5.94 ± 0.72	6.73 ± 0.83
Spleen	6.62 ± 0.64	6.75 ± 0.41	Spleen	4.62 ± 0.34	7.95 ± 0.50
Kidney	5.72 ± 0.78	5.60 ± 0.20	Kidney	3.74 ± 0.57	5.50 ± 0.43
Salivary Gland	5.96 ± 1.00	4.35 ± 0.33	Salivary Gland	8.20 ± 0.35	3.63 ± 0.21
Tumor	4.00 ± 0.35	4.00 ± 0.52	Tumor	6.74 ± 1.11	4.70 ± 0.49
Muscle	0.81 ± 0.14	0.92 ± 0.15	Muscle	0.74 ± 0.03	0.78 ± 0.10

Organ	PET ROI quantification at 24 h after injection (%ID/g ± SD)		Organ	PET ROI quantification at 168 h after injection (%ID/g ± SD)	
	^{89}Zr-Df-nivolumab – PBL	^{89}Zr-Df-nivolumab – NSG		^{89}Zr-Df-nivolumab – PBL	^{89}Zr-Df-nivolumab – NSG
Blood	8.10 ± 0.51	7.38 ± 0.48	Blood	2.70 ± 0.42	1.88 ± 0.10
Liver	6.42 ± 1.39	6.35 ± 0.41	Liver	5.78 ± 0.96	6.63 ± 0.79
Spleen	5.84 ± 0.55	7.48 ± 0.36	Spleen	4.32 ± 0.40	7.48 ± 0.47
Kidney	5.00 ± 0.82	5.05 ± 0.48	Kidney	4.50 ± 0.53	5.35 ± 0.77
Salivary Gland	6.04 ± 0.67	3.98 ± 0.33	Salivary Gland	8.38 ± 0.98	3.30 ± 0.22
Tumor	4.64 ± 0.26	5.00 ± 0.48	Tumor	8.96 ± 3.09	3.88 ± 0.38
Muscle	0.90 ± 0.22	1.00 ± 0.18	Muscle	0.96 ± 0.15	0.69 ± 0.14

Table V. ^{89}Zr-Df-IgG PET Quantification. *Longitudinal analysis of control tracer accumulation in PD-1 TIL imaging study; n=4.*

Organ	**PET ROI quantification at 3 h after injection (%ID/g ± SD)** ^{89}Zr-Df-IgG - PBL	**Organ**	**PET ROI quantification at 48 h after injection (%ID/g ± SD)** ^{89}Zr-Df-IgG - PBL
Blood	12.98 ± 0.46	Blood	6.13 ± 1.04
Liver	12.63 ± 0.60	Liver	14.08 ± 1.80
Spleen	3.73 ± 0.32	Spleen	3.70 ± 0.26
Kidney	5.13 ± 0.54	Kidney	5.73 ± 0.71
Salivary Gland	3.23 ± 0.55	Salivary Gland	4.05 ± 0.42
Tumor	0.74 ± 0.32	Tumor	3.00 ± 0.48
Muscle	0.79 ± 0.14	Muscle	0.95 ± 0.04
Organ	**PET ROI quantification at 6 h after injection (%ID/g ± SD)** ^{89}Zr-Df-IgG – PBL	**Organ**	**PET ROI quantification at 72 h after injection (%ID/g ± SD)** ^{89}Zr-Df-IgG – PBL
Blood	12.53 ± 1.40	Blood	4.63 ± 0.79
Liver	13.53 ± 0.66	Liver	13.80 ± 1.79
Spleen	4.28 ± 0.53	Spleen	4.30 ± 1.06
Kidney	5.40 ± 0.35	Kidney	5.28 ± 0.43
Salivary Gland	3.58 ± 0.68	Salivary Gland	5.15 ± 0.93
Tumor	1.33 ± 0.33	Tumor	3.08 ± 0.40
Muscle	0.90 ± 0.18	Muscle	0.80 ± 0.23
Organ	**PET ROI quantification at 12 h after injection (%ID/g ± SD)** ^{89}Zr-Df-IgG – PBL	**Organ**	**PET ROI quantification at 120 h after injection (%ID/g ± SD)** ^{89}Zr-Df-IgG – PBL
Blood	11.43 ± 1.03	Blood	2.43 ± 0.15
Liver	15.30 ± 1.43	Liver	12.23 ± 1.18
Spleen	4.60 ± 0.78	Spleen	3.78 ± 0.43
Kidney	5.43 ± 0.45	Kidney	4.65 ± 0.68
Salivary Gland	3.73 ± 0.36	Salivary Gland	5.15 ± 0.87
Tumor	2.23 ± 0.10	Tumor	3.03 ± 0.49
Muscle	0.92 ± 0.06	Muscle	0.65 ± 0.10

Organ	**PET ROI quantification at 24 h after injection (%ID/g ± SD)** ^{89}Zr-Df-IgG – PBL	**Organ**	**PET ROI quantification at 168 h after injection (%ID/g ± SD)** ^{89}Zr-Df-IgG – PBL
Blood	8.65 ± 0.84	Blood	1.85 ± 0.55
Liver	13.33 ± 0.93	Liver	13.00 ± 1.54
Spleen	4.23 ± 0.21	Spleen	3.05 ± 0.79
Kidney	7.08 ± 2.01	Kidney	5.70 ± 1.07
Salivary Gland	4.28 ± 0.59	Salivary Gland	4.65 ± 0.39
Tumor	2.93 ± 0.36	Tumor	2.85 ± 0.39
Muscle	0.73 ± 0.17	Muscle	0.91 ± 0.21

Table VI. H460 PD-L1 PET Quantification. *Results of PET quantification following injection of ^{89}Zr-Df-atezolizumab in H460-bearing mice; n=3-5.*

PET ROI Quantification at 1 h after injection (%ID/g ± SD)			
Organ	**Non-irradiated**	**5 Gy x 1 Fx**	**2 Gy x 5 Fx**
Blood	12.73 ± 0.96	13.12 ± 2.20	18.64 ± 2.78
Liver	10.13 ± 0.42	9.70 ± 0.98	13.64 ± 1.60
Spleen	17.20 ± 5.18	14.86 ± 3.41	16.98 ± 1.15
Muscle	1.03 ± 0.24	0.89 ± 0.30	0.86 ± 0.27
H460 Tumor	0.69 ± 0.27	1.16 ± 0.43	1.48 ± 0.47
Brain	0.93 ± 0.04	1.00 ± 0.12	1.58 ± 0.27
PET ROI Quantification at 6 h after injection (%ID/g ± SD)			
Organ	**Non-irradiated**	**5 Gy x 1 Fx**	**2 Gy x 5 Fx**
Blood	5.95 ± 1.34	5.62 ± 0.96	11.66 ± 3.35
Liver	6.80 ± 0.80	6.96 ± 0.62	10.08 ± 1.74
Spleen	16.70 ± 4.42	15.84 ± 3.25	17.68 ± 1.95
Muscle	1.58 ± 0.11	1.66 ± 0.14	1.46 ± 0.40
H460 Tumor	1.63 ± 0.38	2.07 ± 1.08	3.06 ± 1.14
Brain	0.58 ± 0.09	0.56 ± 0.05	1.04 ± 0.20
Lymph node	9.15 ± 1.14	7.20 ± 0.78	8.76 ± 0.89
PET ROI Quantification at 12 h after injection (%ID/g ± SD)			
Organ	**Non-irradiated**	**5 Gy x 1 Fx**	**2 Gy x 5 Fx**
Blood	3.98 ± 0.66	3.90 ± 0.75	9.06 ± 2.86
Liver	6.03 ± 0.98	6.20 ± 0.53	9.14 ± 1.32
Spleen	16.23 ± 5.72	16.50 ± 3.85	15.44 ± 2.20
Muscle	1.45 ± 0.18	1.61 ± 0.51	1.60 ± 0.30
H460 Tumor	1.95 ± 0.59	2.50 ± 1.24	3.92 ± 1.52
Brain	0.47 ± 0.04	0.46 ± 0.04	0.92 ± 0.31
Lymph node	10.80 ± 1.23	8.76 ± 1.21	9.66 ± 0.80
PET ROI Quantification at 24 h after injection (%ID/g ± SD)			
Organ	**Non-irradiated**	**5 Gy x 1 Fx**	**2 Gy x 5 Fx**
Blood	2.08 ± 0.15	1.86 ± 0.21	5.28 ± 1.90
Liver	5.68 ± 1.07	5.66 ± 0.34	7.38 ± 0.84
Spleen	18.00 ± 5.38	16.66 ± 3.01	18.36 ± 2.12
Muscle	1.27 ± 0.20	1.46 ± 0.62	1.52 ± 0.29
H460 Tumor	2.10 ± 0.52	2.44 ± 1.18	4.44 ± 1.53
Brain	0.44 ± 0.03	0.42 ± 0.12	0.61 ± 0.13
Lymph node	12.55 ± 1.63	8.52 ± 1.52	11.82 ± 0.56

PET ROI Quantification at 48 h after injection (%ID/g ± SD)			
Organ	**Non-irradiated**	**5 Gy x 1 Fx**	**2 Gy x 5 Fx**
Blood	1.60 ± 0.21	1.44 ± 0.10	2.38 ± 0.61
Liver	5.43 ± 0.89	5.64 ± 0.29	6.48 ± 0.64
Spleen	16.90 ± 3.14	16.00 ± 3.84	17.90 ± 3.21
Muscle	0.97 ± 0.16	1.28 ± 0.62	1.27 ± 0.32
H460 Tumor	2.03 ± 0.44	2.50 ± 1.08	4.44 ± 1.34
Brain	0.37 ± 0.04	0.29 ± 0.04	0.52 ± 0.14
Lymph node	12.75 ± 2.02	8.30 ± 1.93	11.44 ± 0.96
PET ROI Quantification at 72 h after injection (%ID/g ± SD)			
Organ	**Non-irradiated**	**5 Gy x 1 Fx**	**2 Gy x 5 Fx**
Blood	1.23 ± 0.04	1.06 ± 0.08	1.76 ± 0.39
Liver	5.43 ± 1.17	5.44 ± 0.41	6.24 ± 0.70
Spleen	19.23 ± 5.67	17.12 ± 4.65	21.04 ± 4.33
Muscle	0.88 ± 0.25	1.02 ± 0.45	1.20 ± 0.25
H460 Tumor	2.03 ± 0.33	2.24 ± 0.90	4.08 ± 1.23
Brain	0.28 ± 0.03	0.24 ± 0.04	0.38 ± 0.14
Lymph node	11.65 ± 1.28	7.68 ± 1.60	10.96 ± 1.53
PET ROI Quantification at 96 h after injection (%ID/g ± SD)			
Organ	**Non-irradiated**	**5 Gy x 1 Fx**	**2 Gy x 5 Fx**
Blood	0.88 ± 0.07	0.80 ± 0.11	1.34 ± 0.27
Liver	6.03 ± 1.09	5.92 ± 0.50	6.32 ± 0.76
Spleen	18.55 ± 3.95	18.04 ± 3.43	19.32 ± 3.03
Muscle	0.72 ± 0.20	0.79 ± 0.34	1.13 ± 0.33
H460 Tumor	1.68 ± 0.33	2.04 ± 0.77	4.04 ± 1.26
Brain	0.38 ± 0.33	0.26 ± 0.06	0.44 ± 0.19
Lymph node	12.03 ± 1.50	8.16 ± 2.07	10.82 ± 1.07

Table VII. A549 PD-L1 PET Quantification. *Results of PET quantification following injection of ^{89}Zr-Df-atezolizumab in A549-bearing mice; n=4.*

PET ROI Quantification at 1 h after injection (%ID/g ± SD)			
Organ	**Non-irradiated**	**5 Gy x 1 Fx**	**2 Gy x 5 Fx**
Blood	12.03 ± 0.58	11.82 ± 2.36	17.13 ± 2.18
Liver	9.80 ± 0.78	9.28 ± 0.57	11.95 ± 0.92
Spleen	14.10 ± 3.79	16.38 ± 2.60	12.85 ± 1.01
Muscle	1.10 ± 0.21	0.81 ± 0.28	0.89 ± 0.21
A549 Tumor	1.06 ± 0.31	1.45 ± 0.57	1.23 ± 0.34
Brain	0.92 ± 0.06	0.93 ± 0.17	1.15 ± 0.11
PET ROI Quantification at 6 h after injection (%ID/g ± SD)			
Organ	**Non-irradiated**	**5 Gy x 1 Fx**	**2 Gy x 5 Fx**
Blood	5.90 ± 1.42	6.10 ± 1.48	8.20 ± 0.92
Liver	6.58 ± 0.69	7.14 ± 0.29	14.10 ± 1.34
Spleen	14.18 ± 4.47	15.12 ± 3.80	12.83 ± 0.90
Muscle	1.22 ± 0.19	1.30 ± 0.28	1.03 ± 0.25
A549 Tumor	1.85 ± 0.43	1.64 ± 0.81	1.43 ± 0.19
Brain	0.55 ± 0.11	0.63 ± 0.03	0.70 ± 0.11
Lymph node	7.88 ± 1.34	7.12 ± 0.87	6.63 ± 1.97
PET ROI Quantification at 12 h after injection (%ID/g ± SD)			
Organ	**Non-irradiated**	**5 Gy x 1 Fx**	**2 Gy x 5 Fx**
Blood	3.93 ± 1.03	3.90 ± 0.78	4.50 ± 0.39
Liver	5.70 ± 0.86	6.32 ± 0.22	14.03 ± 1.19
Spleen	13.70 ± 4.93	15.54 ± 4.39	14.05 ± 1.99
Muscle	1.22 ± 0.27	1.18 ± 0.12	1.02 ± 0.17
A549 Tumor	2.38 ± 0.67	2.02 ± 0.87	1.24 ± 0.24
Brain	0.44 ± 0.08	0.51 ± 0.04	0.53 ± 0.10
Lymph node	8.68 ± 1.05	8.64 ± 1.10	8.78 ± 0.86

PET ROI Quantification at 24 h after injection (%ID/g ± SD)			
Organ	**Non-irradiated**	**5 Gy x 1 Fx**	**2 Gy x 5 Fx**
Blood	2.08 ± 0.54	2.16 ± 0.12	1.98 ± 0.13
Liver	5.50 ± 0.92	5.88 ± 0.32	11.75 ± 0.69
Spleen	15.18 ± 5.07	14.94 ± 4.27	15.75 ± 1.93
Muscle	1.06 ± 0.25	1.08 ± 0.28	0.93 ± 0.23
A549 Tumor	2.13 ± 0.81	2.10 ± 0.97	1.64 ± 0.65
Brain	0.36 ± 0.05	0.40 ± 0.04	0.44 ± 0.05
Lymph node	10.50 ± 2.17	10.02 ± 1.36	8.93 ± 1.59
PET ROI Quantification at 48 h after injection (%ID/g ± SD)			
Organ	**Non-irradiated**	**5 Gy x 1 Fx**	**2 Gy x 5 Fx**
Blood	1.40 ± 0.32	1.52 ± 0.25	1.10 0.14
Liver	5.30 ± 0.84	5.88 ± 0.34	10.83 ± 0.79
Spleen	14.25 ± 3.39	15.02 ± 3.75	15.08 ± 1.79
Muscle	0.93 ± 0.17	1.11 ± 0.25	0.80 ± 0.10
A549 Tumor	2.35 ± 0.63	1.92 ± 0.57	1.28 ± 0.47
Brain	0.30 ± 0.06	0.38 ± 0.07	0.32 ± 0.05
Lymph node	9.94 ± 2.49	10.08 ± 2.66	8.15 ± 2.06
PET ROI Quantification at 72 h after injection (%ID/g ± SD)			
Organ	**Non-irradiated**	**5 Gy x 1 Fx**	**2 Gy x 5 Fx**
Blood	1.18 ± 0.24	1.28 ± 0.31	0.87 ± 0.16
Liver	5.18 ± 0.89	5.92 ± 0.46	10.30 ± 0.95
Spleen	15.45 ± 4.00	15.06 ± 3.84	15.05 ± 2.51
Muscle	0.73 ± 0.17	0.81 ± 0.20	0.65 ± 0.06
A549 Tumor	2.30 ± 0.51	1.70 ± 0.72	1.45 ± 0.45
Brain	0.22 ± 0.03	0.37 ± 0.05	0.34 ± 0.05
Lymph node	10.10 ± 3.25	10.72 ± 3.07	8.18 ± 2.48

PET ROI Quantification at 96 h after injection (%ID/g ± SD)			
Organ	**Non-irradiated**	**5 Gy x 1 Fx**	**2 Gy x 5 Fx**
Blood	0.93 ± 0.17	0.83 ± 0.14	0.85 ± 0.07
Liver	5.60 ± 0.89	6.08 ± 0.49	10.63 ± 0.69
Spleen	16.03 ± 3.89	15.30 ± 4.53	15.25 ± 2.12
Muscle	0.62 ± 0.16	0.60 ± 0.14	0.65 ± 0.14
A549 Tumor	1.95 ± 0.41	1.37 ± 0.35	1.36 ± 0.31
Brain	0.37 ± 0.20	0.28 ± 0.04	0.28 ± 0.06
Lymph node	10.03 ± 1.64	9.60 ± 1.73	8.20 ± 1.60

Table VIII. Athymic PD-L1 Fab PET Quantification; *n=3-4.*

PET ROI Quantification at 5 min after injection (%ID/g ± SD)			
Organ	**^{64}Cu-NOTA-αPD-L1**	**^{64}Cu-NOTA-αPD-L1 + blocking**	**^{64}Cu-NOTA-αHer-2**
Heart	9.55 ± 5.25	13.88 ± 2.53	14.20 ± 4.22
Liver	9.65 ± 0.25	7.98 ± 1.39	8.90 ± 3.31
Kidney	35.4 ± 19.2	44.23 ± 9.48	42.13 ± 8.77
Spleen	8.55 ± 0.25	4.83 ± 0.08	5.77 ± 1.64
Muscle	0.96 ± 0.25	0.89 ± 0.09	0.78 ± 0.23
Brown Fat	4.90 ± 0.3	3.05 ± 0.51	3.00 ± 0.36
PET ROI Quantification at 15 min after injection (%ID/g ± SD)			
Organ	**^{64}Cu-NOTA-αPD-L1**	**^{64}Cu-NOTA-αPD-L1 + blocking**	**^{64}Cu-NOTA-αHer-2**
Heart	4.73 ± 1.93	9.53 ± 1.92	7.00 ± 2.11
Liver	8.35 ± 2.61	5.48 ± 0.57	5.20 ± 1.48
Kidney	47.00 ± 30.20	53.70 ± 6.08	60.57 ± 24.81
Spleen	9.63 ± 3.95	3.93 ± 0.26	3.07 ± 0.80
Muscle	0.98 ± 0.32	0.72 ± 0.14	0.49 ± 0.18
Brown Fat	5.70 ± 2.15	2.13 ± 0.40	1.83 ± 0.25
PET ROI Quantification at 45 min after injection (%ID/g ± SD)			
Organ	**^{64}Cu-NOTA-αPD-L1**	**^{64}Cu-NOTA-αPD-L1 + blocking**	**^{64}Cu-NOTA-αHer-2**
Heart	2.89 ± 1.13	4.35 ± 2.61	3.90 ± 0.94
Liver	6.62 ± 2.63	3.10 ± 1.91	3.13 ± 0.62
Kidney	54.87 ± 34.59	70.40 ± 16.45	73.20 ± 25.69
Spleen	9.88 ± 3.39	2.24 ± 1.26	2.30 ± 0.37
Muscle	0.91 ± 0.26	0.50 ± 0.12	0.41 ± 0.10
Brown Fat	5.37 ± 2.00	1.58 ± 0.36	1.63 ± 0.12

Table IX. C57/BL6 PD-L1 Fab PET Quantification; *n=3.*

PET ROI Quantification at 5 min after injection (%ID/g ± SD)		
Organ	**^{64}Cu-NOTA-αPD-L1**	**^{64}Cu-NOTA-αHer-2**
Heart	13.90 ± 1.94	19.83 ± 2.29
Liver	12.20 ± 2.79	12.30 ± 1.34
Kidney	53.77 ± 0.60	57.77 ± 6.24
Spleen	14.87 ± 4.96	8.77 ± 0.90
Muscle	1.47 ± 0.25	1.13 ± 0.05
Brown Fat	7.57 ± 2.00	2.73 ± 0.70
PET ROI Quantification at 15 min after injection (%ID/g ± SD)		
Organ	**^{64}Cu-NOTA-αPD-L1**	**^{64}Cu-NOTA-αHer-2**
Heart	7.90 ± 1.13	10.13 ± 1.25
Liver	9.20 ± 2.98	6.50 ± 0.71
Kidney	71.97 ± 11.97	82.23 ± 9.51
Spleen	13.07 ± 6.33	5.67 ± 1.32
Muscle	1.30 ± 0.22	0.81 ± 0.11
Brown Fat	6.80 ± 1.59	1.97 ± 0.34
PET ROI Quantification at 45 min after injection (%ID/g ± SD)		
Organ	**^{64}Cu-NOTA-αPD-L1**	**^{64}Cu-NOTA-αHer-2**
Heart	5.43 ± 1.15	6.00 ± 1.14
Liver	8.13 ± 3.46	4.30 ± 0.71
Kidney	81.97 ± 14.68	103.90 ± 13.83
Spleen	12.60 ± 5.45	3.73 ± 0.76
Muscle	1.29 ± 0.23	0.69 ± 0.13
Brown Fat	6.17 ± 1.73	1.87 ± 0.25

PET ROI Quantification at 90 min after injection (%ID/g ± SD)		
Organ	**^{64}Cu-NOTA-αPD-L1**	**^{64}Cu-NOTA-αHer-2**
Heart	2.83 ± 0.65	1.63 ± 0.26
Liver	6.10 ± 2.43	2.03 ± 0.21
Kidney	79.70 ± 15.90	99.00 ± 6.80
Spleen	9.43 ± 3.94	2.33 ± 0.76
Muscle	1.10 ± 0.29	0.51 ± 0.11
Brown Fat	5.93 ± 1.32	1.20 ± 0.16

Appendix 2

Biodistribution study results

Table I. CTLA-4 tumor imaging biodistribution results with ^{64}Cu-DOTA-ipilimumab; *n=3-4.*

	Biodistribution at 48 h after injection (%ID/g ± SD)			
Organ	**A549**	**A549 Blocked**	**H460**	**H358**
Blood	13.85 ± 6.08	12.52 ± 1.97	13.13± 2.48	11.56± 1.16
Skin	4.85 ± 3.45	3.13 ± 0.79	3.50± 1.44	3.80± 0.71
Muscle	0.51 ± 0.20	0.62 ± 0.27	0.67± 0.14	0.55± 0.36
Bone	2.37 ± 1.19	1.13 ± 0.14	1.65± 0.32	1.34± 1.04
Heart	2.92 ± 1.50	3.86 ± 0.16	2.87± 1.22	3.15± 2.19
Lung	3.01 ± 2.16	5.10 ± 2.25	3.22± 0.66	2.59± 1.20
Liver	10.24 ± 2.66	5.53 ± 0.35	4.79± 1.29	5.30± 2.37
Kidney	3.24 ± 1.20	4.27 ± 1.09	3.60± 1.25	2.79± 0.29
Spleen	4.24 ± 0.67	3.49 ± 0.35	2.08± 0.63	1.36± 0.38
Pancreas	0.82 ± 0.54	0.70 ± 0.22	0.84± 0.16	0.82± 0.63
Stomach	1.20 ± 0.31	1.70 ± 0.25	1.47± 0.43	1.41± 0.92
Intestine	2.09 ± 1.02	1.64 ± 0.70	1.01± 0.22	1.09± 0.13
Tumor	9.46 ± 2.39	6.80 ± 0.54	7.64± 1.17	4.59± 1.33
Tail	3.96 ± 1.07	2.14 ± 0.48	2.38± 0.16	1.78± 0.55
Brain	0.22 ± 0.07	0.43 ± 0.13	0.22± 0.02	0.23± 0.15

Table II. CTLA-4 T-cell biodistribution results; *n=3-6.*

	Biodistribution at 48 h after injection (%ID/g ± SD)				
Organ	**^{64}Cu-NOTA-ipilimumab - PBL**	**^{64}Cu-NOTA-ipilimumab - NBSGW**	**^{64}Cu-NOTA-ipilimumab-F(ab')$_2$ - PBL**	**^{64}Cu-NOTA-ipilimumab-F(ab')$_2$ - NBSGW**	**^{64}Cu-NOTA-IgG - PBL**
Blood	6.17 ± 2.17	7.17 ± 2.16	0.63± 0.11	0.68± 0.04	12.21± 0.48
Skin	5.89 ± 1.48	2.09 ± 0.09	1.07± 0.51	0.68± 0.05	6.31± 1.02
Muscle	0.71 ± 0.25	0.78 ± 0.18	0.17± 0.03	0.17± 0.03	0.84± 0.32
Bone	0.91 ± 0.36	9.93 ± 0.45	0.41± 0.14	0.70± 0.31	1.06± 0.17
Heart	2.00 ± 0.65	3.02 ± 0.61	0.78± 0.12	0.71± 0.01	3.29± 0.15
Lung	5.74 ± 0.94	5.27 ± 1.00	1.99± 0.63	1.30± 0.05	4.79± 0.30
Liver	4.87 ± 1.78	10.92 ± 1.88	3.77± 0.45	3.27± 0.29	9.09± 1.44
Kidney	3.30 ± 0.97	3.99 ± 0.81	35.63± 4.87	18.03± 2.90	3.78± 0.37
Spleen	8.89 ± 3.51	84.57 ± 13.30	2.47 ± 0.87	3.12± 1.25	3.73± 0.10
Pancreas	0.83 ± 0.35	1.31 ± 0.02	0.49± 0.13	0.34± 0.01	1.61± 0.37
Stomach	1.15 ± 0.38	3.04 ± 0.24	0.84± 0.14	0.68± 0.12	1.45± 0.15
Intestine	0.95 ± 0.22	7.16 ± 1.60	0.67± 0.05	0.85± 0.05	1.30± 0.18
Salivary Gland	6.27 ± 2.14	5.53 ± 0.18	1.53± 0.65	0.56± 0.02	3.43± 0.28
Tail	2.31 ± 0.68	1.90 ± 0.36	2.63± 1.58	0.87± 0.19	2.18± 0.89
Brain	0.32 ± 0.14	0.29 ± 0.01	0.10± 0.05	0.07± 0.02	0.52± 0.16

Table III. ^{89}Zr-Df-nivolumab TIL biodistribution study; n=4.

Biodistribution at 168 h after injection (%ID/g ± SD)			
Organ	**PBL**	**^{89}Zr-Df-IgG- PBL**	**NSG**
Blood	2.22 ± 0.60	1.33 ± 0.88	0.56 ± 0.06
Skin	3.23 ± 0.52	2.38 ± 0.40	1.92 ± 0.15
Muscle	0.46 ± 0.31	0.28 ± 0.06	0.38 ± 0.12
Bone	1.44 ± 0.51	1.53 ± 0.34	5.84 ± 2.24
Heart	2.19 ± 0.30	1.67 ± 0.97	0.87 ± 0.15
Lung	3.26 ± 1.19	0.91 ± 0.32	0.89 ± 0.44
Liver	2.59 ± 0.21	5.79 ± 3.00	8.12 ± 3.79
Kidney	2.37 ± 0.83	2.29 ± 0.83	0.99 ± 0.37
Spleen	3.22 ± 0.54	1.44 ± 0.37	37.90± 10.37
Pancreas	0.74 ± 0.29	0.38 ± 0.11	0.30 ± 0.04
Stomach	0.80 ± 0.35	0.70 ± 0.16	0.47 ± 0.12
Intestine	0.81 ± 0.33	0.67 ± 0.11	1.25 ± 0.54
Tumor	5.54 ± 0.96	0.75 ± 0.21	2.94 ± 0.58
Tail	0.70 ± 0.09	1.20 ± 0.57	0.90 ± 0.17
Brain	0.08 ± 0.01	0.05 ± 0.03	0.05 ± 0.01
Salivary Gland	5.52 ± 1.46	2.18 ± 0.63	5.36 ± 7.52

Table IV. C57/BL6 Biodistribution Study. *Ex vivo gamma counting biodistribution results in C57/BL6 mice with the PD-L1 Fab-based tracers; n=3.*

Biodistribution at 90 min after injection (%ID/g ± SD)		
Organ	**^{64}Cu-NOTA-αPD-L1**	**^{64}Cu-NOTA-αHer-2**
Blood	1.27 ± 0.09	0.81 ± 0.10
Skin	0.71 ± 0.01	0.79 ± 0.08
Muscle	0.71 ± 0.24	0.30 ± 0.04
Bone	1.50 ± 0.64	0.77 ± 0.05
Heart	3.63 ± 1.03	1.53 ± 0.16
Lung	5.02 ± 0.29	1.80 ± 0.31
Liver	6.04 ± 2.44	2.11 ± 0.28
Kidney	157.91 ± 26.58	218.71 ± 28.30
Spleen	20.63 ± 10.40	2.73 ± 0.29
Pancreas	0.75 ± 0.10	0.49 ± 0.13
Stomach	1.47 ± 0.12	0.98 ± 0.19
Intestine	3.25 ± 0.12	0.92 ± 0.19
Brown Fat	4.47 ± 1.46	0.87 ± 0.19
Tail	3.18 ± 1.43	3.44 ± 0.26
Brain	0.11 ± 0.05	0.04 ± 0.01

Table V. H460 Atezolizumab Biodistribution Study. *Ex vivo gamma counting biodistribution studies following injection of ^{89}Zr-Df-atezolizumab; n=3-5.*

Biodistribution at 96 h after injection (%ID/g ± SD)			
Organ	**Non-irradiated**	**5 Gy x 1 Fx**	**2 Gy x 5 Fx**
Blood	0.64 ± 0.37	0.41 ± 0.11	0.76 ± 0.13
Skin	2.32 ± 0.70	1.77 ± 0.16	2.52 ± 1.05
Muscle	0.72 ± 0.42	0.50 ± 0.10	0.51 ± 0.25
Bone	1.54 ± 0.31	2.06 ± 0.24	4.39 ± 1.79
Heart	1.22 ± 0.07	1.07 ± 0.20	1.11 ± 0.15
Lung	3.59 ± 0.60	2.60 ± 0.57	1.94 ± 0.24
Liver	7.28 ± 1.36	7.97 ± 0.31	7.33 ± 1.39
Kidney	3.45 ± 0.76	2.76 ± 0.35	3.69 ± 0.73
Spleen	34.69 ± 7.88	33.32 ± 18.20	38.21 ± 10.20
Pancreas	0.65 ± 0.15	0.51 ± 0.13	0.47 ± 0.14
Stomach	1.11 ± 0.14	0.99 ± 0.20	2.14 ± 1.42
Intestine	2.20 ± 0.85	2.72 ± 1.12	2.50 ± 0.95
H460 Tumor	1.51 ± 0.61	2.18 ± 0.80	3.38 ± 0.66
Tail	2.58 ± 0.51	2.38 ± 0.79	3.21 ± 1.00
Brain	0.11 ± 0.01	0.16 ± 0.05	0.17 ± 0.04
Lymph node	23.05 ± 3.02	24.04 ± 13.84	13.13 ± 0.32

Appendix 3

Dosimetric extrapolation data

Table I. CTLA-4 T-cell dosimetry. *Dosimetric extrapolation of various CTLA-4 imaging agents and controls to an adult human female, using data from PET ROI analysis; n=3-6.*

Effective dose (µSv/MBq)	PBL			NBSGW	
	^{64}Cu-NOTA-ipilimumab	^{64}Cu-NOTA-ipilimumab-F(ab')$_2$	^{64}Cu-NOTA-IgG	^{64}Cu-NOTA-ipilimumab	^{64}Cu-NOTA-ipilimumab-F(ab')$_2$
Adrenals	0.18± 0.01	0.13± 0.04	0.17± 0.01	0.18± 0.01	0.11± 0.04
Brain	0.07± 0.01	0.04± 0.01	0.07± 0.01	0.07± 0.01	0.03± 0.01
Breasts	1.42± 0.06	1.18± 0.02	1.30± 0.01	1.31± 0.03	1.28± 0.01
LLI Wall	4.09± 0.18	3.76± 0.06	3.73± 0.03	3.73± 0.13	3.94± 0.04
Small Intestine	0.16± 0.01	0.12± 0.04	0.15± 0.01	0.15± 0.01	0.10± 0.04
Stomach Wall	4.05± 0.12	3.46± 0.03	3.79± 0.01	3.87± 0.06	3.70± 0.02
ULI Wall	0.18± 0.01	0.12± 0.04	0.16± 0.01	0.16± 0.01	0.11± 0.04
Kidneys	0.25± 0.03	3.50± 2.77	0.34± 0.02	0.35± 0.04	3.53± 1.81
Liver	4.09± 0.83	3.54± 0.41	5.54± 0.30	6.56± 0.92	3.13± 0.23
Lungs	3.81± 0.10	3.18± 0.03	3.61± 0.02	3.65± 0.05	3.42± 0.02
Muscle	0.09± 0.01	0.05± 0.02	0.11± 0.01	0.10± 0.01	0.04± 0.01
Ovaries	6.73± 0.27	6.17± 0.09	6.19± 0.05	6.17± 0.19	6.45± 0.06
Pancreas	0.18± 0.01	0.13± 0.04	0.17± 0.01	0.18± 0.01	0.11± 0.04
Red Marrow	3.13± 0.11	2.73± 0.03	2.92± 0.02	2.93± 0.06	2.90± 0.02
Osteogenic Cells	0.64± 0.03	0.54± 0.01	0.58± 0.01	0.58± 0.02	0.59± 0.01
Skin	0.26± 0.01	0.22± 0.01	0.24± 0.01	0.24± 0.01	0.24± 0.01
Spleen	0.27± 0.07	0.14± 0.05	0.36± 0.04	0.67± 0.07	0.11± 0.04
Thymus	0.16± 0.01	0.10± 0.03	0.15± 0.01	0.15± 0.01	0.09± 0.03
Salivary Gland	17.75± 9.80	10.84± 2.84	15.45± 2.15	16.05± 0.75	6.78± 1.04
Urinary Bladder Wall	1.45± 0.06	13.40± 0.01	1.33± 0.01	1.33± 0.04	9.34± 0.70
Uterus	0.17± 0.01	0.13± 0.04	0.15± 0.01	0.15± 0.01	0.11± 0.04
Total Body Effective Dose (mSv/MBq)	49.13 ± 9.88	53.48 ± 2.80	46.50 ± 2.40	48.55 ± 1.15	46.10 ± 2.39

Table II. Pembrolizumab radiation dosimetry. *Results of dosimetric extrapolation to an adult human female following injection of ^{89}Zr-Df-pembrolizumab; n=4.*

Organ	PBL Mice (mGy/MBq)	NSG Mice (mGy/MBq)
Adrenals	0.028 ± 0.001	0.028 ± 0.001
Brain	0.249 ± 0.005	0.245 ± 0.006
Breasts	0.185 ± 0.001	0.185 ± 0.002
Small Intestine	0.025 ± 0.001	0.025 ± 0.001
Stomach Wall	0.630 ± 0.004	0.630 ± 0.005
Kidneys	0.030 ± 0.001	0.035 ± 0.001
Liver	1.207 ± 0.022	1.196 ± 0.061
Lungs	0.556 ± 0.004	0.562 ± 0.003
Muscle	0.019 ± 0.001	0.019 ± 0.001
Ovaries	1.591 ± 0.006	1.594 ± 0.013
Pancreas	0.029 ± 0.001	0.029 ± 0.001
Red Marrow	0.533 ± 0.003	0.533 ± 0.004
Skin	0.373 ± 0.002	0.373 ± 0.003
Spleen	0.030 ± 0.001	0.028 ± 0.007
Thymus	0.024 ± 0.001	0.024 ± 0.013
Salivary Glands	1.246 ± 0.082	0.838 ± 0.004
Urinary Bladder Wall	0.573 ± 0.004	0.574 ± 0.001
Uterus	0.026 ± 0.001	0.026 ± 0.001
Total Body Effective Dose (mSv/MBq)	0.597 ± 0.005	0.581 ± 0.003

Table III. Nivolumab dosimetric extrapolation. *Estimated radiation absorbed doses to an adult human after intravenous injection of ^{89}Zr-Df-nivolumab in PBL and NSG mice, along with ^{89}Zr-Df-IgG in PBL mice (n = 4).*

Organ	^{89}Zr-Df-nivolumab in NSG (mGy/MBq)	^{89}Zr-Df-nivolumab in PBL (mGy/MBq)	^{89}Zr-Df-IgG in PBL (mGy/MBq)
Adrenals	0.013 ± 0.001	0.012 ± 0.001	0.015 ± 0.001
Brain	0.064 ± 0.005	0.058 ± 0.005	0.055 ± 0.002
Breasts	0.059 ± 0.004	0.056 ± 0.004	0.059 ± 0.001
Small Intestines	0.008 ± 0.001	0.008 ± 0.001	0.008 ± 0.001
Stomach Wall	0.231 ± 0.017	0.211 ± 0.017	0.231 ± 0.003
Kidneys	0.026 ± 0.004	0.020 ± 0.002	0.024 ± 0.001
Liver	0.973 ± 0.077	0.983 ± 0.121	1.708 ± 0.112
Lungs	0.209 ± 0.014	0.200 ± 0.016	0.228 ± 0.003
Muscle	0.007 ± 0.001	0.007 ± 0.001	0.007 ± 0.001
Ovaries	0.495 ± 0.037	0.452 ± 0.036	0.448 ± 0.013
Pancreas	0.013 ± 0.001	0.012 ± 0.001	0.014 ± 0.001
Red Marrow	0.177 ± 0.013	0.164 ± 0.013	0.171 ± 0.003
Skin	0.119 ± 0.009	0.111 ± 0.009	0.113 ± 0.003
Spleen	0.028 ± 0.002	0.021 ± 0.001	0.018 ± 0.001
Thymus	0.008 ± 0.001	0.008 ± 0.001	0.008 ± 0.001
Salivary Glands	0.844 ± 0.036	1.605 ± 0.154	0.999 ± 0.150
Urinary Bladder	0.180 ± 0.014	0.164 ± 0.013	0.160 ± 0.005
Uterus	0.008 ± 0.001	0.007 ± 0.001	0.007 ± 0.001
Total Body Effective Dose (mGy/MBq)	0.387 ± 0.032	0.309 ± 0.019	0.351 ± 0.018

Bibliography

1. Topalian Suzanne L, Drake Charles G, Pardoll Drew M. Immune checkpoint blockade: A common denominator approach to cancer therapy. *Cancer Cell.* 2015;27:450-461.

2. Larimer BM, Wehrenberg-Klee E, Caraballo A, Mahmood U. Quantitative CD3 PET imaging predicts tumor growth response to anti-CTLA-4 therapy. *J Nucl Med.* 2016;ePub ahead of print.

3. Natarajan A, Mayer AT, Xu L, Reeves RE, Gano J, Gambhir SS. Novel radiotracer for immunoPET imaging of PD-1 checkpoint expression on tumor infiltrating lymphocytes. *Bioconjug Chem.* 2015;26:2062-2069.

4. Maute RL, Gordon SR, Mayer AT, et al. Engineering high-affinity PD-1 variants for optimized immunotherapy and immuno-PET imaging. *Proc Natl Acad Sci U S A.* 2015;112:E6506-E6514.

5. Higashikawa K, Yagi K, Watanabe K, et al. (64)Cu-DOTA-Anti-CTLA-4 mAb enabled PET visualization of CTLA-4 on the T-cell infiltrating tumor tissues. *PLoS ONE.* 2014;9:e109866.

6. Alam IS, Mayer AT, Sagiv-Barfi I, et al. Imaging activated T cells predicts response to cancer vaccines. *The Journal of Clinical Investigation.* 2018;128:2569-2580.

7. Chatterjee S, Lesniak WG, Gabrielson M, et al. A humanized antibody for imaging immune checkpoint ligand PD-L1 expression in tumors. *Oncotarget.* 2016;7:10215-10227.

8. Hettich M, Braun F, Bartholoma MD, Schirmbeck R, Niedermann G. High-Resolution PET imaging with therapeutic antibody-based PD-1/PD-L1 checkpoint tracers. *Theranostics.* 2016;6:1629-1640.

9. Ehlerding EB, England CG, McNeel DG, Cai W. Molecular Imaging of Immunotherapy Targets in Cancer. *J Nucl Med.* 2016.

10. Ehlerding EB, Cai W. ImmunoPET: The future of response evaluation for cancer immunotherapy. In: Lopci E, Fanti S, eds. *Atlas of Response to Immunotherapy.* Vol In preparation.: Springer; 2018.

11. Cherry SRS, James A; Phelps, Michael E. *Physics in Nuclear Medicine.* Vol 4. Philadelphia, PA: Elsevier Saunders; 2012.

12. Orbay H, Bean J, Zhang Y, Cai W. Intraoperative Targeted Optical Imaging: A Guide towards Tumor-Free Margins in Cancer Surgery. *Current pharmaceutical biotechnology.* 2014;14:733-742.

13. Jodal L, Le Loirec C, Champion C. Positron range in PET imaging: non-conventional isotopes. *Phys Med Biol.* 2014;59:7419-7434.

14. Price EW, Orvig C. Matching chelators to radiometals for radiopharmaceuticals. *Chemical Society Reviews.* 2014;43:260-290.

15. Pardoll DM. The blockade of immune checkpoints in cancer immunotherapy. *Nat Rev Cancer.* 2012;12:252-264.

16. Decker WK, Safdar A. Bioimmunoadjuvants for the treatment of neoplastic and infectious disease: Coley's legacy revisited. *Cytokine & Growth Factor Reviews.* 2009;20:271-281.

17. Dunn GP, Bruce AT, Ikeda H, Old LJ, Schreiber RD. Cancer immunoediting: from immunosurveillance to tumor escape. *Nature Immunology.* 2002;3:991.

18. Yang Y. Cancer immunotherapy: harnessing the immune system to battle cancer. *The Journal of Clinical Investigation.* 2015;125:3335-3337.

19. Walker LSK, Sansom DM. Confusing signals: Recent progress in CTLA-4 biology. *Trends in Immunology.* 2015;36:63-70.

20. Camacho LH. CTLA-4 blockade with ipilimumab: biology, safety, efficacy, and future considerations. *Cancer Medicine.* 2015;4:661-672.

21. Korn EL, Liu P-Y, Lee SJ, et al. Meta-Analysis of Phase II Cooperative Group Trials in Metastatic Stage IV Melanoma to Determine Progression-Free and Overall Survival Benchmarks for Future Phase II Trials. *Journal of Clinical Oncology.* 2008;26:527-534.

22. Chen L, Han X. Anti–PD-1/PD-L1 therapy of human cancer: past, present, and future. *The Journal of Clinical Investigation.* 2015;125:3384-3391.

23. Hirano F, Kaneko K, Tamura H, et al. Blockade of B7-H1 and PD-1 by Monoclonal Antibodies Potentiates Cancer Therapeutic Immunity. *Cancer Research.* 2005;65:1089-1096.

24. Robert C, Ribas A, Wolchock JD, et al. Anti-programmed-death-receptor-1 treatment with pembrolizumab in ipilimumab-refractory advanced melanoma: a randomised dose-comparison cohort of a phase 1 trial. *Lancet.* 2014;384.

25. Buchbinder EI, Desai A. CTLA-4 and PD-1 pathways: similarities, differences, and implications of their inhibition. *Am J Clin Oncol.* 2016;39:98-106.

26. Villadolid J, Amin A. Immune checkpoint inhibitors in clinical practice: update on management of immune-related toxicities. *Translational Lung Cancer Research.* 2015;4:560-575.

27. Mahoney KM, Atkins MB. Prognostic and predictive markers for the new immunotherapies. *Oncology (Williston Park).* 2014;28 Suppl 3:39-48.

28. Halama N, Michel S, Kloor M, et al. Localization and density of immune cells in the invasive margin of human colorectal cancer liver metastases are prognostic for response to chemotherapy. *Cancer Res.* 2011;71:5670-5677.

29. Madore J, Vilain RE, Menzies AM, et al. PD-L1 expression in melanoma shows marked heterogeneity within and between patients: implications for anti-PD-1/PD-L1 clinical trials. *Pigment Cell Melanoma Res.* 2015;28:245-253.

30. Paulsen E-E, Kilvaer TK, Rakaee M, et al. CTLA-4 expression in the non-small cell lung cancer patient tumor microenvironment: diverging prognostic impact in primary tumors and lymph node metastases. *Cancer Immunology, Immunotherapy.* 2017;66:1449-1461.

31. Geynisman DM, Chien C-R, Smieliauskas F, Shen C, Shih Y-CT. Economic evaluation of therapeutic cancer vaccines and immunotherapy: A systematic review. *Hum Vaccin Immunother.* 2014;10:3415-3424.

32. Gilles R, de Geus-Oei L-F, Mulders PFA, Oyen WJG. Immunotherapy response evaluation with (18)F-FDG-PET in patients with advanced stage renal cell carcinoma. *World J Urol.* 2013;31:841-846.

33. Dimitrakopoulou-Strauss A. Monitoring of patients with metastatic melanoma treated with immune checkpoint inhibitors using PET–CT. *Cancer Immunology, Immunotherapy*. 2018.

34. Tsai KK, Pampaloni MH, Hope C, et al. Increased FDG avidity in lymphoid tissue associated with response to combined immune checkpoint blockade. *Journal for Immunotherapy of Cancer.* 2016;4:58.

35. Dercle L, Seban R-D, Lazarovici J, et al. 18F-FDG PET and CT Scans Detect New Imaging Patterns of Response and Progression in Patients with Hodgkin Lymphoma Treated by

Anti–Programmed Death 1 Immune Checkpoint Inhibitor. *Journal of Nuclear Medicine.* 2018;59:15-24.

36. Wolchok JD, Hoos A, O'Day S, et al. Guidelines for the evaluation of immune therapy activity in solid tumors: immune-related response criteria. *Clin Cancer Res.* 2009;15.

37. Dolan DE, Gupta S. PD-1 pathway inhibitors: changing the landscape of cancer immunotherapy. *Cancer Control.* 2014;21:231-237.

38. Kleffel S, Posch C, Barthel Steven R, et al. Melanoma Cell-Intrinsic PD-1 Receptor Functions Promote Tumor Growth. *Cell.* 2015;162:1242-1256.

39. Ivashko IN, Kolesar JM. Pembrolizumab and nivolumab: PD-1 inhibitors for advanced melanoma. *Am J Health Syst Pharm.* 2016;73:193-201.

40. Tan M, Quintal L. Pembrolizumab: a novel antiprogrammed death 1 (PD-1) monoclonal antibody for treatment of metastatic melanoma. *J Clin Pharm Ther.* 2015;40:504-507.

41. Topalian SL, Sznol M, McDermott DF, et al. Survival, durable tumor remission, and long-term safety in patients with advanced melanoma receiving Nivolumab. *J Clin Oncol.* 2014;32:1020-1030.

42. England CG, Jiang D, Ehlerding EB, et al. 89Zr-labeled nivolumab for imaging of T-cell infiltration in a humanized murine model of lung cancer. *European Journal of Nuclear Medicine and Molecular Imaging.* 2018;45:110-120.

43. Cole EL, Kim J, Donnelly DJ, et al. Radiosynthesis and preclinical PET evaluation of 89Zr-nivolumab (BMS-936558) in healthy non-human primates. *Bioorganic & Medicinal Chemistry.* 2017;25:5407-5414.

44. England CG, Ehlerding EB, Hernandez R, et al. Preclinical Pharmacokinetics and Biodistribution Studies of 89Zr-Labeled Pembrolizumab. *J Nucl Med.* 2017;58:162-168.

45. Natarajan A, Mayer AT, Reeves RE, Nagamine CM, Gambhir SS. Development of a novel immunoPET tracer to image human PD-1 checkpoint expression on tumor infiltrating lymphocytes in a humanized mouse model. *Molecular imaging and biology : MIB : the official publication of the Academy of Molecular Imaging.* 2017;19:903-914.

46. Natarajan A, Patel CB, Habte F, Gambhir SS. Dosimetry Prediction for Clinical Translation of (64)Cu-Pembrolizumab ImmunoPET Targeting Human PD-1 Expression. *Scientific Reports.* 2018;8:633.

47. Patel SP, Kurzrock R. PD-L1 expression as a predictive biomarker in cancer immunotherapy. *Mol Cancer Ther.* 2015;14:847-856.

48. Ahmad SM, Borch TH, Hansen M, Andersen MH. PD-L1-specific T cells. *Cancer Immunol Immunother.* 2016;65:1-8.

49. Herbst RS, Soria JC, Kowanetz M, et al. Predictive correlates of response to the anti-PD-L1 antibody MPDL3280A in cancer patients. *Nature.* 2014;515.

50. Heskamp S, Hobo W, Molkenboer-Kuenen JDM, et al. Noninvasive imaging of tumor PD-L1 expression using radiolabeled anti–PD-L1 antibodies. *Cancer Res.* 2015;75:2928-2936.

51. Josefsson A, Nedrow JR, Park S, et al. Imaging, biodistribution, and dosimetry of radionuclide-labeled PD-L1 antibody in an immunocompetent mouse model of breast cancer. *Cancer Res.* 2016;76:472-479.

52. Kikuchi M, Clump DA, Srivastava RM, et al. Preclinical immunoPET/CT imaging using Zr-89-labeled anti-PD-L1 monoclonal antibody for assessing radiation-induced PD-L1 upregulation in head and neck cancer and melanoma. *OncoImmunology.* 2017;6:e1329071.

53. Truillet C, Oh HLJ, Yeo SP, et al. Imaging PD-L1 Expression with ImmunoPET. *Bioconjugate Chemistry.* 2018;29:96-103.

54. Chatterjee S, Lesniak WG, Miller MS, et al. Rapid PD-L1 detection in tumors with PET using a highly specific peptide. *Biochemical and Biophysical Research Communications.* 2017;483:258-263.

55. Mayer AT, Natarajan A, Gordon S, et al. Practical ImmunoPET radiotracer design considerations for human immune checkpoint imaging. *Journal of Nuclear Medicine.* 2016.

56. Li D, Cheng S, Zou S, et al. Immuno-PET Imaging of 89Zr Labeled Anti-PD-L1 Domain Antibody. *Molecular Pharmaceutics.* 2018;15:1674-1681.

57. Buchbinder E, Hodi FS. Cytotoxic T lymphocyte antigen-4 and immune checkpoint blockade. *J Clin Invest.* 2015;125:3377-3383.

58. Antczak A, Pastuszak-Lewandoska D, Górski P, et al. CTLA-4 Expression and Polymorphisms in Lung Tissue of Patients with Diagnosed Non-Small-Cell Lung Cancer. *BioMed Res Int.* 2013;2013:576486.

59. Kim DW, Trinh VA, Hwu W-J. Ipilimumab in the treatment of advanced melanoma – a clinical update. *Expert Opin Biol Ther.* 2014;14:1709-1718.

60. Ribas A, Kefford R, Marshall MA, et al. Phase III randomized clinical trial comparing Tremelimumab with standard-of-care chemotherapy in patients with advanced melanoma. *J Clin Oncol.* 2013;31:616-622.

61. Wei W, Jiang D, Ehlerding EB, Luo Q, Cai W. Noninvasive PET Imaging of T cells. *Trends in Cancer.* 2018;4:359-373.

62. Wahid B, Ali A, Rafique S, et al. An overview of cancer immunotherapeutic strategies. *Immunotherapy.* 2018;10:999-1010.

63. Zheng P-P, Kros JM, Li J. Approved CAR T cell therapies: ice bucket challenges on glaring safety risks and long-term impacts. *Drug Discovery Today.* 2018;23:1175-1182.

64. Liu G, Swierczewska M, Niu G, Zhang X, Chen X. Molecular imaging of cell-based cancer immunotherapy. *Molecular bioSystems.* 2011;7:993-1003.

65. Emami-Shahri N, Papa S. Dynamic imaging for CAR-T-cell therapy. *Biochemical Society Transactions.* 2016;44:386-390.

66. Beckford Vera DR, Smith CC, Bixby LM, et al. Immuno-PET imaging of tumor-infiltrating lymphocytes using zirconium-89 radiolabeled anti-CD3 antibody in immune-competent mice bearing syngeneic tumors. *PLoS ONE.* 2018;13:e0193832.

67. Rashidian M, Ingram JR, Dougan M, et al. Predicting the response to CTLA-4 blockade by longitudinal noninvasive monitoring of CD8 T cells. *J Exp Med.* 2017;214:2243-2255.

68. Seo JW, Tavaré R, Mahakian LM, et al. CD8+ T-cell density imaging with 64Cu-labeled cys-diabody informs immunotherapy protocols. *Clinical Cancer Research.* 2018.

69. Tavaré R, Escuin-Ordinas H, Mok S, et al. An Effective Immuno-PET Imaging Method to Monitor CD8-Dependent Responses to Immunotherapy. *Cancer Res.* 2016;76:73-82.

70. Hartimath SV, Draghiciu O, van de Wall S, et al. Noninvasive monitoring of cancer therapy induced activated T cells using [18F]FB-IL-2 PET imaging. *OncoImmunology.* 2017;6:e1248014.

71. Larimer BM, Wehrenberg-Klee E, Dubois F, et al. Granzyme B PET Imaging as a Predictive Biomarker of Immunotherapy Response. *Cancer research.* 2017;77:2318-2327.

72. Ehlerding EB, England CG, Majewski RL, et al. ImmunoPET imaging of CTLA-4 expression in mouse models of non-small cell lung cancer. *Molecular pharmaceutics.* 2017;14:1782-1789.

73. Ehlerding EB, Lee HJ, Jiang D, et al. Antibody and fragment-based PET imaging of CTLA-4+ T-cells in humanized mouse models. *Am J Cancer Res.* 2019;9:53-63.

74. McIntosh Brian E, Brown Matthew E, Duffin Bret M, et al. Nonirradiated NOD,B6.SCID Il2rγ(−/−)Kit(W41/W41) (NBSGW) Mice Support Multilineage Engraftment of Human Hematopoietic Cells. *Stem Cell Reports.* 2015;4:171-180.

75. Stabin MG, Sparks RB, Crowe E. OLINDA/EXM: the second-generation personal computer software for internal dose assessment in nuclear medicine. *J Nucl Med.* 2005;46:1023-1027.

76. The 2007 Recommendations of the International Commission on Radiological Protection. ICRP publication 103. *Ann ICRP.* 2007;37:1-332.

77. Levy S, Nagler A, Okon S, Marmary Y. Parotid salivary gland dysfunction in chronic graft-versus-host disease (cGVHD): a longitudinal study in a mouse model. *Bone Marrow Transplant.* 2000;25:1073-1078.

78. Sharma SK, Chow A, Monette S, et al. Fc-Mediated Anomalous Biodistribution of Therapeutic Antibodies in Immunodeficient Mouse Models. *Cancer Research.* 2018;78:1820-1832.

79. Lynch TJ, Bondarenko I, Luft A, et al. Ipilimumab in Combination With Paclitaxel and Carboplatin As First-Line Treatment in Stage IIIB/IV Non–Small-Cell Lung Cancer: Results From a Randomized, Double-Blind, Multicenter Phase II Study. *J Clin Oncol.* 2012;30:2046-2054.

80. Garon EB, Rizvi NA, Hui R, et al. Pembrolizumab for the Treatment of Non–Small-Cell Lung Cancer. *New England Journal of Medicine.* 2015;372:2018-2028.

81. Keating GM. Nivolumab: A Review in Advanced Nonsquamous Non-Small Cell Lung Cancer. *Drugs.* 2016;76:969-978.

82. Contardi E, Palmisano GL, Tazzari PL, et al. CTLA-4 is constitutively expressed on tumor cells and can trigger apoptosis upon ligand interaction. *Int J Cancer.* 2005;117:538-550.

83. Salvi S, Fontana V, Boccardo S, et al. Evaluation of CTLA-4 expression and relevance as a novel prognostic factor in patients with non-small cell lung cancer. *Cancer Immunol Immunother.* 2012;61:1463-1472.

84. CTLA-4. 2017.

85. Zhang Y, Hong H, Engle JW, et al. Positron Emission Tomography Imaging of CD105 Expression with a 64Cu-Labeled Monoclonal Antibody: NOTA Is Superior to DOTA. *PLOS ONE.* 2011;6:e28005.

86. Wright BD, Lapi SE. Designing the Magic Bullet? The Advancement of Immuno-PET into Clinical Use. *Journal of Nuclear Medicine.* 2013;54:1171-1174.

87. Bailly C, Cléry P-F, Faivre-Chauvet A, et al. Immuno-PET for Clinical Theranostic Approaches. *International Journal of Molecular Sciences.* 2017;18:57.

88. Ingram JR, Blomberg OS, Rashidian M, et al. Anti–CTLA-4 therapy requires an Fc domain for efficacy. *Proceedings of the National Academy of Sciences of the United States of America.* 2018;115:3912-3917.

89. Arce Vargas F, Furness AJS, Litchfield K, et al. Fc Effector Function Contributes to the Activity of Human Anti-CTLA-4 Antibodies. *Cancer Cell.* 2018;33:649-663.e644.

90. Young NA, Wu LC, Bruss M, et al. A chimeric human-mouse model of Sjogren's syndrome. *Clin Immunol.* 2015;156:1-8.

91. Nervi B, Rettig MP, Ritchey JK, et al. Factors affecting human T cell engraftment, trafficking, and associated xenogeneic graft-vs-host disease in NOD/SCID beta2mnull mice. *Exp Hematol.* 2007;35:1823-1838.

92. Sandhu JS, Gorczynski R, Shpitz B, Gallinger S, Nguyen HP, Hozumi N. A human model of xenogeneic graft-versus-host disease in SCID mice engrafted with human peripheral blood lymphocytes. *Transplantation.* 1995;60:179-184.

93. Amos SM, Duong CPM, Westwood JA, et al. Autoimmunity associated with immunotherapy of cancer. *Blood.* 2011;118:499-509.

94. Sharma V, McNeill JH. To scale or not to scale: the principles of dose extrapolation. *Br J Pharmacol.* 2009;157:907-921.

95. Casey JL, King DJ, Pedley RB, et al. Clearance of yttrium-90-labelled anti-tumour antibodies with antibodies raised against the 12N4 DOTA macrocycle. *British Journal of Cancer.* 1998;78:1307-1312.

96. Lin JH. Applications and limitations of interspecies scaling and in vitro extrapolation in pharmacokinetics. *Drug Metab Dispos.* 1998;26:1202-1212.

97. Society AC. Cancer Facts & Figures 2016. *American Cancer Society.* 2016.

98. Hernandez R, Sun H, England CG, et al. CD146-targeted immunoPET and NIRF Imaging of Hepatocellular Carcinoma with a Dual-Labeled Monoclonal Antibody. *Theranostics.* 2016;6:1918-1933.

99. Ikebuchi R, Konnai S, Okagawa T, et al. Blockade of bovine PD-1 increases T cell function and inhibits bovine leukemia virus expression in B cells in vitro. *Vet Res.* 2013;44:59.

100. Soret M, Bacharach SL, Buvat I. Partial-Volume Effect in PET Tumor Imaging. *Journal of Nuclear Medicine.* 2007;48:932-945.

101. Natarajan A, Mayer AT, Xu L, Reeves RE, Gano J, Gambhir SS. Novel Radiotracer for ImmunoPET Imaging of PD-1 Checkpoint Expression on Tumor Infiltrating Lymphocytes. *Bioconjug Chem.* 2015;26:2062-2069.

102. Hayashi T. Dysfunction of lacrimal and salivary glands in Sjogren's syndrome: nonimmunologic injury in preinflammatory phase and mouse model. *J Biomed Biotechnol.* 2011;2011:407031.

103. Reynders K, De Ruysscher D. Tumor infiltrating lymphocytes in lung cancer: a new prognostic parameter. *J Thorac Dis.* 2016;8:E833-835.

104. Joseph RW, Elassaiss-Schaap J, Wolchock JD, et al. Baseline tumor size and PD-L1 expression are independently associated wtih clinical outcomes in patients with metastatic melanoma treated with pembrolizumab (MK-3475). *Pigment Cell Melanoma Res.* 2014;27.

105. Li Y, Liang L, Dai W, et al. Prognostic impact of programed cell death-1 (PD-1) and PD-ligand 1 (PD-L1) expression in cancer cells and tumor infiltrating lymphocytes in colorectal cancer. *Molecular Cancer.* 2016;15:55.

106. Hernandez R, Sun H, England CG, et al. CD146-targeted immunoPET and NIRF Imaging of Hepatocellular Carcinoma with a Dual-Labeled Monoclonal Antibody. *Theranostics.* 2016;6:1918-1933.

107. Vosjan MJWD, Perk LR, Visser GWM, et al. Conjugation and radiolabeling of monoclonal antibodies with zirconium-89 for PET imaging using the bifunctional chelate p-isothiocyanatobenzyl-desferrioxamine. *Nature Protocols.* 2010;5:739.

108. Hong H, Severin GW, Yang Y, et al. Positron emission tomography imaging of CD105 expression with(89) Zr-Df-TRC105. *European journal of nuclear medicine and molecular imaging.* 2012;39:138-148.

109. Ellison PA, Valdovinos HF, Graves SA, Barnhart TE, Nickles RJ. Spot-welding solid targets for high current cyclotron irradiation. *Applied radiation and isotopes : including data, instrumentation and methods for use in agriculture, industry and medicine.* 2016;118:350-353.

110. Wang A, Wang HY, Liu Y, et al. The prognostic value of PD-L1 expression for non-small cell lung cancer patients: A meta-analysis. *European Journal of Surgical Oncology (EJSO).* 2015;41:450-456.

111. Pan Z-K, Ye F, Wu X, An H-X, Wu J-X. Clinicopathological and prognostic significance of programmed cell death ligand1 (PD-L1) expression in patients with non-small cell lung cancer: a meta-analysis. *Journal of Thoracic Disease.* 2015;7:462-470.

112. Kalia M. Biomarkers for personalized oncology: recent advances and future challenges. *Metabolism.* 2015;64:S16-S21.

113. Meng X, Huang Z, Teng F, Xing L, Yu J. Predictive biomarkers in PD-1/PD-L1 checkpoint blockade immunotherapy. *Cancer Treatment Reviews.* 2015;41:868-876.

114. Deng L, Liang H, Burnette B, et al. Irradiation and anti–PD-L1 treatment synergistically promote antitumor immunity in mice. *The Journal of Clinical Investigation.* 2014;124:687-695.

115. Dovedi SJ, Illidge TM. The antitumor immune response generated by fractionated radiation therapy may be limited by tumor cell adaptive resistance and can be circumvented by PD-L1 blockade. *Oncoimmunology.* 2015;4:e1016709.

116. Zamarin D, Postow MA. Immune checkpoint modulation: Rational design of combination strategies. *Pharmacology & Therapeutics.* 2015;150:23-32.

117. Lesniak WG, Chatterjee S, Gabrielson M, et al. PD-L1 Detection in Tumors Using [(64)Cu]Atezolizumab with PET. *Bioconjugate chemistry.* 2016;27:2103-2110.

118. Donnelly DJ, Smith RA, Morin P, et al. Synthesis and Biologic Evaluation of a Novel 18F-Labeled Adnectin as a PET Radioligand for Imaging PD-L1 Expression. *Journal of Nuclear Medicine.* 2018;59:529-535.

119. Li D, Cheng S, Zou S, et al. Immuno-PET Imaging of (89)Zr Labeled Anti-PD-L1 Domain Antibody. *Mol Pharm.* 2018;15:1674-1681.

120. González Trotter DE, Meng X, McQuade P, et al. In Vivo Imaging of the Programmed Death Ligand 1 by 18F PET. *Journal of Nuclear Medicine.* 2017;58:1852-1857.

121. Velcheti V, Schalper KA, Carvajal DE, et al. Programmed death ligand-1 expression in non-small cell lung cancer. *Laboratory Investigation.* 2013;94:107.

122. Ahmed S, Sami A, Xiang J. HER2-directed therapy: current treatment options for HER2-positive breast cancer. *Breast Cancer.* 2015;22:101-116.

123. Das R, Verma R, Sznol M, et al. Combination therapy with anti–CTLA-4 and anti–PD-1 leads to distinct immunologic changes in vivo. *J Immunol.* 2015;194:950-959.

124. Boswell CA, Mundo EE, Zhang C, et al. Differential effects of predosing on tumor and tissue uptake of an 111In-labeled anti-TENB2 antibody-drug conjugate. *J Nucl Med.* 2012;53:1454-1461.

125. Kobayashi H, Choyke PL, Ogawa M. Monoclonal antibody-based optical molecular imaging probes; considerations and caveats in chemistry, biology and pharmacology. *Current opinion in chemical biology.* 2016;33:32-38.

126. Lee HJ, Ehlerding EB, Cai W. Antibody-based tracers for PET/SPECT imaging of chronic inflammatory diseases. *ChemBioChem.*0.